

UC Santa Cruz

UC Santa Cruz Electronic Theses and Dissertations

Title

Exploration of Carbonaceous Materials for Supercapacitors

Permalink

<https://escholarship.org/uc/item/69c7r2rx>

Author

Liu, Tianyu

Publication Date

2017

Copyright Information

This work is made available under the terms of a Creative Commons Attribution License, available at <https://creativecommons.org/licenses/by/4.0/>

Peer reviewed|Thesis/dissertation

UNIVERSITY OF CALIFORNIA
SANTA CRUZ

**EXPLORATION OF CARBONACEOUS MATERIALS FOR
SUPERCAPACITORS**

A dissertation submitted in partial satisfaction
of the requirements for the degree of

DOCTOR OF PHILOSOPHY

in

CHEMISTRY

by

Tianyu Liu

June 2017

The Dissertation of Tianyu Liu is
approved:

Professor Yat Li, chair

Professor Scott R. J. Oliver

Professor Jin Zhong Zhang

Tyrus Miller
Vice Provost and Dean of Graduate Studies

Copyright © by

Tianyu Liu

2017

Table of Contents

List of Figures.....	vii
Abstract.....	xvi
Dedication.....	xix
Acknowledgements.....	xx
Chapter 1 – Introduction of Supercapacitors.....	1
Abstract.....	1
Background.....	1
Capacitance.....	4
Charge Storage Mechanism.....	4
Calculations.....	8
Carbonaceous Materials as Supercapacitor Electrodes – An Overview.....	13
Hierarchical Porous Structure.....	15
References.....	17
Chapter 2 –	
Hierarchical Porous Carbon Foams Derived from Potassium Carbonate-embedded Chitosan Aerogels for Electrical Double Layer Capacitors.....	20
Abstract.....	20
Introduction.....	21
Experimental Section.....	24
Results and Discussions.....	27

Conclusions.....	47
References.....	48
Chapter 3 –Three-dimensional Carbon Foams with a Multiscale Pore Network	
Boosts Ultrafast Charging Capacitance.....	55
Abstract.....	55
Introduction.....	55
Experimental Section.....	58
Results and Discussions.....	62
Conclusions.....	85
References.....	86
Chapter 4 – 3D-printed Supercapacitors with Graphene Electrodes.....	
Abstract.....	91
Introduction.....	92
Experimental Section.....	95
Results and Discussions.....	99
Conclusions.....	116
References.....	117
Chapter 5 – Ion-intercalation Induced Capacitance Improvement for	
Graphene-based Supercapacitor Electrodes.....	126
Abstract.....	126
Introduction.....	126

Experimental Section.....	130
Results and Discussions.....	132
Conclusions.....	150
References.....	151
Chapter 6 – Carbon Coated Polyaniline and Polypyrrole Pseudocapacitor	
Electrode with Excellent Stability.....	155
Abstract.....	155
Introduction.....	156
Experimental Section.....	158
Results and Discussions.....	160
Conclusions.....	175
References.....	175
Chapter 7 – Pushing the Cycling Stability Limit of Polypyrrole for	
Supercapacitors.....	180
Abstract.....	180
Introduction.....	180
Experimental Section.....	183
Results and Discussions.....	186
Conclusions.....	201
References.....	201
Chapter 8 – Outlook.....	205

References.....209

List of Figures

Chapter 1

Figure 1.1 Ragone plot and Structure schematic of a supercapacitor.

Figure 1.2 Schematic of the working principle of a supercapacitor

Figure 1.3 Schematic of electrical double layer structure

Figure 1.4 Schematic of three typical pseudo-capacitive reactions

Figure 1.5 Hierarchical porosity

Chapter 2

Figure 2.1 Schematic of the synthesis of porous carbon foams

Figure 2.2 Cross-link reaction and characterizations of cross-linked chitosan gels

Figure 2.3 Schematic of the formation mechanism of porous chitosan aerogels composed of chitosan sheets.

Figure 2.4 Thermo-gravimetric curve of the glutaraldehyde cross-linked chitosan aerogel

Figure 2.5 SEM images of the porous carbon foam and the plain carbon foam

Figure 2.6 SEM images collected from the carbon sheet edge of the porous carbon foam and the plain carbon foam

Figure 2.7 (a) SEM image of the carbon monolith prepared without the cross-linker

Figure 2.8 (a) Nitrogen adsorption-desorption isotherms collected for the porous

carbon foam and the plain carbon foam

Figure 2.9 Pore size distribution of the porous carbon foam and the plain carbon foam

Figure 2.10 TEM images of the porous carbon foam

Figure 2.11 Potential vs. current plots collected from the porous carbon foam and the plain carbon foam

Figure 2.12 Electrochemical performance of the plain carbon foam

Figure 2.13 Electrochemical performance of the porous carbon foam

Figure 2.14 Equivalent electric circuit used for EIS data fitting

Figure 2.15 Cycling stability performance of the porous carbon foam

Figure 2.16 Electrochemical performance of the PCF//PCF symmetric supercapacitor with PVA-KOH as gel electrolyte.

Figure 2.17 Flexibility of the PCF//PCF symmetric supercapacitor

Figure 2.18 Ragone plot of the PCF//PCF device

Chapter 3

Figure 3.1 Schematic of the synthesis protocol Structural characterizations of the CF-SiO₂, CF, and CF-MSP

Figure 3.2 Structural characterizations of the silica spheres

Figure 3.3 Porous structure of CF-MSP

Figure 3.4 Porous structure of CF

- Figure 3.5** TEM Characterizations of CF-MSP
- Figure 3.6** Physical characterizations of CF-MSP
- Figure 3.7** Images of the wetting process
- Figure 3.8** XPS characterization of CF
- Figure 3.9** Electrochemical performance of CF-MSP
- Figure 3.10** Volumetric capacitance of CF-MSP
- Figure 3.11** Cycling stability performance of CF-MSP
- Figure 3.12** Capacitance differentiation of CF-MSP
- Figure 3.13** Equivalent electric circuit employed for fitting Nyquist plots
- Figure 3.14** Synthesis protocols of CF-1, CF-2 and CF-3
- Figure 3.15** Role of pores on capacitance and rate capability of carbon foam
- Figure 3.16** Porous structures of CF-1 and CF-2
- Figure 3.17** SEM images of CF-1, CF-2 and CF-3
- Figure 3.18** Comparison of rate capability of CF-1, CF-2 and CF-3 with CF-MSP
- Figure 3.19** Electrochemical performance of the CF-MSP//CF-MSP symmetric supercapacitor
- Figure 3.20** Ragone plot of the CF-MSP//CF-MSP symmetric supercapacitor
- Figure 3.21** Flexibility of the CF-MSP//CF-MSP symmetric supercapacitor
- Figure 3.22** Gravimetric capacitance, volumetric capacitance and cycling stability of the CF-MSP//CF-MSP symmetric supercapacitor
- Figure 3.23** Rate capability performance of the CF-MSP//CF-MSP symmetric

supercapacitor

Chapter 4

Figure 4.1 Rheological properties of printing inks

Figure 4.2 Schematic illustration of 3D-printing process

Figure 4.3 SEM images collected for different 3D-GCAs

Figure 4.4 Cyclic voltammograms and constant-current charge and discharge profiles of different 3D-GCAs

Figure 4.5 Electrochemical performance of different 3D-GCAs

Figure 4.6 The cycling stability of GO-GNP-SiO₂-2

Figure 4.7 Comparison of electrochemical performance of bulk electrode (with the same composition as GO-GNP-SiO₂-2) and GO-GNP-SiO₂-2

Figure 4.8 SEM images of the bulk pallet with the same composition as GO-GNP-SiO₂-2

Figure 4.9 Electrochemical performance of the 3D-GCA symmetric supercapacitor

Figure 4.10 Gravimetric capacitance and volumetric capacitance of the 3D-GCA symmetric supercapacitor

Figure 4.11 Energy density and power density of the 3D-GCA symmetric supercapacitor

Figure 4.12 Comparison, in a Ragone plot, of the gravimetric energy and power density of the 3D-GCA symmetric supercapacitors and other previously reported symmetric supercapacitors

Chapter 5

Figure 5.1 Schematic illustration of the three-step electrochemical treatment process.

Figure 5.2 Schematic illustration of stage II and I intercalation compound

Figure 5.3 Structural characterizations of the three-step ion intercalation process

Figure 5.4 Structural and elemental characterizations of the treated graphitic paper

Figure 5.5 Comparison of the surface area between untreated graphitic paper and treated graphitic paper

Figure 5.6 SEM images showing the surface morphology of graphitic paper with only positive bias or negative bias treatment

Figure 5.7 SEM image of a graphitic fiber treated with tetra-*n*-butylammonium perchlorate

Figure 5.8 XPS survey spectra of the untreated and the treated graphitic papers

Figure 5.9 Electrochemical performance of the treated graphitic papers

Figure 5.10 Cyclic voltammograms of the graphitic papers treated with different conditions

Figure 5.11 Cyclic voltammograms of the treated graphitic papers at large scan rates

Figure 5.12 Equivalent electric circuit used for fitting of Nyquist plots

Figure 5.13 Electrochemical impedance spectroscopy of the treated and untreated graphitic papers

Figure 5.14 Electrochemical performance of the treated 3D-printed graphene aerogel

Figure 5.15 Cyclic voltammograms and constant-current charge and discharge profiles of the treated and untreated 3D-printed graphene aerogels

Figure 5.16 SEM images of the treated and untreated 3D-printed graphene aerogels

Chapter 6

Figure 6.1 Raman spectra of as-deposited polyaniline and polypyrrole

Figure 6.2 Schematic of the carbon coating protocol and SEM images of carbon coated polypyrrole

Figure 6.3 Cycling performance of bare conducting polymers and carbon coated conducting polymer

Figure 6.4 SEM images collected for bare conducting polymers before and after the long-term stability test

Figure 6.5 Stability performance of PANI@C-1h and PPy@C-1h

Figure 6.6 SEM images collected for carbon coated conducting polymer before and after the long-term stability test

Figure 6.7 Histograms compare the areal capacitance of PANI@C-3h and PPy@C-3h

Figure 6.8 Trasatti method analysis of carbon coated conducting polymers

Figure 6.9 Plots of reciprocal of areal capacitance against square root of scan rate for the carbon coated conducting polymers

Figure 6.10 Cyclic voltammograms and constant-current charge and discharge profiles of the carbon coated conducting polymers

Figure 6.11 Rate capability performance and electrochemical impedance spectroscopy of the carbon coated conducting polymers

Figure 6.12 Equivalent circuit model used for electrochemical impedance spectroscopy data fitting.

Figure 6.13 Comparison of the electrochemical impedance spectroscopy collected for the bare conducting polymers and hydrothermal treated conducting polymer

Chapter 7

Figure 7.1 Molecular structure of β -naphthalene sulfonate anion and sulfate anion

Figure 7.2 Cyclic voltammograms and cycling stability of PPy-S, FEG/PPy-S and FEG/PPy-NS

Figure 7.3 Rate capability curves collected for PPy-S, FEG/PPy-S and FEG/PPy-NS

Figure 7.4 SEM image of untreated graphite foil and FEG

Figure 7.5 SEM images of PPy-S, FEG/PPy-S and FEG/PPy-NS collected before and after the long-term stability test

Figure 7.6 Cycling stability of PPy-S thin film electrode

Figure 7.7 Elemental analyses before and after the long-term stability test

Figure 7.8 XPS characterization of FEG/PPy-S and FEG/PPy-NS

Figure 7.9 C 1s spectra of FEG/PPy-S and FEG/PPy-NS before and after the long-term cycling stability test

Figure 7.10 EIS spectra of PPy-S, FEG/PPy-S and FEG/PPy-NS before and after the long-term cycling stability test

Figure 7.11 SEM image of FEG/MnO₂

Figure 7.12 Electrochemical performance of the FEG/PPy-NS// FEG/MnO₂ asymmetric supercapacitor

Figure 7.13 Cycling stability, energy density and power density of the FEG/PPy-NS// FEG/MnO₂ asymmetric supercapacitor

Figure 7.14 Stability performance of PPy-S//FEG/MnO₂ and FEG/PPy-S//FEG/MnO₂ pseudocapacitors

Chapter 8

Figure 8.1 Comparison of capacitance among conventional carbons, hierarchical porous carbons and the future goal

Abstract

Carbonaceous Materials for Supercapacitors

by

Tianyu Liu

Energy storage techniques are critical for feasible implantation of sustainable energy, as most sustainable energy sources suffer from intermittent nature, uneven geographically distribution and unstable natural availability. Supercapacitors are a family of energy storage devices capable of storing electric energy converted from sustainable energy such as solar energy and wind energy. They distinguish from another family of energy storage devices, *i.e.*, batteries, by their ability to be fully charged and discharged in seconds. The characteristics of two electrodes in supercapacitors largely dictate the overall performance of supercapacitors. Specifically, developing electrode materials with excellent electrical conductivity, large surface area and exceptional long-term stability (or ultra-long lifetimes) is attracting extensive research effort all over the world to push the performance of supercapacitors to a new height.

The scope of this dissertation covers my past five years of study on design and synthesis of carbonaceous materials, with their applications in supercapacitors. Carbonaceous materials refer to materials composed of and contain carbon. Amorphous carbon shell, graphene, 3D-printed graphene aerogel, 3D hierarchical

porous carbon foams and conducting polymers are included in the dissertation. They share common advantages such as they are electrically conductive, economically viable, easy to be processed into versatile architectures with ultra-large surface area ($>1000 \text{ m}^2 \text{ g}^{-1}$).

This dissertation will present my research works associated with carbonaceous materials for supercapacitors carried out in the past five years. Chapter one sets the background for energy storage and introduces key concepts of supercapacitors. Chapter two and chapter three present hierarchical porous carbon foams derived from chitosan, with modifications by incorporation of potassium carbonate (chapter two) and silica hard templates (chapter three), that exhibited superior capacitive performance to other state-of-the-art carbon electrodes. Chapter four introduces a 3D graphene aerogel wood-pile lattice with orderly distributed macropores. This graphene aerogel structure was fabricated by direct ink writing (one of 3D printing techniques). Supercapacitors using these 3D-printed graphene aerogel electrodes with thickness on the order of millimeters display exceptional capacitive retention (approximately 90% from 0.5 to 10 A g^{-1}) and power density ($>4 \text{ kW kg}^{-1}$) that equal or exceed those of reported devices made with electrodes 10-100 times thinner. A three-step ion-intercalation method that can further boost the capacitance of the 3D printed graphene aerogel by two times is discussed in chapter five. Chapter six and seven deal with increasing cycling stability of typical conjugated polymers with capacitive activity, *e.g.*,

polyaniline and polypyrrole by carbonaceous materials. Finally in chapter eight, an outlook on carbonaceous materials will be given. Specifically, current challenges and opportunities for developing hierarchical porous carbons as high-performance supercapacitor electrodes are discussed.

Dedication

DEDICATED

TO

MY PARENTS, ZHAOCHENG LIU & MIN CHEN

Acknowledgements

My five-year graduate study at Department of Chemistry and Biochemistry, University of California, Santa Cruz has shaped me into a mature chemist. Without the support from numerous people, I certainly could not reach this moment. I would like to take this opportunity to express my sincere acknowledgements to all people who motivated, advised, encouraged and helped me along the way.

I would first sincerely thank my advisor, Professor Yat Li. I thank you for your professional guidance in my research. His motivation-driven research philosophy helps me in evaluating whether a project is promising and also practices me about critical thinking. This philosophy has rooted deep in mind and I will continue practicing in my future career. I thank him for your encouragement all the time: Chancellor's Graduate Teaching Fellowship, Chancellor's Dissertation-year Fellowship, Materials Research Society Graduate Student Award, and being reviewers for international peer-reviewed journals. Without your encouragement and recommendation, I could not achieve them. I also thank him for his support in allowing me to expand my interest beyond the lab. I really enjoyed working with him in the I-Corps program, giving guest lectures for your courses and to the undergraduates in the UCSC Chemistry Club, and presenting seminars in local high schools. All these experiences reinforce my presentation, communicating and teaching skills.

My dissertation committee members, Professor Scott Oliver, Professor Yat Li and Professor Jin Zhong Zhang also played a critical role in my past five years. Their strictness and high standards have always been the motivation to reach and push my limit. Thanks Professor Frank Bridges from Department of Physics for serving as an outside committee member and his careful evaluation about my oral exam materials. I still have a fresh memory that he printed out my abstract, edited sentence by sentence and gave me valuable suggestions on how to improve my scientific writing.

I am fortunate to work with and learn from many talented and dedicated peers during my time at University of California, Santa Cruz. I appreciate all the help from doctors who graduated from the Li Lab: Dr. Gongming Wang, Dr. Yichuan Ling, Dr. Hanyu Wang, Dr. Yi Yang; graduate students who are working in the Li Lab: Tianyi Kou, Bin Yao, Daniel Bulmanh and Wang Xiao; scholars who joined or are visiting in the Li Lab: Prof. Xihong Lu, Dr. Ying-Chih Pu, Dr. Feng Luan, Prof. Dingsheng Yuan, Dr. Teng Zhai, Dr. Shan Jiang, Dr. Wei-Hao Lin, Yuhang Wang, Prof. Feng Zhang, Dr. Yang Yang, Mingyang Li, Yu Song, Dr. Jing Zhang, Huarong Peng, Zihang Huang, Prof. Changjin Tang and Xiaoli Fan; Undergraduates who worked with me: Lauren Finn, Edgar Collazo, Cecilia Condes, Prescott Railey and Martina Morelli; Peers from Prof. Jin Zhong Zhang's Lab: Staci Adams, Sarah Lindley, Dr. Binbin Luo, Sara Bonabi, Evan Vickers, and A'Lester Allen; Peers from Dr. Alexander Ayzner's Lab: Michael Roders, Will

Hollingsworth, Carmen Segura, Vincent Duong, Pamela Schleissner and Gregory Pitch; Peers from Prof. Shaowei Chen's Lab: Dr. Yang Song, Dr. Peiguang Hu, Dr. Christopher Deming, Jia Lu, Mauricio Rojas-Andrade, Limei Chen, Samantha Sweeney, Rene Mercado, Gustavo Chata, Yi Peng and Bingzhang Lu; Peers from Prof. Pradip Mascharak's lab: Jorge Jimenez, Dr. Indranil Chakraborty and Miguel Pinto. Prof. Ilan Benjamin, John Karnes, Dr. Yuan Ping also helped me with understanding simulation works. Your presence makes my research colorful and joyful.

I cannot complete my research works without the professional external collaborators. I greatly appreciate Prof. Yexiang Tong and his students for their support in material characterizations; Prof. Xiaoxia Liu and her research group for letting me to participate in their research projects; Scientists at Lawrence Livermore National Lab: Dr. Fang Qian, Dr. Cheng Zhu, Dr. Marcus Worsley, Dr. Swetha Chandrasekaran, Dr. Eric Duoss, Dr. Joshua Kuntz and Dr. Christopher Spadaccini, with whom we worked closely on the project of 3D-printed supercapacitors.

Teaching is another crucial part in my time as a graduate student. I thank Prof. Eugene Switkes, Dr. Gabriel Mednick and Dr. Alexander Azyner for their kind help and valuable suggestions in developing my pedagogical teaching style. I also thank all the students in my discussion sections, as their motivation and honest feedback always propel my improvement.

Last but not least, I need to thank my family, especially my parents. Without their support and understanding, I cannot come here, started my research and make progress. Though I went back to visit them once per year, I know it is far less than enough. I owe them too much but I cherish everything they have done for me. I love you all.

The text of this dissertation includes reprints of the following previously published materials:

1. **Liu T.**, Lauren F., Yu M., Wang H., Zhai T., Lu X., Tong Y. and Li Y. Polyaniline and Polypyrrole Pseudocapacitor Electrodes with Excellent Cycling Stability, *Nano Lett.*, 14, 2522–2527 (2014)
2. Song Y., **Liu T. (co-first author)**, Xu X., Feng D., Li Y., Liu X. Pushing the Cycling Stability Limit of Polypyrrole for Supercapacitors, *Adv. Funct. Mater.*, 25, 4626-4632 (2015)
3. Zhu C., **Liu T. (co-first author)**, Qian F., Han T., Duoss E., Kuntz J., Spadaccini C., Worsley M., Li Y. Supercapacitors Based on 3D Hierarchical Graphene Aerogels with Periodical Macropores, *Nano Lett.*, 16, 3448-3456 (2016)
4. **Liu T.**, Zhu C., Kou T., Worsley M., Qian F., Condes C., Duoss E., Spadaccini C., Li Y. Ion Intercalation Induced Capacitance Improvement for Graphene-based Supercapacitor Electrodes, *ChemNanoMater*, 2, 635-641 (2016)
5. Zhang F., **Liu T. (co-first author)**, Hou G., Kou T., Yue L., Guan R., Li Y.

Hierarchical Porous Carbon Foams for Electrical Double Layer Capacitors, *Nano Res.*, 9, 2875-2888 (2016)

6. Zhang F., **Liu T.** (co-first author), Li M., Yu M., Luo Y., Tong Y., Li Y. Multiscale Pore Network Boosts Capacitance of Carbon Electrodes for Ultrafast Charging, *Nano Lett.*, 17, 3097-3104 (2017)

Chapter 1

Introduction of Supercapacitors

Abstract

Feasible utilization of sustainable energy calls for efficient and reliable energy storage devices. Supercapacitors represent a class of energy storage devices that are capable of storing electric energy converted from sustainable energy sources. They distinguish from batteries by their ability to be charged and discharged much rapidly. Performance of a supercapacitor is largely dictated by its electrode performance. Carbon-based materials, including versatile carbons (*e.g.*, carbon dots, graphene, 3D carbon foams etc.) and carbonaceous materials (*e.g.*, organic compounds and polymers), receive extensive research effort for electrochemical energy storage. This chapter presents background of energy storage, fundamental concepts of supercapacitors, equations for calculations as well as a brief overview of the research progress of carbon based materials for supercapacitors.

1.1 Background

With the ever growing population, diminishing supplies of fossil fuels, and proliferating environmental pollutions, there is an urgent need for clean and sustainable energy. Extensive research efforts have been devoted for technology development to harvest and convert sustainable energies to electricity that can be readily used for electronics. However, due to the intermittent nature, unevenly geographical distribution and unstable natural availability of these sustainable

energy resources, reliable and efficient energy storage technology is required for viable utilization of sustainable energy.

Batteries and supercapacitors (*a.k.a.* electrochemical capacitors or ultra-capacitors) are two major energy storage devices. Figure 1.1a shows the Ragone plot that compares the energy density and power density of supercapacitors and various batteries.¹ Supercapacitors distinguish from batteries by their ultrahigh power density, *i.e.*, the ability to be rapidly charged and discharged, at a timescale of seconds. Therefore, supercapacitors target applications where high power uptake or delivery and pulsed energy are needed: immediate power supply and recovery of stop-and-go systems, industrial energy management systems and electric vehicles (mostly used in conjunction with lithium-ion batteries), *etc.*^{2,3} Figure 1.1b depicts the major components of a supercapacitor, which consists of a positive electrode (*a.k.a.* cathode), a negative electrode (*a.k.a.* anode), a separator in between the two electrodes to prevent electric short circuit, and an electrolyte filled inside the package, serving as an ion reservoir. Commonly used electrolytes of lab-developed supercapacitors include aqueous solutions, organic solutions and ionic liquids.⁴ Commercial products use organic electrolytes, such as ethylene carbonate and propylene carbonate exclusively.⁵

Figure 1.2 depicts the working principle of a supercapacitor. Upon charging, electrons migrate from the negative electrode to the positive electrode driven by

external bias (supplied by power sources such as electrochemical workstation). Simultaneously in the electrolyte, cations and anions diffuse to the positive and negative electrode surface, respectively, under the driving force of the electric field between the positive and negative electrodes. Upon discharging, electrons spontaneously move from the positive electrode, across and power the external load (*e.g.*, an electronic), and eventually are injected into the negative electrode. At the same time,

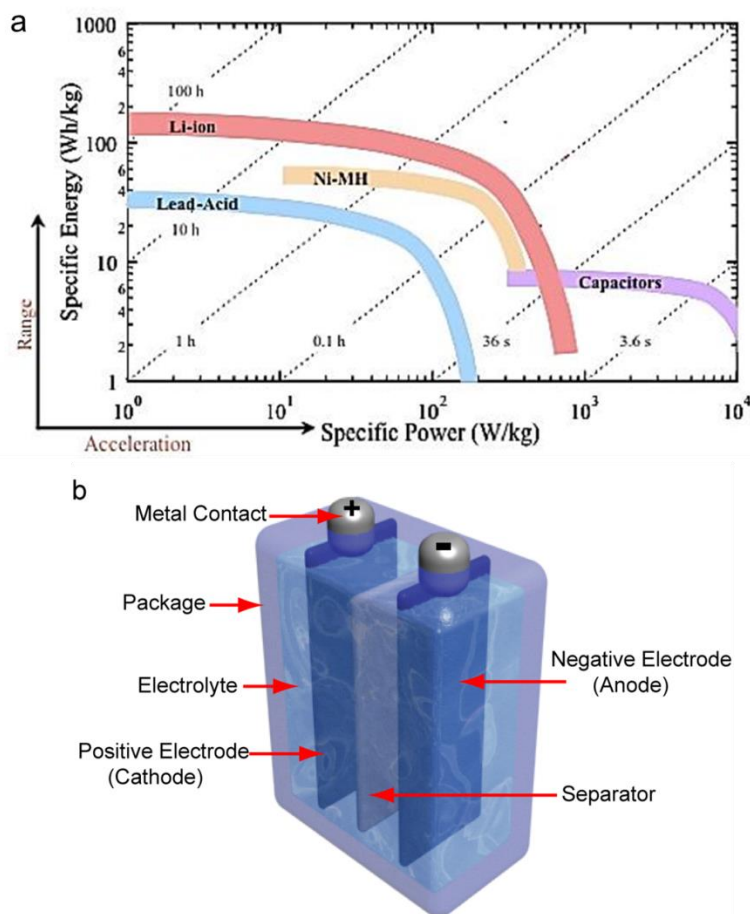


Figure 1.1 (a) Ragone plot compares the specific energy density and specific power density of supercapacitors and other batteries. Reproduced with permission.¹ Copyright 2015, American Chemical Society. (b) Structure schematic of a supercapacitor.

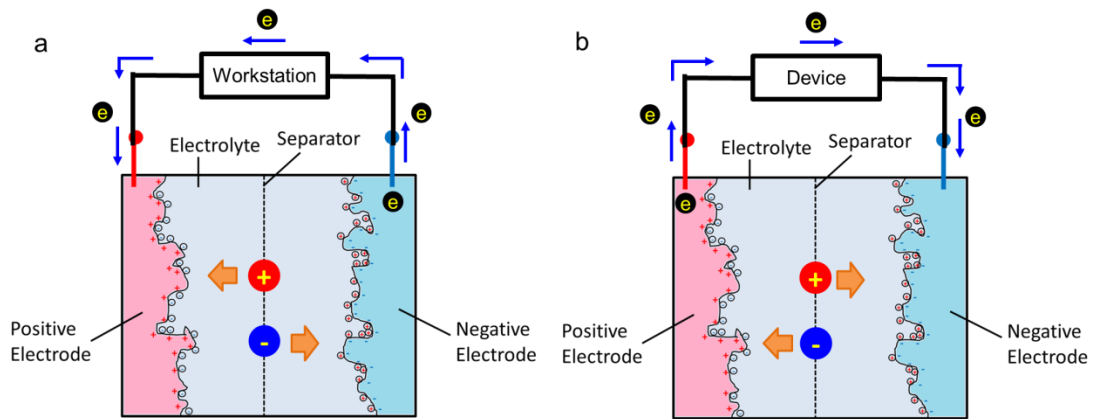


Figure 1.2 Working principle of a supercapacitor: (a) charging process and (b) discharging process.

1.2 Capacitance

Capacitance is a quantity that measures how much charge a supercapacitor can take. The general mathematical expression of capacitance can be written as:

$$C = \frac{\Delta Q}{\Delta U}$$

where C is capacitance (in farad, F), Q is surface charge (in coulomb, C) and U is surface potential (in volt, V). Based on this equation, one can conclude that capacitance equals to how much charge be taken before the surface potential increases 1 V. More equations used in my research will be displayed and discussed in the following “Calculations” section.

1.3 Charge Storage Mechanisms

The superior power density of supercapacitors is rooted in their charge storage mechanism. Two mechanisms are involved for supercapacitors. The first category is electrical double layer (EDL) capacitance. In this case, charges are stored as ions adsorbed at electrode/electrolyte interfaces via electro-static

interactions (Figure 1.3). Suppose the electrode is negatively charged (*i.e.*, charged with electrons), the negative charged electrons near the electrode surface attract cations in the electrolyte due to the electrostatic attraction. These first anchored cations align with each other and form a compact and ordered layer named the inner Helmholtz layer (IHL). The second layer, coined outer Helmholtz layer (OHL), is built up with counter ions (*e.g.*, anions in this case) that are attracted by the ions in the IHL. Anions in the OHL tend to pack more loosely and disorderly than cations in the IHL. It is because that the electrostatic attraction force imposed by the counter ions is weakened by dielectric nature of the solvent as well as solvation sheaths surrounding the counter ions. The IHL and the OHL together are termed “electrical double layer”. The thickness of the electrical double layer capacitance depends on the size of ions, electrolyte concentration and electrode surface charge density. The typical thickness is less than 10 nm.⁶ For EDLs, electrons are stored at the interface of electrode and electrolyte. Generally, increasing electrode’s ion-accessible surface area can enhance the magnitude of electrical double layer capacitance. Carbon materials stored charges mainly via the formation of EDL as aforementioned.

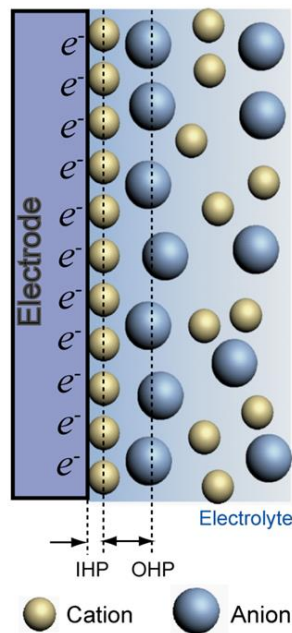


Figure 1.3 Schematic of EDL structure

The second category is pseudo-capacitance from pseudo-capacitive reactions (Figure 1.4). It is widely accepted that the pseudo-capacitive reactions can be classified into three groups: ⁷

- Under-potential deposition (Figure 1.4a);
- Near-surface redox reaction (Figure 1.4b);
- Fast ion insertion and extrusion that trigger no phase transitions (Figure 1.4c).

Under-potential deposition refers to electrodeposition of a species at a potential lower than its corresponding theoretical reduction potential. A typical example is the deposition of lead (Pb) thin films onto gold (Au) substrates. ⁷ But under-potential deposition is rarely explored for energy storage because of its limited capacitance (under-potential deposition can only deposit single-atom thick

layers), slow kinetics and poor reversibility. Near-surface redox reaction is the most common type of pseudo-capacitive reaction among the three. Redox chemical reactions (*i.e.*, reactions involving electron transfer) on the surface of some pseudo-capacitive materials, such as ruthenium dioxide, store electrons via valence state change of the active site(s). The typical example is the protonation and de-protonation of ruthenium dioxide (RuO_2). When applying a negative bias, electrons from the power source will be injected into ruthenium dioxide and reduce Ru^{4+} to Ru^{3+} . To balance the overall charge of the entire electrode, protons in electrolyte will diffuse into ruthenium dioxide. In this case, electrons are stored as lower valence states of pseudo-capacitive sites in the near-surface region of the electrode. Fast ion insertion-deinsertion is a type of pseudo-capacitive reaction demonstrated recently. It is similar as ion intercalation-deintercalation processes commonly observed in lithium ion batteries. The distinction between a battery-type reaction and a capacitive reaction is whether the process will trigger accompanied phase transition(s). Pseudo-capacitive reactions should not alter the phase of corresponding electrode materials. Electrode materials exhibiting this behavior must possess layered structures hosting guest ions. Representative materials belonging to this category are $T\text{-Nb}_2\text{O}_5$ (orthorhombic niobium pentoxide)⁸ and $h\text{-WO}_3$ (hexagonal tungsten trioxide)⁹.

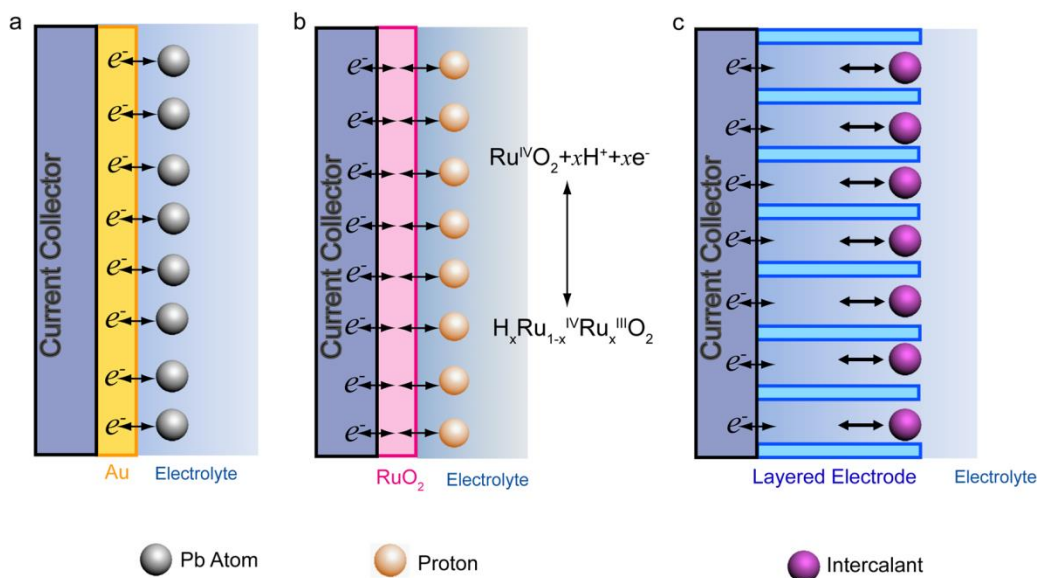


Figure 1.4 Three typical types of pseudo-capacitive reactions. (a) Under-potential deposition: electro-deposition of Pb thin films onto Au substrate. (b) Near-surface redox reactions: protonation and de-protonation of RuO₂ in aprotic electrolytes. (c) Fast ion insertion-deinsertion.

Supercapacitors that store charges based primarily on EDLs and pseudo-capacitive reactions are called EDL capacitors and pseudo-capacitors, respectively. No matter charges are stored by EDLs or pseudo-capacitive reactions, they are managed to accumulate and dissipate rapidly because they only interact with the electrode surface (for EDL capacitance, under-potential depositions and near-surface redox reactions) or diffuse swiftly in bulk materials (for fast ion insertion-deinsertion). This property renders supercapacitors the superior rate performance.¹

1.4 Calculations

This section summarizes all the equations or methods that are used for evaluating capacitive performance.

Capacitance

Gravimetric (*a.k.a.* specific) capacitance C_{sp} (F g^{-1}) is obtained by C/m , and m is the mass loading (mg cm^{-2}).

The gravimetric capacitance can also be calculated based on constant-current (*a.k.a.* galvanostatic) charge and discharge profiles:

$$C = \frac{I_m \Delta t}{\Delta U}$$

where C (F g^{-1}) is the gravimetric capacitance, I_m (A g^{-1}) is the current density, Δt (s) is the discharge time, and ΔU (V) is the potential window.

The areal capacitance can be calculated based on constant-current charge and discharge profiles according to:

$$C_s = \frac{I \times t}{\Delta U \times S} \quad (\text{Equation S1})$$

Where C_s (in mF cm^{-2}) are the areal capacitance, I the discharge current (mA), t the time (s), ΔU the potential window (V), S the working area of electrode (cm^2), m is the mass of active material.

The volumetric capacitance (C_v , unit in F cm^{-3}) of NOC// MnO_2 can be calculated based on galvanostatic charge-discharge experiments according to:

$$C_v = \frac{I \times t}{\Delta U \times V}$$

where I is the charge-discharge current (A), t the discharge time (s), ΔU the potential window (V) and V the total volume (cm^3) of an entire supercapacitor device stack including two electrodes, electrolyte-soaked separator and packages.

Energy Density and Power Density

Energy density (E , Wh kg^{-1}) and power density (P , W kg^{-1}) were evaluated by

the following equation:

$$E = \frac{C_{dev} \times \Delta U_{dev}^2}{2 \times 3.6}$$

$$P = \frac{3600 \times E}{\Delta t}$$

where C_{dev} represents the gravimetric capacitance of the symmetric device calculated using Equation (1). ΔU_{dev} and Δt is the potential window of the device and discharge time of GCD profiles, respectively. Energy density and power density reflect how much energy a device can store and how fast a device can be fully charged, respectively.

Electrochemical Impedance Spectroscopy Analysis

Imaginary capacitances (C'') were evaluated via the following equation:

$$C'' = \frac{Z'(\omega)}{\omega \times |Z(\omega)|^2}$$

Here the electrochemical impedance $Z(\omega)$ is defined as $Z(\omega) = Z'(\omega) + jZ''(\omega)$, where $Z'(\omega)$ and $Z''(\omega)$ are the real part and the imaginary part (in ohm), respectively. ω is the frequency (in Hz) and j is the imaginary number.

$$|Z(\omega)|^2 = |Z'(\omega)|^2 + |Z''(\omega)|^2$$

The electrical conductivity can be estimated by the following equation:

$$S = \frac{1000}{l} \frac{dI}{dV}$$

where S is the electrical conductivity (in $S \text{ m}^{-1}$), l is the distance between two probes (=1 cm), $\frac{dI}{dV}$ is the slope of the I - V curve (in S).

Trasatti Method for Capacitance Differentiation

The Trasatti method was used to differentiate the capacitance contribution

from electrical double layer and pseudo-capacitive reactions. Cyclic voltammograms of CF-MP were first collected with the scan rate ranging from 10 mV s^{-1} to 1000 mV s^{-1} . Then, corresponding gravimetric capacitances were evaluated based on the following equation:

$$C = \frac{S}{2 \cdot \Delta U \cdot \nu}$$

where C stands for the gravimetric capacitance (in F g^{-1}), ΔU the potential window (in V), S the area enclosed by corresponding cyclic voltammograms (in A V g^{-1}) and ν the scan rate (in V s^{-1}).

Plotting the reciprocal of the gravimetric capacitances (C^{-1}) against the square root of scan rates ($\nu^{1/2}$) should yield a linear correlation between them, assuming semi-infinite diffusion of ions. Specifically, the correlation can be described by the following equation:

$$C^{-1} = \text{constant} \cdot \nu^{1/2} + C_T^{-1}$$

where C , ν and C_T is the experimental gravimetric capacitance, the scan rate and the total capacitance, respectively. Data points collected at larger scan rates deviated from this linear relationship due to intrinsic resistance of the electrode and deviation from semi-infinite ion diffusion. These deviated data points were masked during linear fitting. The “total capacitance” equals the sum of electrical double layer capacitance and pseudo-capacitance.

Plotting the gravimetric capacitances (C) against the reciprocal of square root of scan rates ($\nu^{1/2}$) should also give a linear correlation described by the following

equation (if assuming a semi-infinite diffusion of ions):

$$C = \text{constant} \cdot \nu^{-1/2} + C_{EDL}$$

where C , ν and C_{EDL} is the experimental gravimetric capacitance, the scan rate and the electrical double capacitance, respectively. Linear fit the plot and extrapolate the fitting line to y-axis gives the maximum electrical double layer. Subtraction of C_{EDL} from C_T yields the maximum pseudo-capacitance.

Dunn Method for Capacitance Differentiation

The Dunn method enables one to differentiate quantitatively the capacitance contribution from surface capacitive effects (herein we regard them as EDL capacitive effects) and diffusion-controlled processes (herein we regard them as pseudo-capacitive reactions) capacitive effects. At a fixed potential, the current density [$i(V)$] read from a cyclic voltammograms can be expressed as a combination of two terms, *i.e.*,

$$i(V) = k_1\nu + k_2\nu^{1/2}$$

where the term $k_1\nu$ accounts for the current density contributed from EDL capacitive effects while the term $k_2\nu^{1/2}$ is the current density associated with pseudo-capacitive reactions. Dividing $\nu^{1/2}$ on both sides of the above equation yields:

$$i(V)/\nu^{1/2} = k_1\nu^{1/2} + k_2$$

Therefore, by reading the $i(V)$ from cyclic voltammograms collected at a series of scan rates followed by plotting $i(V)/\nu^{1/2}$ vs. $\nu^{1/2}$, one expects to

obtain a linear fitting line with its slope equals k_1 and its y-intercept equals k_2 . Figure S10d displays an example of the $i(V)/\nu^{1/2}$ vs. $\nu^{1/2}$ plot collected for CF-MSP using the anodic current at a potential of -0.1 V vs. Hg/HgO. Plugging the obtained k_1 and k_2 into Equation (9) allows one to differentiate the capacitance contribution from EDLC and PC at the specific potential V and a selected scan rate, ν .

Repeat the aforementioned steps for other potentials within the potential window. The capacitance ratio of EDLC to PC equals the ratio of the area of the colored region to the area of the blank region.

1.5 Carbonaceous Materials as Supercapacitor Electrodes – An Overview

Among various materials, carbonaceous materials, including carbon materials and organic matters, stand out as promising supercapacitor electrode candidates owing to a number of characteristics: electrically conductive, inexpensive, chemically stable, abundant and easy to be engineered into versatile structures. At the time of writing, the majority of commercial supercapacitors utilize highly porous carbon powders, *i.e.*, activated carbon, to fabricate electrodes.¹⁰ Carbonaceous materials represent a diverse family of materials: zero-dimensional carbon dots,¹¹ one-dimensional carbon nanotubes¹² and polymer fibers,¹³ two-dimensional graphene¹⁴ and three-dimensional carbon foams¹⁵ have been extensively studied as components for supercapacitors.

One of the ultimate goals for supercapacitor research is to achieve high charge storage capacity (measured by capacitance or energy density) at ultra-high scan rates or current densities. Carbon materials are promising candidates for realizing such a goal owing to their high electrical conductivities. The small electrical resistance enables fast electron transfer and transport, which is essential for high-rate performance. However, the gravimetric capacitance of carbon had remained at a mediocre level between 100 and 200 F g⁻¹ for decades.¹⁶ Previous studies found that the relatively small ion-accessible area of carbon materials is the main cause for the limited capacitance and energy density. Factors that lead to the limited ion-accessible area include: i) inadequate inherent surface area and/or ii) restricted ion accessibility to a large amount of surface. For example, carbon cloth woven by micron sized carbon fibers only have a specific surface area of ~5 m² g⁻¹ [determined by the Brunauer-Emmett-Teller (BET) method].¹⁷ Activated carbon powder, though has an ultra-high surface area surpassing 1000 m² g⁻¹, its abundant micro-pores are barely accessible for ions. As a result, the typical gravimetric capacitance of activated carbons is only around 100 F g⁻¹.¹⁸ The capacitance decreased to an even lower level when increasing scan rate or current density, due to the sluggish ion diffusion in the micro-pore dominated structures. Therefore, to enlarge the ion-accessible area of carbon materials while maintaining charge diffusion pathways becomes crucial to achieve high capacitance at ultrafast charging rates.

The aforementioned challenge is being addressed. Capacitances that exceed 300 F g^{-1} have been achieved by a new class of carbon materials termed hierarchical porous carbons. They possess multi-scale pores interconnected together and assembled into hierarchical patterns. The hierarchical porosity facilitates electrolyte infiltration and ion diffusion, thus improves ion accessibility of the entire electrode.

1.6 Hierarchical Porous Structure

The basic requirement for hierarchical porous structure is that a porous system must contain multi-scale pores, *i.e.*, must have at least two kinds of pores. In 1985, the International Union of Pure and Applied Chemistry (IUPAC) classified pores according to pore width. The pore width is defined as pore diameter, or specifically for slit-shaped pores (*i.e.*, space between two layers), inter-layer distance. According to IUPAC, pores are classified into three categories:

19

- Macropores, with pore widths larger than 50 nm;
- Mesopores, with pore widths smaller than 50 nm but larger than 2 nm;
- Micropores, with pore widths smaller than 2 nm.

With the development of nanomaterials, the IUPAC elaborated their classifications in 2015 to introduce three new pore types:²⁰

- Nanopores, with pore widths smaller than 100 nm;

- Supermicropores, *a.k.a.* large micropores, with pore widths smaller than 2 nm but larger than 0.7 nm;
- Ultramicropores, *a.k.a.* small micropores, with pore widths smaller than 0.7 nm.

Based on the new definitions, nanopores include micropores, mesopores and macropores but with an upper limit of pore width of 100 nm. Supermicropores and ultramicropores are two subtypes of micropores. The classifications of these six pore types are summarized in Figure 1.5a.

Porous systems that solely contain different sizes of pores is not necessarily be qualified as hierarchical porous systems. The notion of “hierarchy” in a material requires a clear presentation of interplay between all different pores and formation of a hierarchical network. For supercapacitors that rely on ion diffusion for operation, different types of pores should be at least interconnected with each other and be accessible for ions. Figure 1.5b presents an illustration of a typical ion diffusion path in a hierarchical porous structure: ions enter first in largest pores and then flow into smaller ones that are subdivided from the larger pores. This pattern continues until ions reach the smallest pores.

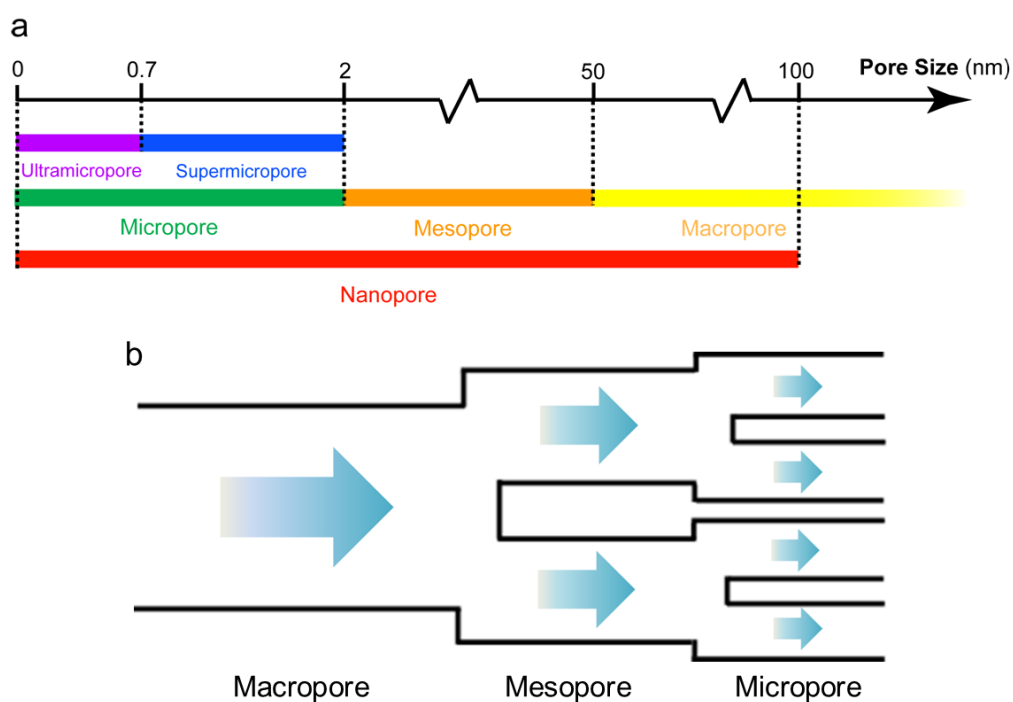


Figure 1.5 (a) IUPAC classifications of pores based on pore width. (b) Schematic illustration of an ion diffusion pattern in a typical hierarchical porous structure.

The rest part of my dissertation will elaborate on the topic of carbon and carbonaceous materials for supercapacitors, by demonstrating strategies to enhance the capacitive performance of carbons as well as exploring other functions of carbons for supercapacitors.

References

1. McCloskey, B. D. *J. Phys. Chem. Lett.* **2015**, *6*, 3592-3593.
2. Lu, X.; Yu, M.; Wang, G.; Tong, Y.; Li, Y. *Energy Environ. Sci.* **2014**, *7*, 2160-2181.
3. Salunkhe, R. R.; Lee, Y.-H.; Chang, K.-H.; Li, J.-M.; Simon, P.; Tang, J.;

- Torad, N. L.; Hu, C.-C.; Yamauchi, Y. *Chem.-Eur. J.* **2014**, *20*, 13838-13852.
4. B éguin, F.; Presser, V.; Balducci, A.; Frackowiak, E. *Adv. Mater.* **2014**, *26*, 2219-2251.
 5. Simon, P.; Burke, A. *Electrochem. Soc. Interface* **2008**, *17*, 38-43.
 6. Bohinc, K.; Kralj-Iglič, V.; Iglič, A. *Electrochimica Acta* **2001**, *46*, 3033-3040.
 7. Augustyn, V.; Simon, P.; Dunn, B. *Energy Environ. Sci.* **2014**, *7*, 1597-1614.
 8. Augustyn, V.; Come, J.; Lowe, M. A.; Kim, J. W.; Taberna, P.-L.; Tolbert, S. H.; Abruña, H. D.; Simon, P.; Dunn, B. *Nat. Mater.* **2013**, *12*, 518-522.
 9. Zhu, M.; Meng, W.; Huang, Y.; Huang, Y.; Zhi, C. *ACS Appl. Mater. Interfaces* **2014**, *6*, 18901-18910.
 10. Chen, T.; Tang, Y.; Qiao, Y.; Liu, Z.; Guo, W.; Song, J.; Mu, S.; Yu, S.; Zhao, Y.; Gao, F. *Sci. Report* **2016**, *6*, 23289.
 11. Bhattacharya, K.; Deb, P. *Dalton Trans.* **2015**, *44*, 9221-9229.
 12. Pham, D. T.; Lee, T. H.; Luong, D. H.; Yao, F.; Ghosh, A.; Le, V. T.; Kim, T. H.; Li, B.; Chang, J.; Lee, Y. H. *ACS Nano* **2015**, *9*, 2018-2027.
 13. Liu, T.; Finn, L.; Yu, M.; Wang, H.; Zhai, T.; Lu, X.; Tong, Y.; Li, Y. *Nano Lett.* **2014**, *14*, 2522-2527.
 14. Zhi, L.; Li, T.; Yu, H.; Chen, S.; Dang, L.; Xu, H.; Shi, F.; Liu, Z.; Lei, Z. *Carbon* **2017**, *113*, 100-107.
 15. Zhang, F.; Liu, T.; Hou, G.; Kou, T.; Yue, L.; Guan, R.; Li, Y. *Nano Res.* **2016**,

9, 2875-2888.

16. Zhang, L. L.; Zhao, X. S. *Chem. Soc. Rev.* **2009**, *38*, 2520.

17. Wang, G.; Wang, H.; Lu, X.; Ling, Y.; Yu, M.; Zhai, T.; Tong, Y.; Li, Y. *Adv. Mater.* **2014**, *26*, 2676-2682.

18. Li, Y.; Roy, S.; Ben, T.; Xu, S.; Qiu, S. *Phys. Chem. Chem. Phys.* **2014**, *16*, 12909.

19. Sing, K. S. W.; Everett, D. H.; Haul, R. A. W.; Moscou, L.; Pieroti, R. A.; Rouquerol, J.; Siemieniewska, T. *Pure Appl. Chem.* **1985**, *57*, 603-609.

20. Thommes, M.; Kaneko, K.; Neimark, A. V.; Olivier, J. P.; Rodriguez-Reinoso, F.; Rouquerol, J.; Sing, K. S. W. *Pure Appl. Chem.* **2015**, *87*, 9-10.

Chapter 2

Hierarchical Porous Carbon Foams Derived from Potassium Carbonate-embedded Chitosan Aerogels for Electrical Double Layer Capacitors

Abstract

Increasing demand for portable electronic devices calls for the need of light-weight power source. Electrical double layer capacitors (EDLCs) are promising candidates due to their high power density and outstanding charge/discharge cycling stability. Three-dimensional (3D) self-supporting carbon-based materials have been extensively studied for light-weight EDLCs. Yet, a major challenge for 3D carbon electrodes is the limited ion diffusion rate in their internal space. To address this limitation, preparation of hierarchical porous 3D structures that provide additional channels for internal ion diffusion is favorable. Herein, we report a new template-free method for synthesis of ultralight (9.92 mg/cm^3) 3D porous carbon foam (PCF) involving carbonization of glutaraldehyde cross-linked chitosan aerogel in the presence of potassium carbonate. Electron microscopy images reveal that the carbon foam is an interconnected network of carbon sheets with uniformly dispersed macro-pores, while Brunauer–Emmett–Teller measurements confirm the hierarchical porous structure. Electrochemical data show that the PCF electrode can achieve an outstanding gravimetric capacitance of 246.5 F g^{-1} at a current density of 0.5 A g^{-1} , and a remarkable

capacitance retention of 67.5% when current density increased from 0.5 A g⁻¹ to 100 A g⁻¹. A quasi-solid-state symmetric supercapacitor fabricated via assembly of two pieces of PCF and delivered an ultrahigh power density of 25 kW kg⁻¹ at an energy density of 2.8 Wh kg⁻¹. This work demonstrates the ability to synthesize ultralight and hierarchical porous carbon foam with high capacitive performance.

2.1 Introduction

Increasing demand for portable electronic devices calls for the need of light-weight power source. Electrical double layer capacitors (EDLCs) are promising candidates due to their high power density and outstanding charge/discharge cycling stability.^{1,2} An ideal EDLC electrode should have large surface area, excellent electrical conductivity, chemical and mechanical stability. To increase the gravimetric capacitance of EDLC, it is also critical that the electrode is self-supporting material without the need of current collectors and non-conductive binders.^{3,4}

Three-dimensional (3D) self-supporting carbon-based materials, such as graphene/carbon aerogels,^{5,6} carbon monoliths,⁷ carbon nanotube sponge,⁸ and carbon nanofiber foams⁹ have been extensively studied for light-weight EDLCs. For instance, Niu *et al.* synthesized a free-standing CNT paper that can be directly fabricated into a compact-designed supercapacitor.¹⁰ Sun *et al.* developed an EDLC based on bamboo-like carbon fibers without the need of additional mechanical support.¹¹ Zhai *et al.* fabricated 3D graphene scaffolds using nickel

foam as sacrificial template.³ A major challenge for 3D carbon electrodes is the limited ion diffusion rate in their internal structures.¹²⁻¹⁴ In a rapid charge and discharge process, the ion diffusion limit causes undesirable capacitance loss and the reduction of rate capability and power density. To address this limitation, preparation of highly porous 3D structures that provide additional channels for ion diffusion is favorable. It has been reported that the existence of macro-pores and meso-pores can facilitate ion diffusion within 3D structures, whilst the presence of micro-pores can increase gravimetric capacitance by increasing ion-accessible surface area.^{4,14-16} It is expected that 3D porous carbon materials can achieve enhanced specific capacitances as well as rate capability compared to 3D non-porous counterparts. For instance, Xu *et al.* demonstrated that the porous reduced graphene hydrogel retained a gravimetric capacitance of 212 F g^{-1} (~75% of its initial value) at a large current density of 100 A g^{-1} while its non-hole counterpart achieved only 136 F g^{-1} (~66% of its initial value) at the same current density.¹⁷ Hao *et al.* synthesized porous carbon foams from bagasse activated with KOH.¹⁸ The porous carbon foam obtained at $700 \text{ }^\circ\text{C}$ exhibited the highest gravimetric capacitance of 268.4 F g^{-1} at a scan rate of 2 mV s^{-1} and maintained *ca.* 75% capacitance when scan rate increased to 200 mV s^{-1} , which is much better compared to carbon foams without KOH activation (88 F g^{-1} @ 2 mV s^{-1} and maintained *ca.* 68% capacitance @ 200 mV s^{-1}).

Here we report for the first time a template-free method to fabricate 3D

hierarchical porous carbon foams (PCF) derived from K_2CO_3 -embedded chitosan aerogels. Chitosan is the second most abundant natural bio-polymer that makes it a sustainable precursor for synthesis of carbonaceous materials.^{14,19,20} Moreover, chitosan forms graphitic carbonaceous materials with excellent electrical conductivity upon pyrolysis due to intrinsic N-doping.²¹⁻²⁴ Previous studies of chitosan-derived carbonaceous materials have been primarily focused on preparation of carbon powders^{21,23,25,26} and pellets.^{22,24,25} However, carbon powders and pellets may not be the best candidates for EDLC electrodes. The fabrication of carbon powder electrode requires the addition of non-conductive binders and conductive substrate as mechanical support. While carbon pellets are self-supporting structure, they are typically assembled with very thick sheets (*ca.* 2 μm in thickness) that limit the electrode surface area. In this work, we use glutaraldehyde to cross-link with chitosan in solution at ambient temperature to form chitosan aerogels. Subsequent pyrolysis of the as-formed aerogel yields a 3D porous carbon network with interconnected porous thin carbon sheets (~ 90 nm). Conventional methods for producing porous carbon structure can be mainly grouped into two approaches: i) template methods that involves the incorporation and removal of templates such as silica spheres^{11,27} and polystyrene spheres²⁸ to generate pores. ii) KOH activation methods in that carbonized structures are usually mixed with KOH powder and annealed at high temperature (> 600 °C) to create pores.^{22,29} Both approaches require at least two steps to obtain the porous

carbon structure. Our method, on the contrary, takes only one step to simultaneously carbonize chitosan and generate meso- and micro-pores. The as-formed PCF structure has a fairly low mass density of 9.92 mg cm^{-3} . Moreover, the porous configuration and thin walls allow rapid ion diffusion and provide ultra-high surface area ($1013 \text{ m}^2 \text{ g}^{-1}$) for charge storage. The self-supporting PCF electrode achieved outstanding electrochemical performance with an outstanding gravimetric capacitance of 246.5 F g^{-1} (at 0.5 A g^{-1}) based on the entire mass of the electrode, and a remarkable capacitance retention of 67.5% when current density increased from 0.5 A g^{-1} to 100 A g^{-1} . A quasi-solid-state symmetric supercapacitor assembled using two pieces of PCF delivered an ultrahigh power density of 25 kW kg^{-1} at an energy density of 2.8 Wh kg^{-1} based on the total weight of two electrodes (equivalent to a power density of 6.25 kW kg^{-1} and an energy density of 0.68 Wh/kg based on the total mass of device considering a packing factor of 0.4).³⁰

2.2 Experimental Section

Preparation of chitosan-derived PCF: 1 mL 10 wt% K_2CO_3 aqueous solution was slowly added into 20 mL of 1 wt% chitosan solution (with 1 wt% acetic acid as solvent) under vigorous stirring. Then, 240 μL of 25 wt% glutaraldehyde aqueous solution was added dropwise into the solution. After adding glutaraldehyde solution, the mixed solution was immediately transferred into a plastic container (*e.g.*, a petri dish). The solution slowly solidified in the air and

formed the hydrogel. The as-formed hydrogel was exposed in air for 1 day to age and then was frozen in a freezer. The frozen K_2CO_3 -embedded chitosan hydrogel was freeze-dried for 48 h to form the chitosan aerogel. Pyrolysis of the aerogel was carried out in a home-built tube furnace in nitrogen atmosphere at 800 °C for 2 h to obtain the porous carbon foam (denoted as PCF). The PCF was washed with 0.1 M hydrochloric acid solution and de-ionized water to remove any soluble residuals. For comparison, carbon foam without hierarchical porous structure (denoted as CF) were prepared by the same procedures as PCF but without adding K_2CO_3 .

Fabrication of quasi-solid-state symmetric supercapacitor devices: The symmetric supercapacitor device was assembled by two identical pieces of PCF [1.4 mg in total based on the mass of PCF used, based on three consecutive measurements using a micro-balance (Citizen, Model CX205, 0.1 mg sensitivity)]. The PCFs were pressed onto two pieces of nickel foam under 10 MPa (FY-15 Micro-presser, Shenyang Kejing Co.) without adding any binders. Polyvinyl alcohol (PVA)/KOH gel was used as the electrolyte. To prepare the PVA/KOH gel, 3.36 g of KOH powder was firstly dissolved in 30 mL of de-ionized water and heated to 90 °C. Then 2.0 g of PVA powder was slowly added to the solution under vigorous stirring. The solution was kept stirring until a clear gel was formed. The two pieces of PCF along with a piece of membrane (TF 4804, NKK, serves as the separator) were soaked in the as-prepared electrolyte at 90 °C for half an hour

prior to assembly. Then, the electrolyte-soaked separator was sandwiched between electrodes and kept at 45 °C for 6 h to remove excess water in the electrolyte. Finally, the assembled device was wrapped with parafilm (Pechiney Plastic Packaging, US) and sealed with epoxy resin (Red Extra Fast, Hardman Double Bubble) at two ends to avoid absorbing air moisture.

Characterizations: Morphology was probed by scanning electron microscopy (SEM, FEI Quanta 3D Dual-beam scanning electron microscope) and transmission electron microscopy (TEM, JEM2010-HR, 200 kV accelerating voltage). The specific surface area and pore volumes were determined by Brunauer–Emmett–Teller experiment conducted with a Micromeritics porosimetry analyzer (ASAP 2010) at the temperature of liquid nitrogen (77 K) using nitrogen as adsorbate. Raman spectra were recorded with a Raman spectrometer (Reinshaw RAMAN) with an excitation wavelength of 760 nm. Peaks in Raman spectra were analyzed using the “Multiple Peak Fit” function in the Origin 8.0 software. The qualitative comparison of electrical conductivities was carried out using a CHI 660D electrochemical workstation (CH Instruments, Inc.). Materials were connected to the workstation with two probes on each end. The distance between two probes was 1 cm.

Electrochemical Measurements: Cyclic voltammetry, galvanostatic charge-discharge experiments were performed using a CHI 660D electrochemical

workstation (CH Instruments, Inc.) in a traditional three-electrode electrolytic cell. A graphite rod (*ca.* 5 mm in diameter), a saturated calomel electrode (SCE) and 3 M KOH aqueous solution were used as counter electrode, reference electrode and electrolyte, respectively. The working electrodes were prepared by pressing the PCF or CF (~ 1 mg) onto a piece of nickel foam under 10 MPa (FY-15 Micro-presser, Shenyang Kejing Co.) without adding any binders. Electrochemical impedance spectroscopy (EIS) was conducted in a frequency range from 0.1 Hz to 1000 kHz at open circuit potential with a perturbation of 5 mV. All the EIS spectra were fitted using *ZSimpWin* software. Stability test of the single electrode was carried out in 3 M KOH electrolyte at a scan rate of 200 mV s⁻¹ for 10000 cycles. Stability test of the symmetric device was performed using GCD experiment with a current density of 10 A g⁻¹ for 10000 consecutive charge-discharge cycles.

2.3 Results and Discussions

Synthesis of PCF

Figure 2.1 illustrates the procedure for preparation of PCF and CF. Chitosan hydrogels were prepared by an intermolecularly cross-link reaction between the amine groups of chitosan molecules and aldehyde groups of glutaraldehyde molecules (Figure 2.2) in aqueous solution at ambient temperature. For preparing PCF structure, 1 mL of 10 wt% K₂CO₃ aqueous solution was first

added in chitosan solution and then the solution was mixed with glutaraldehyde to form K_2CO_3 -embedded chitosan hydrogel. The as-prepared chitosan hydrogels were freeze-dried for 24 h to form aerogel structure. Scanning electron microscopy (SEM) studies revealed that the aerogels exhibit 3D network of interconnected sheets. The formation mechanism of the 3D network can be described as the follows:

- 1) In diluted chitosan solution, many liquid water “islands” are randomly dispersed among chitosan polymer chains, due to the limited interaction between chitosan polymers and water. Addition of glutaraldehyde cross-links chitosan chains and forms chitosan “cages” that hold water inside (Figure 2.3a).
- 2) During freezing, water “islands” expand and squeeze the as-formed chitosan “cage” walls to thin chitosan sheets (Figure 2.3b).
- 3) During freeze-drying process, ice “islands” sublimate and leaves the porous chitosan network composed of chitosan sheets behind, as observed in the SEM images (Figure 2.3c).

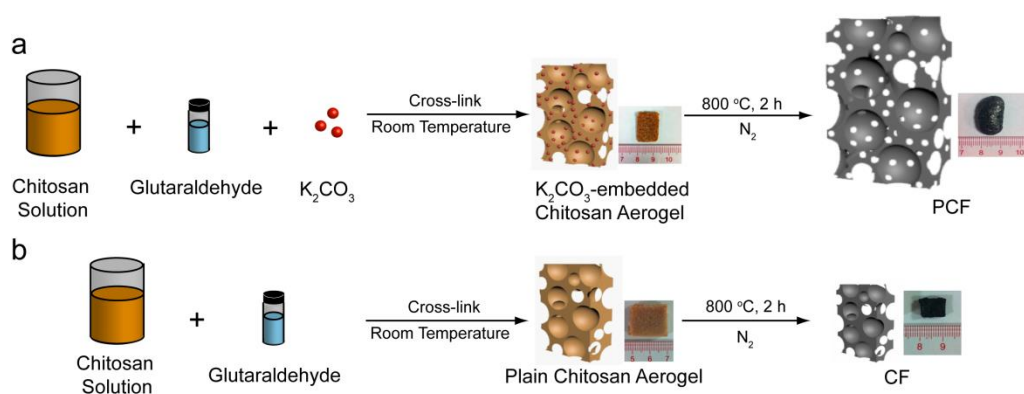


Figure 2.1 Schematic of the synthesis of (a) PCF and (b) CF.

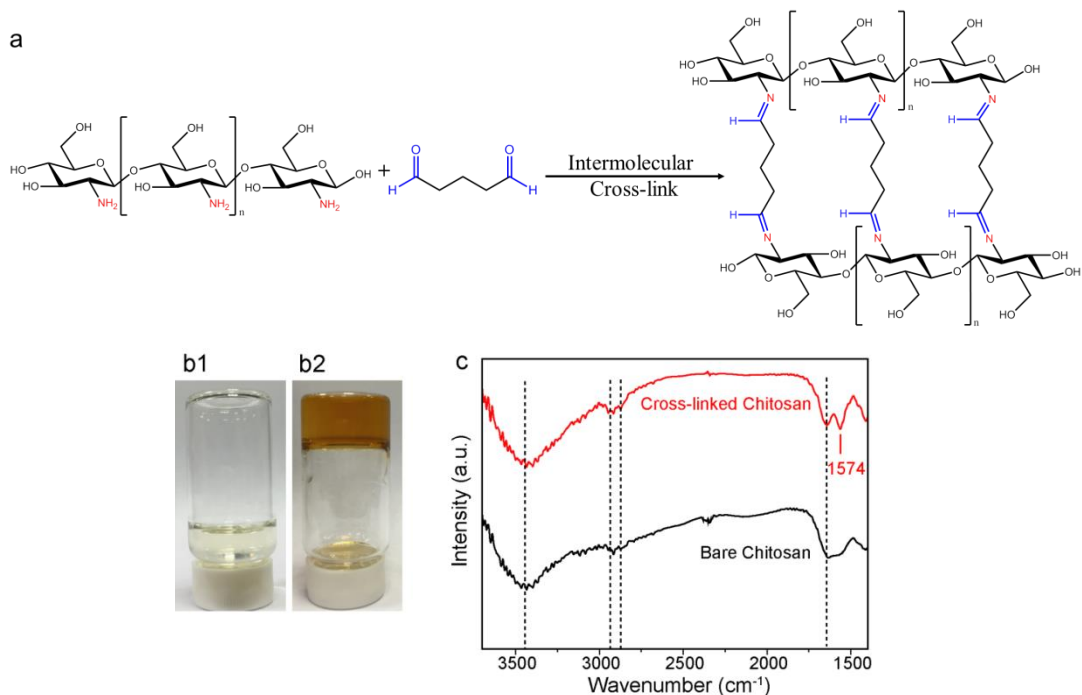


Figure 2.2 (a) Simplified illustration of the cross-link reaction between chitosan and glutaraldehyde. The active functional groups involved in the reaction are labelled in red (amine groups) and blue (aldehyde groups). (b) Digital pictures of b1) chitosan solution and b2) chitosan hydrogel obtained after the cross-link reaction. (c) FT-IR spectrum collected for crosslinked chitosan and bare chitosan. Characteristic peaks of O-H, C-H, N-H and C=O are highlighted by dashed lines and the characteristic C=N stretching peak at 1574 cm^{-1} is labeled. Peaks around 2400 cm^{-1} are due to presence of carbon dioxide in air.

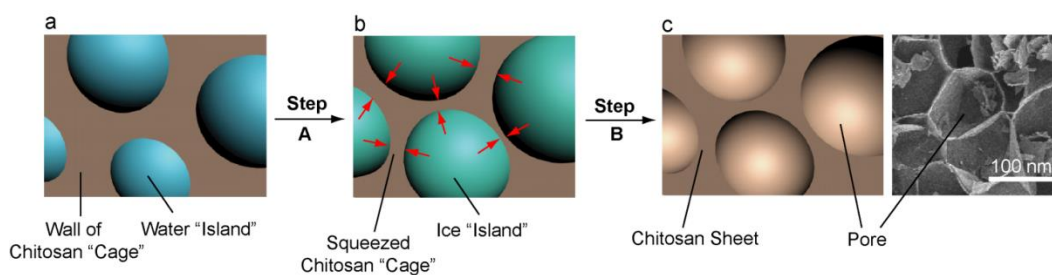


Figure 2.3 Schematic of the formation mechanism of porous chitosan aerogels composed of chitosan sheets. (a) Chitosan solution. (b) Frozen chitosan solution. (c) Freeze-dried chitosan aerogel. SEM image shows the porous structure created by ice sublimation. Step A: Freezing. The expansion of liquid water squeezes the chitosan “cages” along the directions indicated by red arrows. Step B: Freeze-drying. Ice “islands” sublimates and leaves the porous chitosan aerogel.

K_2CO_3 -embedded chitosan aerogel showed an equally smooth surface as

plain chitosan aerogel, indicating that K_2CO_3 was well impregnated in the aerogel. These aerogels were carbonized in nitrogen atmosphere at $800\text{ }^\circ\text{C}$. Thermogravimetric (TG) analysis (Figure 2.4) reveals the decomposition temperature of the cross-linked aerogels is *ca.* $220\text{ }^\circ\text{C}$ and the carbonization rate is 0.2 mg min^{-1} . The volume of plain chitosan aerogel shrank considerably with the density greatly increased from 29.75 mg cm^{-3} to 62.53 mg cm^{-3} upon carbonization. The shrinkage can be attributed to the structural collapse as a result of dehydrogenation and intermolecular dehydration during annealing.³¹ In contrast, the K_2CO_3 -embedded chitosan aerogel forms a slightly swollen carbon foam structure upon carbonization, with the density reduced substantially from 167.8 mg cm^{-3} to 9.92 mg cm^{-3} , which is much lighter than most conventional carbon materials such as carbon black powder (typically $1800\text{-}2100\text{ mg cm}^{-3}$), carbon cloth (typically $1700\text{-}1800\text{ mg cm}^{-3}$),³² graphene-carbon nanotube composite (1060 mg cm^{-3}),³³ carbon aerogel ($500\text{-}600\text{ mg cm}^{-3}$),³⁴ activated carbon powder (typically $400\text{-}500\text{ mg cm}^{-3}$), graphene-carbon hybrid texture (70 mg cm^{-3}),³⁵ and graphene aerogels obtained by supercritical CO_2 drying or freeze drying ($12\text{-}96\text{ mg cm}^{-3}$).³⁶

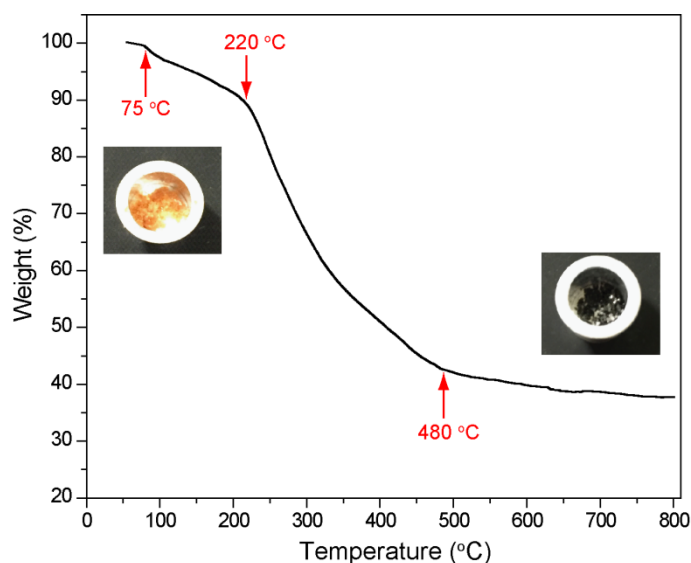


Figure 2.4 TG curve of the glutaraldehyde cross-linked chitosan aerogel with a scan rate of 20 K min^{-1} . Insets: Digital pictures of the sample before and after carbonization.

Structural properties of PCF

The SEM images collected for the carbonized aerogels, disclosing a couple of important structural differences between the two samples (Figure 2.5). First, the carbonized sample derived from K_2CO_3 -embedded chitosan aerogel exhibits lower density of carbon sheets compared to the one derived from plain chitosan aerogel. Second, the sheet thickness of K_2CO_3 -embedded sample is about 90 nm, which is also considerably thinner than the plain sample (*ca.* 500 nm, Figure 2.6). More importantly, the sheets of K_2CO_3 -embedded sample are porous with uniformly dispersed pores of $\sim 1 \mu\text{m}$ in diameter (originate from the phase separation between hydrophobic carbon and water during the pyrolysis.^{37,38}), while the sheets of plain sample are smooth and non-porous. The two carbonized samples are denoted as porous carbon foam (PCF) and carbon foam (CF)

respectively, based on their structural feature. The density reduction observed for PCF is believed to be due to the reduced thickness of carbon sheets and the volumetric expansion as a result of gas releasing during thermal decomposition of K_2CO_3 . It has been reported that K_2CO_3 can decompose into K_2O and CO_2 or directly react with carbon at temperatures beyond 700 °C, as shown in Equation 1-3.^{29,39}



The large amount of gases released from the processes can exfoliate and expand the carbon sheets. Meanwhile, the pores can be created from corrosion of carbon by potassium carbonate and potassium oxide (Eq. 2 and Eq. 3).

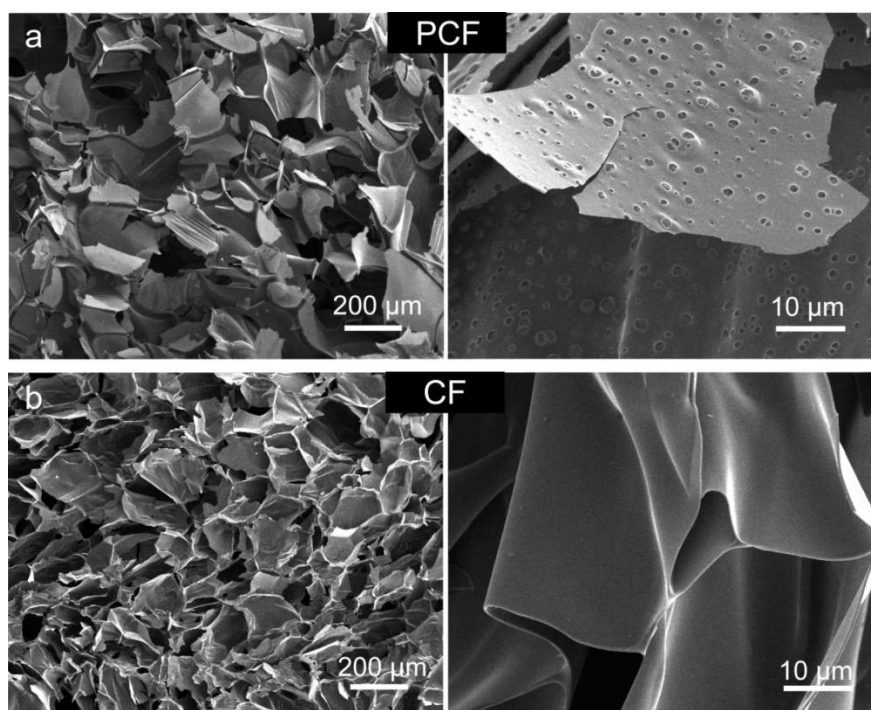


Figure 2.5 SEM images of (a) PCF and (b) CF.

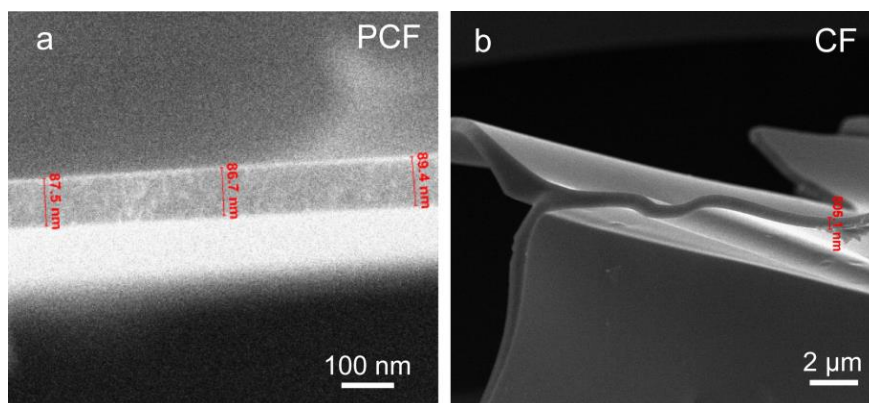


Figure 2.6 SEM images collected from the carbon sheet edge of (a) PCF and (b) CF structures showing the sheet thickness.

To further explore the role of glutaraldehyde and the effect of crosslinking chitosan molecules, we prepared a control sample using the same procedure for PCF but without adding glutaraldehyde and K_2CO_3 . In the absence of glutaraldehyde, chitosan aerogel was obtained after freeze drying. Subsequent carbonization of the chitosan aerogel yielded a carbon monolith (Figure 2.7a inset). SEM images (Figure 2.7a and 2.7b) revealed that the control sample is composed of a layered structure. Each carbon layer has a lateral size of *ca.* 2 μm . This morphology is consistent with that of other chitosan-derived carbon monoliths synthesized in the absence of cross-linkers.^{18,40} On the contrary, the carbon film obtained in the presence of glutaraldehyde possesses a 3D network of carbon sheets (Figure 2.5b) with a much thinner lateral sheet thickness (*ca.* 500 nm, Figure 2.6). These results prove that the glutaraldehyde mediated cross-linking plays a crucial role in creating the 3D macro-porous network

structure.

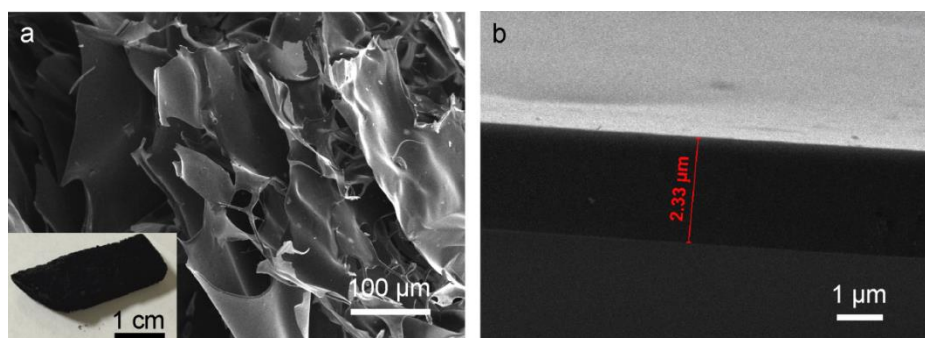


Figure 2.7 (a) SEM image of the carbon monolith prepared without glutaraldehyde. Inset shows the digital picture of a piece of carbon foam. (b) SEM image of a carbon layer showing the lateral thickness.

To characterize the porous structure of PCF and compare the surface area between the two carbon foams, nitrogen adsorption and desorption isotherms were collected. As shown in Figure 2.8a, PCF exhibits combined characteristics of type I and type IV isotherms. The steep increase of adsorbed nitrogen volume at low relative pressure ($P/P_0 < 0.1$) indicates the presence of micro-pores in PCF.³¹ The hysteresis observed at $P/P_0 > 0.4$ also proves the existence of meso-pores.⁴¹ On the contrary, CF displays a type III adsorption-desorption isotherm (Figure 2.8a inset) with limited nitrogen adsorption capacity. The surface area and pore volumes of PCF and CF are summarized in Table 2.1 and the pore size distribution of the two carbon foams is shown in Figure 2.9. Obviously, PCF has higher porosity than CF, consistent with the SEM images. The surface area of PCF was determined to be $1013 \text{ m}^2 \text{ g}^{-1}$, which is higher than graphite powders (typically $6 \text{ m}^2 \text{ g}^{-1}$), carbon black powders (*ca.* $100 \text{ m}^2 \text{ g}^{-1}$), carbon aerogel particles ($800 \text{ m}^2 \text{ g}^{-1}$)⁴², graphene aerogels ($960 \text{ m}^2 \text{ g}^{-1}$)⁶ and is comparable to

ordered meso-porous carbon templates (*ca.* 1030 m² g⁻¹).⁴³ The micro-pores/meso-pores ratio of PCF is 2.994 while that of CF is only 0.067. The increased amount of micro-pores is a direct result of K₂CO₃ activation. It has been reported that micro-pores are more efficient than meso-pores in terms of enhancing the capacitance.⁴⁴ This high micro-pores to meso-pores ratio is beneficial for achieving large capacitance. TEM images proved the existence of macro-pores and micro-pores on a single PCF carbon nanosheet (Figure 2.10). The BET together with the SEM and TEM results suggest that PCF is a 3D hierarchical porous structure containing micro-, meso- and macro-pores.

Furthermore, the degree of graphitization of the two carbon foams was evaluated by Raman spectroscopy (Figure 2.8b). Both samples show two distinct bands centered at 1340 and 1580 cm⁻¹, which can be assigned to D and G band of carbon,⁴⁵ respectively. The integral intensity ratio of the G and D band (denoted as I_G/I_D) is directly proportional to the degree of graphitization.⁴⁶ As shown in Table 1, the I_G/I_D value of PCF (0.503) is higher than CF (0.345), suggesting the PCF exhibit higher degree of graphitization that can be attributed to the partial sp^2 -carbon lattice recovery by reducing gas, *e.g.* CO, generated during carbonization. The increased degree of graphitization would enhance electrical conductivity of carbon foam, which is favorable for achieving excellent rate capability. As shown in Figure 2.11, the electrical resistance of the PCF electrode is comparable to the highly conductive nickel foam, and is much smaller than that

of stainless steel plate, the graphite paper and the carbon cloth. The small electrical resistance of PCF allows fast electron transport.

Table 2.1 Textural parameters of PCF and CF

Sample	BET Surface Area, S (m^2/g)	Total Pore Volume, V_{total} (cm^3/g)	Micro-pore Volume, V_{micro} (cm^3/g)	Meso-pore Volume, V_{meso} (cm^3/g)	Ratio of V_{micro} to V_{meso}	$I_{\text{G}}/I_{\text{D}}$
PCF	1013.0	0.576	0.461	0.154	2.994	0.503
CF	8.9	0.027	0.002	0.030	0.067	0.345

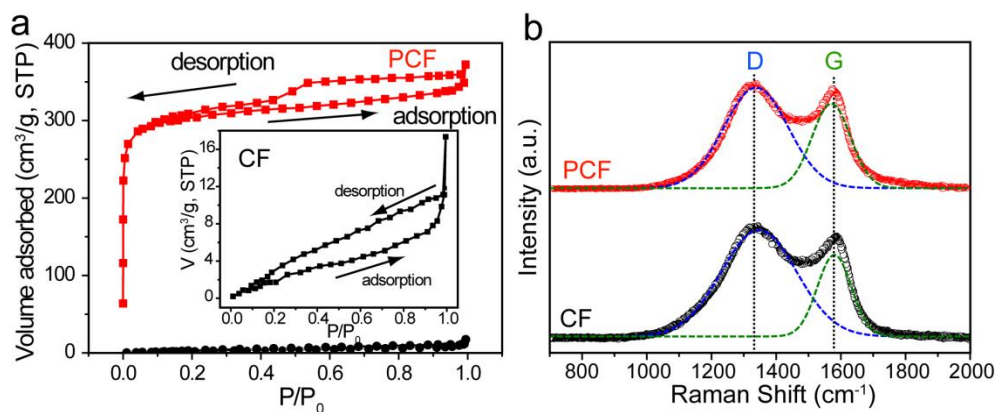


Figure 2.8 (a) Nitrogen adsorption-desorption isotherms collected for PCF and CF (inset); (b) Raman spectra of PCF and CF. Dashed lines highlight the D and G peak positions.

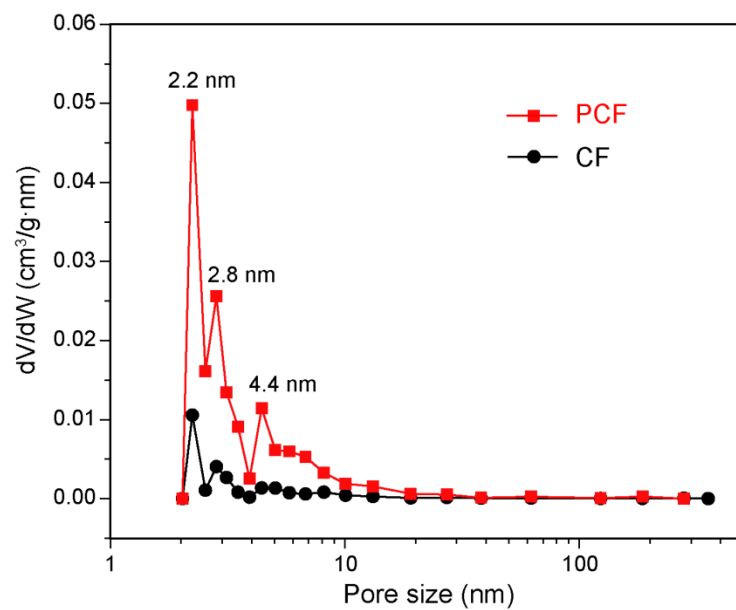


Figure 2.9 Pore size distribution of PCF and CF.

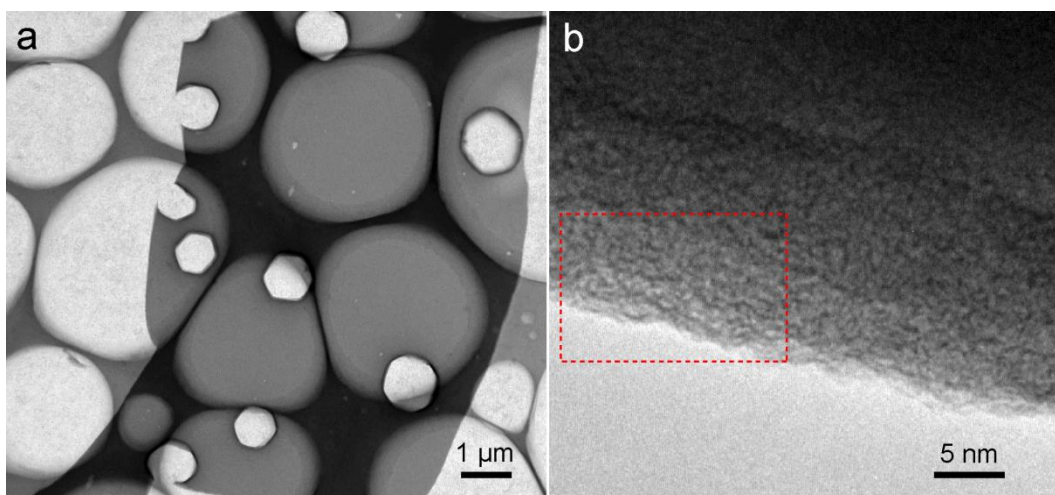


Figure 2.10 (a) The low magnification and (b) high magnification TEM images of a piece of PCF carbon sheet. The dashed box highlights the micro-pores.

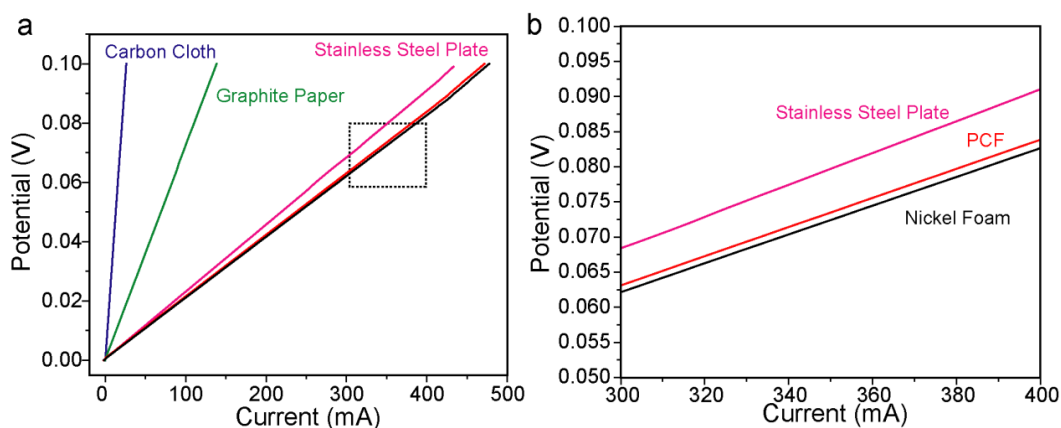


Figure 2.11 Potential vs. current plots collected from the PCF and other commonly used current collectors. The distance between two probes is 1 cm. (b) shows the zoomed-in part highlighted by the dashed box of (a). In a potential vs. current plot, the electrical resistance is directly proportional to the slope of the straight line.

Capacitive performance of PCF electrode

The hierarchical porous structure and ultralight property of PCF makes it a promising electrode material for fabricating light-weight supercapacitors. To evaluate the electrochemical performance of PCF, we conducted cyclic voltammetry (CV), galvanostatic charge-discharge (GCD) and electrochemical impedance spectroscopy (EIS) in a three-electrode electrolytic cell in 3 M KOH aqueous electrolyte (Experimental Section). Figure 2.12a compares the CV curves collected at a scan rate of 100 mV s^{-1} for PCF and CF. The capacitance of PCF is substantially higher than CF. In addition, all the CV curves of PCF collected at different scan rates showed a nearly rectangular shape (Figure 2.13a), indicating the capacitive performance of PCF is superior.⁴⁷ The steep slope (close to 90°) of the CV curve, also suggests that PCF is highly electrically conductive.⁴⁸ GCD

curves collected for PCF at various current densities exhibit symmetric charging/discharging profiles (Figure 2.13b). The gravimetric capacitance of PCF calculated from the discharge time at 0.5 A g^{-1} is 246.5 F g^{-1} . Figure 4c shows the specific capacitances calculated from GCD profiles at different current densities. Significantly, PCF was able to retain 80.1% of gravimetric capacitance when current density increased from 0.5 A g^{-1} to 10 A g^{-1} , and an outstanding value of 67.5% capacitance retention when the current density further increased to 100 A g^{-1} (Figure 2.13c). The gravimetric capacitances of PCF at large current densities and rate capability are among the best performance achieved by self-supporting carbon based materials under comparable testing conditions, and much better than conventional resorcinol-formaldehyde carbon aerogels (Table 2.2). Moreover, the PCF electrode delivers an excellent volumetric capacitance of 43.10 F cm^{-3} at a current density of 0.5 A g^{-1} , and still retains 29.10 F cm^{-3} at a current density of 100 A g^{-1} . The performance is better than a number of other carbon monolith electrodes with comparable volume, including the conventional R-C carbon aerogel (*ca.* 40 F cm^{-3} , 5 mV s^{-1}),⁴⁹ activated carbon (24.8 F cm^{-3} , 5 mA cm^{-2}),⁵⁰ waste paper based activated carbon (36.7 F cm^{-3} , 5 mA cm^{-2}),⁵¹ and exfoliated carbon cloth (2.2 F cm^{-3} , 10 mA cm^{-2}).³² The exceptional rate capability performance is believed to be due to the 3D hierarchical porous structure that facilitates ion diffusion and the high electrical conductivity that enables fast charge transfer at interfaces and electron transport in the carbon sheet.

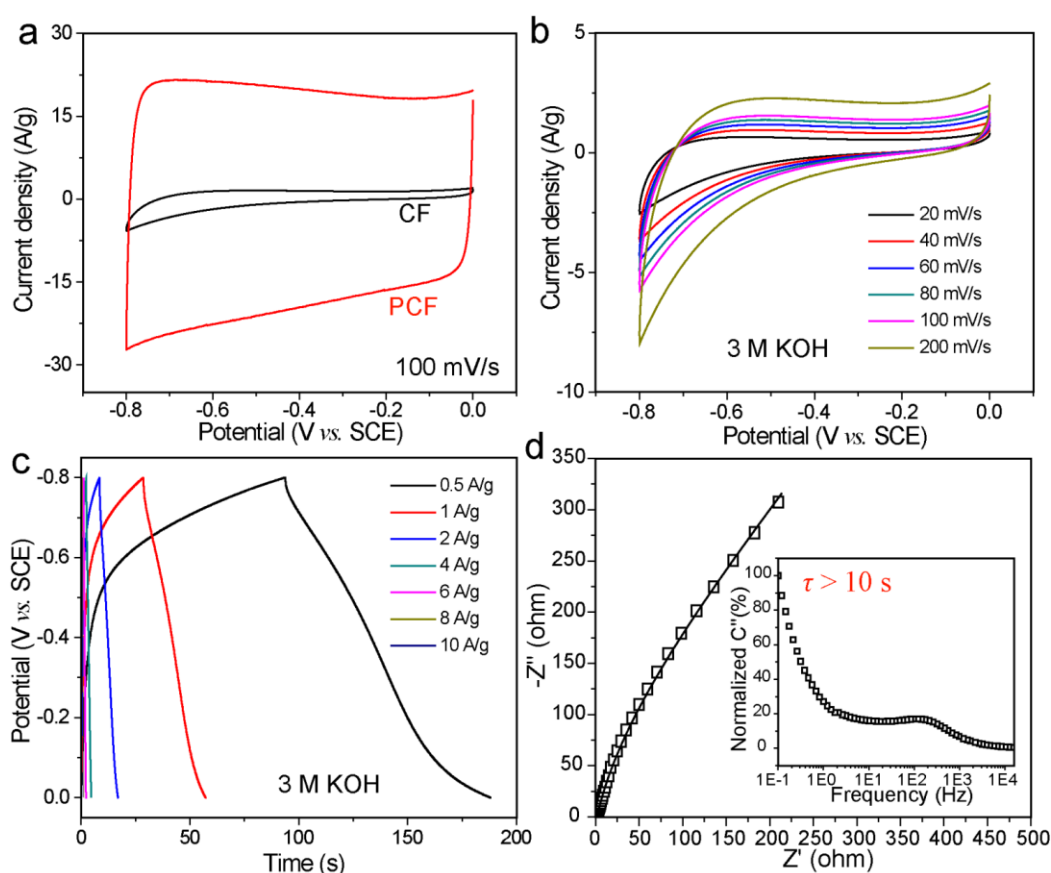


Figure 2.12 (a) CV curves collected for PCF and CF at a scan rate of 100 mV s^{-1} in 3 M KOH aqueous electrolyte; (b) CV curves of CF. (c) GCD profiles of CF. (d) Nyquist plot collected at open-circuit potential. Open dots and solid lines are experimental data and fitting curves, respectively. Inset shows the normalized C'' vs. frequency plot.

Table 2.2 Capacitive performance of self-supporting carbonaceous electrodes

Description	Electrolyte	Specific capacitance	Rate capability	Ref.
Chitosan-derived carbon pellet	6 M KOH	$ca. 10 \text{ F g}^{-1}$ (200 mV s^{-1})	$ca. 4.8\%$ (2 mV to 200 mV s^{-1})	22
Activated carbon monolith	1 M H_2SO_4	20 F g^{-1} (5 A g^{-1})	80% (0.5 A g^{-1} to 5 A g^{-1})	7
CNT sponge	6 M KOH	20 F g^{-1} (200 mV s^{-1})	71% (20 mV s^{-1} to 200 mV s^{-1})	8
Three-dimensional hierarchical ordered porous carbon (3D)	6 M KOH	56 F g^{-1} (100 mV s^{-1})	91% (5 mV s^{-1} to 100 mV s^{-1})	27

HOPC)				
RF carbon aerogel	6 M KOH	67.2 F g ⁻¹ (10 mV s ⁻¹)	61.0% (1 mV to 10 mV s ⁻¹)	52
Pd-decorated graphene aerogel	0.1 M Na ₂ SO ₄	80 F g ⁻¹ (500 mV s ⁻¹)	45.7% (5 mV s ⁻¹ to 500 mV s ⁻¹)	53
Graphene aerogel	6 M KOH	ca. 82 F g ⁻¹ (10 A g ⁻¹)	68.3% (0.5 A g ⁻¹ to 100 A g ⁻¹)	36
Three-dimensional graphene-based framework (3D-GF)	1 M H ₂ SO ₄	83 F g ⁻¹ (100 mV s ⁻¹)	36.7% (1 mV s ⁻¹ to 100 mV s ⁻¹)	54
Mesoporous carbon thin film	6 M KOH	85 F g ⁻¹ (5 A g ⁻¹)	62.5% (0.5 A g ⁻¹ to 5 A g ⁻¹)	55
Activated carbon wrapped carbon nanotube buckypaper	6 M KOH	ca. 100 F g ⁻¹ (10 A g ⁻¹)	71.4% (0.5 A g ⁻¹ to 100 A g ⁻¹)	56
Microporous carbon nanosphere (MCNS)	6 M KOH	110 F g ⁻¹ (2 A g ⁻¹)	57.9% (0.2 A g ⁻¹ to 2 A g ⁻¹)	57
Macro-/Meso-porous CNT sponge	6 M KOH	150 F g ⁻¹ (200 mV s ⁻¹)	75% (20 mV s ⁻¹ to 200 mV s ⁻¹)	8
Bamboo-like carbon nanofiber	3 M KOH	165.2 F g ⁻¹ (100 A g ⁻¹)	ca. 70% (5 A g ⁻¹ to 100 A g ⁻¹)	11
Carbon nanotube supported graphene aerogel	6 M KOH	169.3 F g ⁻¹ (10 A g ⁻¹)	79.6% (0.5 A g ⁻¹ to 10 A g ⁻¹)	58
Nitrogen-doped graphene aerogel (NGA)	1 M H ₂ SO ₄	174 F g ⁻¹ (10 A g ⁻¹)	78% (0.2 A g ⁻¹ to 10 A g ⁻¹)	59
N-doped carbon nanofiber network (CLCF)	1 M H ₂ SO ₄	175.6 F g ⁻¹ (50 A g ⁻¹)	78.5% (0.5 A g ⁻¹ to 50 A g ⁻¹)	9
RGO-fabrics	6 M KOH	195 F g ⁻¹ (5 A g ⁻¹)	49.8% (0.1 A g ⁻¹ to 5 A g ⁻¹)	60
Porous chitosan-derived carbon pellet	6 M KOH	214.5 F g ⁻¹ (200 mV s ⁻¹)	73.5% (2 mV s ⁻¹ to 200 mV s ⁻¹)	22

PCF	3 M KOH	246.5 F g ⁻¹ (0.5 A g ⁻¹)	80.1%	This work
		197.3 F/g (10 A g ⁻¹)	(0.5 A g ⁻¹ to 10 A g ⁻¹) 72.8%	
		179.4 F g ⁻¹ (50 A g ⁻¹)	(0.5 A g ⁻¹ to 50 A g ⁻¹) 67.5%	
		166.3 F g ⁻¹ (100 A g ⁻¹)	(0.5 A g ⁻¹ to 100 A g ⁻¹)	

To gain further insights about the outstanding performance of PCF, EIS spectra were collected and fitted by the equivalent electric circuit provided in Figure 2.14.^{10,61} All parameters of the equivalent electric circuit are listed in Table S1 (in the ESM). The combined series resistance (R_s) of PCF is *ca.* 0.179 Ω , comparable to other highly conductive carbonaceous materials.^{48,62,63} As shown in Figure 2.13d, the EIS spectrum of PCF exhibits a clear semi-circle in the middle-frequency domain and a nearly vertical straight line in the low-frequency domain, indicative of small charge transfer resistance (R_{ct}) and Warburg element (W).⁶⁴ Furthermore, we have evaluated the relaxation time constant (τ_0) of PCF to determine its efficiency of charge transfer and frequency response. τ_0 corresponds to the frontier between the capacitive and resistive behavior and is the time required to deliver the stored energy and power efficiently.⁶⁵ It can be evaluated as $\tau_0=1/f_0$, where f_0 is the frequency at the peak in the normalized imaginary capacitance (C'') vs. frequency plot (Figure 2.13d inset).⁶⁶ The τ_0 of the PCF electrode is 2.3 s. Such a small relaxation time explains the outstanding rate capability of the PCF. Besides, PCF shows a stable cycling performance with

capacitance retention of 98% after 10000 scans in 3 M KOH aqueous electrolyte

(Figure 2.15).

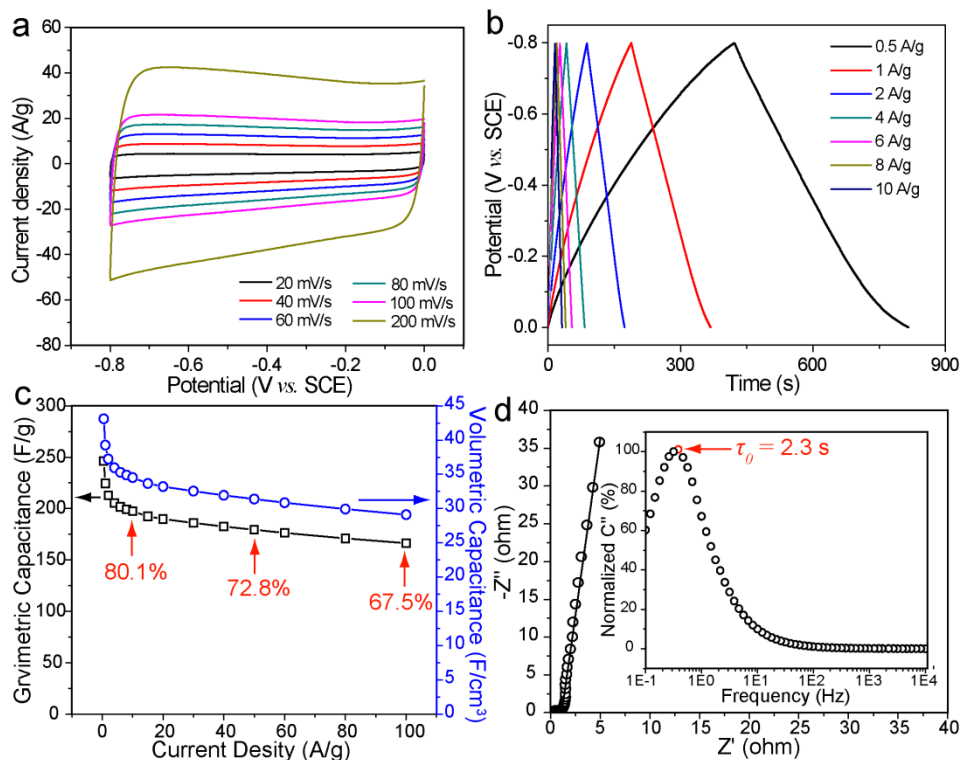


Figure 2.13 Electrochemical performance of PCF measured in 3 M KOH aqueous electrolyte. (a) CV curves collected at various scan rates (b) GCD profiles collected at various current densities. (c) Gravimetric capacitance and volumetric capacitance of the PCF electrode plotted as a function of current density. (d) Nyquist plot collected at open-circuit potential. Open dots and solid lines are experimental data and fitting curves, respectively. Inset shows the normalized C'' vs. frequency plot.

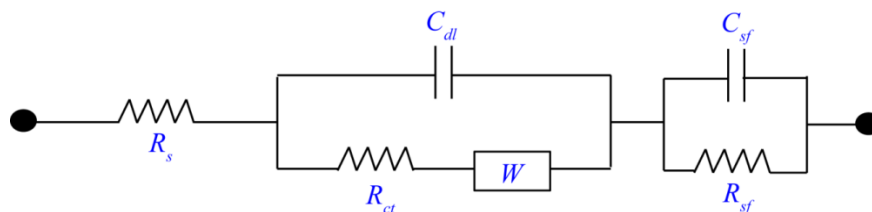


Figure 2.14 Equivalent electric circuit used for EIS data fitting. Parameters: R_s - combined series resistance; R_{ct} - charge-transfer resistance; W - Warburg element; C_{dl} - electrical-double-layer capacitance; C_{sf} - surface capacitance (related to pseudocapacitance); R_{sf} - surface resistance

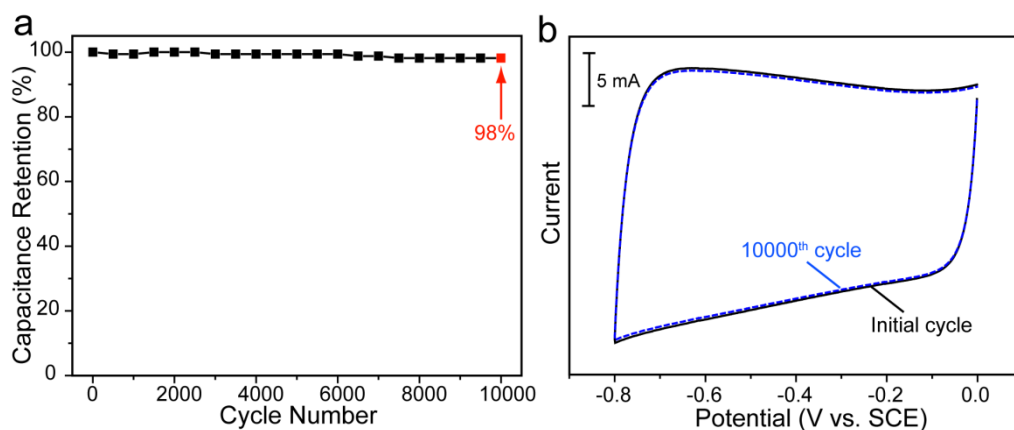


Figure 2.15 (a) Cycling stability of PCF in 3 M KOH at a scan rate of 200 mV s^{-1} ; (b) The CV curves collected before and after 10000 scans.

Capacitive performance of PCF//PCF supercapacitor

A symmetric supercapacitor (SSC) was fabricated via assembly of two identical PCF electrodes with a separator in polyvinyl alcohol (PVA)/KOH gel electrolyte (Figure 2.16d inset). The device is denoted as PCF//PCF. Figure 2.16a displays the CV curves of the PCF//PCF SSC collected at different scan rates. All the curves showed quasi-rectangular shapes. The GCD profiles (Figure 2.16b) showed nearly linear potential-time behavior and symmetric charging/discharging curves. These results proved that the PCF//PCF device has a predominant electrical double layer capacitive behavior. The specific capacitance calculated based on the total mass of the two electrodes is 42.5 F g^{-1} at 0.2 A g^{-1} . The value is about one-fourth of the gravimetric capacitance of the single electrode, as expected.⁶⁷ Remarkably, the PCF//PCF device retained 71.1% of the gravimetric capacitance when the current density increased from 0.2 A g^{-1} to 10 A g^{-1} and 45.4% of the gravimetric capacitance when the current density further increased to 50 A

g^{-1} (Figure 5c). This excellent rate capability is higher than other EDLCs including cross-linked N-doped carbon fiber SSC (*ca.* 43%, 0.2 A g^{-1} to 10 A g^{-1}),⁹ meso-microporous carbon SSC (52.4%, 0.25 A g^{-1} to 10 A g^{-1}),⁶⁸ hierarchical porous carbon SSC (*ca.* 63%, 0.5 A g^{-1} to 10 A g^{-1}).¹⁸ We have also evaluated the volumetric capacitance based on the total volume of our device [0.6 cm (L) \times 0.8 cm (W) \times 0.45 mm (H), 0.022 cm^3] (Figure 2.16c). The device volumetric capacitance obtained at a current density of 0.2 A g^{-1} was 2.38 F cm^{-3} and the device still retained 1.08 F cm^{-3} when the current density increased by 250 times. This performance is substantially better than a number of quasi-solid symmetric supercapacitors (SSCs) with comparable volume, including $\text{TiO}_2@\text{C}$ SSC (0.125 F cm^{-3} at 0.1 mA cm^{-2}),⁶⁹ $\text{ZnO}@\text{C}@\text{MnO}_2$ SSC (0.325 F cm^{-3} at 0.5 mA cm^{-2}),⁷⁰ and TiN SSC (0.33 F cm^{-3} at a current density of 2.5 mA cm^{-2}).⁷¹ Moreover, the PCF//PCF device exhibited an excellent capacitance retention of 97.1% after testing for 10000 charge-discharge cycles (Figure 2.16d) and outstanding flexibility (Figure 2.17).

The calculated energy densities and power densities of PCF are summarized in the Ragone plot (Figure 2.18). Notably, the power density can vary within a broad range without significantly change the energy density, owing to the excellent rate capability. The PCF//PCF device delivers an impressive power density of 25 kW kg^{-1} (equivalent to 1.6 kW cm^{-3}) at the energy density of 2.8 Wh kg^{-1} (equivalent to 0.17 mWh cm^{-3}). This performance is better than previously

reported symmetric device assembled with self-supporting carbon electrodes, such as carbon nanotube (CNT) sponge//CNT sponge (0.3 kW kg^{-1} , 0.34 Wh kg^{-1}),⁸ activated carbon monolith (ACM)//ACM (12 kW kg^{-1} , 1 Wh kg^{-1}),⁷ N-doped carbon nanofiber (NCNF)//NCNF SSC (9 kW kg^{-1} , 2 Wh kg^{-1}),⁹ and graphene thin film (GTF)//GTF SSC (1.81 kW kg^{-1} , 2.9 Wh kg^{-1}).⁷² Two fully-charged PCF//PCF devices connected in series (charging current density: 6 A g^{-1} , voltage 2 V , charging time: *ca.* 15 s) can power an electric fan (1.5 V nominal voltage) for tens of seconds and three light emitting diodes (LEDs) for about three minutes, demonstrating its potential for practical applications.

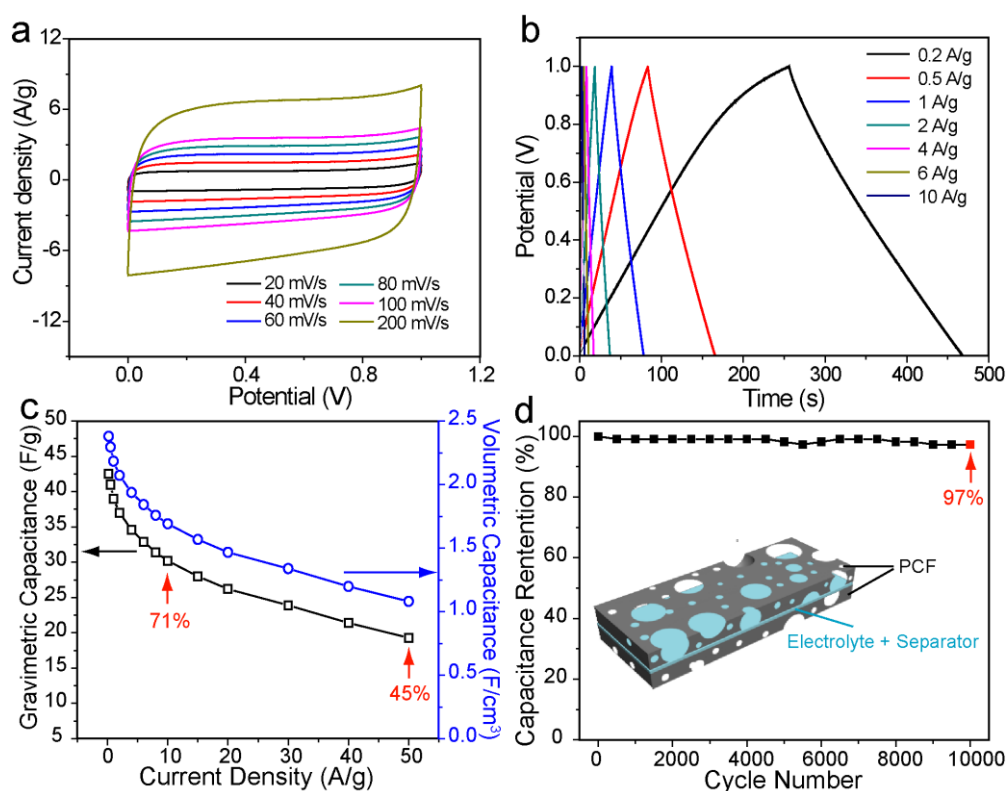


Figure 2.16 Electrochemical performance of PCF//PCF SSC with PVA-KOH as gel electrolyte. (a) CV curves collected at various scan rates. (b) Galvanostatic charge-discharge profiles collected at various current densities. (c) Gravimetric capacitance and volumetric capacitance of the PCF//PCF SSC plotted as a

function of current density. (d) Cycling stability collected at 10 A g^{-1} , inset shows the schematic illustration of PCF//PCF device.

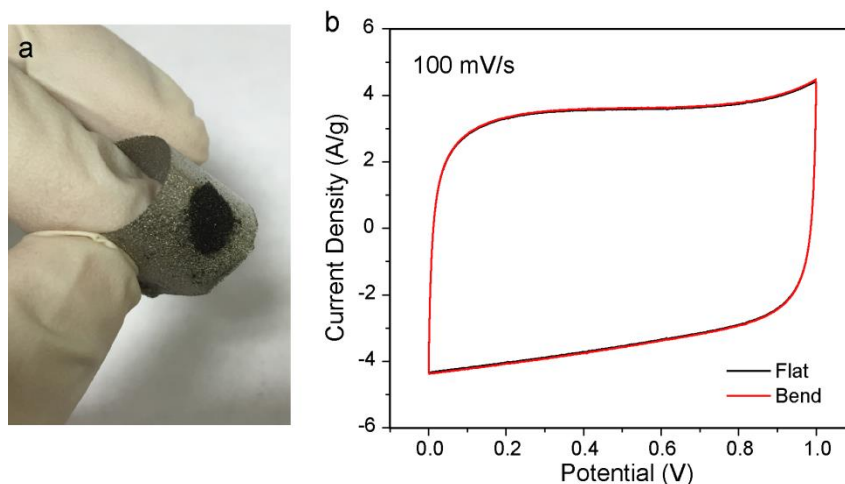


Figure 2.17 (a) Digital picture showing a PCF film pressed on a piece of nickel foam under bending condition. (b) Cyclic voltammograms collected for PCF//PCF symmetric supercapacitor at a scan rate of 100 mV s^{-1} under flat (black curve) and bending condition (red curve).

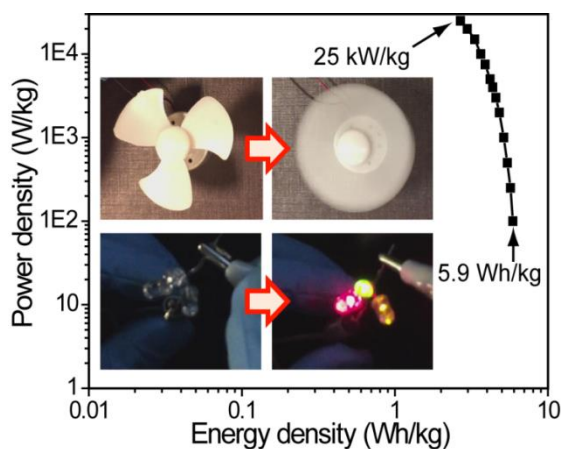


Figure 2.18 Ragone plot of the PCF//PCF device. Insets show the digital pictures of an electric fan and three LED light bulbs powered by two PCF//PCF devices connected in series.

2.4 Conclusions

In conclusion, we demonstrated a simple and template-free method to prepare self-supporting and ultralight hierarchical porous carbon foam containing 3D

interconnected macro-porous framework with meso- and micro-porous walls. Significantly, the PCF electrode shows outstanding specific capacitance (246.5 F g⁻¹ at a current density of 0.5 A g⁻¹) and rate capability (67.5% retention from 0.5 A g⁻¹ to 100 A g⁻¹). The quasi-solid-state PCF//PCF electrical double layer capacitor delivers an ultrahigh power density of 25 kW kg⁻¹ at an energy density of 2.8 Wh kg⁻¹, holding a great promise for practical applications. We believe that these robust, highly porous and electrically conductive carbon foams can also serve as an excellent supporting scaffold for making lightweight pseudo-capacitors and lithium-ion batteries.

References

1. Simon, P.; Gogotsi, Y. *Nat. Mater.* **2008**, *7*, 845-854.
2. Bonaccorso, F.; Colombo, L.; Yu, G.; Stoller, M.; Tozzini, V.; Ferrari, A. C.; Ruoff, R. S.; Pellegrini, V. *Science* **2015**, *347*, 1246501-1246501.
3. Zhai, T.; Lu, X.; Wang, H.; Wang, G.; Mathis, T.; Liu, T.; Li, C.; Tong, Y.; Li, Y. *Nano Lett.* **2015**, *15*, 3189-3194.
4. Chabi, S.; Peng, C.; Hu, D.; Zhu, Y. *Adv. Mater.* **2014**, *26*, 2440-2445.
5. Xu, Y.; Lin, Z.; Huang, X.; Liu, Y.; Huang, Y.; Duan, X. *ACS Nano* **2013**, *7*, 4042-4049.
6. Xu, Y.; Shi, G.; Duan, X. *Acc. Chem. Res.* **2015**, *48*, 1666-1675.
7. Ruiz, V.; Blanco, C.; Santamaría, R.; Ramos-Fernández, J. M.; Martínez-Escandell, M.; Sepúlveda-Escribano, A.; Rodríguez-Reinoso, F. *Carbon*

2009, *47*, 195-200.

8. Yang, Y.; Li, P.; Wu, S.; Li, X.; Shi, E.; Shen, Q.; Wu, D.; Xu, W.; Cao, A.; Yuan, Q. *Chem.-Eur. J.* **2015**, *21*, 6157-6164.

9. Cheng, Y.; Huang, L.; Xiao, X.; Yao, B.; Yuan, L.; Li, T.; Hu, Z.; Wang, B.; Wan, J.; Zhou, J. *Nano Energy* **2015**, *15*, 66-74.

10. Niu, Z.; Zhou, W.; Chen, J.; Feng, G.; Li, H.; Ma, W.; Li, J.; Dong, H.; Ren, Y.; Zhao, D.; Xie, S. *Energy Environ. Sci.* **2011**, *4*, 1440-1446.

11. Sun, Y.; Sills, R. B.; Hu, X.; Seh, Z. W.; Xiao, X.; Xu, H.; Luo, W.; Jin, H.; Xin, Y.; Li, T.; Zhang, Z.; Zhou, J.; Cai, W.; Huang, Y.; Cui, Y. *Nano Lett.* **2015**, *15*, 3899-3906.

12. Xu, Y.; Lin, Z.; Zhong, X.; Huang, X.; Weiss, N. O.; Huang, Y.; Duan, X. *Nat. Commun.* **2014**, *5*, 4554.

13. Chen, Z.; Wen, J.; Yan, C.; Rice, L.; Sohn, H.; Shen, M.; Cai, M.; Dunn, B.; Lu, Y. *Adv. Energy Mater.* **2011**, *1*, 551-556.

14. Dutta, S.; Bhaumik, A.; Wu, K. C.-W. *Energy Environ. Sci.* **2014**, *7*, 3574-3592.

15. B éguin, F.; Presser, V.; Balducci, A.; Frackowiak, E. *Adv. Mater.* **2014**, *26*, 2219-2251.

16. Zhang, L. L.; Gu, Y.; Zhao, X. S. *J. Mater. Chem. A* **2013**, *1*, 9395-9408.

17. Xu, Y.; Chen, C.-Y.; Zhao, Z.; Lin, Z.; Lee, C.; Xu, X.; Wang, C.; Huang, Y.; Shakir, M. I.; Duan, X. *Nano Lett.* **2015**, *15*, 4605-4610.

18. Hao, P.; Zhao, Z.; Tian, J.; Li, H.; Sang, Y.; Yu, G.; Cai, H.; Liu, H.; Wong, C. P.; Umar, A. *Nanoscale* **2014**, *6*, 12120-12129.
19. White, R. J.; Budarin, V.; Luque, R.; Clark, J. H.; Macquarrie, D. J. *Chem. Soc. Rev.* **2009**, *38*, 3401-3418.
20. White, R. J.; Brun, N.; Budarin, V. L.; Clark, J. H.; Titirici, M.-M. *ChemSusChem* **2014**, *7*, 670-689.
21. Primo, A.; Atienzar, P.; Sanchez, E.; Delgado, J. M.; Garc ía, H. *Chem. Commun.* **2012**, *48*, 9254-9256.
22. Hao, P.; Zhao, Z.; Leng, Y.; Tian, J.; Sang, Y.; Boughton, R. I.; Wong, C. P.; Liu, H.; Yang, B. *Nano Energy* **2015**, *15*, 9-23.
23. Latorre-S áncchez, M.; Primo, A.; Atienzar, P.; Forneli, A.; Garc ía, H. *Small* **2015**, *11*, 970-975.
24. Primo, A.; S áncchez, E.; Delgado, J. M.; Garc ía, H. *Carbon* **2014**, *68*, 777-783.
25. Kucinska, A.; Cyganiuk, A.; Lukaszewicz, J. P. *Carbon* **2012**, *50*, 3098-3101.
26. Olejniczak, A.; Lezanska, M.; Wloch, J.; Kucinska, A.; Lukaszewicz, J. P. *J. Mater. Chem. A* **2013**, *1*, 8961-8967.
27. Zhao, Q.; Wang, X.; Liu, J.; Wang, H.; Zhang, Y.; Gao, J.; Lu, Q.; Zhou, H. *Electrochim. Acta* **2015**, *154*, 110-118.
28. Zhao, C.; Yu, C.; Liu, S.; Yang, J.; Fan, X.; Huang, H.; Qiu, J. *Adv. Funct. Mater.* **2015**, *25*, 6913-6920.
29. Zhu, Y.; Murali, S.; Stoller, M. D.; Ganesh, K. J.; Cai, W.; Ferreira, P. J.;

- Pirkle, A.; Wallace, R. M.; Cychosz, K. A.; Thommes, M.; Su, D.; Stach, E. A.; Ruoff, R. S. *Science* **2011**, *332*, 1537-1541.
30. Chen, Z.; Augustyn, V.; Wen, J.; Zhang, Y.; Shen, M.; Dunn, B.; Lu, Y. *Adv. Mater.* **2011**, *23*, 791-795.
31. He, P.; Liu, L.; Song, W.; Xiong, G.; Fisher, T. S.; Chen, T. *RSC Adv.* **2015**, *5*, 31837-31844.
32. Wang, G.; Wang, H.; Lu, X.; Ling, Y.; Yu, M.; Zhai, T.; Tong, Y.; Li, Y. *Adv. Mater.* **2014**, *26*, 2676-2682.
33. Pham, D. T.; Lee, T. H.; Luong, D. H.; Yao, F.; Ghosh, A.; Le, V. T.; Kim, T. H.; Li, B.; Chang, J.; Lee, Y. H. *ACS Nano* **2015**, *9*, 2018-2027.
34. Kim, S. J.; Hwang, S. W.; Hyun, S. H. *J. Mater. Sci.* **2005**, *40*, 725-731.
35. Song, W.-L.; Guan, X.-T.; Fan, L.-Z.; Cao, W.-Q.; Wang, C.-Y.; Cao, M.-S. *Carbon* **2015**, *93*, 151-160.
36. Zhang, X.; Sui, Z.; Xu, B.; Yue, S.; Luo, Y.; Zhan, W.; Liu, B. *J. Mater. Chem.* **2011**, *21*, 6494.
37. Qie, L.; Chen, W.; Xu, H.; Xiong, X.; Jiang, Y.; Zou, F.; Hu, X.; Xin, Y.; Zhang, Z.; Huang, Y. *Energy Environ. Sci.* **2013**, *6*, 2497.
38. Wu, X.; Jiang, L.; Long, C.; Fan, Z. *Nano Energy* **2015**, *13*, 527-536.
39. Wang, J.; Kaskel, S. *J. Mater. Chem.* **2012**, *22*, 23710-23725.
40. Ling, Z.; Yu, C.; Fan, X.; Liu, S.; Yang, J.; Zhang, M.; Wang, G.; Xiao, N.; Qiu, J. *Nanotechnology* **2015**, *26*, 374003.

41. Xu, J.; Gao, Q.; Zhang, Y.; Tan, Y.; Tian, W.; Zhu, L.; Jiang, L. *Sci. Rep.* **2014**, *4*, 5545.
42. Horikawa, T.; Hayashi, J. i.; Muroyama, K. *Carbon* **2004**, *42*, 169-175.
43. Liu, R.; Wan, L.; Liu, S.; Pan, L.; Wu, D.; Zhao, D. *Adv. Funct. Mater.* **2015**, *25*, 526-533.
44. Ghosh, A.; Lee, Y. H. *ChemSusChem* **2012**, *5*, 480-499.
45. Song, Y.; Feng, D.; Liu, T.; Li, Y.; Liu, X. *Nanoscale* **2015**, *7*, 3581-3587.
46. Ferrari, A. C.; Basko, D. M. *Nature Nanotech.* **2013**, *8*, 235-246.
47. Yang, P.; Mai, W. *Nano Energy* **2014**, *8*, 274-290.
48. Bo, Z.; Zhu, W.; Ma, W.; Wen, Z.; Shuai, X.; Chen, J.; Yan, J.; Wang, Z.; Cen, K.; Feng, X. *Adv. Mater.* **2013**, *25*, 5799-5806.
49. Pröbstle, H.; Wiener, M.; Fricke, J. *J. Porous Mater.* **2011**, *10*, 213-222.
50. Liu, M.-C.; Kong, L.-B.; Zhang, P.; Luo, Y.-C.; Kang, L. *Electrochim. Acta* **2012**, *60*, 443-448.
51. Liu, M.-C.; Kong, L.-B.; Lu, C.; Li, X.-M.; Luo, Y.-C.; Kang, L. *RSC Adv.* **2012**, *2*, 1890.
52. Li, J.; Wang, X.; Huang, Q.; Gamboa, S.; Sebastian, P. J. *J. Power Sources* **2006**, *158*, 784-788.
53. Yu, Z.; McInnis, M.; Calderon, J.; Seal, S.; Zhai, L.; Thomas, J. *Nano Energy* **2015**, *11*, 611-620.
54. Wu, Z.-S.; Sun, Y.; Tan, Y.-Z.; Yang, S.; Feng, X.; Müllen, K. *J. Am. Chem.*

Soc. **2012**, *134*, 19532-19535.

55. Feng, D.; Lv, Y.; Wu, Z.; Dou, Y.; Han, L.; Sun, Z.; Xia, Y.; Zheng, G.; Zhao, D. *J. Am. Chem. Soc.* **2011**, *133*, 15148-15156.

56. Chen, H.; Di, J.; Jin, Y.; Chen, M.; Tian, J.; Li, Q. *J. Power Sources* **2013**, *237*, 325-331.

57. Li, Z.; Wu, D.; Liang, Y.; Fu, R.; Matyjaszewski, K. *J. Am. Chem. Soc.* **2014**, *136*, 4805-4808.

58. Ma, Z.; Zhao, X.; Gong, C.; Zhang, J.; Zhang, J.; Gu, X.; Tong, L.; Zhou, J.; Zhang, Z. *J. Mater. Chem. A* **2015**, *3*, 13445-13452.

59. Sui, Z.-Y.; Meng, Y.-N.; Xiao, P.-W.; Zhao, Z.-Q.; Wei, Z.-X.; Han, B.-H. *ACS Appl. Mater. Inter.* **2015**, *7*, 1431-1438.

60. Song, W.-L.; Song, K.; Fan, L.-Z. *ACS Appl. Mater. Inter.* **2015**, *7*, 4257-4264.

61. Liu, T.; Ling, Y.; Yang, Y.; Finn, L.; Collazo, E.; Zhai, T.; Tong, Y.; Li, Y. *Nano Energy* **2015**, *12*, 169-177.

62. Weng, Z.; Su, Y.; Wang, D.-W.; Li, F.; Du, J.; Cheng, H.-M. *Adv. Energy Mater.* **2011**, *1*, 917-922.

63. Wang, H.; Li, Z.; Tak, J. K.; Holt, C. M. B.; Tan, X.; Xu, Z.; Amirkhiz, B. S.; Harfield, D.; Anyia, A.; Stephenson, T.; Mitlin, D. *Carbon* **2013**, *57*, 317-328.

64. Zhai, T.; Lu, X.; Ling, Y.; Yu, M.; Wang, G.; Liu, T.; Liang, C.; Tong, Y.; Li, Y. *Adv. Mater.* **2014**, *26*, 5869-5875.

65. Portet, C.; Yushin, G.; Gogotsi, Y. *Carbon* **2007**, *45*, 2511-2518.
66. Kim, D.; Shin, G.; Kang, Y. J.; Kim, W.; Ha, J. S. *ACS Nano* **2013**, *7*, 7975-7982.
67. Qu, D.; Shi, H. *J. Power Sources* **1998**, *74*, 99-107.
68. Zhao, Z.; Hao, S.; Hao, P.; Sang, Y.; Manivannan, A.; Wu, N.; Liu, H. *J. Mater. Chem. A* **2015**, *3*, 15049-15056.
69. Zheng, H.; Zhai, T.; Yu, M.; Xie, S.; Liang, C.; Zhao, W.; Wang, S. C. I.; Zhang, Z.; Lu, X. *J. Mater. Chem. C* **2013**, *1*, 225-229.
70. Yang, P.; Xiao, X.; Li, Y.; Ding, Y.; Qiang, P.; Tan, X.; Mai, W.; Lin, Z.; Wu, W.; Li, T.; Jin, H.; Liu, P.; Zhou, J.; Wong, C. P.; Wang, Z. L. *ACS Nano* **2013**, *7*, 2617-2626.
71. Lu, X.; Wang, G.; Zhai, T.; Yu, M.; Xie, S.; Ling, Y.; Liang, C.; Tong, Y.; Li, Y. *Nano Lett.* **2012**, *12*, 5376-5381.
72. Choi, B. G.; Chang, S.-J.; Kang, H.-W.; Park, C. P.; Kim, H. J.; Hong, W. H.; Lee, S.; Huh, Y. S. *Nanoscale* **2012**, *4*, 4983-4988.

Chapter 3

Three-dimensional Carbon Foams with a Multiscale Pore Network Boosts

Ultrafast Charging Capacitance

Abstract

Increasing charge storage capability during fast charging (at ultrahigh current densities) has been a long-standing challenge for supercapacitors. In this work a novel porous carbon foam electrode with multi-scale pore network is reported that achieves a remarkable gravimetric capacitance of $374.7 \pm 7.7 \text{ F g}^{-1}$ at a current density of 1 A g^{-1} . More importantly, it retains $235.9 \pm 7.5 \text{ F g}^{-1}$ (60% of its capacitance at 1 A g^{-1}) at an ultrahigh current density of 500 A g^{-1} . Electron microscopy studies reveal that this carbon structure contains multiple-scale pores assembled in a hierarchical pattern. The outstanding capacitive performance is benefited from its extremely large surface area of $2905 \text{ m}^2 \text{ g}^{-1}$, as around 88% of the electric charges are stored via electrical double layer. Significantly, electrochemical analyses show that the hierarchical porous structure containing macro-, meso- and micro-pores allows efficient ion diffusion and charge transfer, resulting in the excellent rate capability. The findings pave the way for improving rate capability of supercapacitors and enhancing their capacitances at ultrahigh current densities.

3.1 Introduction

Supercapacitors are capable of storing and delivering energy rapidly.¹⁻⁵

Increasing the amount of electric charges that can be stored during fast charging and discharging is critical for supercapacitors.⁶ The poor electrical conductivity of pseudo-capacitive material limits their capacitance during fast charging/discharging, despite they have large theoretical capacitances.⁷ Alternatively, electrical double layer (EDL) capacitive materials such as carbons are able to be charged and discharged more rapidly than pseudo-capacitive materials owing to their excellent electrical conductivities. EDL capacitance is directly proportional to the electrolyte accessible electrode surface area, therefore increasing porosity is a possible solution to improve EDL capacitance.⁸ Yet, in most cases, the enhancement of capacitance through creation of micro-pores is accompanied with the decrease of rate capability. For example, despite activated porous fullerene/graphitic carbon composites exhibited an excellent capacitance of 362.2 F g^{-1} at a current density of 0.1 A g^{-1} , the capacitance decreased quite rapidly to 191.6 F g^{-1} when the current density increased to 5 A g^{-1} .⁹ Holey graphene aerogel film yielded a gravimetric capacitance of 311 F g^{-1} at a current density of 1 A g^{-1} , while only 237 F g^{-1} was retained at 100 A g^{-1} .¹⁰ The capacitance loss at high current density is believed to be due to sluggish ion diffusion within micro-pores that is unable to keep up with the fast rate of charge and discharge.¹¹⁻¹³ Thus, a better understanding of the relationship between pore structure and capacitive performance is critical for improving the performance of EDL electrodes. In 2010, Black *et al.* simulated charge accumulation behavior of different pore shapes using a transmission line model and concluded that electrode with multi-scale pores is beneficial for charge accumulation.¹⁴ Later, Ervin found that the presence of such multiple-scale pores can facilitate ion diffusion in a thick

graphene film.¹⁵ These findings suggest that an electrode with multiple-scale pores is favorable for ion diffusion, which is crucial to achieve large capacitance at ultrahigh current densities. Recently, Zhao *et al.* demonstrated a hierarchical porous carbon electrode that retained *ca.* 92% of capacitance ($\sim 56 \text{ F g}^{-1}$) when the scan rate increased from 5 mV s^{-1} to 100 mV s^{-1} .¹⁶ Our previous study also revealed that micro-porous graphene aerogels with periodic macro-porosity achieved an excellent rate capability of 88.7% when current density increased from 0.5 A g^{-1} to 10 A g^{-1} .¹⁷ However, the capacitances of these electrodes were relatively low ($< 100 \text{ F g}^{-1}$) due to limited surface area. In addition to the aforementioned experimental results, molecular dynamic simulations coupled with state-of-the-art experimental techniques have also elucidated that the existence of multi-scale pores can facilitate ion diffusion. For example, Péan *et al.* observed that pores larger than 0.7 nm could serve as electrolyte reservoirs to store ions in proximity to smaller pores. Upon applying an electric field, the stored ions can diffuse into the nearby micro-pores within less time compared to ions in bulk electrolyte because of the shortened ion diffusion length.¹⁸ Forse *et al.* studied the ion interactions with electrodes using *in-situ* diffusion nuclear magnetic resonance spectroscopy. They concluded that the presence of pores wider than 2 nm was helpful in alleviating ion confinement inside micro-pores, which notably increased the effective ion self-diffusion coefficient and was beneficial for achieving outstanding rate capability.¹⁹

Inspired by these previous studies, we synthesized a 3D carbon foam contains a significant amount of multi-scale pores. This unique porous structure has an

ultrahigh surface area of $2905 \text{ m}^2 \text{ g}^{-1}$. It achieved an outstanding gravimetric capacitance of $235.9 \pm 7.5 \text{ F g}^{-1}$ at an ultrahigh current density of 500 A g^{-1} with more than 60% of the capacitance retained when the current density increased from 1 A g^{-1} to 500 A g^{-1} . To our knowledge, the rate capability and the gravimetric capacitances obtained at large current densities are record values for carbon electrodes.

3.2 Experimental Section

Chemicals: Chitosan (M.W. 100,000~300,000, 85% deacetylation), acetic acid (glacial, 99.9%), tetraethyl ortho-silicate (TEOS), potassium hydroxide (KOH), hydrochloric acid (HCl), denatured alcohol (95 vol%) and absolute ethanol were purchased from Acros Organics. Glutaraldehyde aqueous solution (50 vol%) was purchased from Tokyo Chemical Industry Co. Ltd. All chemicals were used without further purifications.

Preparation of silica (SiO_2) spheres: SiO_2 spheres were prepared via a modified Stöber method. Briefly, 100 mL absolute ethanol, 15 mL de-ionized water, and 5 mL ammonia aqueous solution (25 wt%) were mixed in a 250-mL round-bottom flask. The mixture was stirred at 500 rpm and heated up to $40 \text{ }^\circ\text{C}$ in a water bath. 6.0 g of TEOS was quickly added into the solution mixture and the solution was kept stirring for 6 h at $40 \text{ }^\circ\text{C}$. The solution gradually turned from clear to cloudy. White precipitates (*i.e.*, SiO_2 spheres) in the cloudy solution were collected by centrifugation, followed by thorough rinsing with alcohol (95 vol%) and

de-ionized water until the pH value reached 7. The precipitates were re-dispersed in 20 mL de-ionized water prior to use.

Preparation of silica-embedded carbon foam (CF-SiO₂): The SiO₂ spheres dispersed in water was slowly added into 18 g 1.2 wt% chitosan solution (with 1 wt% acetic acid as solvent) under vigorous magnetic stirring. The mass ratio of added SiO₂ particles and chitosan was 1:1. Then, 216 μ L 50 wt% glutaraldehyde aqueous solution was added into the mixture dropwise (weight ratio of chitosan: glutaraldehyde = 2:1). After 30 s, the mixture was poured into a petri dish to allow gelation at room temperature. The as-formed hydrogel was aged at room temperature overnight and then lyophilized to obtain the sponge-like SiO₂-embedded chitosan aerogel. This aerogel was then carbonized in a tube furnace at 800 °C for 2 h in nitrogen atmosphere to form CF-SiO₂.

Removal of silica spheres: A piece of CF-SiO₂ was soaked in 2 M sodium hydroxide (NaOH) aqueous solution at 90 °C for 10 h to dissolve the embedded SiO₂ spheres. The sample was then put in 50 mL de-ionized water to remove any residual NaOH or silicate salts overnight and dried in an electric oven at 80 °C for 2 h.

Preparation of CF-MSP: CF was immersed in 1.0 M KOH aqueous solution for 8 h and then dried in an electric oven at 80 °C for 2 h. The KOH-treated CF was then annealed in a tube furnace at 800 °C in nitrogen atmosphere for 1 h to obtain the CF-MSP. After annealing, the sample was immediately washed with

de-ionized water to dissolve any soluble impurities. Finally, the CF-MSP was rinsed by 0.5 M HCl and ample amount of water until the pH reached 7, and then dried in an electric oven at 80 °C for 2 h.

Preparation of CF-MSP//CF-MSP quasi-solid state symmetric

supercapacitors: The quasi-solid state symmetric supercapacitor was fabricated via assembly of two pieces of identical CF-MSP electrodes. The electrodes were soaked in lithium hydroxide/polyvinyl alcohol (LiOH/PVA) gel electrolyte for 6 h to allow gel electrolyte infiltration. The two electrodes were separated by a piece of separator (NKK TF40, 40 µm thick). Then the entire device was wrapped with parafilm (Pechiney Plastic Packaging, US). To prepare the LiOH/PVA gel electrolyte, 2.0 g LiOH was first dissolved in 50 mL de-ionized water to form a clear solution. Then 4 g PVA powder was added into the solution under vigorous stirring heated at 85 °C until a clear gel was obtained.

Material Characterizations: Scanning electron microscopy (SEM) images were acquired using a FEI Quanta 3D Dual-beam scanning electron microscope. Transmission electron microscopy (TEM) images were collected using a JEM 2010-HR transmission electron microscope (accelerating voltage: 200 kV). Nitrogen absorption/desorption measurements were conducted with a Micromeritics ASAP 2010 porosimetry analyzer at liquid nitrogen temperature (77 K). X-ray photoelectron spectroscopy (XPS) was performed by a RBS upgraded PHI-5000C ESCA system with Mg-monochromatic X-ray at a power of 25 W and

a beam diameter of 10 mm. All XPS peak positions were calibrated using the C 1s photoelectron peak at 284.6 eV as the reference. Raman spectra were collected with a Raman spectrometer (Reinshaw RAMAN, 632.8 nm excitation wavelength). X-ray diffractions were conducted by a Rigaku Americas Miniflex Plus X-ray diffractometer. BET data were collected by a V-Sorb 2800 P surface area and porosimetry analyzer. Contact angle measurement was carried out using a SL 150 surface tensiometer (Kenuo Industry Co. Ltd., Shanghai, China).

Electrochemical Measurements: Cyclic voltammetry (CV), Galvanostatic charge-discharge (GCD) experiments were performed with a CHI 660D electrochemical workstation (CH Instruments, Inc.) in a three-electrode electrolytic cell. A graphite rod (*ca.* 5 mm in diameter), a mercury/mercury oxide electrode (Hg/HgO in 1 M NaOH aqueous solution, 0.165 V vs. Standard Hydrogen Electrode) and 3 M KOH aqueous solution were used as the counter electrode, reference electrode and electrolyte, respectively. The working electrode was prepared by pressing the carbon foam onto a piece of clean nickel foam without addition of binder (mass loading: 2.5 mg cm⁻², packing density: 250 mg cm⁻³). To ensure the weight accuracy, an analytical balance (Citizen Scale, Model CX265) with a precision of 0.1 mg was used for all weight measurements. Three CF-MSP electrodes were made and tested under the same testing condition to evaluate standard deviation of capacitance. Electrochemical impedance spectroscopy (EIS) was conducted in a frequency range from 0.1 Hz to 100 kHz at

open circuit potentials with a perturbation of 5 mV. All EIS spectra were fitted using the *ZSimpWin* software. Cycling Stability test of the single electrode was carried out in 3 M KOH aqueous electrolyte using CV at a scan rate of 200 mV s⁻¹ for 10000 cycles. Cycling stability of the symmetric device was evaluated by CV with various scan rates (100, 200, and 400 mV s⁻¹).

3.3 Results and Discussions

Figure 3.1a illustrates the synthesis procedure of CF-MSP. Silica-embedded carbon foam (CF-SiO₂) was prepared by mixing silica spheres (*ca.* 200 nm in diameter, Figure 3.2a and 3.2b) with chitosan solution, followed by gelation with glutaraldehyde, freeze-drying and carbonization (refer to the Experimental Section). As shown in Figure 3.1b, carbonization of chitosan-derived polymer yields a self-standing 3D porous structure with micron size cavities formed by interconnected carbon sheets. These micron size cavities are generated during the freeze drying process, resulting from the sublimation of water in the chitosan solution.²⁰ Silica spheres are embedded in each sheet (Figure 3.1c), owing to the electrostatic attraction between inherently negatively charged silica spheres and positively charged chitosan polymers with protonated amine groups. Dissolving the silica spheres leaves spherical sub-micron size cavities (macro-pores) on each carbon sheet (Figure 3.1d and Figure 3.1e). This sample is denoted as CF. Fourier-transform infrared spectrum and powder X-ray diffraction pattern collected from CF confirmed the complete removal of silica spheres (Figure 3.2c

and 3.2d). CF was then soaked in 1.0 M KOH aqueous solution, followed by drying and further annealing at 800 °C in nitrogen atmosphere to create meso- and micro-pores on the surface of carbon sheets, yielding a piece of self-standing hierarchical porous carbon foam (Figure 3.1f inset). KOH was selected as the activation agent because of its ability to yield activated carbons with higher surface area and larger population of micro- and small meso-pores than other chemical activation agents.²¹ Removal of silica spheres and subsequent annealing process did not damage the structural integrity of the carbon sheets (Figure 3.1f and Figure 3.1g). The resultant morphology of the CF-MSP is completely different from conventional activated carbon powder. The latter one lacks a three-dimensional structure and is composed of thick chunks decorated with excessive amount of micro-pores.²² It should also be mentioned here that although the silica-embedded chitosan aerogel is compressible, its compressibility is lost after the pyrolysis of chitosan polymer to carbon (CF and CF-MSP).

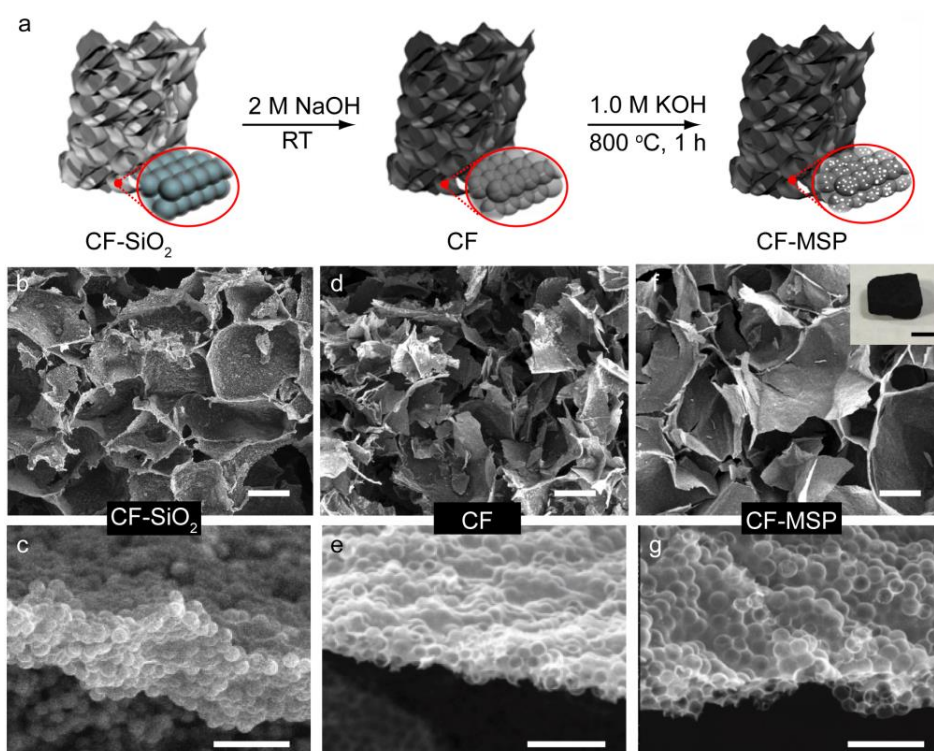


Figure 3.1 (a) Schematic illustration of the synthesis of CF-MSP. (b,d,f) SEM images of CF-SiO₂, CF and CF-MSP. Scale bars are 25 μm. (c,e,g) SEM images collected from the edge of a carbon sheet in (b,d,f). Scale bars are 1 μm. Figure 1f inset shows a digital picture of a piece of self-standing CF-MSP foam, scale bar is 1 mm.

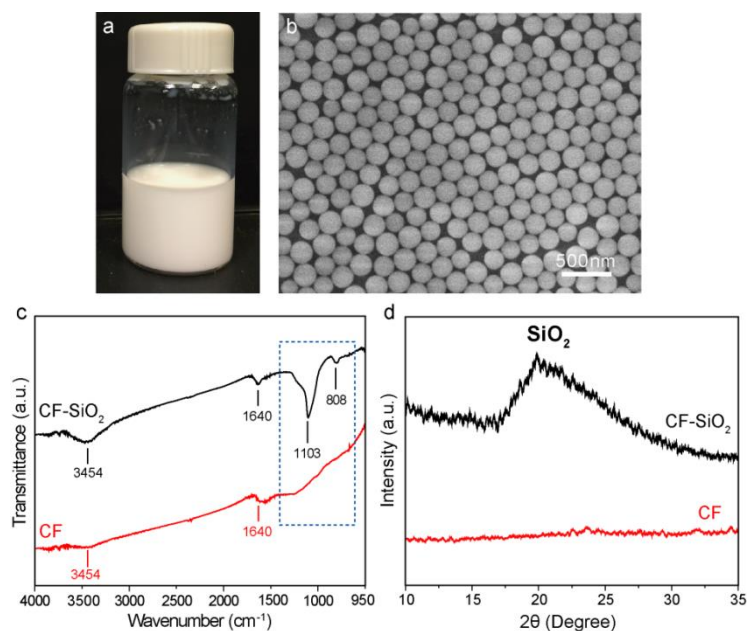


Figure 3.2 (a) Digital picture of silica sphere suspension. (b) SEM image of silica spheres with an average diameter of 200 nm. (c) FT-IR spectra of CF-SiO₂ and CF. The characteristic peaks of SiO₂ are highlighted in the blue dashed box. Peaks at

3454 cm^{-1} (O-H stretching) and 1640 cm^{-1} (H-O-H bending) are originated from physically absorbed water. (d) PXRD pattern of CF-SiO₂ and CF. The broad peak centered at $\sim 21^\circ$ is consistent with the value reported for SiO₂.

Brunauer–Emmett–Teller (BET) measurements and transmission electron microscopy (TEM) studies were carried out to characterize the porous structure of CF-MSP. Figure 3.3a compares the nitrogen adsorption-desorption isotherm of CF-MSP and CF. It is clear that CF-MSP has significantly higher absorbed nitrogen volume than CF, confirming the increase of surface area after KOH activation. For CF-MSP, the steep increase in the amount of nitrogen absorbed at both low relative pressure ($P/P_0 < 0.1$) and high relative pressure ($P/P_0 > 0.9$) indicate the existence of large amount of micro-pores and macro-pores, respectively.²³ The hysteresis located at $0.4 < P/P_0 < 1.0$ suggests the presence of meso-pores.²⁴ As shown in Figure 3.3b, CF-MSP possesses a porous structure containing multi-scale pores with pore size spanning from sub-nanometer to sub-micron. Table 3.1 summarizes key structural parameters of CF-MSP and CF obtained from the BET tests. CF-MSP has substantially higher amount of micro-pores and meso-pores than CF (Figure 3.4). The increased pore volume should be attributed to KOH activation. During the annealing process, the KOH deposited on carbon sheets melt and consequently etch carbon,^{4,21,25} resulting in the distortion of carbon network and the formation of small (micro- and meso-) pores (Figure 3.5a). The high resolution TEM (HR-TEM) images collected for CF and CF-MSP, as shown in Figure 3.5b, reveal the presence of small pores in

CF-MSP and the amorphous nature of each carbon sheet. Significantly, CF-MSP exhibits an ultra-high BET surface area of $2905 \text{ m}^2 \text{ g}^{-1}$, which is considerably larger than that of CF ($143.5 \text{ m}^2 \text{ g}^{-1}$).

Table 3.1 BET results of CF and CF-MSP

Sample	BET surface area [$\text{m}^2 \text{ g}^{-1}$]	Micropore volume, $V_{micro}^a)$ [$\text{cm}^3 \text{ g}^{-1}$]	Non-micropore volume, $V_{non-micro}^b)$ [$\text{cm}^3 \text{ g}^{-1}$]	$V_{micro}/V_{non-micro}$
CF	143.5	0.024	1.012	0.024
CF-MSP	2905.6	0.930	3.407	0.273

a) t-plot micro-pore volume; b) BJH desorption cumulative volume ($> 2 \text{ nm}$).

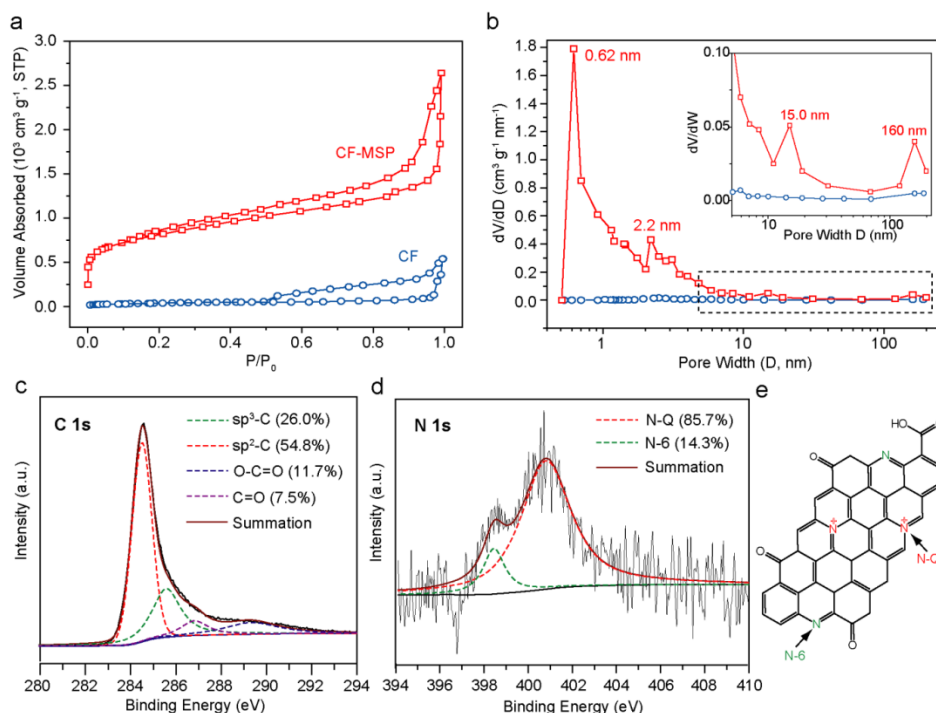


Figure 3.3 (a) Nitrogen adsorption-desorption isotherms of CF-MSP and CF collected at liquid nitrogen temperature (77 K). (b) Pore size distribution calculated from the absorption-desorption isotherm using Barrett-Joyner-Halenda (BJH) method (for pore size ranges between 2 nm and 300 nm) and Saito-Foley (SF) method (for pore size $< 2 \text{ nm}$). (c) C 1s XPS spectrum and (d) N 1s XPS spectrum. The black lines are experimental data that can be de-convoluted into several synthetic peaks (dashed curves). The solid curve is the summation of all

the synthetic peaks. Percentages of different carbon species and N-functionalities are evaluated based on area of synthetic peaks. (e) Schematic illustration of the chemical structure of CF-MSP derived from XPS spectra.

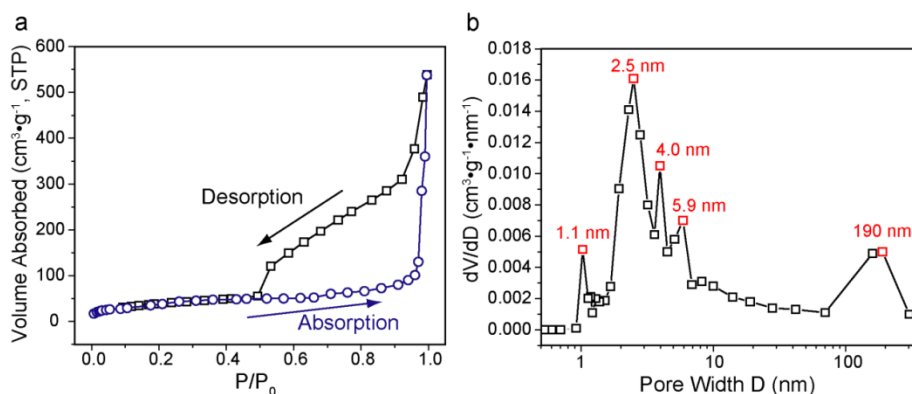


Figure 3.4 Porous structure of CF. (a) Nitrogen adsorption-desorption isotherm collected at liquid nitrogen temperature (77 K). (b) Pore size distribution. Small macro-pore/meso-pore and micro-pore size distribution were derived from the BJH and SF method, respectively.

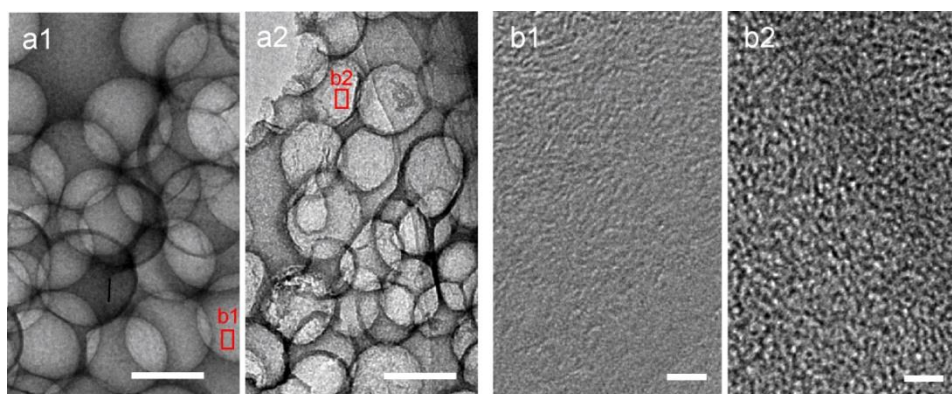


Figure 3.5 TEM Characterizations of CF-MSP. TEM images of (a1, b1) CF and (a2, b2) CF-MSP. Scale bars in (a) and (b) are 200 nm and 5 nm, respectively. The red boxes highlight the portion shown in b1 and b2.

The X-ray photoelectron spectroscopy (XPS) survey spectrum of CF-MSP displays strong carbon and oxygen signal (Figure 3.6a), indicating the carbon surface is functionalized with oxygen functionalities. As shown in the C 1s spectrum (Figure 3.3c), CF-MSP exhibits a large portion of sp^2 -hybridized carbon (54.8% based on the synthetic peak area) and oxygen functional groups. It has

been reported that oxygen-functionalities can increase wettability of carbon materials and ease electrolyte permeation into porous structure,²⁶ which is also confirmed by our contact angle measurement showing that CF-MSP has superior electrolyte wettability (Figure 3.7). In the survey spectrum, there is an additional weak signal centered at a binding energy of *ca.* 400 eV which can be assigned to nitrogen. This small amount of nitrogen (1.95 at.%) is believed to be originated from the amine and amide groups of partially-deacetylated chitosan. High resolution N 1s spectrum (Figure 3.3d) further verifies that the nitrogen-containing groups are pyridine-like nitrogen (N-6) and quaternary nitrogen (N-Q) (Figure 3.3e). N-doping has found to be useful in improving the electrical conductivity, and thus, facilitate electron transfer in carbon electrode. Specifically, N-6 atoms can contribute pseudo-capacitance in basic electrolytes and thus are able to enhance the overall capacitance of CF-MSP.²⁶ N-Q atoms exhibit electron donor ability, which facilitates electron transfer as well as enhances the electrical conductivity.^{26,27} Both types of the N atoms are beneficial for achieving high capacitance at ultrahigh current densities. We also observed that the N content decreased after the KOH activation step. The N content of CF is about 4.12 at.% (Figure 3.8a), which is considerably higher than that of CF-MSP (1.95 at.%). Analysis of the N 1s XPS spectrum of CF (Figure 3.8b) revealed that the reduction of N-6 accounts for the reduced N content. Our observation is consistent with previous observations that N atoms at edge (*e.g.*, N-6) are not

quite stable and tend to convert to N atoms embedded in graphene lattice (*e.g.*, N-Q) at elevated temperatures.^{27,28} In addition, CF-MSP exhibits a high degree of graphitization (Figure 3.6b). The electrical conductivity of CF-MSP is estimated to be 300 S m^{-1} , which is comparable with highly conductive copper tape or copper foil, and significantly larger than the commercial carbon cloth (Figure 3.6c). Combination of multi-scale pore system, ultrahigh surface area and excellent electrical conductivity render CF-MSP a promising electrode material for electrical double layer capacitors.

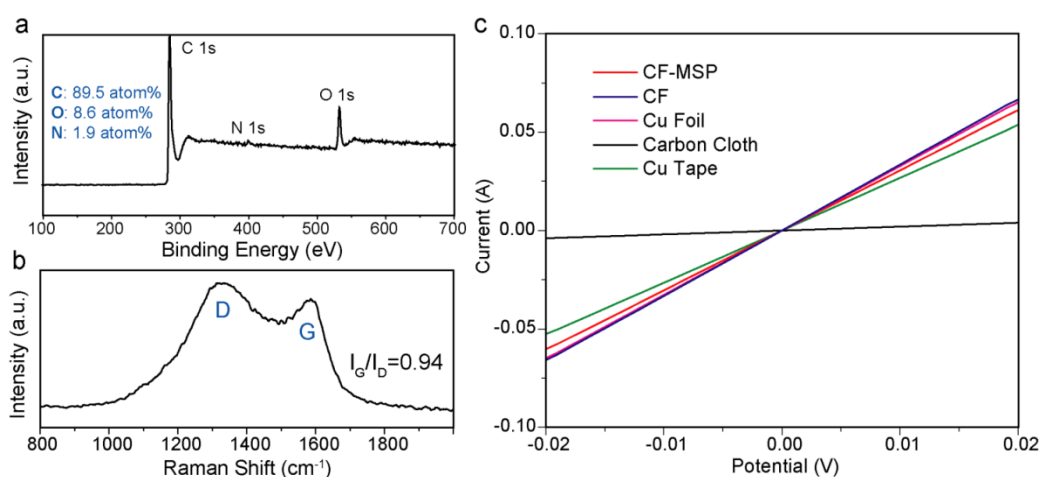


Figure 3.6 Physical characterizations of CF-MSP. (a) The XPS survey spectrum of CF-MSP. (b) Raman spectrum. Two characteristic peaks (D and G) are labeled. I_G/I_D represents the ratio of G to D peak intensity. The larger the I_G/I_D indicates the higher the degree of graphitization. (c) I - V curves collected for CF-MSP using two-probe measurement by an electrochemical workstation. I - V curves of CF, copper tape, copper foil and carbon cloth are added for comparison. The distance between the two probes was 1 cm.



Figure 3.7 Images of the wetting process. CF-MSP was used as the substrate and 3 M aqueous KOH was used as the liquid. CF-MSP can be completely wetted by the aqueous KOH electrolyte, suggesting its superior wettability contributed by the surface oxygen functionalities.

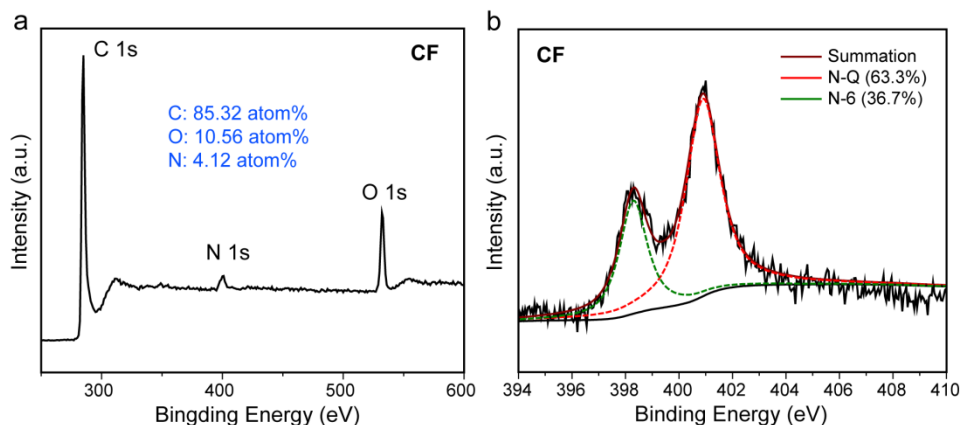


Figure 3.8 (a) XPS survey spectrum of CF. (b) N 1s XPS spectrum of CF. The black lines are experimental data that can be de-convoluted into two synthetic peaks (dashed curves). The solid curve is the summation of both the synthetic peaks. Percentages of different carbon species and N-functionalities are evaluated based on the area of the synthetic peaks.

The capacitive performance of CF-MSP was investigated in a three-electrode electrolytic cell filled with 3 M KOH aqueous electrolyte. The quasi-rectangular cyclic voltammetry (CV) curves obtained at fast scan rates and isosceles triangular-shaped galvanostatic charge-discharge (GCD) profiles collected at large current densities indicate that CF-MSP has nearly ideal capacitive performance and efficient ion transfer (Figure 3.9a and 3.9b).^{10,29} There are negligible IR drops in GCD profiles collected at large current densities, suggesting the CF-MSP electrode is highly electrically conductive. Figure 3.6c shows the gravimetric capacitances of CF-MSP measured at different current densities from 1 A g^{-1} to 500 A g^{-1} . CF-MSP yields an outstanding gravimetric capacitance of $374.7 \pm 7.7 \text{ F g}^{-1}$ at a current density of 1 A g^{-1} . More importantly, the electrode achieves a remarkable specific capacitance of $235.9 \pm 7.5 \text{ F g}^{-1}$ at an ultrahigh current density

of 500 A g^{-1} , retaining more than 60% of the capacitance when the current density increased by 500 times. To our knowledge, the gravimetric capacitances obtained at current densities beyond 100 A g^{-1} are the best values reported for carbon electrodes and is much better than conventional activated carbon powder. Moreover, the CF-MSP electrode also exhibited outstanding volumetric capacitance with 94.13 F cm^{-3} at 1 A g^{-1} , and retained 78.5 F cm^{-3} and 59.4 F cm^{-3} at 100 A g^{-1} and 500 A g^{-1} , respectively (Figure 3.10). These values are higher than a number of carbon-based supercapacitors tested in aqueous electrolytes and particularly promising given highly porous materials are disadvantageous in volumetric capacitance. As a carbon-based material, the CF-MSP also has impressive cycling stability, with 98.0% retention after 20000 cycles (Figure 3.11).

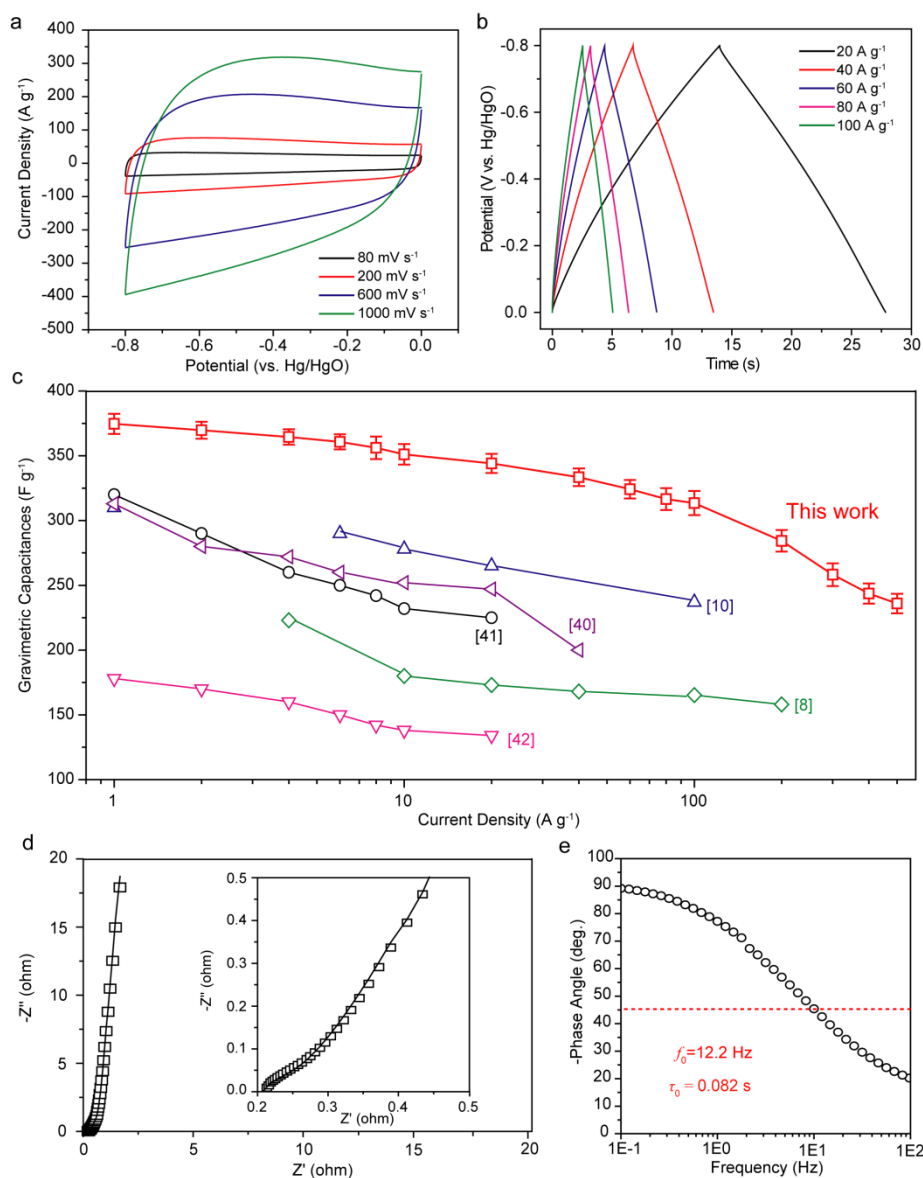


Figure 3.9 (a) Cyclic voltammograms collected at various scan rates. (b) GCD profiles collected at various current densities. (c) Gravimetric capacitance measured at different current densities. The error bars represent standard deviations evaluated based on data collected in triplicate. The gravimetric capacitances of some previously reported carbon-based supercapacitor electrodes are added for comparison.^{8,10,40-42} Ref.8: bamboo-shaped carbon fiber; Ref.10: holey graphene aerogel film; Ref.40: B,N-codoped porous carbon; Ref.41: hierarchical porous carbon/graphene composite; Ref.42: N-doped hierarchical porous carbon. (d) Nyquist plot collected at open circuit potential from 0.1 Hz to 10^5 Hz with a perturbation of 5 mV. Open dots and solid line represent experimental data and fitting curve, respectively. Inset shows the low-frequency region of the Nyquist plot. (e) Bode phase plot. Dashed line highlights the characteristic frequency f_0 ($1/\tau_0$) at the phase angle of -45° .

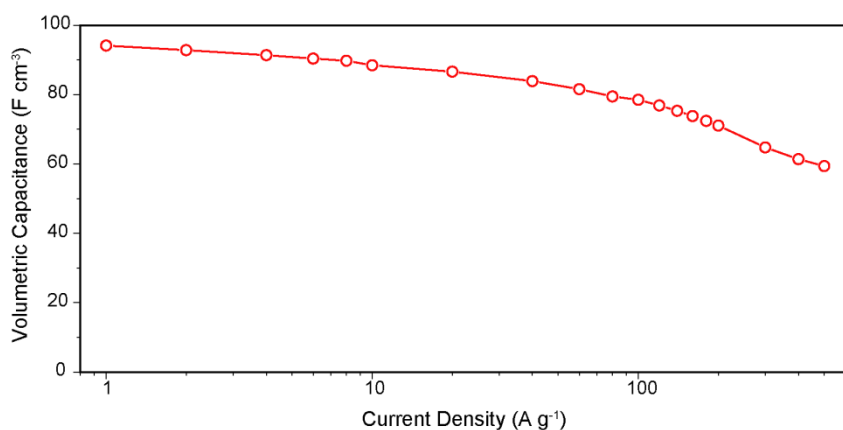


Figure 3.10 Plot of the volumetric capacitance of CF-MSP obtained in 3 M KOH aqueous electrolyte as a function of current density.

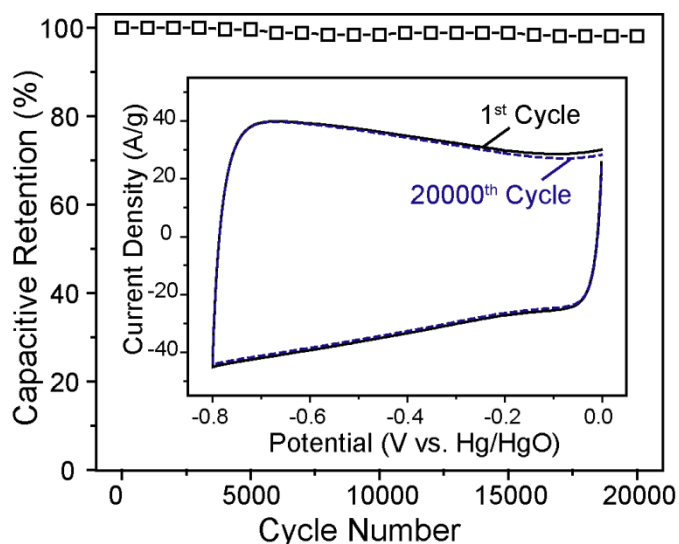


Figure 3.11 Cycling stability performance of CF-MSP. Capacitive retention measurement of CF-MSP performed by CV at a scan rate of 200 mV s^{-1} in 3 M KOH aqueous solution for 20000 cycles. Inset shows the CV curves of the first and last cycle.

A number of electrochemical measurements including capacitance differentiation and electrochemical impedance spectroscopy (EIS) were performed to understand the scientific basis for the exceptional capacitive performance of CF-MSP. Trasatti analysis³⁰ showed that the maximum capacitance of CF-MSP is 380.22 F g^{-1} . The contribution from EDL capacitance and pseudo-capacitance are

87% and 13%, respectively (Figure 3.12a-c). This conclusion is in accordance with the result analyzed by another method, *i.e.*, the Dunn method³¹ as shown in Figure 3.12d-f. In addition, the maximum area-normalized capacitance of CF-MSP, obtained by dividing the maximum gravimetric capacitance by BET specific surface area is calculated to be $13 \mu\text{F cm}^{-2}$, which falls in the range of electrical double layer capacitance ($5\text{-}20 \mu\text{F cm}^{-2}$),³² confirming that the EDL capacitance is the dominated capacitance. The ultra-large surface area of CF-MSP is thus believed to be critical for achieving such high specific capacitance. On the other hand, rate capability is determined by the efficiency of charge transport and ion diffusion.³³ EIS analysis (Figure 3.13) reveals that CF-MSP has a very small combined series resistance (R_s) of 0.21Ω , which is comparable to other highly conductive carbon materials.³⁴⁻³⁶ The steep slope in the low frequency domain in the Nyquist plot indicates ion transport in the porous electrode is very efficient (Figure 3.9d).³⁷ Lack of semi-circle in the middle frequency domain further suggests the charge transfer resistance (R_{ct}) at the electrode/electrolyte interface is negligible (Figure 3.9d inset). Bode phase diagram (Figure 3.9e) also discloses some key information. First, the phase angle at 0.1 Hz is close to the ideal phase angle, *i.e.*, -90° , again revealing the nearly ideal capacitive behavior. Second, the characteristic frequency (f_0) at the phase angle of -45° is estimated to be 12.2 Hz , corresponding to a characteristic time constant ($\tau_0 = 1/f_0$) of 0.082 s . This τ_0 is considerably smaller than activated carbon (10 s),³⁸ 3D graphene scaffold (0.53

s),³⁷ multi-walled carbon nanotubes (0.7 s),³⁹ holey graphene film (0.17 s)¹⁰ and is comparable to highly conductive onion-like carbons synthesized at ultrahigh temperature (*ca.* 0.1 s).³⁹ The ultra-small τ_0 marks the rapid frequency response of CF-MSP and is in agreement with its exceptional rate capability. The capacitance of CF-MSP is also evaluated in a two-electrode configuration and the results will be discussed along with the electrochemical performance of an assembled supercapacitor device in following sections.

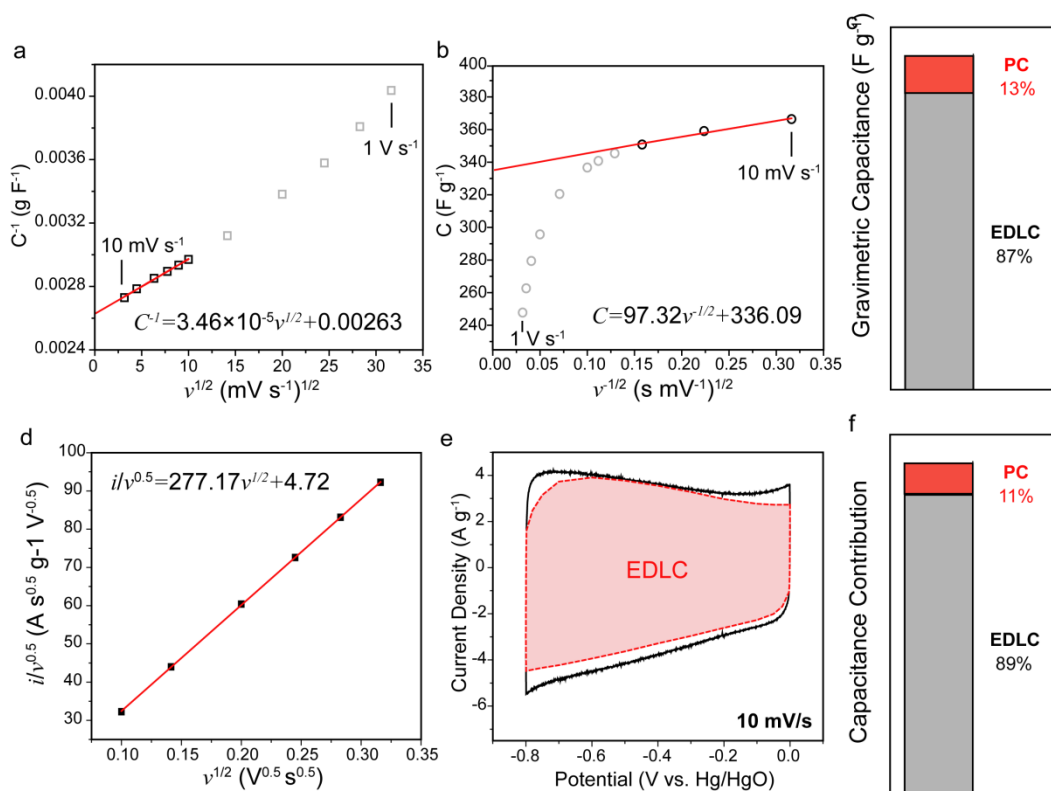


Figure 3.12 (a-c) Trasatti method: (a) Plots of reciprocal of gravimetric capacitance (C^{-1}) against square root of scan rate ($v^{1/2}$). (b) Plots of gravimetric capacitance (C) against reciprocal of square root of scan rate ($v^{-1/2}$). The red lines are the linear fitting of data points collected at slow scans. The algebraic equations are used for fittings. Data points in grey are masked during linear fitting. (c) Histogram showing the capacitance contribution from electrical double layer capacitance (EDLC) and pseudocapacitance (PC). (d-f) Dunn method: (d) $i(V)/v^{1/2}$ vs. $v^{1/2}$ plot collected for CF-MSP using the anodic current at a potential of -0.1 V vs. Hg/HgO (e) Dunn method analysis of capacitance

contribution of CF-MSP. The colored region outlines the current contributed from EDLC. (f) Histogram showing the capacitance contribution from EDLC and PC.

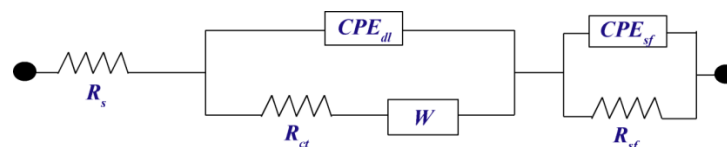


Figure 3.13 Equivalent electric circuit employed for fitting Nyquist plots. Parameters: R_s - combined series resistance; R_{ct} - charge-transfer resistance; W - Warburg element; CPE_{dl} - constant phase element related to electrical-double-layer capacitance; CPE_{sf} - constant phase element related to pseudocapacitance; R_{sf} - surface resistance.

To understand the role of pores on the capacitive performance of CF-MSP, we prepared three control samples by modifying the synthetic procedure as illustrated in Figure 3.14. The control samples are denoted as CF-1, CF-2 and CF-3, respectively. CF-1 is a piece of carbon plate with sub-micron cavities and small (meso- and micro-) pores, but without 3D network structure (micron pores). CF-2 is a piece of 3D carbon foam with small (meso- and micro-) pores, but lacks sub-micron cavities. CF-3 is a piece of 3D carbon foam with sub-micron cavities (macro-pores), but no small (meso- and micro-) pores. Corresponding nitrogen sorption isotherms and representative SEM images of the three carbon foams are presented in Figure 3.16 and Figure 3.17, respectively. Figure 3.18 compares the gravimetric capacitances of these control samples with CF-MSP at current densities ranging from 1 A g^{-1} to 100 A g^{-1} . It is clear that eliminating any type of pores causes significantly reduction of both gravimetric capacitance and rate capability. It confirms that the combination of multiple-scale pores is indispensable to achieve the outstanding performance of CF-MSP. To further

illustrate the specific function of each type of pores, we evaluated their imaginary capacitances (C'') as a function of frequency and compared to the C'' of CF-MSP (Figure 3.15). As shown in Figure 3.15a and 3.15b, in the absence of micron-sized pores or sub-micron pores, a significant loss of capacitance in relatively high frequency region (from 1 Hz to 1000 Hz) is observed, while the capacitance at low frequencies remains almost unchanged. In contrast, CF-3 exhibits much smaller capacitance in the entire frequency range from 0.1 Hz to 1000 Hz than all other samples (Figure 3.15c). These results unveil two important pieces of information. First, the presence of micron-pores and sub-micron pores plays a critical role in facilitating ion diffusion into small pores. The loss of capacitance at high frequencies observed for CF-1 and CF-2 can be ascribed to the sluggish ion diffusion that impedes the formation of EDL in small pores. Second, a major portion of the capacitance of CF-MSP must be related to the presence of small (meso- and micro-) pores, which increase the surface area by ~20 times. These conclusions drawn from EIS results are also consistent with the capacitive performance of the control samples. As shown in Table 3.2, CF-3 exhibits the highest rate capability but smallest capacitance, whilst CF-1 and CF-2 show improved capacitance (compared to CF-3) but inferior rate capability.

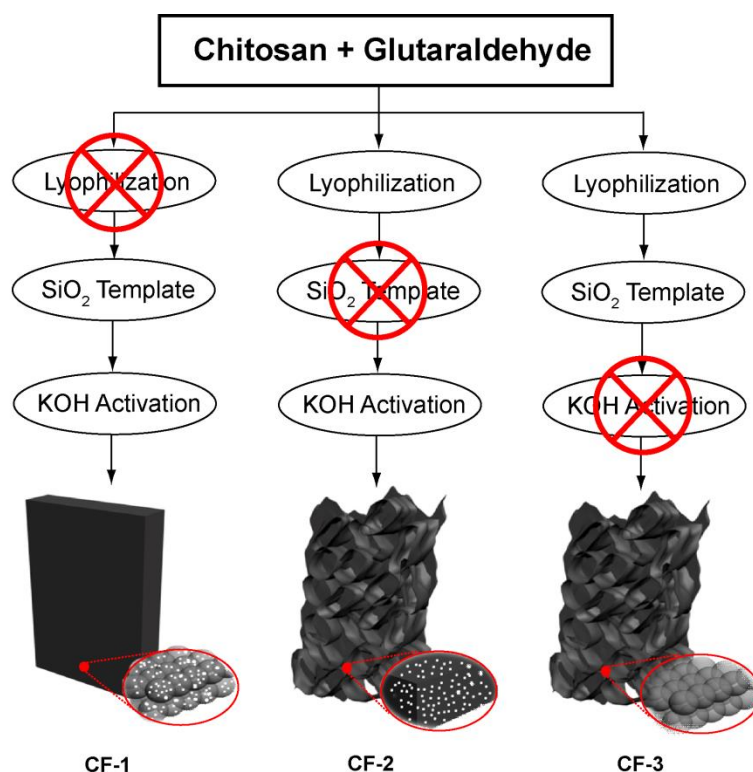


Figure 3.14 CF-1 is a carbon plate with sub-micron cavities and small (meso- and micro-) pores, but without 3D network structure (micron pores). CF-2 is a 3D carbon foam with small (meso- and micro-) pores, but lacks sub-micron cavities. CF-3 is a 3D carbon foam with sub-micron cavities (macro-pores), but no small (meso- and micro-) pores.

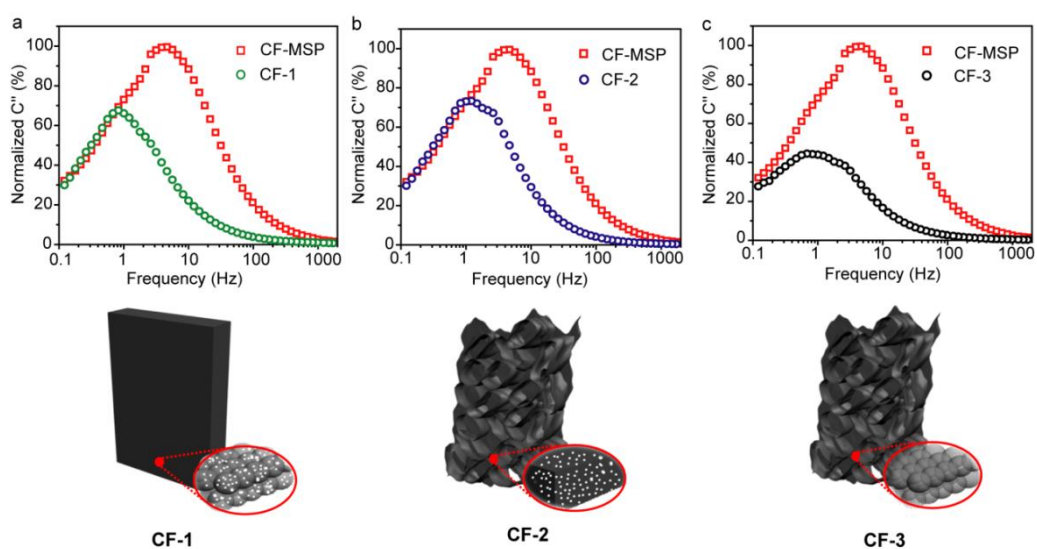


Figure 3.15 Role of pores on capacitance and rate capability of carbon foam. Plot of normalized C'' (normalized to the maximum C'') as a function of frequency for (a) CF-1, (b) CF-2, (c) CF-3 and CF-MSP. Schematic illustrations present corresponding structural characteristics of CF-1, CF-2 and CF-3.

Table 3.2 Summary of capacitive performance of carbon foams

Sample	Pore Type			Capacitance @ 1 A g ⁻¹ [F g ⁻¹]	Capacitance @ 100 A g ⁻¹ [F g ⁻¹]	Rate Capability ^{a)}
	Micron pores	Sub-micron pores	Meso- and micro-pores			
CF-1	✗	✓	✓	193.4	96.9	50.1%
CF-2	✓	✗	✓	181.1	107.5	59.4%
CF-3	✓	✓	✗	142.3	88.3	62.1%
CF-MSP	✓	✓	✓	376.5	314.0	83.4%

^{a)} From 1 A g⁻¹ to 100 A g⁻¹

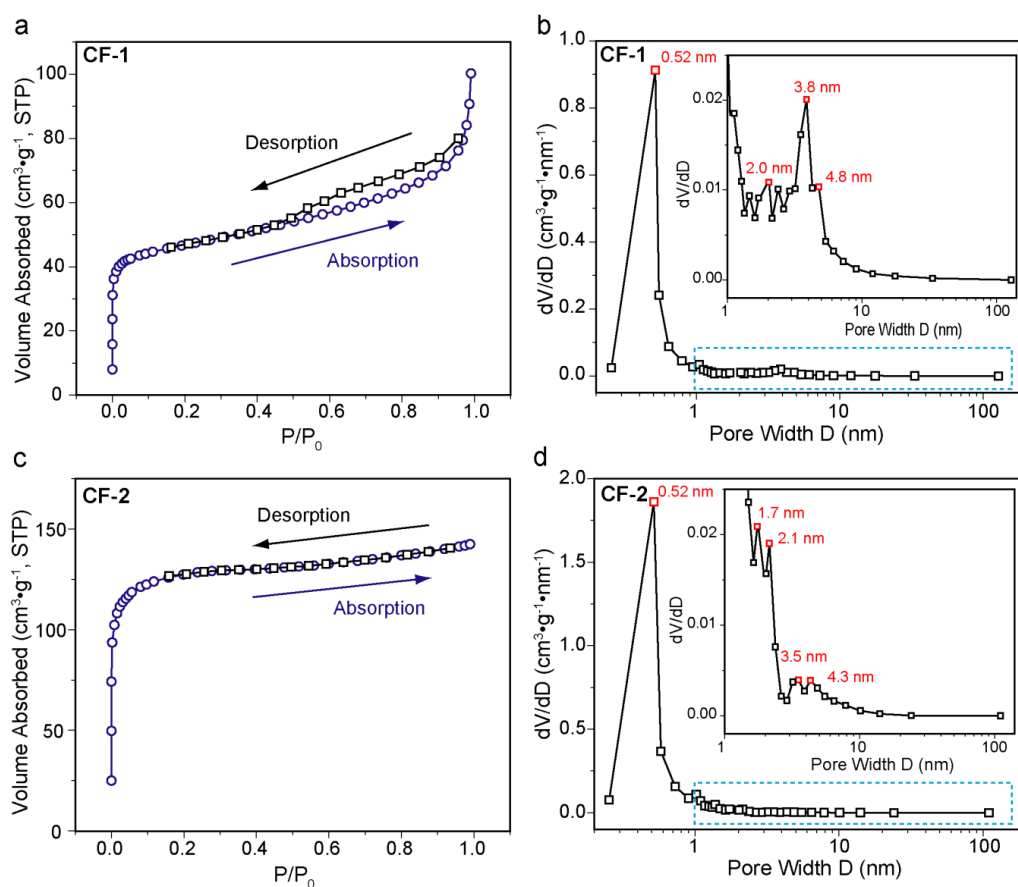


Figure 3.16 Nitrogen sorption isotherms of (a) CF-1 and (c) CF-2, and pore size distribution curve of (b) CF-1, (d) CF-2. Small macro-pore/meso-pore and micro-pore size distribution were derived from the BJH and SF method, respectively.

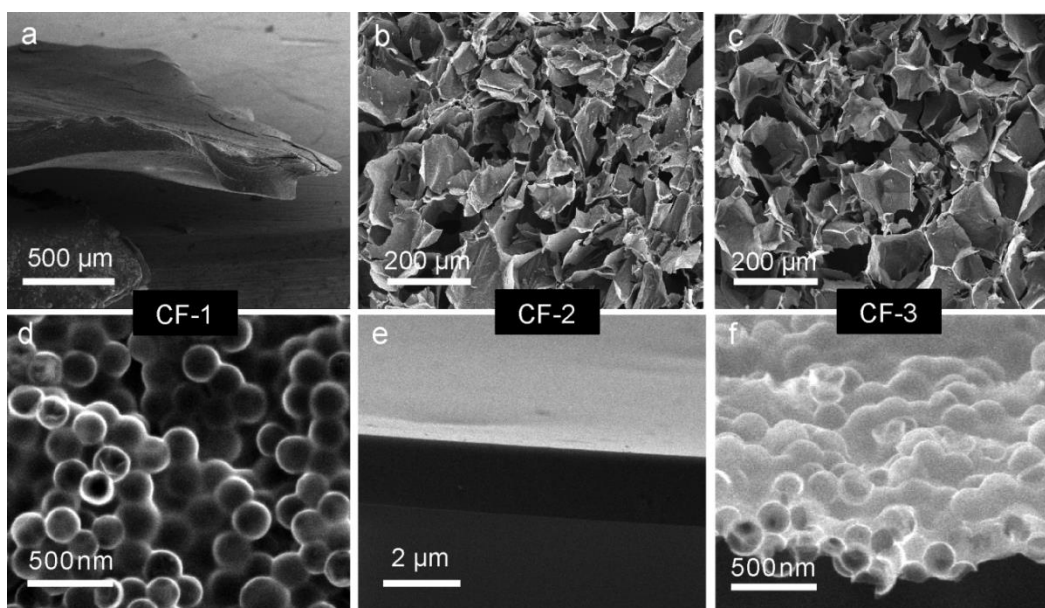


Figure 3.17 SEM images of (a, c) CF-1, (b, d) CF-2 and (e, f) CF-3.

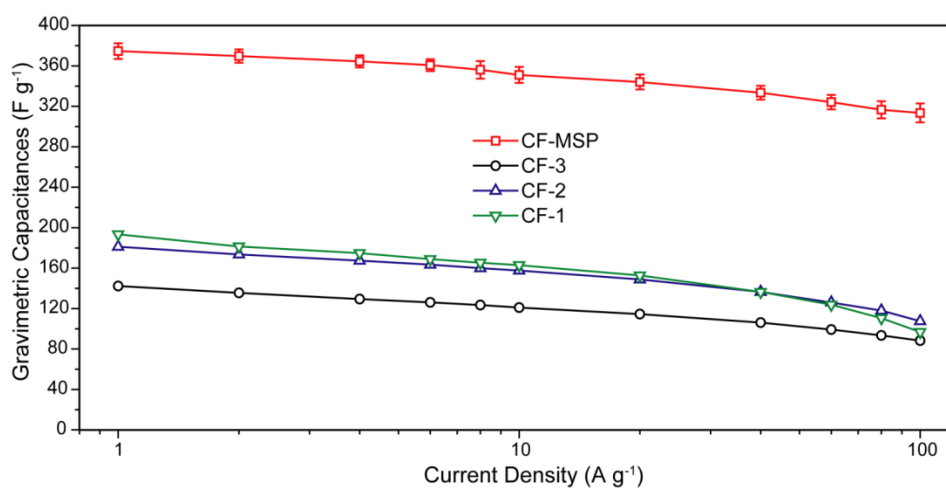


Figure 3.18 Comparison of rate capability of CF-1, CF-2 and CF-3 with CF-MSP. Error bars represent standard deviation evaluated based on data collected in triplicate.

A symmetric quasi-solid state supercapacitor device (denoted as CF-MSP SSC) was fabricated via assembly of two identical pieces of CF-MSP electrodes filled with LiOH-PVA gel electrolyte (see the Experimental Section). The device has excellent EDL capacitive behavior (Figure 3.19a and 3.19b), indicating the infiltration of gel electrolyte and ion diffusion in the electrodes are efficient.⁴³ The

small IR drop observed in the GCD curves reveals that the device internal resistance is fairly small. By fitting the Nyquist plot (Figure 3.19c), the R_s is determined to be 0.38Ω , which is substantially smaller than most other quasi-solid-state carbon-based supercapacitors including carbon nanotube SSC (30.5Ω),⁴⁴ carbon nanotube coated bacterial nanocellulose paper SSC (*ca.* 31Ω),⁴⁵ activated carbon SSC (*ca.* 5.8Ω),⁴⁶ and Nafion-functionalized reduced graphene oxide SSC (*ca.* 1.7Ω).⁴⁷ The small value of R_{ct} (0.025Ω) suggests that charges are stored via the formation of EDL and ion diffusion near electrode/electrolyte interface is fast.⁴⁸ Significantly, the τ_0 of the SSC device (0.089 s, Figure 3.19d) is only slightly higher than that of CF-MSP electrode (0.082 s). This is particularly impressive because typically gel electrolytes hinder ion diffusion and a significantly increased τ_0 is expected for quasi-solid-state devices. We believe the presence of the macro-sized cavities allows efficient infiltration of electrolyte. The excellent electrical conductivity of CF-MSP also enables swift transport of electrons, which reduces the τ_0 . As a result, CF-MSP SSC reaches an outstanding power density of 250 kW kg^{-1} at an energy density of 2.8 Wh kg^{-1} (Figure 3.19e). The performance of our CF-MSP SSC outperforms most other carbon-based SSCs tested in the same voltage window, including B, N co-doped carbon SSC (1.5 kW kg^{-1} , 1.6 Wh kg^{-1}),⁴⁹ nitrogen-doped carbon nanofiber SSC (15 kW kg^{-1} , 5.38 Wh kg^{-1}),⁵⁰ meso-porous carbon SSC (0.75 kW kg^{-1} , 5.95 Wh kg^{-1}),⁵¹ strutted graphene SSC (0.893 kW kg^{-1} , 1.13 Wh kg^{-1}),⁵² meso-porous carbon/graphene

aerogel SSC (3.5 kW kg^{-1} , 3.8 Wh kg^{-1})⁵³ and condiment-derived carbon SSC (20 kW kg^{-1} , 4.9 Wh kg^{-1}).⁵⁴ Additionally, the energy density and power density based on the total mass of the SSC device is shown in Figure 3.20. The assembled SSC is also highly flexible without obvious capacitance degradation under different bending conditions (Figure 3.21). Moreover, the CF-MSP SSC achieved a gravimetric capacitance (normalized to the total mass of CF-MSP) and a volumetric capacitance (normalized to the total volume, including the volume of two electrodes, the separator and gel electrolyte of CF-MSP) of 81.3 F g^{-1} and 21.68 F cm^{-3} at 1 A g^{-1} , respectively, which outperforms other carbon-based SSCs (Figure 3.22a). The converted gravimetric capacitance of the CF-MSP electrode in the gel electrolyte is shown in Figure 3.23. Moreover, the device exhibits excellent cycling stability with 97.6% of the initial capacitance after cycling for 10000 cycles at different scan rates (Figure 3.22b). Taken together, the outstanding capacitive performance of CF-MSP SSC at high power density makes it particularly suitable for applications that require ultrafast charging and/or discharging.

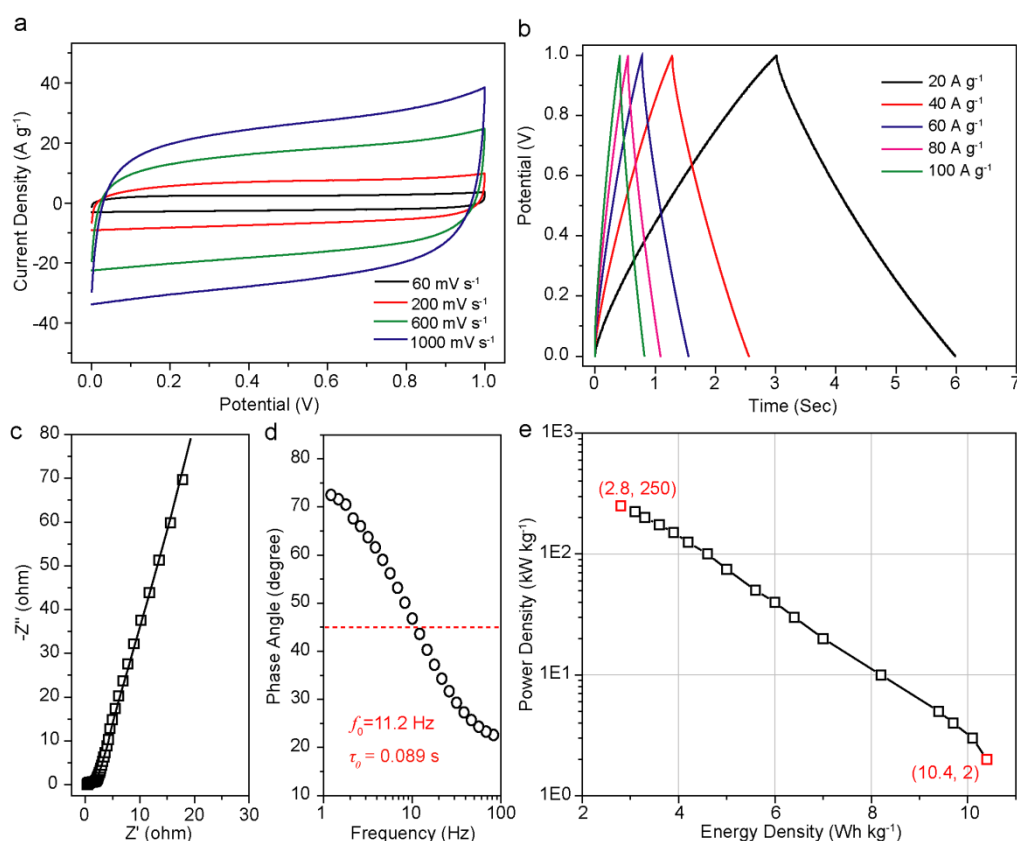


Figure 3.19 (a) Cyclic voltammograms at various scan rates and (b) GCD profiles collected under different current densities. (c) Nyquist plot collected at open circuit potential from 0.1 Hz to 10^5 Hz with a perturbation of 5 mV. Open squares are experimental data and the solid line is a fitting curve. (d) Bode phase plot. Dashed line highlights the characteristic frequency f_0 ($1/\tau_0$) at the phase angle of -45° . (e) Ragone plot: gravimetric power density and energy density of the device were calculated based on the mass of CF-MSP electrodes (2.0 mg).

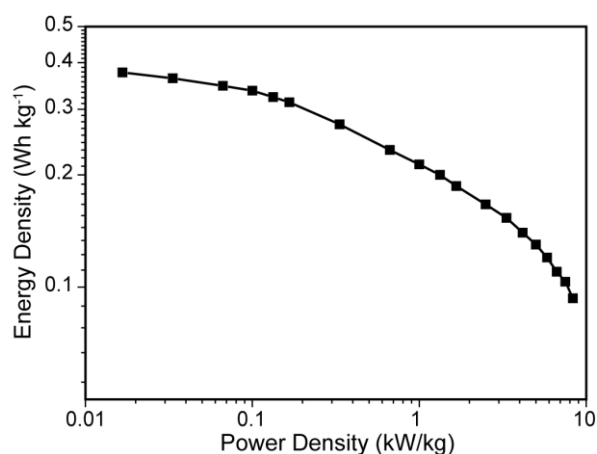


Figure 3.20 Ragone plot showing the gravimetric power density and energy density of the device calculated based on the mass of the entire CF-MSP SSC (~ 60 mg).

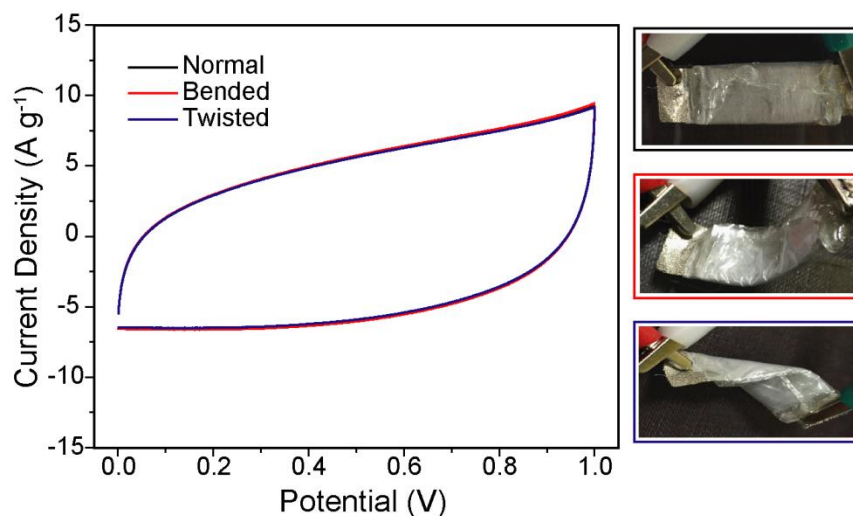


Figure 3.21 CV curves collected at a scan rate of 200 mV s^{-1} under different bending conditions. Digital pictures of the assembled device under different bending conditions.

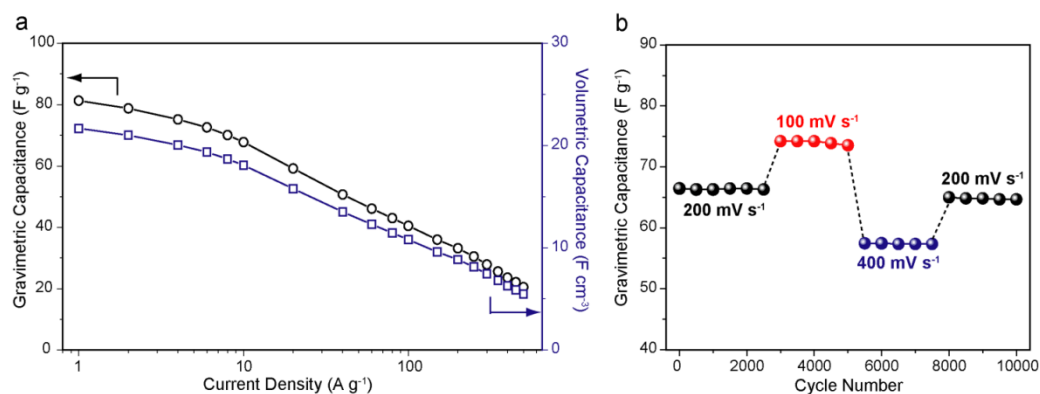


Figure 3.22 (a) Gravimetric capacitance and volumetric capacitance at various current densities. (b) Cycling stability. The gravimetric capacitances were calculated using GCD profiles.

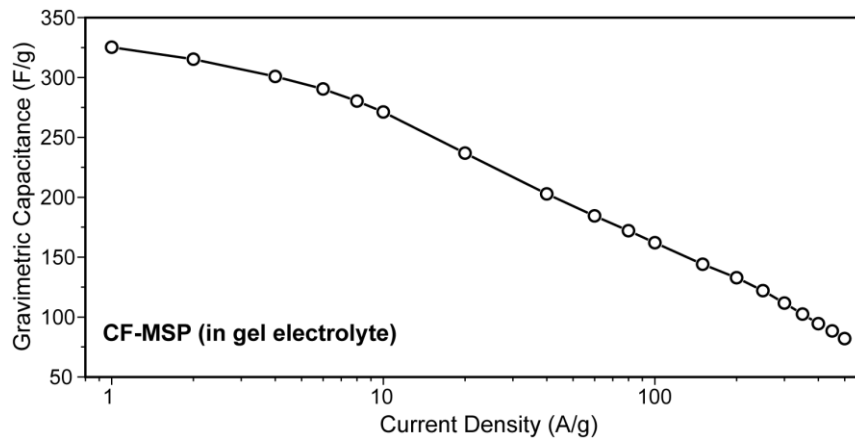


Figure 3.23 Rate capability performance of the CF-MSP evaluated by a two-electrode testing configuration in a KOH gel electrolyte. Gravimetric capacitance is based on the mass of CF-MSP.

3.4 Conclusions

In conclusion, the outstanding capacitive performances of CF-MSP electrode can be attributed to its unique structural features. First, it has ultrahigh surface area of $2905 \text{ m}^2 \text{ g}^{-1}$ that ensures a large amount of charges can be stored via EDL. Second, ion diffusion is facilitated by the presence of multiple-scale pores. The 3D interconnected pore network eases electrolyte infiltration, and the sub-micron cavities on each carbon sheet hold electrolyte in proximity to the meso- and micro-pores that can significantly shorten the ion diffusion path. Third, the highly conductive carbon structure allows rapid electron transport. Both CF-MSP and CF-MSP SSC exhibit ultra-small τ_0 , as a result of small electrical resistance and charge transfer resistance. Taking together, we have demonstrated that the combination of multiple-scale pores is the key to improve capacitive performance of porous carbon materials for ultrafast charging. The demonstrated strategy can potentially be extended to other polymers that are positively charged in acetic acid solutions since polymers containing amine groups that can be protonated and form sols in acetic acid aqueous solutions, such as polyacrylamide is possible for achieving uniform incorporation of silica spheres. Further improvement of the CF-MSP electrode performance could be achieved by optimizing the size and spatial distribution of pores, the ratio between different sized pores, and the

periodicity of different pores. The findings on CF-MSP offer useful insights for realizing high performance supercapacitors that can be rapidly charged at ultrahigh current density.

References

1. Miller, J. R.; Simon, P. *Science* **2008**, *321*, 651-652.
2. Simon, P.; Gogotsi, Y.; Dunn, B. *Science* **2014**, *343*, 1210-1211.
3. El-Kady, M. F.; Kaner, R. B. *Nat. Commun.* **2013**, *4*, 1475.
4. Zhu, Y.; Murali, S.; Stoller, M. D.; Ganesh, K. J.; Cai, W.; Ferreira, P. J.; Pirkle, A.; Wallace, R. M.; Cychosz, K. A.; Thommes, M.; Su, D.; Stach, E. A.; Ruoff, R. S. *Science* **2011**, *332*, 1537-1541.
5. Yang, P.; Ding, Y.; Lin, Z.; Chen, Z.; Li, Y.; Qiang, P.; Ebrahimi, M.; Mai, W.; Wong, C. P.; Wang, Z. L. *Nano Lett.* **2014**, *14*, 731-736.
6. Lee, J. A.; Shin, M. K.; Kim, S. H.; Cho, H. U.; Spinks, G. M.; Wallace, G. G.; Lima, M. D.; Lepro, X.; Kozlov, M. E.; Baughman, R. H.; Kim, S. J. *Nat. Commun.* **2013**, *4*, 1970.
7. Song, Y.; Feng, D.; Liu, T.; Li, Y.; Liu, X. *Nanoscale* **2015**, *7*, 3581-3587.
8. Sun, Y.; Sills, R. B.; Hu, X.; Seh, Z. W.; Xiao, X.; Xu, H.; Luo, W.; Jin, H.; Xin, Y.; Li, T.; Zhang, Z.; Zhou, J.; Cai, W.; Huang, Y.; Cui, Y. *Nano Lett.* **2015**, *15*, 3899-3906.
9. Zheng, S.; Ju, H.; Lu, X. *Adv. Energy Mater.* **2015**, *5*, 1500871.
10. Xu, Y.; Lin, Z.; Zhong, X.; Huang, X.; Weiss, N. O.; Huang, Y.; Duan, X. *Nat.*

Commun. **2014**, *5*, 4554.

11. Zhu, Z.; Hu, Y.; Jiang, H.; Li, C. *J. Power Sources* **2014**, *246*, 402-408.
12. Ghosh, A.; Lee, Y. H. *ChemSusChem* **2012**, *5*, 480-499.
13. Zhu, Z.; Jiang, H.; Guo, S.; Cheng, Q.; Hu, Y.; Li, C. *Sci. Rep.* **2015**, *5*, 15936.
14. Black, J. M.; Andreas, H. A. *J. Phys. Chem. C* **2010**, *114*, 12030-12038.
15. Ervin, M. H. *Nanotechnology* **2015**, *26*, 234003.
16. Zhao, Q.; Wang, X.; Liu, J.; Wang, H.; Zhang, Y.; Gao, J.; Lu, Q.; Zhou, H. *Electrochim. Acta* **2015**, *154*, 110-118.
17. Zhu, C.; Liu, T.; Qian, F.; Han, T. Y.-J.; Duoss, E. B.; Kuntz, J. D.; Spadaccini, C. M.; Worsley, M. A.; Li, Y. *Nano Lett.* **2016**, *16*, 3448-3456.
18. P éan, C.; Merlet, C.; Rotenberg, B.; Madden, P. A.; Taberna, P.-L.; Daffos, B.; Salanne, M.; Simon, P. *ACS Nano* **2014**, *8*, 1576-1583.
19. Forse, A. C.; Griffin, J. M.; Merlet, C.; Carretero-Gonzalez, J.; Raji, A.-R. O.; Trease, N. M.; Grey, C. P. *Nat. Energy* **2017**, *2*, 16216.
20. Zhang, F.; Liu, T.; Hou, G.; Kou, T.; Yue, L.; Guan, R.; Li, Y. *Nano Res.* **2016**, *9*, 2875-2888.
21. Wang, J.; Kaskel, S. *J. Mater. Chem.* **2012**, *22*, 23710-23725.
22. Yang, Y.; Liu, T.; Liao, Q.; Ye, D.; Zhu, X.; Li, J.; Zhang, P.; Peng, Y.; Chen, S.; Li, Y. *J. Mater. Chem. A* **2016**, *4*, 15913-15919.
23. Zhao, J.; Lai, H.; Lyu, Z.; Jiang, Y.; Xie, K.; Wang, X.; Wu, Q.; Yang, L.; Jin,

- Z.; Ma, Y.; Liu, J.; Hu, Z. *Adv. Mater.* **2015**, *27*, 3541-3545.
24. Wang, G.; Wang, H.; Lu, X.; Ling, Y.; Yu, M.; Zhai, T.; Tong, Y.; Li, Y. *Adv. Mater.* **2014**, *26*, 2676-2682.
25. Pachfule, P.; Shinde, D.; Majumder, M.; Xu, Q. *Nature Chem.* **2016**, *8*, 718-724.
26. Wei, X.; Jiang, X.; Wei, J.; Gao, S. *Chem. Mater.* **2016**, *28*, 445-458.
27. Jurewicz, K.; Babel, K.; Ziolkowski, A.; Wachowska, H. *J. Phys. Chem. Solids* **2004**, *65*, 269-273.
28. Pels, J. R.; Kapteijn, F.; Moulijn, J. A.; Zhu, Q.; Thomas, K. M. *Carbon* **1995**, *33*, 1641-1653.
29. Liu, T.; Ling, Y.; Yang, Y.; Finn, L.; Collazo, E.; Zhai, T.; Tong, Y.; Li, Y. *Nano Energy* **2015**, *12*, 169-177.
30. Ardizzone, S.; Fregonara, G.; Trasatti, S. *Electrochim. Acta* **1990**, *35*, 263-267.
31. Wang, J.; Polleux, J.; Lim, J.; Dunn, B. *J. Phys. Chem. C* **2007**, *111*, 14925-14931.
32. Ling, Z.; Yu, C.; Fan, X.; Liu, S.; Yang, J.; Zhang, M.; Wang, G.; Xiao, N.; Qiu, J. *Nanotechnology* **2015**, *26*, 374003.
33. Hou, Y.; Cheng, Y.; Hobson, T.; Liu, J. *Nano Lett.* **2010**, *10*, 2727-2733.
34. Weng, Z.; Su, Y.; Wang, D.-W.; Li, F.; Du, J.; Cheng, H.-M. *Adv. Energy Mater.* **2011**, *1*, 917-922.

35. Wang, H.; Li, Z.; Tak, J. K.; Holt, C. M. B.; Tan, X.; Xu, Z.; Amirkhiz, B. S.; Harfield, D.; Anyia, A.; Stephenson, T.; Mitlin, D. *Carbon* **2013**, *57*, 317-328.
36. Bo, Z.; Zhu, W.; Ma, W.; Wen, Z.; Shuai, X.; Chen, J.; Yan, J.; Wang, Z.; Cen, K.; Feng, X. *Adv. Mater.* **2013**, *25*, 5799-5806.
37. Zhai, T.; Lu, X.; Wang, H.; Wang, G.; Mathis, T.; Liu, T.; Li, C.; Tong, Y.; Li, Y. *Nano Lett.* **2015**, *15*, 3189-3194.
38. El-Kady, M. F.; Strong, V.; Dubin, S.; Kaner, R. B. *Science* **2012**, *335*, 1326-1330.
39. Portet, C.; Yushin, G.; Gogotsi, Y. *Carbon* **2007**, *45*, 2511-2518.
40. Ling, Z.; Wang, G.; Zhang, M.; Fan, X.; Yu, C.; Yang, J.; Xiao, N.; Qiu, J. *Nanoscale* **2015**, *7*, 5120-5125.
41. Sun, G.; Li, B.; Ran, J.; Shen, X.; Tong, H. *Electrochim. Acta* **2015**, *171*, 13-22.
42. Tang, J.; Wang, T.; Salunkhe, R. R.; Alshehri, S. M.; Malgras, V.; Yamauchi, Y. *Chem.-Eur. J.* **2015**, *21*, 17293-17298.
43. Xu, Y.; Lin, Z.; Huang, X.; Liu, Y.; Huang, Y.; Duan, X. *ACS Nano* **2013**, *7*, 4042-4049.
44. Kang, Y. J.; Chung, H.; Han, C.-H.; Kim, W. *Nanotechnology* **2012**, *23*, 289501.
45. Kang, Y. J.; Chun, S.-J.; Lee, S.-S.; Kim, B.-Y.; Kim, J. H.; Chung, H.; Lee, S.-Y.; Kim, W. *ACS Nano* **2012**, *6*, 6400-6406.

46. Yu, H.; Wu, J.; Fan, L.; Lin, Y.; Xu, K.; Tang, Z.; Cheng, C.; Tang, S.; Lin, J.; Huang, M.; Lan, Z. *J. Power Sources* **2012**, *198*, 402-407.
47. Choi, B. G.; Hong, J.; Hong, W. H.; Hammond, P. T.; Park, H. H. *ACS Nano* **2011**, *5*, 7205-7213.
48. Li, X.; Rong, J.; Wei, B. *ACS Nano* **2010**, *4*, 6039-6049.
49. Wu, Z.-S.; Winter, A.; Chen, L.; Sun, Y.; Turchanin, A.; Feng, X.; Müllen, K. *Adv. Mater.* **2012**, *24*, 5130-5135.
50. Chen, L.-F.; Zhang, X.-D.; Liang, H.-W.; Kong, M.; Guan, Q.-F.; Chen, P.; Wu, Z.-Y.; Yu, S.-H. *ACS Nano* **2012**, *6*, 7092-7102.
51. He, X.; Li, R.; Qiu, J.; Xie, K.; Ling, P.; Yu, M.; Zhang, X.; Zheng, M. *Carbon* **2012**, *50*, 4911-4921.
52. Wang, X.; Zhang, Y.; Zhi, C.; Wang, X.; Tang, D.; Xu, Y.; Weng, Q.; Jiang, X.; Mitome, M.; Golberg, D.; Bando, Y. *Nat. Commun.* **2013**, *4*, 2905.
53. Liu, R.; Wan, L.; Liu, S.; Pan, L.; Wu, D.; Zhao, D. *Adv. Funct. Mater.* **2015**, *25*, 526-533.
54. Qian, W.; Zhu, J.; Zhang, Y.; Wu, X.; Yan, F. *Small* **2015**, *11*, 4959-4969.

Chapter 4

3D-printed Supercapacitors with Graphene Electrodes

Abstract

Graphene is an atomically-thin, two-dimensional (2D) carbon material that offers a unique combination of low density, exceptional mechanical properties, thermal stability, large surface area, and excellent electrical conductivity. Recent progress has resulted in macro-assemblies of graphene, such as bulk graphene aerogels for a variety of applications. However, these three-dimensional (3D) graphenes exhibit physicochemical property attenuation compared to their 2D building blocks due to one-fold composition and tortuous, stochastic porous networks. These limitations can be offset by developing a graphene composite material with an engineered porous architecture. Here, we report the fabrication of 3D periodic graphene composite aerogel microlattices for supercapacitor applications, via a 3D printing technique known as direct-ink writing (DIW). The key factor in developing these novel aerogels is to create an extrudable graphene oxide (GO) based composite ink and modify the 3D printing method to accommodate aerogel processing. The 3D-printed graphene composite aerogel (3D-GCA) electrodes are lightweight, highly conductive and exhibit excellent electrochemical properties. In particular, the supercapacitors using these 3D-GCA electrodes with thicknesses on the order of millimeters, display exceptional capacitive retention (*ca.* 90% from 0.5 to 10 A·g⁻¹) and power densities (> 4

$\text{kW}\cdot\text{kg}^{-1}$) that equal or exceed those of reported devices made with electrodes 10-100 times thinner. This work provides an example of how 3D-printed materials, such as graphene aerogels, can significantly expand the design space for fabricating high performance and fully integrable energy storage devices optimized for a broad range of applications.

4.1 Introduction

The recent spike in portable and wearable electronics, such as micro-electro-mechanical systems (MEMS),¹ implantable devices,² and wireless sensors³ is driving the push for high-performance, rechargeable energy storage components with proportionate dimensions.^{4,5} Supercapacitors are now becoming a primary compact power source for this emerging market due to their high power density, fast charging/discharging rate, ultra-long cycle lifetime, and especially high frequency response on a small scale.^{6,7,8} A number of carbonaceous materials, including carbon nanotubes (CNT),^{9,10} activated carbons,¹¹ carbide derived carbons,⁴ carbon onions,¹² carbon cryogels,¹³ carbon-coated particles¹⁴ and graphenes^{15,16} have been widely investigated as electrode materials. Specifically, graphene-based materials¹⁷⁻¹⁹ hold a large advantage in supercapacitor applications due to their large specific surface area,²⁰ superior elasticity,²¹ chemical stability,¹⁹ and excellent electrical conductivity.^{22,23} However, graphene's propensity towards aggregation and restacking²⁴ can significantly affect capacitive performance by reducing the ion-accessible surfaces, and limiting ion and electron

transport due to narrower channels.²⁵ Therefore, a variety of 3D graphene-based materials (*i.e.*, hydrogels,²⁶ aerogels,²⁷ sponges,²⁸ and porous films²⁹) have been extensively explored to overcome these limitations by providing a network of interconnected pores.³⁰ Their unique properties and porous morphology not only provide additional ion-accessible surface for charge storage, but also facilitate the ion diffusion within the structure.³¹ A key challenge for 3D graphene lies in controllable large-scale assembly into desired architectures while maintaining inherent properties of the graphene (*e.g.* large surface area, high electrical conductivity, exceptional mechanical properties, *etc.*).

Several synthesis methods for 3D graphene have been proposed to realize a wide range of pore morphologies from ultrafine (<100 nm) to mesoscale (>1 μm) pore size.^{31,32} For example, template-guided methods, such as chemical vapor deposition (CVD) coatings on metallic foams have been reported for the creation of graphene monoliths.^{33,34} But this process is not scalable and the materials obtained from these methods are generally brittle under low compression.³⁵ Besides, template-free approaches are also widely used for scalable synthesis of graphene macro-assemblies due to their simple and versatile synthesis scheme. Currently, chemically-derived graphene oxide (GO)-based aerogels are the most common 3D graphene found in the literature.^{27,35-49} The main strategy of this method is the self-assembly or gelation of the GO suspension via hydrothermal reduction,³⁵⁻³⁷ chemical reduction,^{27,42-45} or direct crosslinking of the GO

sheets.^{47,48} In addition, other conventional material processing methods, such as ice-templating or freeze-casting^{40,49} have also demonstrated some control over the pore morphology. However, the architecture of these graphene networks remains largely stochastic and highly tortuous, which severely limits mass transport and results in non-optimal mechanical properties. Thus, the fabrication of 3D graphene materials with tailored macro-architectures via a controllable and scalable assembly method is still a significant challenge.

As an alternative approach, the use of 3D printing techniques to produce free-standing reduced GO (rGO) assemblies have been reported.^{50,51} However, these attempts have several drawbacks, such as the inability to synthesize samples with large surface area and the need for polymer matrices. Recently, we utilized an extrusion-based 3D printing technique,^{52,53} known as direct-ink writing (DIW) to fabricate highly compressible graphene aerogel microlattices.⁵⁴ These 3D-printed graphene aerogels showed even better mechanical strength than most bulk graphene assemblies while maintaining the large surface area of single graphene sheets. The DIW technique employs a three-axis motion stage to assemble 3D structures by robotically extruding a continuous “ink” filament through a micro-nozzle at room temperature in a layer-by-layer scheme.⁵⁵ The prerequisite for this method is to design gel-based viscoelastic ink materials possessing shear thinning behavior to facilitate extrusion flow under pressure and a rapid pseudo-plastic to dilatant recovery resulting in shape retention after

deposition.^{56,57} Furthermore, the inks' physical and electrochemical properties can be significantly improved to even realize multifunctionality by the addition of functional fillers, such as conductive nanoparticles, nanotube/wires, as well as nanofibers.^{58,59}

Here, we demonstrate a fabrication strategy for 3D-printed graphene composite aerogels (3D-GCAs) with designed architecture for micro-supercapacitor applications. Our approach is based on a printable ink consisting of both GO and graphene nanoplatelets (GNP). By adding GNP into the GO solution, the electrical conductivity of the GO-GNP composite is greatly improved without a detrimental loss of surface area. Furthermore, by building the electrodes with engineered macro-porosity to facilitate mass transport, extremely thick electrodes (*ca.* 1 mm) were produced with capacitance retention (*ca.* 90% from 0.5 to 10 A·g⁻¹) and power densities (> 4 kW·kg⁻¹) that equal or exceed those of reported devices made with electrodes 10-100 times thinner. As such this work provides an example of how 3D printing can help to overcome traditional design barriers as the library of 3D-printable materials inevitably expands.

4.2 Experimental Section

GO-GNP Ink Preparation: The raw GO powders were produced by using the Hummer method⁸³. The GO suspension (40 mg·cm⁻³) was prepared via ultra-sonication in water. The GO-GNP inks were gelled using organic sol-gel chemistry with sol-gel mixture consisted of an aqueous solution of resorcinol (R),

formaldehyde (F), and sodium carbonate catalyst (C). The mole ratios of R to F and R to C were adjusted to be 1:2 and 200:1, respectively. The concentration of R-F was 11 wt%. In a typical preparation of ink, 3.6 g 40 mg·cm⁻³ GO suspensions, 2 g R-F solution, 0.3 g GNP, and 0.9 g fumed silica are mixed, respectively. A planetary centrifugal mixer (Thinky) was used for mixing these samples for 2 min in a 35 mL container using a custom adaptor.

Ink Rheology Characterizations: Rheological properties of the ink were characterized using a stress-controlled Rheometer (AR 2000ex, TA) with a 40 mm flat plate geometry and a gap of 500 μm for the GO inks. All measurements were preceded by a one minute conditioning step at a constant shear rate of 1 s⁻¹, followed by a 10 minute rest period to allow the ink structure to reform. A stress sweep from 10⁻² to 10³ Pa at a constant frequency of 1 Hz was conducted to record the storage modulus and loss modulus variations as a function of sweep stress. The yield stress (τ_y) was defined as the stress where storage modulus falls to 90% of the plateau value. A strain sweep from 10⁻¹ to 10² s⁻¹ was also performed to record the apparent viscosity at varying shear rates.

3D Printing: The GO-GNP ink was housed in a 3 cm³ syringe barrel (EFD) attached by a luer-lok to a smooth-flow tapered nozzle (250 mm inner diameter, d). An air-powered fluid dispenser (Ultimus V, EFD) provided the appropriate pressure to extrude the ink through the nozzle. The target patterns were printed using an x - y - z 3-axis air bearing positioning stage (ABL 9000, Aerotech), whose

motion was controlled by writing the appropriate G-code commands. The 3D GO structures were printed onto silicon wafers in an isooctane bath, with a nozzle height (h) of $0.7d$ to ensure moderate adhesion to the substrate and between adjacent printed layers. Printed parts were cured in sealed glass vials at $85\text{ }^{\circ}\text{C}$. After gelation, the wet GO gels were removed from the glass vials and washed with acetone to remove water from the pores. Supercritical carbon dioxide was used to dry the as-prepared GO gels, followed by pyrolysis at $1050\text{ }^{\circ}\text{C}$ in nitrogen atmosphere for 3h. Finally, silica fillers were etched away in 5 wt% hydrofluoric acid aqueous solution for 2 days followed by solvent exchange in absolute ethanol for additional 2 days.

Fabrication of supercapacitor devices: Symmetric supercapacitors were fabricated via assembly of two pieces of identical 3D printed aerogel (4.2 wt% GNP + 12.5 wt% SiO_2) and a piece of separator (TF 4804, NKK). Lithium hydroxide (LiOH)/polyvinyl alcohol (PVA) was used as gel electrolyte. To prepare the gel electrolyte, 5 g PVA powder was gradually poured in 50 mL 1 M LiOH aqueous solution under vigorous stirring. The mixture was heated to $85\text{ }^{\circ}\text{C}$ and was kept stirring until a clear gel was formed. Prior to assembly, the two electrodes and separator were soaked in the LiOH/PVA gel electrolyte for 5 min and then dried in air for 10 min. This procedure was repeated 5 times. Then the electrolyte-soaked separator was sandwiched between the two electrodes and kept at $45\text{ }^{\circ}\text{C}$ for 6 h to form the quasi-solid-state supercapacitor device. Finally, the

assembled device was wrapped with parafilm (Pechiney Plastic Packaging, US) to avoid absorbing air moisture. The total mass of the device (including two electrodes, separator and quasi-solid electrolyte) was about 32.4 mg. The mass of the active material (two electrodes) was about 6.5 mg.

Physical properties characterizations: The dimension and weight of the samples were determined using a caliper with an accuracy of 0.01 mm and an ultra-micro balance (XP24, Mettler Toledo) with an accuracy of 0.001 mg. The morphology of the printed samples was observed by an optical camera and field-emission scanning electron microscopy (SEM). SEM was performed on a JEOL 7401-F at 10 keV (20 mA) in secondary electron imaging mode with a working distance of 2-8 mm. Textural properties were determined by Brunauer-Emmett-Teller (BET) methods using an ASAP 2020 Surface Area Analyzer (Micromeritics Instrument Corporation) via nitrogen porosimetry. The sheet resistance was measured by a four-point probe method on a Jandel RM3000.

Electrochemical properties characterizations: 3D aerogels were used directly as electrodes for testing. To fabricate electrodes, one end of the aerogel was carefully affixed to a piece of pressed nickel foam with a thin layer of silver paste and then sealed with epoxy. All the electrochemical characterizations of single electrodes were conducted in a conventional three-electrode electrolytic cell using an electrochemical workstation (CHI 660D, CH Instruments, Inc.). A graphite rod (*ca.* 5 mm in diameter) and a saturated calomel electrode (SCE, 0.244 V *vs.*

standard hydrogen electrode) were used as the counter electrode and reference electrode, respectively. Cyclic voltammograms and chronopotentiometry profiles were collected in 3 M KOH aqueous electrolyte. Stability tests were carried out in the same electrolyte at a scan rate of 200 mV/s for 10000 cycles. The cycling stability of the symmetric supercapacitor was tested at a scan rate of 60 mV/s. Electrochemical impedance spectra were recorded in 3 M KOH aqueous electrolyte in a frequency range from 10^{-1} to 10^6 Hz at open circuit potential with a perturbation of 5 mV.

4.3 Results and Discussions

In our previous report,⁵⁴ 3D-printed pure graphene aerogel microlattices were made via development of a printable GO ink and adapting the DIW process to print into a liquid bath. However, the 3D-printed pure graphene aerogels are not ideal for supercapacitor applications as their electrical resistance is still high. Thus, to further decrease resistance, GNP is added to the GO ink in this work. Though GNP will lower resistance, it will also decrease the surface area of the composite. Therefore, the GNP loading needs to be optimized to ensure sufficient rate capability and capacitance of final composite electrode. Recently, high concentration GO suspensions (*e.g.* 10-20 $\text{mg}\cdot\text{cm}^{-3}$ GO) have been used to fabricate high quality graphene aerogels with complex structures by tailoring their rheology.^{45,47,60} However, even at these concentrations, the GO suspensions did not have the ideal rheological behavior for 3D printable inks.^{35,61} To achieve the

ideal printable ink, the GO concentration was increased to $40 \text{ mg}\cdot\text{cm}^{-3}$, and hydrophilic fumed silica was added to serve as a viscosifier to meet the rheology requirements of reliable flow through a fine nozzle under shear force and shape retention after deposition. The silica, in particular, imparted both shear thinning behavior and a shear yield stress to the GO suspension to further enhance the printability of the GO-based inks. Finally, the GNPs were added along with the reactants used to induce gelation post-printing via organic sol-gel chemistry [*e.g.* resorcinol-formaldehyde (R-F) solution].⁴⁸ Figure 4.1 shows the rheological properties comparison of the starting GO suspension ($40 \text{ mg}\cdot\text{cm}^{-3}$) and a representative GO-GNP ink (4.2 wt% GNP and 12.5 wt% SiO_2). The apparent viscosity of composite ink shows orders of magnitude higher than that of the GO suspension at varying shear rates⁶¹ and both of them are shear-thinning non-Newtonian fluids (Figure 4.1a). Meanwhile, we can find that GNP and silica fillers increase the storage modulus and yield stress of pure GO suspensions by over an order magnitude (Figure 4.1b). The magnitudes of these key rheological parameters are in good agreement with those reported for other colloidal inks designed for 3D filamentary printing.⁵⁷

The fabrication process scheme of 3D-GCAs is illustrated in Figure 4.2. The composite inks are prepared by mixing GO precursor suspension ($40 \text{ mg}\cdot\text{cm}^{-3}$), GNP and silica fillers, as well as R-F gel and a catalyst (sodium carbonate) to form a homogenous, highly viscous and thixotropic ink. Then, the composite ink

is loaded into a syringe barrel and extruded through a micro-nozzle to pattern 3D structures. In order to convert the 3D printed GO-GNP structure to an aerogel afterward, the ink must remain wet through printing and gelation such that the liquid in the 3D-printed gel can be removed via critical drying to avoid gel collapse due to capillary forces. Therefore, the printing is conducted in an organic solvent (2,2,4-trimethylpentane) that is not only less dense than water but immiscible with our aqueous inks. Finally, the printed structures can be processed into aerogels through gelation, supercritical drying, and carbonization according to standard literature methods^{44,45} followed by etching of the silica with hydrofluoric acid. To demonstrate 3D printing of 3D-GCAs, we printed thin woodpile cubic lattices consisting of multiple orthogonal layers of parallel cylindrical filaments by repeating x and y layers alternately. These 3D simple cubic lattices are designed with an in-plane center-to-center rod spacing (L) of 0.8 mm, a rod diameter (d) of 0.25 mm, resulting in a spacing-to-diameter ratio (L/d) of *ca.* 3. The printed composite aerogel lattice shows excellent structural integrity and micro-architecture accuracy, which indicates the high quality printing.

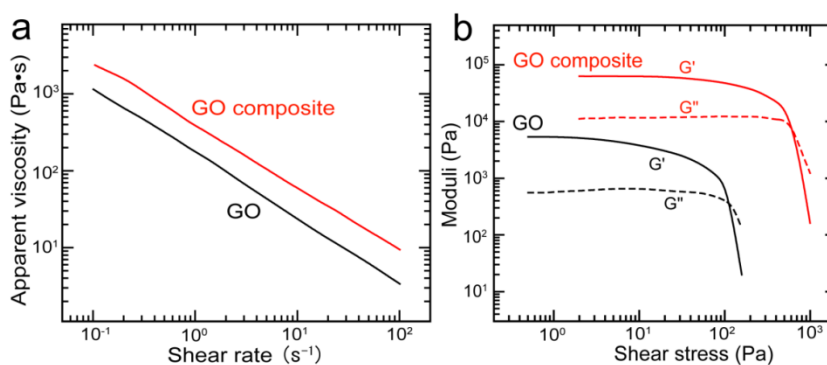


Figure 4.1 Rheological properties of graphene oxide (GO) and GO composite (3.3 wt% GO + 4.2 wt% GNP + 12.5 wt% SiO₂): (a) apparent viscosity, (b) storage modulus (G') and loss modulus (G'') vs. shear stress collected for GO and GO composite.

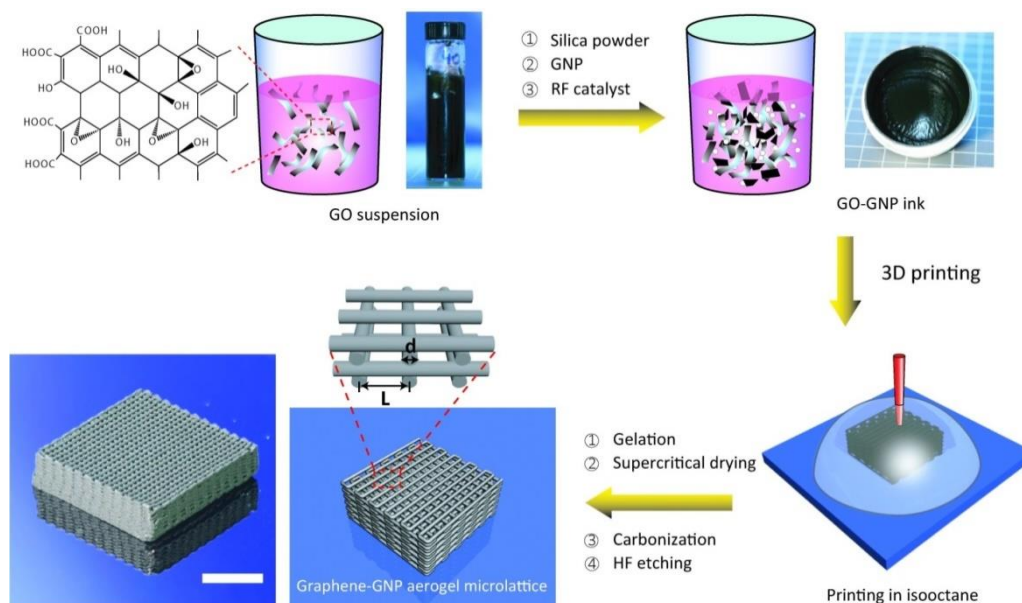


Figure 4.2 Schematic illustration of fabrication process: hydrophilic fumed silica powder, GNPs and R-F solution were added into the as-prepared aqueous GO suspension. After mixing, a homogeneous GO ink with designed rheological properties was received. The GO ink was extruded through a micro-nozzle in an isooctane bath to prevent structural shrinkage during printing. The printed lattice was gelled at 85 °C overnight, and then dried using supercritical carbon dioxide. Afterwards, the structure was heated to 1050 °C in nitrogen atmosphere for 3 h. Finally, the silica fillers were etched away using diluted hydrofluoric acid aqueous solution (5 wt%). Scale bar is 10 mm.

Scanning electron microscopy (SEM) of the 3D-GCAs with varying compositions shows how the morphology is impacted by the introduction of the GNP fillers at various loadings. The aforementioned cubic aerogel lattice is shown in Figure 4.3a. Figure 4.3 shows that, at lower concentrations, the GNPs do not drastically alter the sheet-like network structure of the aerogel seen in previous work.^{47,48} However, at the highest concentration of GNPs (no silica fillers), the sheet-like morphology of the sample is no longer visible. In fact the aerogel with

16.7 wt% GNP in Figure 4.3d was very brittle, indicative of the loss of the elastic graphene-like network. Table 4.1 provides a summary of the physical and textural properties of the 3D-GCAs. Lower GNP concentrations do indeed reduce the resistance of the 3D-GCA up to almost two orders of magnitude compared to the aerogel without GNPs. Surface area analysis of the aerogels as a function of GNP loading was also performed using Brunauer–Emmett–Teller (BET) measurements. With no GNP (silica only) in the ink, the aerogel showed a large surface area of over $700 \text{ m}^2\cdot\text{g}^{-1}$, consistent with previous studies.^{47,48} The addition of GNP does reduce the surface area but it still remains over $400 \text{ m}^2\cdot\text{g}^{-1}$ of the 3D-GCA with the lowest resistance. Thus, it is confirmed that the addition of GNPs to the aerogel can reduce electrical resistance while maintaining a high surface area, which is favorable for improving capacitive performance of 3D-GCAs.

Table 4.1 Physical and textural properties of 3D-GCAs of varying compositions

Sample	GO (wt%)	GNP (wt%)	SiO ₂ (wt%)	Surface Area (m ² ·g ⁻¹)	Resistance (Ω·sq ⁻¹)
GO-SiO ₂	3.3	0.0	16.7	739	61.1
GO-GNP-SiO ₂ -1	3.3	4.2	12.5	302	10.3
GO-GNP-SiO ₂ -2	3.3	12.5	4.2	418	0.96
GO-GNP	3.3	16.7	0.0	436	2.22

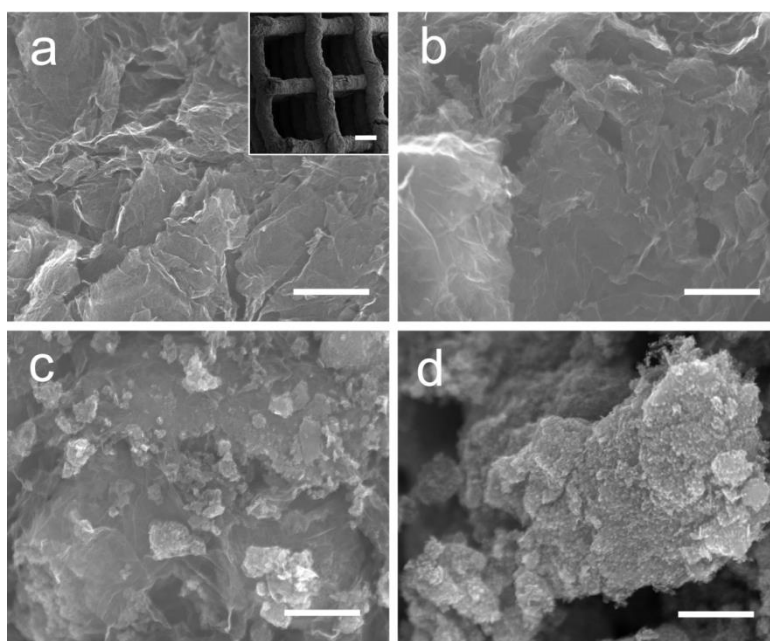


Figure 4.3 SEM images collected for different 3D-GCAs. (a) GO-SiO₂ with the inset shows the cubic aerogel lattice, (b) GO-GNP-SiO₂-1, (c) GO-GNP-SiO₂-2 and (d) GO-GNP. The scale bar in the inset represents 250 μm and other scale bars represent 1 μm.

The electrochemical performance of 3D-GCA electrodes was evaluated in 3 M KOH aqueous electrolyte by cyclic voltammetry (CV), chronopotentiometry (CP) tests and electrochemical impedance spectroscopy (EIS). All samples showed quasi-rectangular shaped CV curves and isosceles triangular CP profiles, indicating that they have near-ideal electrical double layer capacitive behavior (Figure 4.4).⁶²⁻⁶⁴ EIS studies reveal that three 3D-GCAs with varying GNP concentration have substantially smaller combined series resistance (R_s , the intercept at Z' -axis, related to the internal resistance of the entire electrode) than the GO-SiO₂ (Figure 4.5a). These results are in good agreement with the four point probe data (Table 4.1) showing that adding GNP can greatly reduce electrical resistance. Consistent with the four-point probe data, the

GO-GNP-SiO₂-2 showed the smallest charge transfer resistance (R_{ct}) among the three 3D-GCAs.

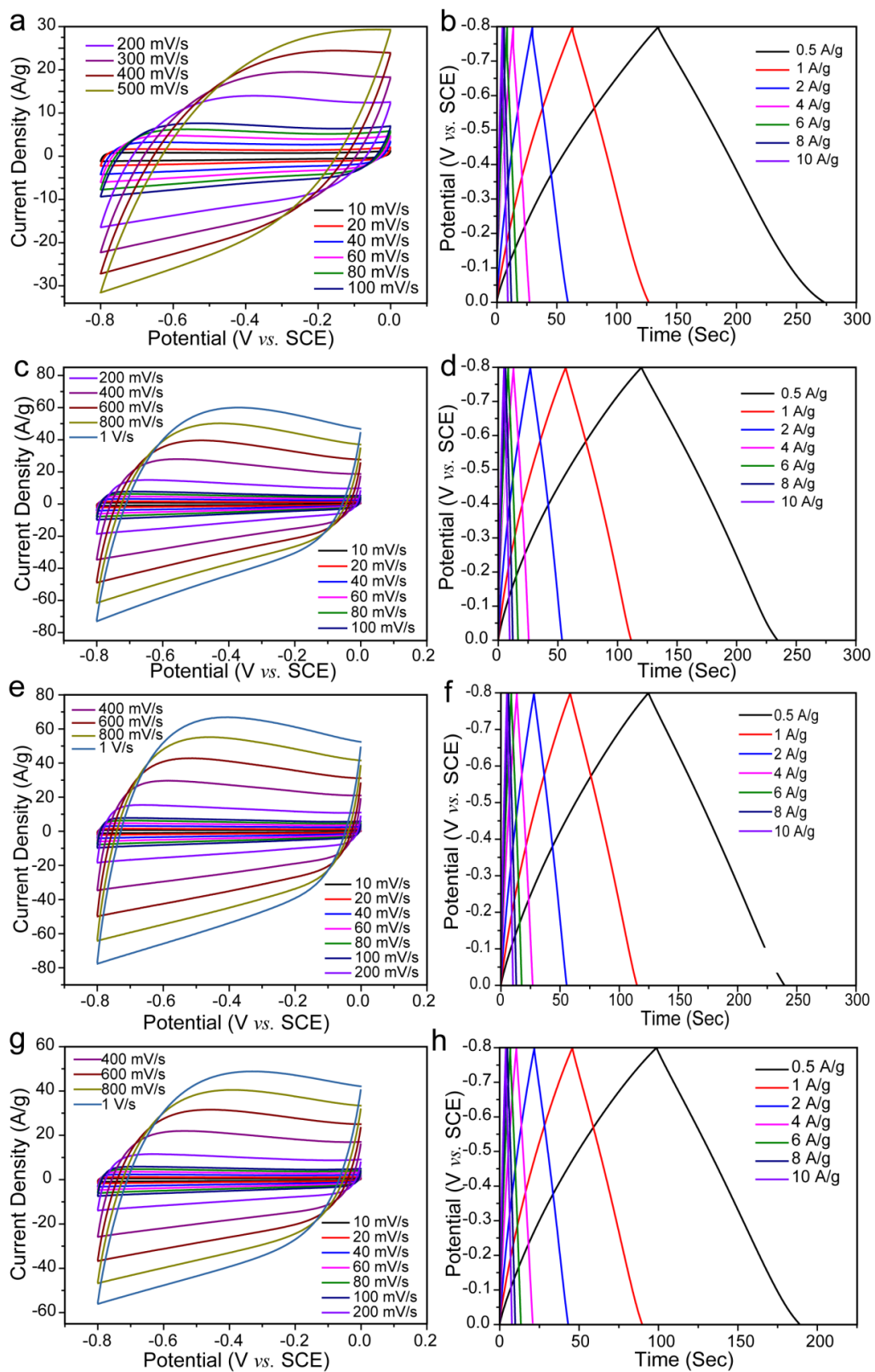


Figure 4.4 CV curves (left) and CP profiles (right) of 3D-GCAs with different compositions: (a,b) 3.3 wt% GO + 16.7 wt% SiO₂, (c,d) 3.3 wt% GO + 4.2 wt% GNP + 12.5 wt% SiO₂, (e,f) 3.3 wt% GO + 12.5 wt% GNP + 4.2 wt% SiO₂ and (g,

h) 3.3 wt% GO + 16.7 wt% GNP.

The gravimetric capacitances of each sample calculated based on their CP profiles collected at various current densities are summarized in Figure 4.5b and 4.5c. Among them, the GO-SiO₂ sample exhibited the highest specific capacitance at low current densities (0.5 to 4 A·g⁻¹) as expected because it possessed the largest surface area characterized by BET experiments. However, the electrode retained only ~65% of the gravimetric capacitance when current density increased from 0.5 to 10 A·g⁻¹. At large current densities, efficient electron transport is required to support the quick build-up of the electrical double layer. The relatively low electrical conductivity of the GO-SiO₂ sample limited its capacitance at large current densities, leading to the poor rate capability.⁶⁵ Significantly, the rate capability of the other 3D-GCAs with varying GNP concentration showed substantial improvement (Figure 4.5b), though their gravimetric capacitances at low current densities are slightly lower than that of GO-SiO₂ due to reduced surface area. The GO-GNP-SiO₂-2 achieves a remarkable *ca.* 90% capacitive retention when current density increased from 0.5 to 10 A·g⁻¹, which is among the best values reported for carbon based electrodes. This performance is even more impressive as the 3D-GCA electrode is *ca.* 1 mm thick while most other high performance carbon electrodes have thickness less than 100 μm. The superior rate capability is believed to be due to improved electrical conductivity by incorporating GNP fillers. Moreover 3D-GCAs function as self-supporting electrodes without the need of adding non-conductive binders that can generate

unfavorable contact resistance.⁶⁶ Furthermore, the GO-GNP-SiO₂-2 electrodes are extremely stable, with no loss of capacitance after 10000 consecutive charge and discharge cycles (Figure 4.6).

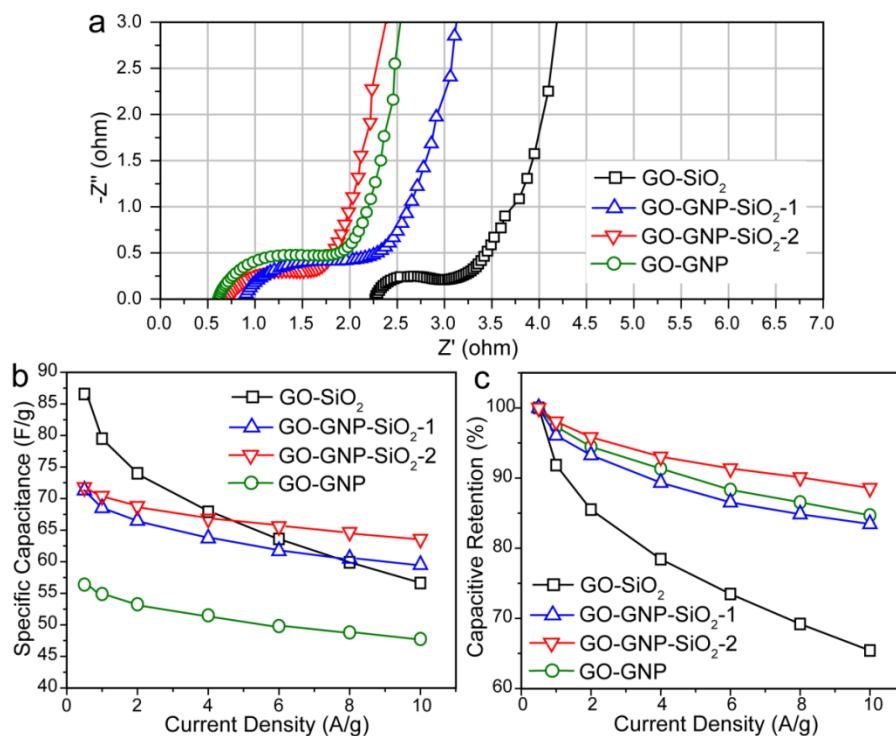


Figure 4.5 (a) Nyquist plots of 3D-GCAs with different amount of GNP and silica fillers collected in 3 M KOH aqueous electrolyte in a frequency range from 10^{-1} to 10^6 Hz at open circuit potential with a perturbation of 5 mV. (b) Specific capacitance and (c) capacitive retention of 3D-GCAs calculated as a function of current density.

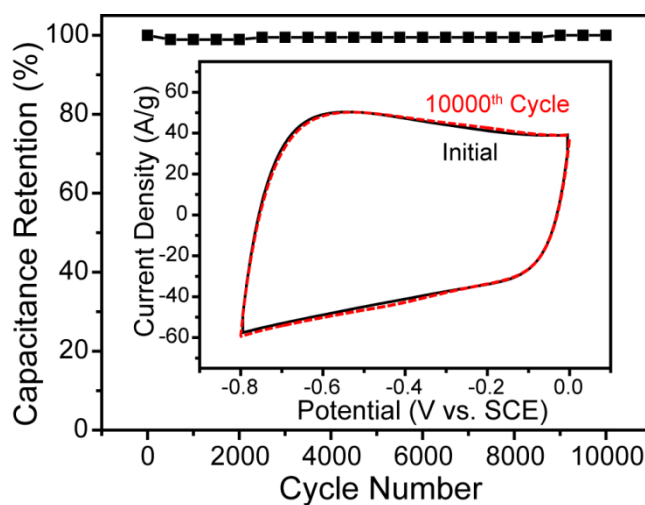


Figure 4.6 The cycling stability of GO-GNP-SiO₂-2 (3.3 wt% GO + 12.5 wt% GNP + 4.2 wt% SiO₂) collected in 3 M KOH aqueous electrolyte at a scan rate of 200 mV s⁻¹ for 10000 cycles. Inset shows the first and last CV curves.

The excellent electrochemical behavior and rate capability is also believed to be due to the 3D-printed macro-architecture that enables fast ion diffusion through the thick electrode. To test this hypothesis, we fabricated a piece of bulk GO-GNP-SiO₂-2 aerogel and compared its electrochemical performances with the 3D sample (Figure 4.7a and 4.7b). Notably, the gravimetric capacitances of the bulk aerogel are smaller than that of 3D-GCA obtained at the same current density (Figure 4.7c). EIS spectra collected for the two electrodes revealed that the R_s and R_{ct} of the two electrodes are comparable because they have the identical chemical composition (Figure 4.7d). The bulk aerogel displayed a less steep straight line in the low-frequency domain compared to GO-GNP-SiO₂-2, implying that it has higher diffusion resistance.⁸² The low porosity of the bulk aerogel electrode (Figure 4.8) is the likely reason for the large diffusion resistance, as ion diffusion within packed layers is expected to be sluggish.⁸³ These results suggest that the presence of macro-pores is critical for ion diffusion, and the 3D-printed micro-lattice morphology is clearly advantageous over its bulk counterpart.

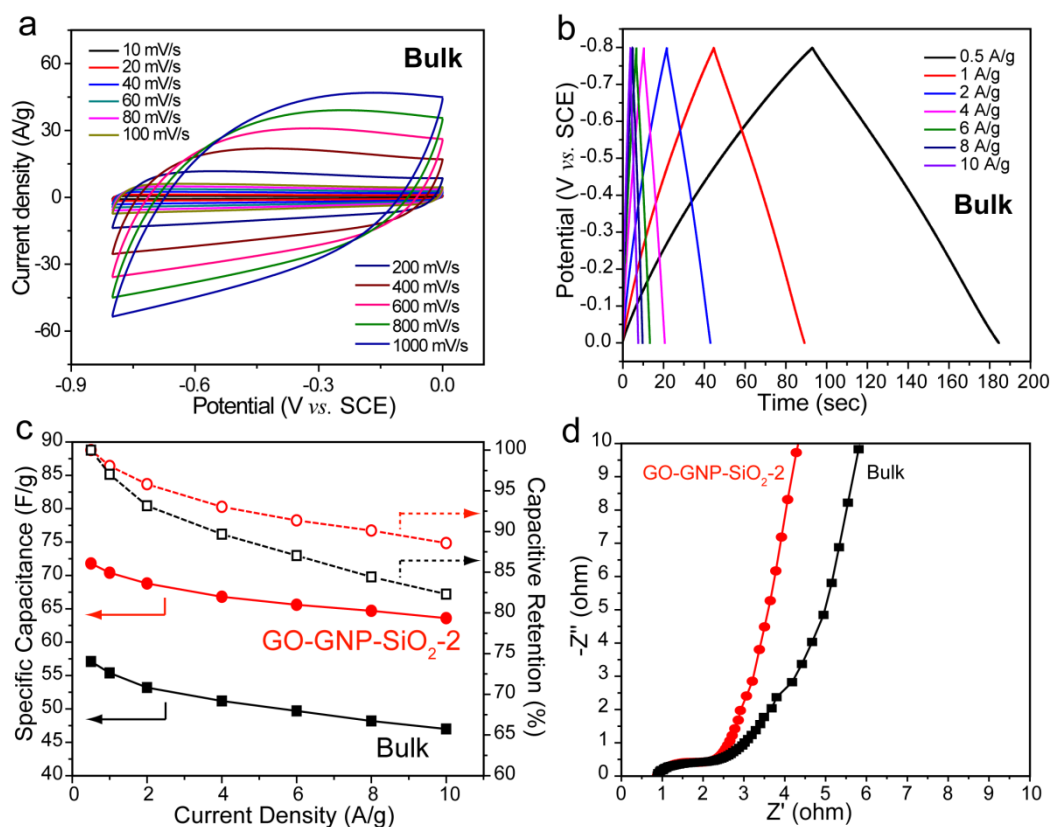


Figure 4.7 Comparison of electrochemical performance of bulk electrode (with the same composition as GO-GNP-SiO₂-2) and GO-GNP-SiO₂-2: (a) Cyclic voltammograms, (b) constant-current charge and discharge profiles, (c) rate capability performance and (d) EIS spectra collected in 3 M KOH aqueous electrolyte.

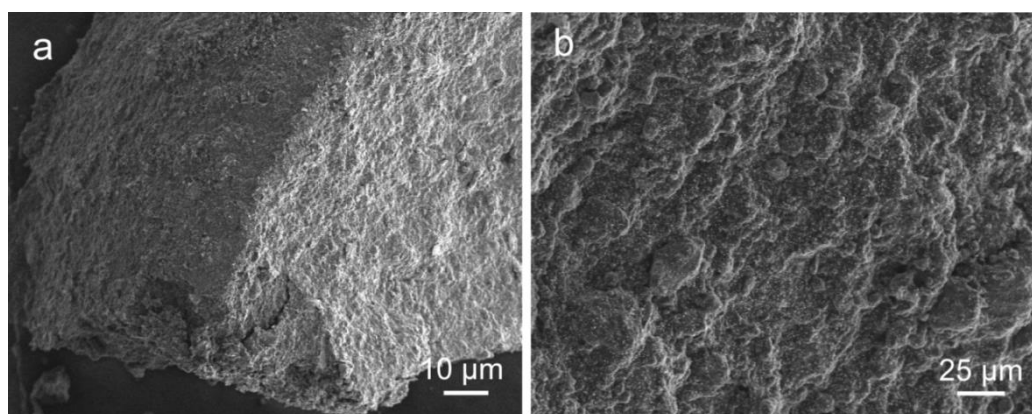


Figure 4.8 SEM images of the bulk pallet with the same composition as GO-GNP-SiO₂-2.

In comparison to other macro-porous electrodes with less ordered pores, we believe the ordered macro-pore structure could facilitate mass transfer and reduce

diffusion resistance in a thick electrode structure. Diffusion coefficient (D_{eff}) of a fluid diffuse through a porous structure can be calculated according to the following equation:⁸⁴

$$D_{eff} = \epsilon \frac{D}{\tau}$$

where ϵ is the porosity, D the diffusion coefficient within pores and τ the tortuosity. The τ of periodic porous structure is much smaller than that of porous structure with less ordered pores. ϵ , D are the same for ordered and less ordered porous structures if they have the same chemical composition. Therefore, the 3D-printed sample with a periodic porous structure is expected to have smaller D_{eff} compared to other 3D graphene structures with less ordered pores, and thus, the enhanced rate capability. This is consistent with our experimental results. 3D-GCA exhibits considerably higher rate capability (*ca.* 90% capacitive retention from 0.5 A·g⁻¹ to 10 A·g⁻¹) than other 3D graphene electrodes with less ordered pores, such as few layer meso-porous graphene coated Ni foam (*ca.* 52% from 1 A·g⁻¹ to 7.5 A·g⁻¹),⁸¹ and CVD graphene-coated Ni foam (62.7% from 5 mV·s⁻¹ to 100 mV·s⁻¹).⁸⁰ Our results also agree with a previous study in that a templated carbon electrode with periodic pores achieves better rate capability than its counterpart with randomly distributed pores.⁸⁵

A quasi-solid-state symmetric supercapacitor (SSC) was fabricated via assembly of a thin separator and two identical GO-GNP-SiO₂-2 electrodes (Figure 4c inset). The supercapacitor device is denoted as 3D-GCA SSC. Significantly, all

CV curves remained quasi-rectangular shape when scan rate increased from 10 to 500 $\text{mV}\cdot\text{s}^{-1}$ (Figure 4.9a). CP profiles collected at all current density also displayed linear and symmetric shape with negligible IR drops (Figure 4.9b). These results indicate that the device internal resistance is small. The as-prepared SSC delivered a maximum gravimetric capacitance of $4.76 \text{ F}\cdot\text{g}^{-1}$ at a current density of $0.4 \text{ A}\cdot\text{g}^{-1}$ and still retained 61% of the maximum gravimetric capacitance ($2.95 \text{ F}\cdot\text{g}^{-1}$) when current density increased by 20 times to $8 \text{ A}\cdot\text{g}^{-1}$ (Figure 4.9c). It is noteworthy that all gravimetric capacitances and current densities were calculated based on the mass of the entire device including separator, electrodes and gel electrolyte (32.4 mg). These values are higher than a number of SSCs, including CNT coated paper-based SSC ($0.38 \text{ F}\cdot\text{g}^{-1}$)⁸⁶ and activated carbon cloth-based SSC ($0.765 \text{ mF}\cdot\text{g}^{-1}$, based on the total mass of two electrodes),⁶² despite some structural parameters of the 3D-GCA (number of layers, pore size and fiber thickness *etc.*) have not yet been optimized. In general, ion diffusion within the electrode becomes more difficult with the increase of electrode thickness, resulting in reduced rate capability.⁸⁷ It is noteworthy that 3D-GCA SSC achieved outstanding rate capability (87% capacitive retention from $2 \text{ A}\cdot\text{g}^{-1}$ to $10 \text{ A}\cdot\text{g}^{-1}$, Figure 4.10), even though it is assembled with very thick electrodes (thickness of each electrode is $1000 \mu\text{m}$). This value is better than most carbon-based symmetric supercapacitors (SSCs) with much thinner electrodes (*ca.* $100 \mu\text{m}$), such as the exfoliated carbon cloth SSC (81.0% capacitive retention

from $0.5 \text{ mA}\cdot\text{g}^{-1}$ to $5 \text{ mA}\cdot\text{g}^{-1}$),⁶² the bagasse-derived carbon SSC (68.7% capacitive retention from $1 \text{ A}\cdot\text{g}^{-1}$ to $10 \text{ A}\cdot\text{g}^{-1}$),⁶⁹ the hierarchically porous carbon SSC (53% capacitive retention from $0.2 \text{ A}\cdot\text{g}^{-1}$ to $15 \text{ A}\cdot\text{g}^{-1}$),⁸⁸ and the pillared graphene framework SSC (41.0% from $0.2 \text{ A}\cdot\text{g}^{-1}$ to $20 \text{ A}\cdot\text{g}^{-1}$).⁸⁹ The exceptional rate capability can be ascribed to two reasons: i) the presence of the ordered macro-pores improves the infiltration of gel electrolyte,⁹⁰ and thus, the ion diffusion; and ii) the small electrical resistance of the graphene aerogel enables fast charge transport. Moreover, the SSC show excellent electrochemical stability with capacitance retention of 95.5% after testing for 10000 consecutive charge and discharge cycles (Figure 4.9d).

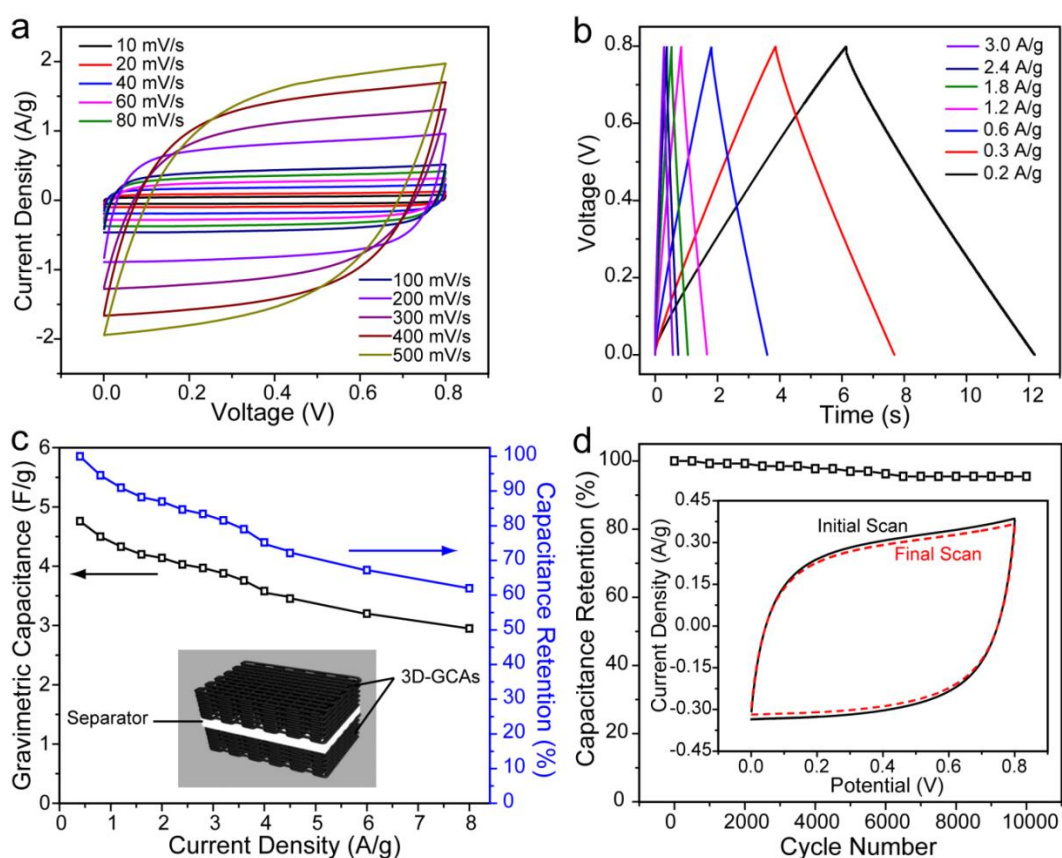


Figure 4.9 Electrochemical performance of 3D-GCA SSC. (a) Cyclic voltammograms collected in 3M KOH as a function of scan rate. (b) Charge and discharge profiles collected at different current densities. (c) Gravimetric capacitance and capacitive retention calculated as a function of current density. Inset: schematic illustration of the 3D-GCA SSC. (d) Cycling stability tested at a scan rate of 200 mV/s for 10000 cycles. Inset shows the first and last cyclic voltammograms collected during the cycling stability test.

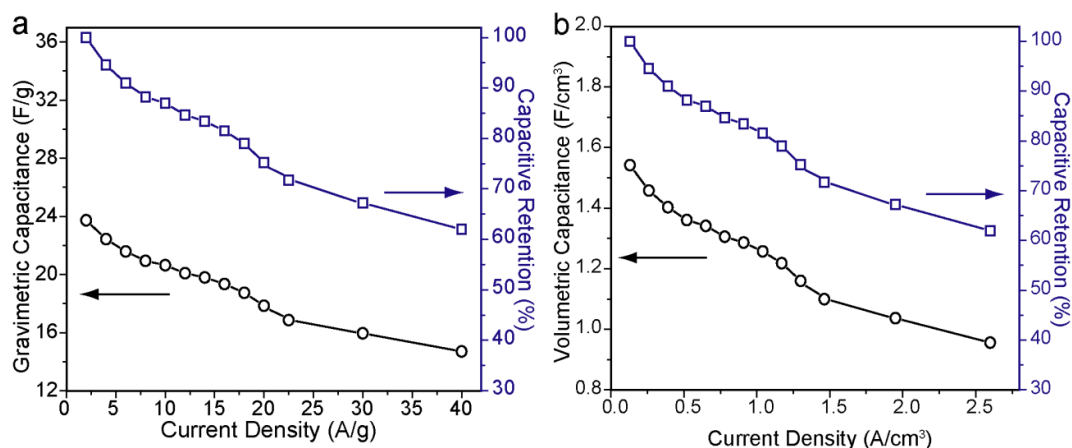


Figure 4.10 (a) Gravimetric capacitances and capacitive retention of 3D-GCA SSC calculated as a function of current density (normalized to the total mass of two electrodes). (b) Volumetric capacitances and capacitive retention of 3D-GCA SSC calculated as a function of current density (normalized to the total volume of the devices).

The gravimetric energy density and power density of the 3D-GCA SSC were evaluated based on the total mass of the entire device (Figure 4.11a) as well as the mass of two electrodes (Figure 4.12) and compared with other carbon based SSCs. As shown in the Ragone plot (Figure 4.11a), the 3D-GCA SSC delivers a maximum power density of $4079.9 \text{ W}\cdot\text{kg}^{-1}$ (at the energy density of $0.26 \text{ Wh}\cdot\text{kg}^{-1}$) and a maximum energy density of $0.43 \text{ Wh}\cdot\text{kg}^{-1}$ (at the power density of $76.36 \text{ W}\cdot\text{kg}^{-1}$). These values are comparable to other electrical double layer capacitors.^{26,62,86,91,92} Moreover, we have calculated the volumetric power density and energy density based on the total volume of 3D-GCA SSC device [0.1 cm^3 , 1

cm (L) \times 0.5 cm (W) \times 0.2 cm (H)]. It achieved a maximum volumetric power density of 2643 mW/cm³ (at the energy density of 0.08 mWh/cm³) and a maximum volumetric energy density of 0.14 mWh/cm³ (at the power density of 49.48 mW/cm³), which are substantially better than a number of quasi-solid-state symmetric SSCs (Figure 4.11b).^{62,92-95} Two fully-charged SSCs combined in series (charging current density: 3 A·g⁻¹, charging time: *ca.* 2 s) can power a red light emitting diode bulb (LED, 1.5 V nominal voltage) for *ca.* 3 min, a digital timer (1.5 V nominal voltage) for *ca.* 5 min and a small electric fan (1.5 V nominal voltage) for several seconds (Figure 4.11a insets).

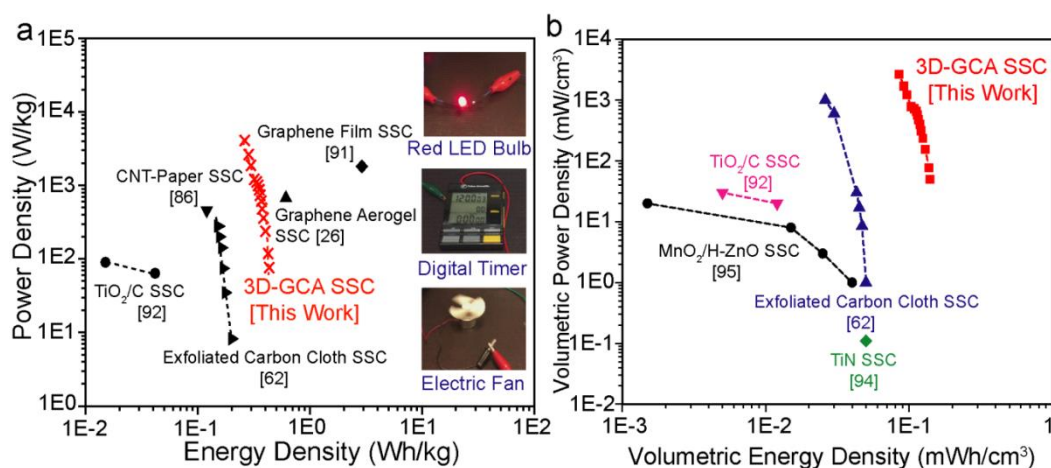


Figure 4.11 (a) Ragone plot of the 3D-GCA SSC with reported values added for comparison. Gravimetric energy densities and gravimetric power densities presented in this plot are normalized by the entire mass of device except the values reported in refs. 62 and 92 are normalized by the total mass of two electrodes. Insets are digital pictures showing a red LED, a digital timer and an electric fan that are powered by the 3D-GCA SSC. (b) Comparison, in a Ragone plot, of the volumetric energy and power density of 3D-GCA SSC and other previously reported SSCs.

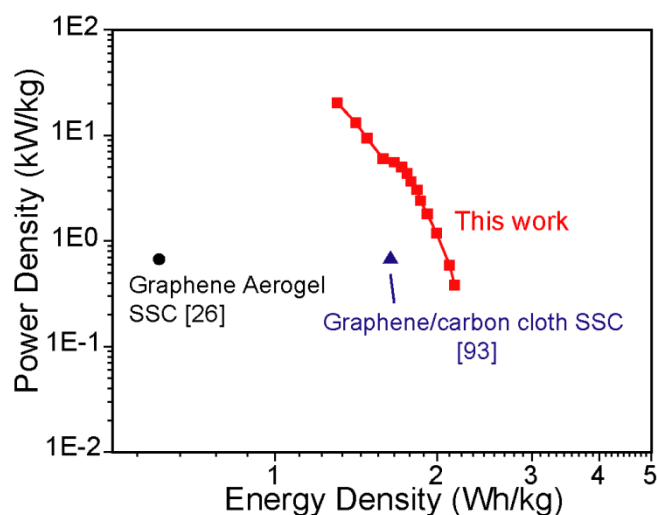


Figure 4.12 Comparison, in a Ragone plot, of the gravimetric energy and power density of the 3D-GCA SSC and other previously reported SSCs (normalized to the total mass of two electrodes).

4.4 Conclusions

In this work, we have demonstrated that the 3D-printed electrode structure with ordered macro-pores enables efficient ion diffusion within thick electrodes and substantially improved the rate capability of quasi-solid-state devices assembled with thick electrodes. Key factors for successful 3D printing of the graphene aerogels include modifying the GO precursor suspension served as printable ink, and adapting the 3D printing process to prevent premature drying of the printed structure. The critical elements of achieving capacitance retention and power densities that equal or exceed those of reported devices made with electrodes less than 100 microns thick in the 3D-GCA SSC with electrodes around a millimeter thick, include the development of the GO-GNP composites and the use of 3D printing to create periodic macro-porosity in the electrode which facilitates fast mass transport. The physical and electrochemical properties of the

electrodes can be easily tuned by changing the ratio of GNP and silica fillers in the ink. It was determined that the 3D-GCA electrode made from the ink with 12.5 wt% GNP and 4.2 wt% SiO₂ showed the best rate capability, with a remarkable 90% capacitance retention when current density increased from 0.5 to 10 A·g⁻¹. The quasi-solid-state symmetric supercapacitor made with this electrode also demonstrated outstanding energy density and power density when compared to other reports. More importantly, we believe 3D printing can be used to build unique electrode and device structures such as integrable electrodes with irregular shapes and 3D interdigitated supercapacitors, which are not possible to be achieved using conventional synthetic and fabrication techniques. The capability of creating unique functional structures with well-controlled structural parameters can open up tremendous opportunities in design and fabrication of supercapacitors as well as other charge storage devices.

References

1. Cook-Chennault, K. A., Thambi, N., Sastry, A. M. *Smart Mater. Struct.* **2008**, *17*, 043001.
2. Meng, C., Gall, O. Z., Irazoqui, P. P. *Biomed. Microdevices* **2013**, *15*, 973-983.
3. Roundy, S., Wright, P. K., Rabaey, J. M. *Energy scavenging for wireless sensor networks*; Springer: New York, **2004**.

4. Chmiola, J., Largeot, C., Taberna, P. L., Simon, P., Gogotsi, Y. *Science* **2010**, 328, 480-483.
5. Wu, H., Geng, J., Wang, Y., Wang, Y., Peng, Z., Zheng, G. *Nanoscale* **2014**, 6, 15316-15320.
6. El-Kady, M. F., Kaner, R. B. *Nat. Commun.* **2013**, 4, 1475.
7. Beidaghi, M., Wang, C. *Adv. Funct. Mater.* **2012**, 22, 4501-4510.
8. Simon, P., Gogotsi, Y. *Nat. Mater.* **2008**, 7, 845-854.
9. An, K. H., Kim, W. S., Park, Y. S., Choi, Y. C., Lee, S. M., Chung, D. C., Bae, D. J., Lim, S. C., Lee, Y. H. *Adv. Mater.* **2001**, 13, 497-500.
10. Kim, S., Koo, H., Lee, A., Braun, P. V. *Adv. Mater.* **2014**, 26, 5108-5112.
11. Gamby, J., Taberna, P. L., Simon, P., Fauvarque, J. F., Chesneau, M. *J. Power Sources* **2001**, 101, 109-116.
12. Pech, D., Brunet, M., Durou, H., Huang, P., Mochalin, V., Gogotsi, Y., Taberna, P. L., Simon, P. *Nat. Nanotechnol.* **2010**, 5, 651-654.
13. Zhou, Y., Candelaria, S.L., Liu, Q., Huang, Y., Uchaker, E., Cao, G. *J. Mater. Chem. A* **2014**, 2, 8472-8482.
14. Li, J., Wang, Y., Tang, J., Wang, Y., Wang, T., Zhang, L., Zheng, G. *J. Mater. Chem. A* **2015**, 3, 2876-2882.
15. Huang, Y., Liang, J., Chen, Y. *Small* **2012**, 8, 1805-1834.
16. Liu, C., Yu, Z., Neff, D., Zhamu, A., Jang, B. *Z. Nano Lett.* **2010**, 10, 4863-4868.

17. Geim, A. K., Novoselov, K. S. *Nat. Mater.* **2007**, *6*, 183-191.
18. Li, D., Kaner, R. B. *Nat Nanotechnol.* **2008**, *3*, 101.
19. Geim, A. K. *Science* **2009**, *324*, 1530-1534.
20. Peigney, A., Laurent, C., Flahaut, E., Bacsa, R. R., Rousset, A. *Carbon* **2001**, *39*, 507-514.
21. Lee, C., Wei, X., Kysar, J. W., Hone, J. *Science* **2008**, *321*, 385-388.
22. Balandin, A. A., Ghosh, S., Bao, W., Calizo, I., Teweldebrhan, D., Miao, F., Lau, C. N. *Nano Lett.* **2008**, *8*, 902-907.
23. Li, X., Zhang, G., Bai, X., Sun, X., Wang, X., Wang, E., Dai, H. *Nat. Nanotechnol.* **2008**, *3*, 538-542.
24. Yan, J., Wang, Q., Wei, T., Fan, Z. *Adv. Energy Mater.* **2014**, *4*, 1300816.
25. Jiang, X. F., Wang, X. B., Dai, P., Li, X., Weng, Q., Wang, X., Tang, D. M., Tang, J., Bando, Y., Golberg, D. *Nano Energy* **2015**, *16*, 81-90.
26. Xu, Y., Lin, Z., Huang, X., Liu, Y., Huang, Y., Duan, X. *ACS Nano* **2013**, *7*, 4042-4049.
27. Zhang, X., Sui, Z., Xu, B., Yue, S., Luo, Y., Zhan, W., Liu, B. *J. Mater. Chem.* **2011**, *21*, 6494-6497.
28. Zhao, Y., Liu, J., Hu, Y., Cheng, H., Hu, C., Jiang, C., Jiang, L., Cao, A., Qu, L. *Adv. Mater.* **2013**, *25*, 591-595.
29. Zhang, L. L., Zhao, X., Stoller, M.D., Zhu, Y., Ji, H., Murali, S., Wu, Y., Perales, S., Clevenger, B. and Ruoff, R.S. *Nano Lett.* **2012**, *12*, 1806-1812.

30. Gibson, L. J., Ashby, M. F. *Cellular solids: structure and properties*. Cambridge University Press: Cambridge, **1999**.
31. Cao, X., Yin, Z., Zhang, H. *Energy Environ. Sci.* **2014**, *7*, 1850-1865.
32. Cong, H. P., Chen, J. F., Yu, S. H. *Chem. Soc. Rev.* **2014**, *43*, 7295-7325.
33. Chen, Z., Ren, W., Gao, L., Liu, B., Pei, S., Cheng, H. M. *Nat. Mater.* **2011**, *10*, 424-428.
34. Wang, Y., Tang, J., Kong, B., Jia, D., Wang, Y., An, T., Zhang, L., Zheng, G. *RSC Adv.* **2015**, *5*, 6886-6891.
35. Xu, Y., Sheng, K., Li, C., Shi, G. *ACS Nano* **2010**, *4*, 4324-4330.
36. Bi, H., Yin, K., Xie, X., Zhou, Y., Wan, N., Xu, F., Banhart, F., Sun, L., Ruoff, R.S. *Adv. Mater.* **2012**, *24*, 5124-5129.
37. Zhao, J., Ren, W., Cheng, H. M. *J. Mater. Chem.* **2012**, *22*, 20197-20202.
38. Bai, H., Li, C., Wang, X., Shi, G. *Chem. Commun.* **2010**, *46*, 2376-2378.
39. Lin, Y., Ehlert, G. J., Bukowsky, C., Sodano, H. A. *ACS Appl. Mater. Interfaces* **2011**, *3*, 2200-2203.
40. Qiu, L., Liu, J. Z., Chang, S. L., Wu, Y., Li, D. *Nat. Commun.* **2012**, *3*, 1241.
41. Tang, Z., Shen, S., Zhuang, J., Wang, X. *Angew. Chem.* **2010**, *122*, 4707-4711.
42. Chen, W., Yan, L. *Nanoscale* **2011**, *3*, 3132.
43. Sun, H. Y., Xu, Z., Gao, C. *Adv. Mater.* **2013**, *25*, 2554-2560.

44. Worsley, M. A., Charnvanichborikarn, S., Montalvo, E., Shin, S. J., Tylski, E. D., Lewicki, J. P., Nelson, A. J., Satcher, J. H., Biener, J., Baumann, T. F., Kucheyev, S. O. *Adv. Funct. Mater.* **2014**, *24*, 4259-4264.
45. Worsley, M. A., Kucheyev, S. O., Mason, H. E., Merrill, M. D., Mayer, B. P., Lewicki, J., Valdez, C. A., Suss, M. E., Stadermann, M., Pauzauskie, P. J., Satcher, J. H. *Chem. Commun.* **2012**, *48*, 8428-8430.
46. Bai, H., Li, C., Wang, X., Shi, G. *J. Phys. Chem. C* **2011**, *115*, 5545-5551.
47. Worsley, M. A., Pauzauskie, P. J., Olson, T. Y., Biener, J., Satcher Jr, J. H., Baumann, T. F. *J. Am. Chem. Soc.* **2010**, *132*, 14067-14069.
48. Worsley, M. A., Olson, T. Y., Lee, J. R., Willey, T. M., Nielsen, M. H., Roberts, S. K., Pauzauskie, P. J., Biener, J., Satcher Jr, J. H., Baumann, T. F. *J. Phys. Chem. Lett.* **2011**, *2*, 921-925.
49. Barg, S., Perez, F. M., Ni, N., do Vale Pereira, P., Maher, R.C., Garcia-Tuñon, E., Eslava, S., Agnoli, S., Mattevi, C., Saiz, E. *Nat. Commun.* **2014**, *5*, 4328.
50. Kim, J. H., Chang, W. S., Kim, D., Yang, J. R., Han, J. T., Lee, G. W., Kim, J. T., Seol, S. K. *Adv. Mater.* **2015**, *27*, 157-161.
51. García-Tuñon, E., Barg, S., Franco, J., Bell, R., Eslava, S., D'Elia, E., Maher, R. C., Guitian, F., Saiz, E. *Adv. Mater.* **2015**, *27*, 1688-1693.
52. Duoss, E. B., Weisgraber, T. H., Hearon, K., Zhu, C., Small, W., Metz, T. R., Vericella, J. J., Barth, H. D., Kuntz, J. D., Maxwell, R. S., Spadaccini, C. M. *Adv. Funct. Mater.* **2014**, *24*, 4905-4913.

53. Compton, B. G., Lewis, J. A. *Adv. Mater.* **2014**, *26*, 5930-5935.
54. Zhu, C., Han, T. Y. J., Duoss, E. B., Golobic, A. M., Kuntz, J. D., Spadaccini, C. M., Worsley, M. A. *Nat. Commun.* **2015**, *6*, 6962.
55. Lewis, J. A. *Adv. Funct. Mater.* **2006**, *16*, 2193-2204.
56. Smay, J. E., Gratson, G. M., Shepherd, R. F., Cesarano, J. I. I. I., Lewis, J. A. *Adv. Mater.* **2002**, *14*, 1279-1283.
57. Zhu, C., Smay, J. E. *J. Rheol.* **2011**, *55*, 655-672.
58. Meng, H., Li, G. *Polymer* **2013**, *54*, 2199-2221.
59. Meng, Q., Hu, J. *Composites Part A* **2009**, *40*, 1661-1672.
60. Naficy, S., Jalili, R., Aboutalebi, S. H., Gorkin III, R. A., Konstantinov, K., Innis, P. C., Spinks, G. M., Poulin, P., Wallace, G. G. *Mater. Horiz.* **2014**, *1*, 326-331.
61. Le, L. T., Ervin, M. H., Qiu, H., Fuchs, B. E., Lee, W. Y. *Electrochem. Commun.* **2011**, *13*, 355-358.
62. Wang, G., Wang, H., Lu, X., Ling, Y., Yu, M., Zhai, T., Tong, Y., Li, Y. *Adv. Mater.* **2014**, *26*, 2676-2682.
63. Yu, G., Xie, X., Pan, L., Bao, Z., Cui, Y. *Nano Energy* **2013**, *2*, 213-234.
64. Yang, P., Mai, W. *Nano Energy* **2014**, *8*, 274-290.
65. Salunkhe, R. R., Lee, Y. H., Chang, K. H., Li, J. M., Simon, P., Tang, J., Torad, N. L., Hu, C. C., Yamauchi, Y. *Chem. Eur. J.* **2014**, *20*, 13838-13852.

66. Lu, X., Yu, M., Zhai, T., Wang, G., Xie, S., Liu, T., Liang, C., Tong, Y., Li, Y. *Nano Lett.* **2013**, *13*, 2628-2633.
67. Gryglewicz, G., Śliwak, A., Béguin, F. *ChemSusChem* **2013**, *6*, 1516-1522.
68. Bao, L., Li, X. *Adv. Mater.* **2012**, *24*, 3246-3252.
69. Hao, P., Zhao, Z., Tian, J., Li, H., Sang, Y., Yu, G., Cai, H., Liu, H., Wong, C. P., Umar, A. *Nanoscale* **2014**, *6*, 12120-12129.
70. Liu, X., Zheng, M., Xiao, Y., Yang, Y., Yang, L., Liu, Y., Lei, B., Dong, H., Zhang, H., Fu, H. *ACS Appl. Mater. Interfaces* **2013**, *5*, 4667-4677.
71. Weng, Z., Su, Y., Wang, D. W., Li, F., Du, J., Cheng, H. M. *Adv. Energy Mater.* **2011**, *1*, 917-922.
72. Liu, M. C., Kong, L. B., Zhang, P., Luo, Y. C., Kang, L. *Electrochim. Acta* **2012**, *60*, 443-448.
73. Ruiz, V., Blanco, C., Santamaría, R., Ramos-Fernández, J.M., Martínez-Escandell, M., Sepúlveda-Escribano, A., Rodríguez-Reinoso, F. *Carbon* **2009**, *47*, 195-200.
74. Yang, Y., Li, P., Wu, S., Li, X., Shi, E., Shen, Q., Wu, D., Xu, W., Cao, A., Yuan, Q. *Chem. Eur. J.* **2015**, *21*, 6157-6164.
75. Yu, Z., McInnis, M., Calderon, J., Seal, S., Zhai, L. and Thomas, J. *Nano Energy* **2015**, *11*, 611-620.
76. Choi, B. G., Yang, M., Hong, W. H., Choi, J. W., Huh, Y. S. *ACS Nano* **2012**, *6*, 4020-4028.

77. Yun, Y. S., Cho, S. Y., Shim, J., Kim, B. H., Chang, S. J., Baek, S. J., Huh, Y. S., Tak, Y., Park, Y. W., Park, S., Jin, H. J. *Adv. Mater.* **2013**, *25*, 1993-1998.
78. Carriazo, D., Picó F., Gutiérrez, M.C., Rubio, F., Rojo, J.M. and del Monte, F. *J. Mater. Chem.* **2010**, *20*, 773-780.
79. Xu, Y., Lin, Z., Zhong, X., Huang, X., Weiss, N.O., Huang, Y., Duan, X. *Nat. Commun.* **2014**, *5*, 4554.
80. Chen, W., Fan, Z., Zeng, G., Lai, Z. *J. Power Sources* **2013**, *225*, 251-256.
81. Shim, J. J. *J. Power Sources* **2015**, *273*, 110-117.
82. Zhai, T., Lu, X., Ling, Y., Yu, M., Wang, G., Liu, T., Liang, C., Tong, Y., Li, Y. *Adv. Mater.* **2014**, *26*, 5869-5875.
83. Cao, J., Li, X., Wang, Y., Walsh, F.C., Ouyang, J.H., Jia, D., Zhou, Y. *J. Power Sources* **2015**, *293*, 657-674.
84. Cussler, E. L. *Diffusion: Mass Transfer in Fluid Systems*. Cambridge University Press: Cambridge, **1997**.
85. Xing, W., Qiao, S. Z., Ding, R. G., Li, F., Lu, G. Q., Yan, Z. F., Cheng, H. M. *Carbon* **2006**, *44*, 216-224.
86. Kang, Y. J., Chung, H., Han, C. H., Kim, W. *Nanotechnol.* **2012**, *23*, 065401.
87. Tsay, K. C., Zhang, L., Zhang, J. *Electrochim. Acta* **2012**, *60*, 428-436.
88. Feng, H., Hu, H., Dong, H., Xiao, Y., Cai, Y., Lei, B., Liu, Y., Zheng, M. *J. Power Sources* **2016**, *302*, 164-173.

89. Jiang, L., Sheng, L., Long, C., Wei, T., Fan, Z. *Adv. Energy Mater.* **2015**, *5*, 201500771.
90. Nykypanchuk, D., Strey, H. H., Hoagland, D. A. *Science* **2002**, *297*, 987-990.
91. Choi, B. G., Chang, S. J., Kang, H. W., Park, C. P., Kim, H. J., Hong, W. H., Lee, S., Huh, Y. S. *Nanoscale* **2012**, *4*, 4983-4988.
92. Zheng, H., Zhai, T., Yu, M., Xie, S., Liang, C., Zhao, W., Wang, S. C. I., Zhang, Z., Lu, X. *J. Mater. Chem. C* **2013**, *1*, 225-229.
93. Wang, S., Pei, B., Zhao, X., Dryfe, R. A. *Nano Energy* **2013**, *2*, 530-536.
94. Lu, X., Wang, G., Zhai, T., Yu, M., Xie, S., Ling, Y., Liang, C., Tong, Y., Li, Y. *Nano Lett.* **2012**, *12*, 5376-5381.
95. Yang, P., Xiao, X., Li, Y., Ding, Y., Qiang, P., Tan, X., Mai, W., Lin, Z., Wu, W., Li, T., Jin, H. *ACS Nano* **2013**, *7*, 2617-2626.

Chapter 5

Ion-intercalation Induced Capacitance Improvement for Graphene-based Supercapacitor Electrodes

Abstract

Here we demonstrate a facile electrochemical method that can substantially improve the capacitance of graphene-based electrodes while still retains their excellent rate capability. This method involves two ion-intercalation steps (lithium-ion intercalation and perchlorate-ion intercalation), followed by hydrolysis of perchlorate ion intercalation compounds. Lithium ion intercalation mainly leads to surface exfoliation, whilst the hydrolysis of perchlorate ion intercalation compounds functionalizes graphene surface with oxygen moieties. Electrochemically treated graphitic paper electrode shows 1000 times enhancement in areal capacitance. Without the need of post-treatment annealing, the treated graphitic paper maintains an outstanding rate capability of 84% (0.5 mA cm^{-2} to 5 mA cm^{-2}). The same strategy can also be extended to boost the gravimetric capacitance of lightweight 3D printed graphene aerogels. The treated graphene aerogel achieved an outstanding gravimetric capacitance of 101.7 F g^{-1} (10 A/g) with an excellent rate capability of 81.6% (0.5 A g^{-1} to 10 A g^{-1}).

5.1 Introduction

Graphene-based materials, owing to their excellent electrical conductivity, have been extensively used in supercapacitors as substrates/current collectors as well as

active charge storage materials.¹ They store charges via the formation of electrical double layer at the interface between electrode and electrolyte.² Yet, the ion-accessible surface area of graphene-based materials is often limited due to π - π stacking of graphene sheets, which significantly reduce the capacitance of graphene based electrode. Currently, there are three major approaches to improve the capacitance of graphene-based electrodes. The most widely adopted approach is to combine these materials with pseudo-capacitive materials. For example, Sevilla *et al.* synthesized graphene-iron oxide composite hydrogels that delivers a capacitance of *ca.* 168 F g⁻¹ at a current density of 0.1 A g⁻¹.³ Song *et al.* integrated manganese dioxide onto thin graphene sheets.⁴ The electrode achieved a high areal capacitance of 244 mF cm⁻² at a current density of 0.23 mA cm⁻². Wang *et al.* reported a free-standing 3D graphene/cobalt sulfide composite electrode that delivered a high capacitance of 443 F g⁻¹ at a current density of 1 A g⁻¹.⁵ However, in most composite electrodes, graphene only serves as current collector and the capacitance is mainly contributed by pseudo-capacitive materials. As a result, the capacitance enhancement of these composite electrodes is observed at slow discharge rates. It decreases rapidly with the increase of current density due to poor electrical conductivity of the pseudo-capacitive materials. An alternative approach is to engineer graphene sheets into porous structures (with hetero-atom doping in some cases) to increase the surface area. Pores with different sizes can be created by template methods,^{6,7} high-temperature activation using inorganic

salts⁸ or introduction of spacers (*e.g.* carbon nanotubes⁹) between graphene layers. For example, Yu *et al.* reported a porous carbon/graphene nanosheets composite that achieved a specific capacitance of 205 F g⁻¹ at 2 A g⁻¹.¹⁰ Zheng *et al.* synthesized porous nitrogen-doped graphene that exhibited a capacitance of 132.4 F g⁻¹ at 0.1 A g⁻¹.¹¹ The enhanced capacitances were attributed to the presence of the micro-pores in the structure. Nonetheless, ion diffusion in those micro-pores becomes more difficult at large current densities,^{12,13} which limits the rate capability performance. The third approach is to increase surface area via exfoliation of stacked graphene sheets. It has been demonstrated that by treating the material in a strong acid bath to introduce oxygen-containing functional groups (*e.g.* hydroxyl and carboxyl groups), analogous to the production of graphene oxide, can effectively exfoliate the surface to provide more ion-accessible surface area for charge storage.¹⁴⁻¹⁶ However, oxidized graphene is less conductive, and typically requires post-treatment thermal annealing to partially restore its electrical conductivity. For example, Wang *et al.* used the hydrazine atmosphere followed by annealing in ammonia atmosphere at 1000 °C to reduce the oxidized carbon cloth.¹⁴ Ji *et al.* de-oxidized the exfoliated graphitic fibers via a two-step annealing in nitrogen atmosphere.¹⁶ Yu *et al.* reduced the as-prepared graphene aerogel with hydrazine vapor at 85 °C for 24 h.¹⁵ The high temperature annealing or use of toxic chemicals (*e.g.* hydrazine and ammonia) poses energy and environmental concern. In addition to the aforementioned

chemical exfoliations, graphene materials can also be exfoliated by electrochemical methods. It exfoliates the graphene layers in aqueous solutions by introducing ions, oxygen gas and oxygen moieties between graphene layers.^{4,17-20} However, graphene will be oxidized by hydroxyl and oxygen radicals produced from oxidation of water at large positive potentials.²¹ Besides, gas evolution due to water oxidation/reduction tends to disintegrate electrode. Therefore, a facile and environmentally friendly strategy to activate graphene-based electrodes in conjunction with sustaining graphene's exceptional rate capability and structural integrity still remains to be explored.

Inspired by recent works on the exfoliation of the highly orientated pyrolytic graphite (HOPG) to produce high-quality single layer graphene in organic solvents,²¹⁻²³ we developed a facile ion intercalation strategy that can considerably improve the capacitance of graphene-based materials, including commercially available graphitic papers and 3D printed graphene aerogels, without significantly affect their rate capability performance and structural integrity. The electrochemically treated graphitic paper shows three orders of magnitude enhancement in capacitance, reaching $108.88 \text{ mF cm}^{-2}$ at a current density of 0.5 mA cm^{-2} , while maintaining an excellent rate capability of 84.1% (0.5 mA cm^{-2} to 5 mA cm^{-2}). The treated 3D printed graphene aerogel electrodes achieves an outstanding specific capacitance of 101.7 F g^{-1} at a large current density of 10 A g^{-1} .

5.2 Experimental Section

Preparation of Graphene-based Electrodes: graphitic papers (TGP-H-60, 190 μm) were purchased from Toray Industries. Three-dimensional graphene aerogel were fabricated via direct ink writing using a graphene oxide based ink. Electrodes were fabricated by attaching the graphitic papers/3D graphene aerogel onto a piece of copper foil using conductive silver epoxy. The metal contact was sealed with epoxy resin after silver epoxy solidifies.

Ion intercalation: a two-step Ion intercalation was performed via a three-electrode system in a 10 mL glass vial. The graphitic paper/3D graphene aerogel electrode was used as working electrode. A platinum plate and a Ag^+/Ag non-aqueous electrode (1 mM Ag^+ in acetonitrile) served as the counter electrode and reference electrode, respectively. 1 M LiClO_4 solution dissolved in propylene carbonate was used as electrolyte. It was bubbled with nitrogen gas for 30 min to remove dissolved oxygen. The electrochemical treatment was performed using electrochemical workstation (CHI 660D, CH Instrument, US). A constant negative potential of -2.5 V was first applied for 2 h followed by a constant positive potential of +2.5 V for another 2 h. The working electrode was then taken out and soaked in water until no bubbles were observed on the electrode surface. Finally, the working electrode was thoroughly rinsed by water to remove any salt and solvent residues and dried in an electric oven at 60 $^\circ\text{C}$ for 3 h.

Material characterizations: Raman spectra were collected using a Reinshaw

Raman spectrometer with an excitation wavelength of 632.8 nm. X-ray diffractions were carried out using a X-ray diffractometer (Rigaku Americas Miniflex Plus). The chemical compositions of oxygen moieties was probed by Fourier-transform infrared spectrometer (Spectrum One, Perkin-Elmer, spectral resolution: 4 cm^{-1}) and X-ray photoelectron spectrometer (RBD upgraded PHI-5000C ESCA system, Perkin-Elmer). All XPS spectra were calibrated using the C 1s peak located at 284.6 eV as reference. All peaks were fitted by using the *XPSPeak* software. Methylene blue dye adsorption/desorption (according to a method published elsewhere)²⁴ and scanning electron microscope (FEI Quanta 3D Dual-beam scanning electron microscope) were used to characterize the surface morphology of the graphitic papers. UV-Vis spectra were collected on an Agilent Cary 60 UV-vis spectrometer.

Electrochemical characterizations: cyclic voltammetry, Galvano-static charge-discharge profiles and electrochemical impedance spectra were performed using a conventional three-electrode electrolytic cell with an electrochemical workstation (CHI 600D, CH Instrument, US). A graphite rod (5 mm in diameter), treated electrode (graphitic papers or 3D printed graphene aerogels), saturated calomel electrode (SCE) and 3 M KOH aqueous solution were used as counter electrode, working electrode, reference electrode and electrolyte, respectively. All EIS were collected in a frequency range from 0.1 Hz to 1000 kHz at open-circuit potential with a perturbation of 5 mV. Cycling stability performance was

evaluated by CV in 3 M KOH aqueous electrolyte for 10000 cycles with a scan rate of 200 mV s^{-1} .

5.3 Results and Discussions

Figure 5.1 illustrates the three-step treatment process carried out in propylene carbonate solution containing lithium perchlorate (LiClO_4). Graphitic paper or 3D printed graphene aerogel was used as a working electrode. Initially, a negative voltage of -2.5 V is applied to allow lithium ions (Li^+) intercalate into the graphitic regions of the material. During the intercalation, we anticipate that Li^+ , along with co-intercalated propylene carbonate molecules would distort the layered structure of graphene and roughen the electrode surface.²⁵ Afterwards, a positive potential of 2.5 V is applied. Then the anions in the electrolyte, *i.e.*, perchlorate ions (ClO_4^-) are expected to be attracted to the surface of the positively charged electrode surface due to electrostatic attraction and further intercalate into the layered structure (whilst Li^+ ions de-intercalate from electrode) through the distorted edges and partially exfoliated regions created in the first step. The intercalated solvent molecules are mainly responsible for preserving the exfoliated structure during the early stage of this step. Finally, when the electrode is immersed in de-ionized water, the as-formed ClO_4^- intercalation compounds ($\text{C}_G^+-\text{ClO}_4^-$) should be readily hydrolyzed in water and form hydroxyl groups (with a small amount of carbonyl groups) according to Equation (1) and release oxygen gas as shown by Equation (2):²⁶ (C_G represents graphite lattice)

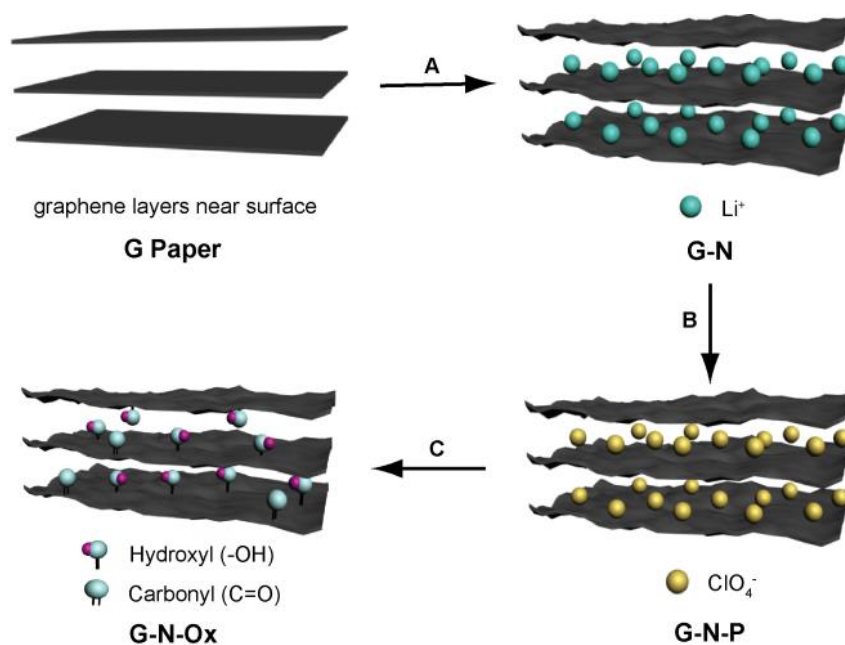
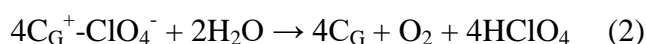
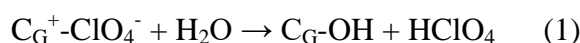


Figure 5.1 Schematic illustration of the three-step electrochemical treatment process. Step A: lithium ion intercalation induced by -2.5 V (*vs.* Ag/Ag^+) for 2 h. Step B: perchlorate ion intercalation induced by $+2.5 \text{ V}$ (*vs.* Ag/Ag^+) for 2 h; Step C: decomposition of perchlorate ion intercalation compounds formed in step B in water, resulting in introduction of oxygen moieties on/between graphene sheets.

Graphitic paper (G paper) is a commercially available self-supporting electrode material made of graphitic fibers that randomly stack together.¹⁶ The highly graphitized fiber surface makes it suitable for investigating ion intercalation processes. Figure 5.3a shows the cyclic voltammetry (CV) curve collected at a slow scan rate (1 mV s^{-1}) using G paper as the working electrode (Experimental Section). During the anodic scan, there is a drastic increase in current at *ca.* 1.1 V , which has been observed when anions intercalate into graphite layers.^{4,27,28} Beyond the onset potential, two peaks labelled as I and II can

be ascribed to the formation of stage \geq II and stage I intercalation ClO_4^- compounds (Figure 5.2). In the cathodic scan, a broad peak centered at *ca.* 1 V (peak III) was observed. This peak corresponds to the de-intercalation of ClO_4^- .^{4,27,28} Additionally, there are three peaks (peak IV, V and VI) located at negative potentials, which are corresponding to Li^+ intercalation/de-intercalation process.²⁸ Further increase the voltage to 3 V and -3 V results in gas evolution and lithium dendrite deposition, respectively, indicating the electrolyte is decomposed. Based on this CV data, we chose the potential window used in the electrochemical treatment between +2.5 V and -2.5 V, to induce ion-intercalations (Li^+ and ClO_4^- ions) while minimizing the oxidative decomposition of electrolyte and lithium dendrite formation.²⁹

To support the proposed mechanism (Figure 5.1), we characterized the electrode material at different stages of our electrochemical treatment. Figure 5.3b shows the Raman spectra collected from the same piece of G paper treated at different stages. All samples exhibited a characteristic G band (*ca.* 1600 cm^{-1}) and 2D band (*ca.* 2650 cm^{-1}) of graphene, corresponding to E_{2g} vibrational mode of in-plane sp^2 -carbon and double-resonance scattering process within the layered graphite lattice, respectively.⁴ Notably, only electrochemically treated samples exhibit D band that locates at *ca.* 1300 cm^{-1} ³⁰ (G-N, G-N-P and G-N-Ox represents the electrode obtained after first, second and third step, respectively.). The intensity of D band is proportional to the degree of surface disorder or the

amount of sp^3 -hybridized carbon atoms,^{4,30} suggesting the electrochemical treatment causes significant surface disorder. Moreover, all the 2D bands of electrochemically treated samples are blue-shifted, which has been found to be due to the presence of exfoliated graphene sheets.⁴ Investigation of the G bands further revealed the presence of intercalation compounds (Figure 5.3c). The G band of G paper and G-N-Ox sample can be fitted by a single Gaussian peak centered at *ca.* 1580 cm^{-1} , whilst the G band of G-N and G-N-P can be deconvoluted into two synthetic peaks. The splitting of G band indicates the presence of intermediate intercalation compounds as observed in previous studies with HOPG.^{31,32} The broadened G band of G-N-Ox is due to the existence of defects, as observed in the Raman spectra of reduced graphene oxide.³³

XRD studies were also performed to probe the structural modification of electrode upon electrochemical treatment (Figure 5.3d). In the XRD spectra of G-N and G-N-P, they exhibit not only the peak located at *ca.* 26° ($d = 0.337\text{ nm}$) that can be correlated to diffraction from (0 0 2) lattice plane of graphite,¹⁶ but also additional peaks located at lower diffraction angles, suggesting the d -spacing is increased. Diffraction peak at 19.39° corresponds to a d -spacing of 0.457 nm . This interlayer distance is larger than the theoretical value of Li^+ intercalation compound with maximum stoichiometry (LiC_6 , $d = 0.370\text{ nm}$),³² possibly because of the co-intercalation of solvent molecules or solvated Li^+ .²⁸ The d -spacing (0.65 nm) of the weak peak at 13.55° observed in the pattern of G-N-P matches well

with the interlayer distance of ClO_4^- intercalation compound ($\text{ClO}_4\text{C}_{18}$) predicted by density functional theory.³⁴ The diffraction peak at higher diffraction angle of 20.36° is believed to be originated from higher stage ClO_4^- intercalation compounds. G-N-Ox displayed a broad peak at 10.01° ($d = 0.883$ nm), which is a characteristic peak of graphene oxide,³⁵ confirming the formation of oxygen-containing functional groups after hydrolysis of the ClO_4^- intercalation compounds. Besides, no XRD peaks associated with intercalation compounds ($2\theta \sim 19.39^\circ$) were observed in the pattern of G-N-P, indicating lithium ions were completely de-intercalated during the second step. Additionally, we observed gas evolution when immersing the ClO_4^- intercalation G paper in de-ionized water, which is consistent with the prediction according to Equation (2). Moreover, electrode surface disordering was supported by the broadening of (0 0 2) diffraction peak of G-N, G-N-P and G-N-Ox, in agreement with the increased intensity of D band in Raman spectra. Taken together, the CV, Raman spectroscopy and XRD results support the proposed reaction mechanism illustrated in Figure 5.1.

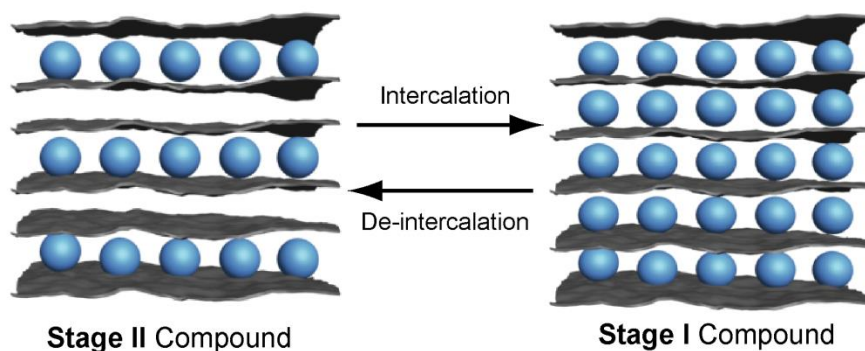


Figure 5.2 Schematic illustration of stage II and I intercalation compound,

according to the Daumas-Hérold model. The blue spheres and wrinkled black sheets represent intercalants and distorted graphene sheets, respectively.

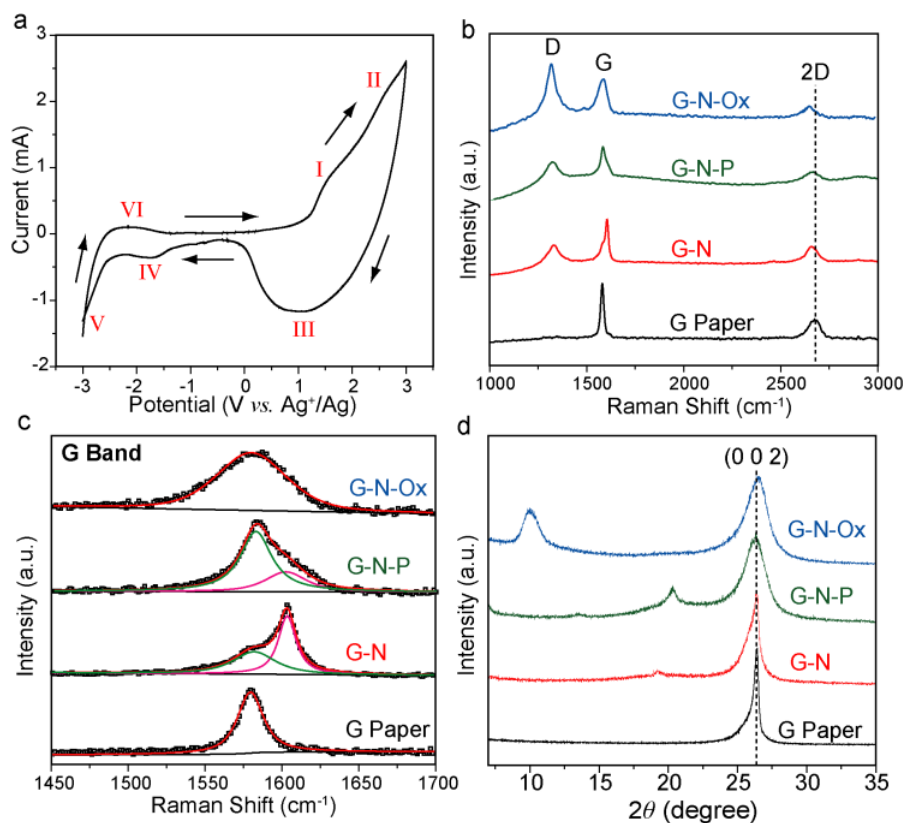


Figure 5.3 (a) CV curve of G paper collected at a scan rate of 1 mV/s in propylene carbonate containing 1 M LiClO₄. Six peaks are labelled in the figure. (b) Raman spectra of G paper and electrochemically treated G papers. The dashed line highlights the position of 2D band of G paper. (c) Deconvolution of G bands. The G band of G paper and G-N-Ox are fitted by a single Gaussian peak, while the G band of G-N and G-N-P are deconvoluted into two synthetic peaks, which correspond to the E_{2g} interior (green curve) and boundary (pink curve) mode of graphite intercalation compounds. The black dots represent experimental data. (d) XRD spectra of G paper and electrochemically treated G papers. Dashed line highlights the (0 0 2) diffraction peak originated from graphitic carbon. Other peaks are originated from the expanded/exfoliated graphite layers.

Furthermore, we have performed a number of microscopy and spectroscopy measurements to characterize the morphology and chemical composition of the final product, G-N-Ox. As shown in Figure 5.4a and 5.4b, the fiber of G paper has

smooth surface, while the surface of G-N-Ox fiber is full of wrinkles that is believed to be created by ion intercalations. Dye absorption-desorption experiment (Figure 5.5) proved that the G-N-Ox has enhanced surface area compared to G paper. The surface area of G-N-Ox and G paper calculated by the MB absorption method is $73.9 \text{ m}^2 \text{ g}^{-1}$ and $14.0 \text{ m}^2 \text{ g}^{-1}$, respectively. Figure 5.6 shows SEM images of graphitic paper treated with only negative potential or positive potential. Under positive potential (ClO_4^- intercalation), the morphology of fiber surface did not change obviously, possibly due to the fact that ClO_4^- has a larger size than Li^+ , which makes it more difficult to intercalate deeply into the layered structure. On the contrary, the surface of G paper was roughened under negative potential (Li^+ intercalation). Therefore, Li^+ intercalation (the first step in our electrochemical treatment) is mainly responsible for surface exfoliation and it is consistent with the increased intensity of D band observed for G-N. It is also evident from the observation that replacing Li^+ with bulky cations (*e.g.*, tetra-*n*-butylammonium cations, which are less favourable for intercalation than Li^+) during the first step cannot exfoliate the fibre surface (Figure 5.7). Fourier-transform infrared (FT-IR) spectra confirm the presence of oxygen moieties in G-N-Ox sample. As shown in Figure 5.4c, both G paper and G-N-Ox have strong absorption peaks centred at 2930 cm^{-1} and 2853 cm^{-1} , corresponding to the C-H stretching³⁶ that possibly come from graphene edges and defects. Another peak at 1630 cm^{-1} can be assigned to the aromatic C=C stretch from the

graphitic regions and O-H bending from hydroxyl groups.³⁶ Notably, G-N-Ox has a number of additional peaks: the broad peak at 3443 cm^{-1} (O-H stretching)³⁷ indicates the presence of hydroxyl groups, and peaks at 1721 cm^{-1} (C=O stretching) and 1574 cm^{-1} (C=C stretching of the quinonoid rings) prove the presence of carbonyl groups.³⁸ In addition, XPS survey spectra (Figure 5.8) also reveal that the atomic percent of oxygen atoms increases from 7.0% to 10.1% after treatment. The carbon-oxygen atomic ratio is around 9, which is consistent to the value reported for other reduced graphene oxide with excellent electrical conductivity^{39,40} Notably, there is no detectable signal of Cl (binding energy: *ca.* 200 eV) or Li (binding energy: *ca.* 55 eV), indicating all Li^+ are de-intercalated and ClO_4^- intercalation compounds are completely decomposed after the last step. Analysis of the C 1s peak (Figure 5.4d) further confirms that the electrode surface is functionalized with mainly hydroxyl groups (signal from carbonyl groups at 287.9 eV was not detected due to its limited amount). These oxygen functional groups can serve as the pseudo-capacitive sites for charge storage.^{14,41} Given that the G-N-Ox has large surface area and increased amount of pseudo-capacitive functional groups, it is anticipated to be a suitable electrode for supercapacitors.

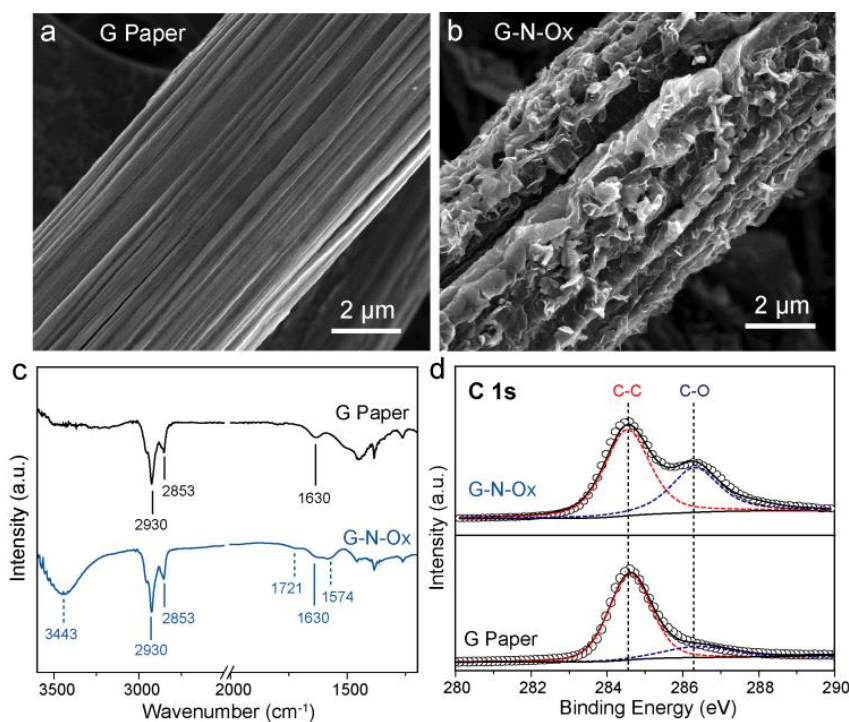


Figure 5.4 (a) SEM image of G paper. (b) SEM image collected for the same G paper after the electrochemical treatment (G-N-Ox). (c) FT-IR spectra of G paper and G-N-Ox. Dashed lines highlight the peaks correspond to oxygen-containing functional groups (hydroxyl and carbonyl groups). (d) C 1s XPS spectra of G paper and G-N-Ox. The black circles are experimental data that can be deconvoluted into two synthetic peaks (red and blue dashed curves). The black curve is the summation of the two synthetic peaks. Dashed lines highlight the binding energies reported for C-C and C-O.

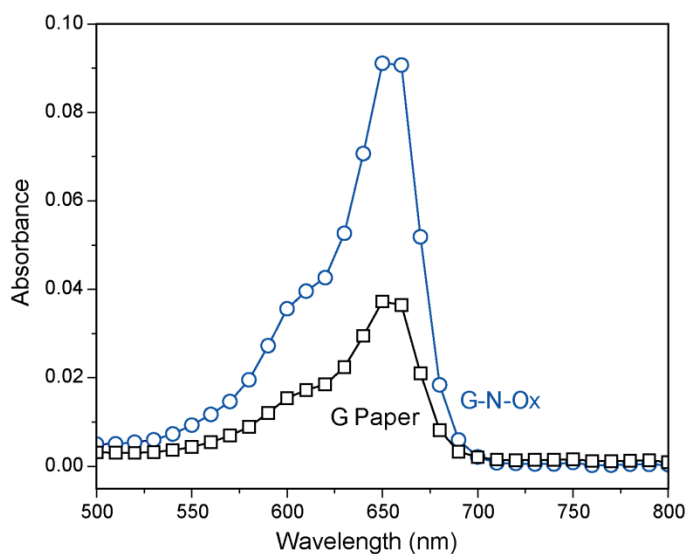


Figure 5.5 UV-Vis spectra collected for the solutions (acetonitrile as the solvent) containing desorbed methylene blue molecules from G paper and G-N-Ox. G-N-Ox sample showed a higher absorbance at the absorption maximum wavelength of methylene blue (655 nm), suggesting more dye molecules were desorbed from the surface of G-N-Ox. The increased amount of desorbed methylene blue molecules is a direct evidence showing the surface area of G-N-Ox is enlarged.

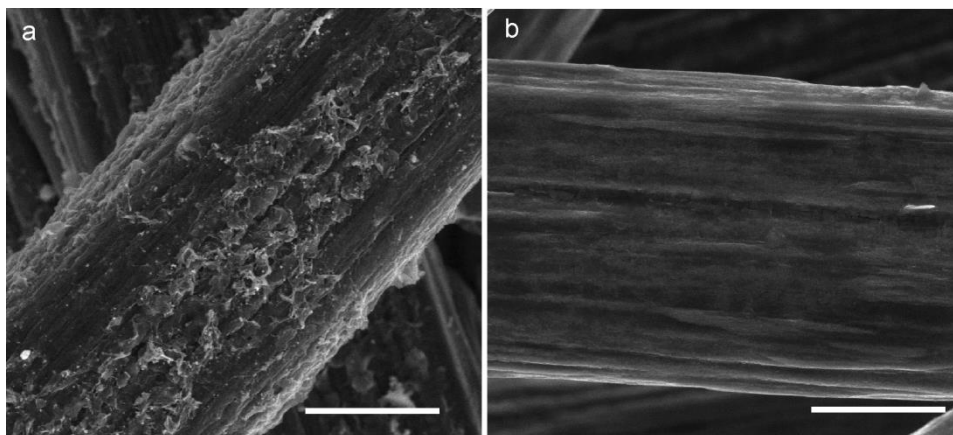


Figure 5.6 Representative SEM images showing the surface morphology of a G paper fiber treated with (a) -2.5 V, 2 h only and (b) +2.5 V, 2 h only.

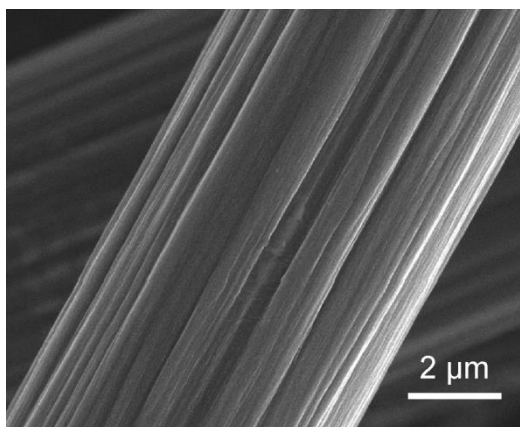


Figure 5.7 SEM image of a graphitic fiber treated at -2.5 V vs. Ag/Ag⁺ for 2 h in propylene carbonate containing 1 M tetra-*n*-butylammonium perchlorate.

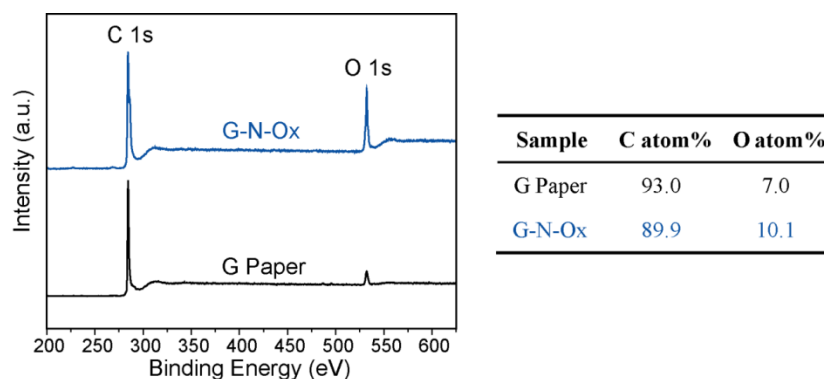


Figure 5.8 XPS survey spectra of G Paper and G-N-Ox. The table on the right summarizes the content of carbon and oxygen in each sample based on the C 1s and O 1s peak area.

The capacitive performance of G-N-Ox was investigated in a three-electrode electrolytic cell in 3 M KOH aqueous electrolyte (Experimental Section). Figure 5.9a compares the CV curves collected for G paper and G-N-Ox. As expected, the capacitance of G-N-Ox is much larger than that of G paper. The enhancement can be ascribed to the increased surface area and contribution from pseudo-capacitance. Moreover, G-N-Ox also exhibited larger capacitance than graphitic papers treated with $\text{Li}^+/\text{ClO}_4^-$ intercalation only (Figure 5.10), suggesting that Li^+ and ClO_4^- intercalation are indispensable for achieving the superior electrochemical performance of G-N-Ox. The quasi-rectangular shaped CV curves (Figure 5.9b and Figure 5.11) and isosceles triangular shaped galvanostatic charge-discharge (GCD) profiles (Figure 5.9c) indicate that G-N-Ox has superior capacitive performance.²⁴ It delivers an excellent areal capacitance of $108.88 \text{ mF cm}^{-2}$ (equivalent to a volumetric capacitance 5.73 F cm^{-3}) at a current density of 0.5 mA cm^{-2} , which is *ca.* 1000 times higher than that of G paper (Figure 5.9d). More importantly, the G-N-Ox also retains a high rate capability of 84.0% when

current density increased 10 times to 5 mA cm^{-2} , maintaining 91.44 mF cm^{-2} (equivalent to 4.81 F cm^{-3}) capacitance. The remarkable rate capability performance is due to the small internal resistance of G-N-Ox (Figure 5.12 and Figure 5.13). The combined series resistance (R_s) and charge transfer resistance (R_{ct}) of G-N-Ox are only slightly larger than that of G paper.

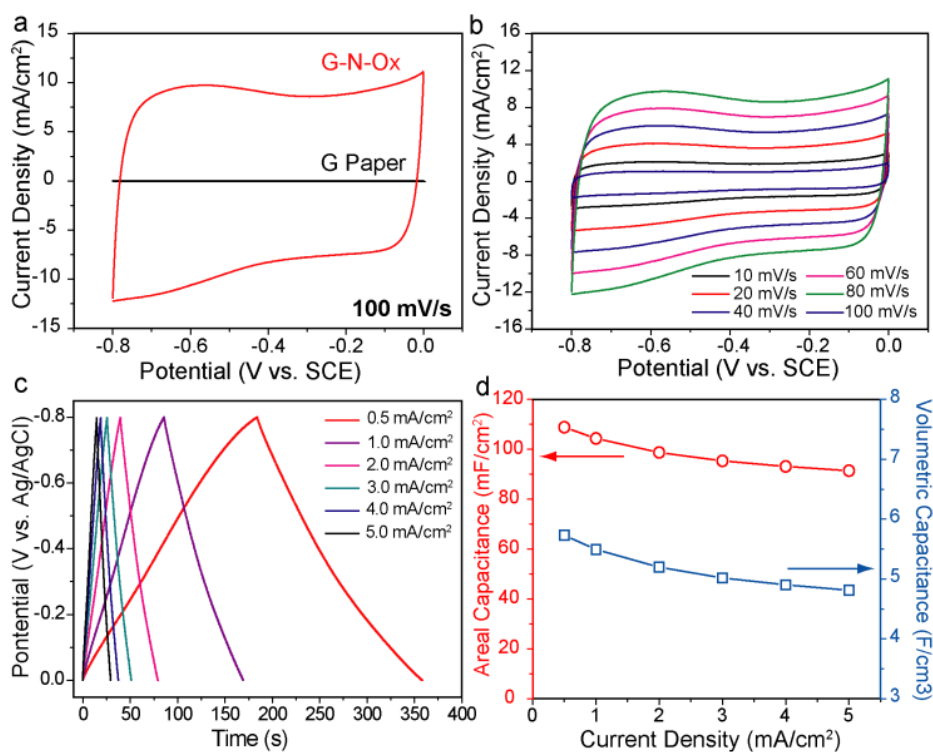


Figure 5.9 (a) Comparison of CV curves collected for G paper and G-N-Ox at a scan rate of 100 mV s^{-1} . (b) CV curves of G-N-Ox collected from 10 mV s^{-1} to 100 mV s^{-1} . (c) GCD profiles of G-N-Ox collected from 0.5 mA cm^{-2} to 5.0 mA cm^{-2} . (d) Plots of areal capacitance and volumetric capacitance of G-N-Ox as a function of current density. All areal capacitances and volumetric capacitances are evaluated based on the discharge time of the GCD profiles shown in (c).

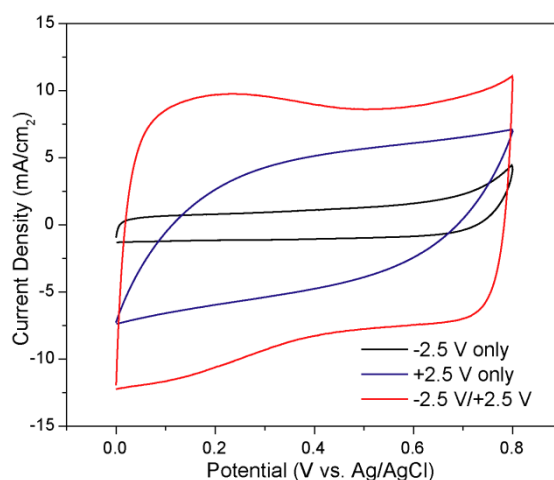


Figure 5.10 CV curves collected for graphitic paper treated by -2.5 V for 2 h only, +2.5 V for 2 h only and G-N-Ox (treated by -2.5 V for 2 h followed by +2.5 V for 2 h) in 3 M KOH aqueous electrolyte at scan rate of 100 mV s^{-1} .

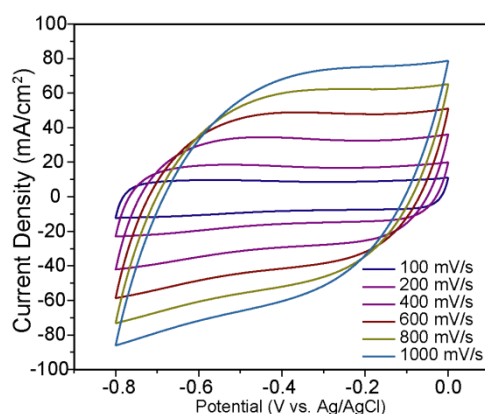


Figure 5.11 CV curves of G-N-Ox collected in 3 M KOH aqueous electrolyte at large scan rates ($100 - 1000 \text{ mV s}^{-1}$).

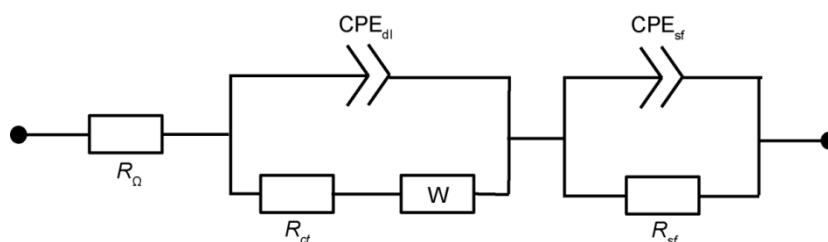


Figure 5.12 Equivalent electric circuit used for fitting of Nyquist plots. R_Ω : combined series resistance; R_{ct} : charge-transfer resistance; W : Warburg element; CPE_{dl} : constant phase element associated with electrical-double-layer capacitance; CPE_{sf} : constant phase element associated with pseudo-capacitance; R_{sf} : surface resistance

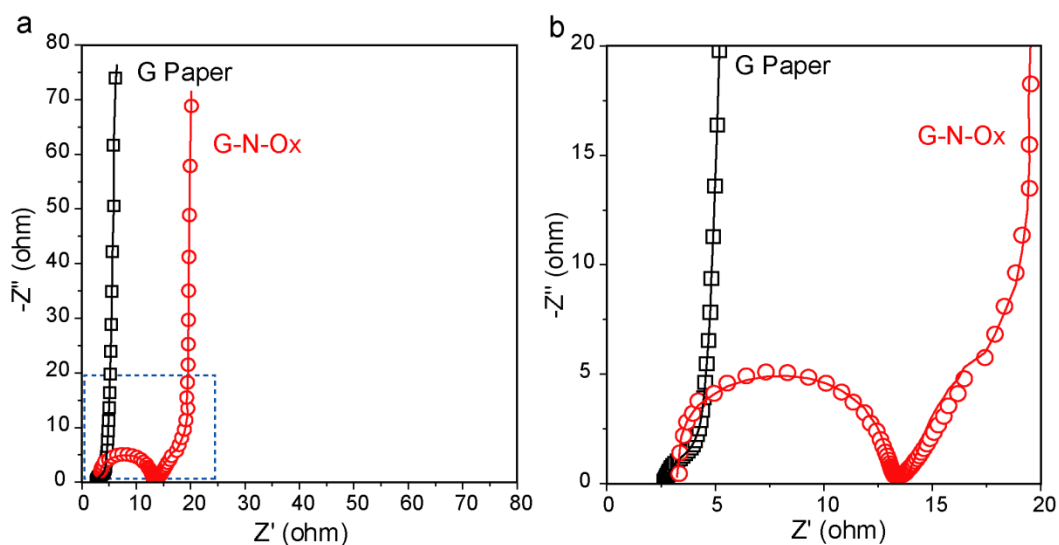


Figure 5.13 (a) EIS spectra of G Paper and G-N-Ox collected at open circuit potential with a perturbation of 5 mV in 3 M KOH aqueous solution. (b) Zoomed-in region of the EIS spectra highlighted by the dashed box in (a) to show the difference in diameter of the semi-circle in middle frequency domain. The Z' -intercept and diameter of the semi-circle in the middle frequency domain represents the combined series resistance (R_s) and charge transfer resistance (R_{ct}), respectively. Open dots are experimental data and solid lines are fitting lines.

Despite the substantial enhancement of capacitance, the performance of G paper is still limited by its large mass density (*ca.* 400 mg cm⁻³). The majority of the mass was used only as supporting material for the activated layer. To obtain an even better performed electrode, we have applied the same electrochemical treatment strategy to a lightweight graphene aerogel lattice structure fabricated by 3D printing. This unique 3D graphene architecture (3DG) that not only reduces the mass density to *ca.* 50 mg cm⁻³, but also facilitates ion diffusion in the thick electrodes, making it a promising electrode material for portable supercapacitors.⁴² 3DG suffers from relatively low gravimetric capacitance (63.6 F g⁻¹ at 10 A g⁻¹) due to limited surface area, which can be addressed by our

electrochemical treatment strategy. We treated the 3DG using the same aforementioned method and obtained the 3DG-N-Ox. Figure 5.14a compares the CV curves of 3DG and 3DG-N-Ox at a small scan rate of 20 mV s^{-1} . 3DG-N-Ox shows a considerably enhanced capacitance than 3DG, which is consistent with the longer discharge time of 3DG-N-Ox observed in the GCD experiment (Figure 5.14b). Gravimetric capacitances and rate capability of 3DG and 3DG-N-Ox are evaluated using the GCD profiles collected from 0.5 A g^{-1} to 10 A g^{-1} (Figure 5.15), and are summarized in Figure 5.14c and Table 5.1. 3DG-N-Ox achieved a remarkable specific capacitance of 124.7 F g^{-1} (6.93 F cm^{-3}) at a current density of 0.5 A g^{-1} , nearly doubled the specific capacitance of 3DG obtained at the identical current density (71.8 F g^{-1}). Significantly, 3DG-N-Ox still retained a high capacitance of 101.7 F g^{-1} (5.65 F cm^{-3}) when current density increased 20 times to 10 A g^{-1} . Such a capacitance is considerably higher than the gravimetric capacitances achieved by 3DG and also some other carbon-based materials tested under similar conditions, including activated carbon-carbon black powder (14 F g^{-1} @ 10 A g^{-1}),⁴³ reduced graphene oxide coated graphitic fiber (87.9 F g^{-1} @ 10 A g^{-1}),¹⁶ and activated carbon monolith (20 F g^{-1} @ 5 A g^{-1})⁴⁴. Significantly, the 3DG-N-Ox also retains 97% of capacitance after 10000 consecutive charge and discharge cycles (Figure 5.14e). To understand the capacitance improvement, we collected SEM images and electrochemical impedance spectra (EIS) for before and after the treatment. As shown in Figure 5.16, the surface of 3DG-N-Ox

becomes much rougher after treatment, thus can provide more surface area for holding charges. Figure 5.14d shows the EIS spectra with the R_s and R_{ct} values listed in the inset. Both R_s and R_{ct} only slightly increases after treatment. We ascribe such changes to the surface functionalization by oxygen moieties. The presence of these oxygen moieties is also supported by the redox peaks located at *ca.* -0.4 V (*vs.* SCE) in the CV curve of 3DG-N-Ox (Figure 5.14a). These results suggest that the enhanced specific capacitance is due to the increased surface area and incorporation of functional groups induced by electrochemical treatment, consistent with the results observed for G paper.

Table 5.1 Electrochemical performance of 3DG and 3DG-N-Ox

Sample	Gravimetric Capacitance @ 0.5 A g ⁻¹ (F g ⁻¹)	Gravimetric Capacitance @ 10 A g ⁻¹ (F g ⁻¹)	Rate Capability (%) ^[a]
3DG	71.8	63.6	88.6
3DG-N-Ox	124.7	101.7	81.6

[a] from 0.5 A g⁻¹ to 10 A g⁻¹

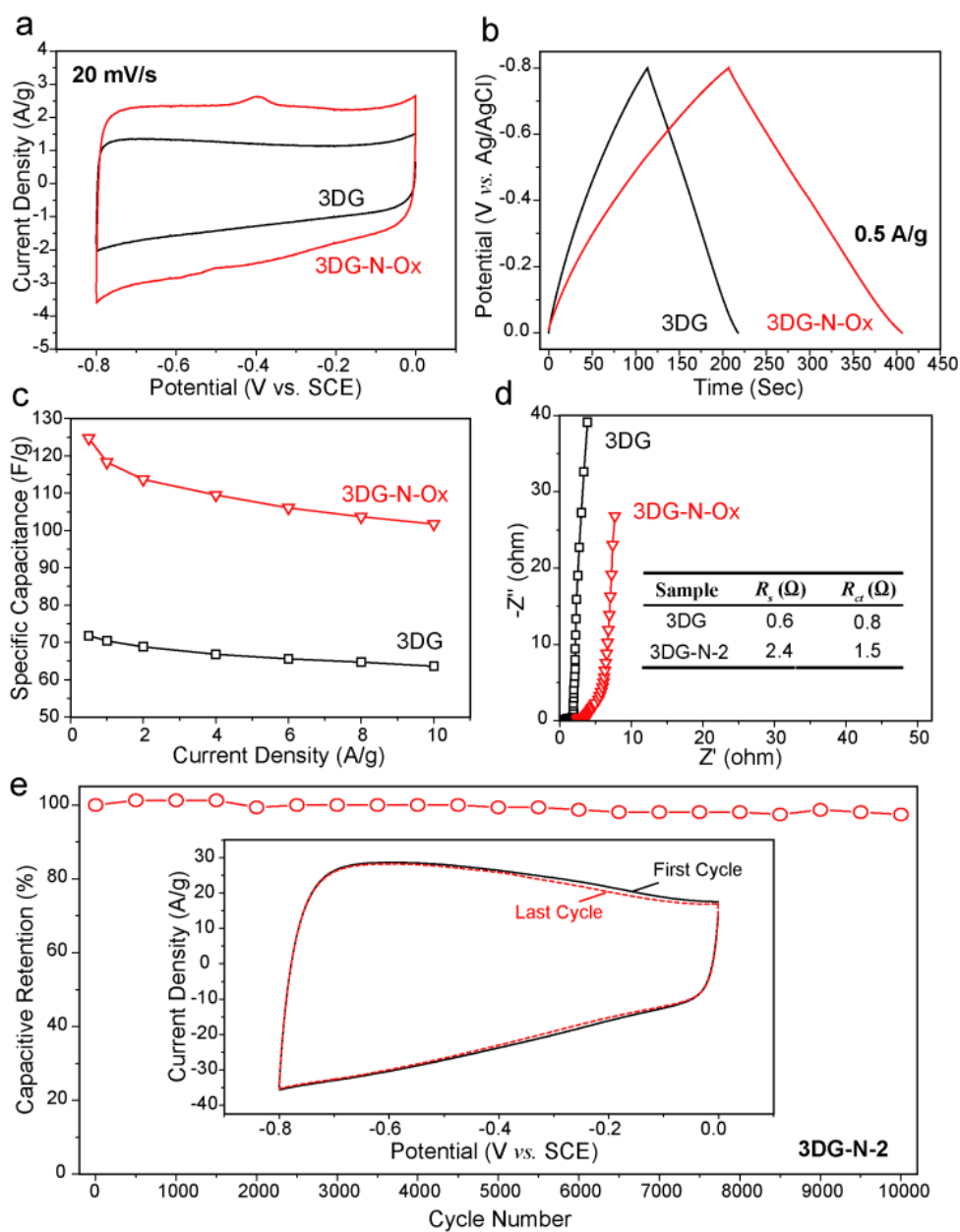


Figure 5.14 (a) CV curves collected at a scan rate of 20 mV s^{-1} . (b) GCD profiles collected at a current density of 0.5 A g^{-1} . (c) Plots of specific capacitance of 3DG and 3DG-N-Ox as a function of current density. (d) EIS collected at open-circuit potential with a perturbation of 5 mV from 0.1 Hz to 10000 Hz . Inset lists the R_s and R_{ct} values of 3DG and 3DG-N-Ox. Open dots are experimental data and solid lines are fitting curves. (e) Cycling stability of 3DG-N-Ox measured at a scan rate of 200 mV s^{-1} . Inset compares the CV curves of the first and last cycle.

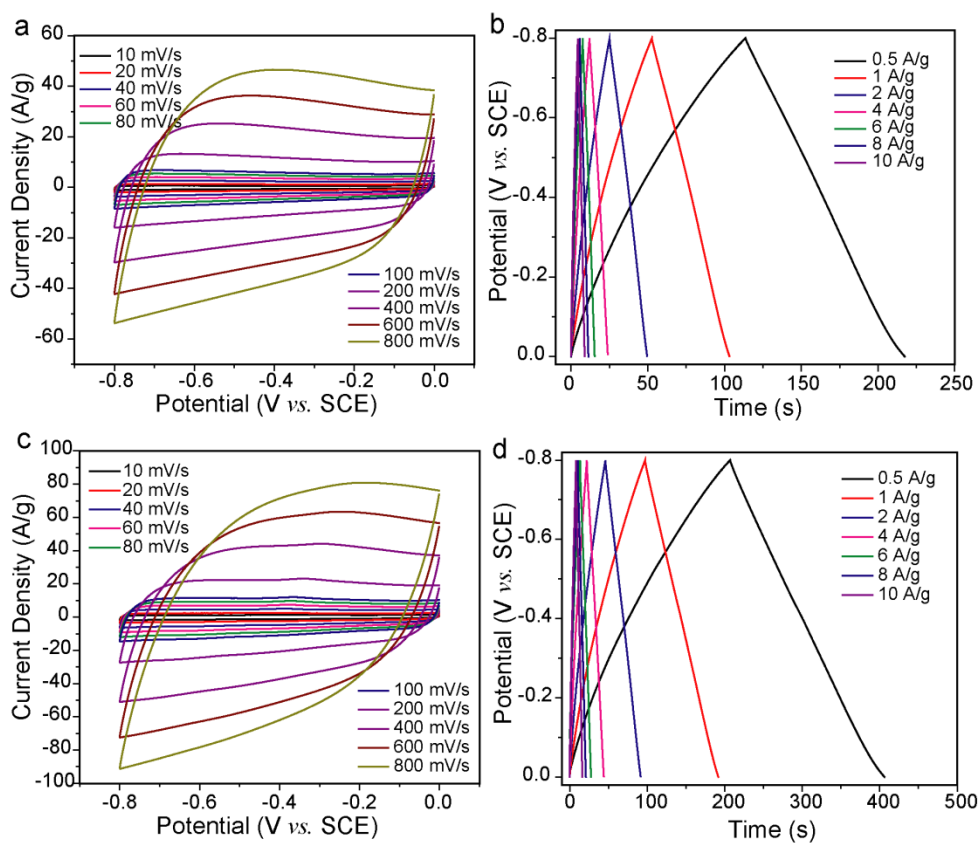


Figure 5.15 Cyclic voltammograms (left column) and GCD profiles (right column) of (a, b) 3DG and (c, d) 3DG-N-Ox collected in 3 M KOH aqueous electrolyte with a three-electrode testing configuration.

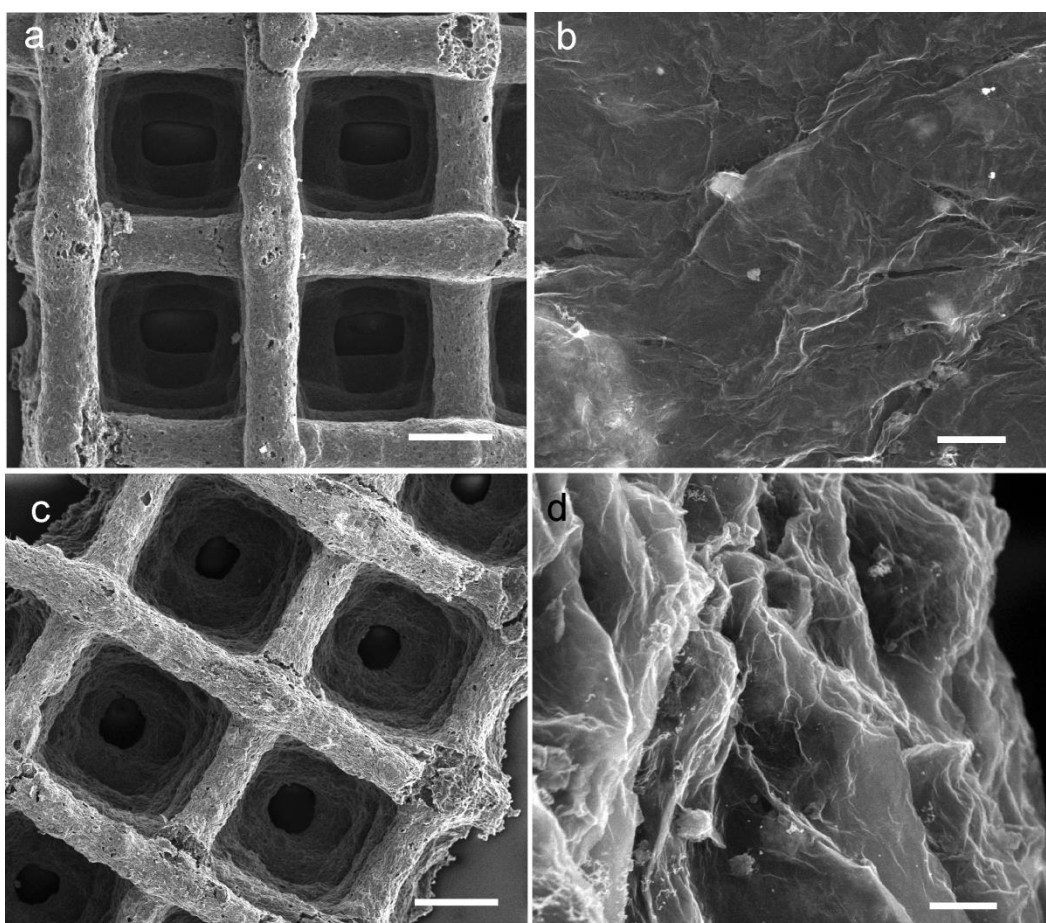


Figure 5.16 SEM images with different magnifications collected for (a, b) 3DG and (c, d) 3DG-N-Ox to compare the surface roughness. Scale bars: (a, c) 250 μm and (b, d) 1 μm .

5.4 Conclusions

We have demonstrated a two-step ion intercalation method that can considerably enhance the capacitance of graphene-based electrodes. The method is facile and energy efficient without the need of post-treatment annealing. The treated G Paper electrode showed a three orders of magnitude enhancement in capacitance, reaching 109 mF cm^{-2} at a current density of 0.5 mA cm^{-2} and more importantly, maintained an excellent rate capability of 84% when current density increased by 10 times. Besides, this method can also be extended to improve

capacitive performance of 3D printed three-dimensional graphene aerogels. The gravimetric capacitance almost doubled after treatment without sacrificing their excellent rate capability. We believe our method represent a general strategy to boost capacitive performance of other graphene-based supercapacitor electrodes, *e.g.*, chemically reduced graphene oxide (rGO). Moreover, the oxygen functionalized graphene electrodes could also be used in other electrochemical applications including catalysis and electrochemical sensors.

References

1. Bonaccorso, F.; Colombo, L.; Yu, G.; Stoller, M.; Tozzini, V.; Ferrari, A. C.; Ruoff, R. S.; Pellegrini, V. *Science* **2015**, *347*, 1246501-1246501.
2. Miller, J. R.; Simon, P. *Science* **2008**, *321*, 651-652.
3. Sevilla, M.; Ferrero, G. A.; Vu, T. T.; Fuertes, A. B. *ChemNanoMat* **2016**, *2*, 33-36.
4. Song, Y.; Feng, D.; Liu, T.; Li, Y.; Liu, X. *Nanoscale* **2015**, *7*, 3581-3587.
5. Wang, Y.; Tang, J.; Kong, B.; Jia, D.; Wang, Y.; An, T.; Zhang, L.; Zheng, G. *RSC Adv.* **2015**, *5*, 6886-6891.
6. Liu, X.; Wen, N.; Wang, X.; Zheng, Y. *ACS Sustainable Chem. Eng.* **2015**, *3*, 475-482.
7. Sun, Y.; Sills, R. B.; Hu, X.; Seh, Z. W.; Xiao, X.; Xu, H.; Luo, W.; Jin, H.; Xin, Y.; Li, T.; Zhang, Z.; Zhou, J.; Cai, W.; Huang, Y.; Cui, Y. *Nano Lett.* **2015**, *15*, 3899-3906.

8. Zhu, Y.; Murali, S.; Stoller, M. D.; Ganesh, K. J.; Cai, W.; Ferreira, P. J.; Pirkle, A.; Wallace, R. M.; Cychosz, K. A.; Thommes, M.; Su, D.; Stach, E. A.; Ruoff, R. S. *Science* **2011**, *332*, 1537-1541.
9. Du, F.; Yu, D.; Dai, L.; Ganguli, S.; Varshney, V.; Roy, A. K. *Chem. Mater.* **2011**, *23*, 4810-4816.
10. Yu, S.; Li, Y.; Pan, N. *RSC Adv.* **2014**, *4*, 48758-48764.
11. Zheng, B.; Chen, T.-W.; Xiao, F.-N.; Bao, W.-J.; Xia, X.-H. *J. Solid State Electrochem.* **2013**, *17*, 1809-1814.
12. Xu, J.; Zhang, R.; Chen, P.; Ge, S. *J. Power Sources* **2014**, *246*, 132-140.
13. Lv, B.; Zheng, C.; Xu, L.; Zhou, X.; Cao, H.; Liu, Z. *ChemNanoMat* **2015**, *1*, 422-429.
14. Wang, G.; Wang, H.; Lu, X.; Ling, Y.; Yu, M.; Zhai, T.; Tong, Y.; Li, Y. *Adv. Mater.* **2014**, *26*, 2676-2682.
15. Yu, M.; Huang, Y.; Li, C.; Zeng, Y.; Wang, W.; Li, Y.; Fang, P.; Lu, X.; Tong, Y. *Adv. Funct. Mater.* **2015**, *25*, 324-330.
16. Ji, Q.; Zhao, X.; Liu, H.; Guo, L.; Qu, J. *ACS Appl. Mater. Inter.* **2014**, *6*, 9496-9502.
17. Song, Y.; Xu, J.; Liu, X. *J. Power Sources* **2014**, *249*, 48-58.
18. Wang, W.; Liu, W.; Zeng, Y.; Han, Y.; Yu, M.; Lu, X.; Tong, Y. *Adv. Mater.* **2015**, *27*, 3572-3578.
19. Cheng, Q.; Tang, J.; Ma, J.; Zhang, H.; Shinya, N.; Qin, L.-C. *J. Phys. Chem.*

- C* **2011**, *115*, 23584-23590.
20. Abdelkader, A. M.; Cooper, A. J.; Dryfe, R. A. W.; Kinloch, I. A. *Nanoscale* **2015**, *7*, 6944-6956.
21. Lu, J.; Yang, J.-x.; Wang, J.; Lim, A.; Wang, S.; Loh, K. P. *ACS Nano* **2009**, *3*, 2367-2375.
22. Zhong, Y. L.; Swager, T. M. *J. Am. Chem. Soc.* **2012**, *134*, 17896-17899.
23. Ambrosi, A.; Pumera, M. *Chem.-Eur. J.* **2016**, *22*, 153-159.
24. Liu, T.; Ling, Y.; Yang, Y.; Finn, L.; Collazo, E.; Zhai, T.; Tong, Y.; Li, Y. *Nano Energy* **2015**, *12*, 169-177.
25. Huang, H.; Xia, Y.; Tao, X.; Du, J.; Fang, J.; Gan, Y.; Zhang, W. *J. Mater. Chem.* **2012**, *22*, 10452-10456.
26. Noel, M.; Santhanam, R. *J. Power Sources* **1998**, *72*, 53-65.
27. Lu, X.; Zhao, C. *Phys. Chem. Chem. Phys.* **2013**, *15*, 20005.
28. Suryanarayanan, V.; M, N. *J. Power Sources* **2001**, *94*, 137-141.
29. Xing, L.; Wang, C.; Li, W.; Xu, M.; Meng, X.; Zhao, S. *J. Phys. Chem. B* **2009**, *113*, 5181-5187.
30. Deng, D.; Pan, X.; Yu, L.; Cui, Y.; Jiang, Y.; Qi, J.; Li, W.-X.; Fu, Q.; Ma, X.; Xue, Q.; Sun, G.; Bao, X. *Chem. Mater.* **2011**, *23*, 1188-1193.
31. Afanasov, I. M.; Shornikova, O. N.; Kirilenko, D. A.; Vlasov, I. I.; Zhang, L.; Verbeeck, J.; Avdeev, V. V.; Van Tendeloo, G. *Carbon* **2010**, *48*, 1862-1865.
32. Sole, C.; Drewett, N. E.; Hardwick, L. J. *Farad. Discuss.* **2014**, *172*, 223-237.

33. Kaniyoor, A.; Ramaprabhu, S. *AIP Adv.* **2012**, *2*, 032183.
34. Tasaki, K. *J. Phys. Chem. C* **2014**, *118*, 1443-1450.
35. Feng, H.; Cheng, R.; Zhao, X.; Duan, X.; Li, J. *Nat. Commun.* **2012**, *4*, 1539.
36. Pham, V. H.; Cuong, T. V.; Hur, S. H.; Oh, E.; Kim, E. J.; Shin, E. W.; Chung, J. S. *J. Mater. Chem.* **2011**, *21*, 3371-3377.
37. Wang, X.; Song, L.; Yang, H.; Xing, W.; Kandola, B.; Hu, Y. *J. Mater. Chem.* **2012**, *22*, 22037-22043.
38. Li, M.; Huang, X.; Wu, C.; Xu, H.; Jiang, P.; Tanaka, T. *J. Mater. Chem.* **2012**, *22*, 23477.
39. Oh, Y. J.; Yoo, J. J.; Kim, Y. I.; Yoon, J. K.; Yoon, H. N.; Kim, J.-H.; Park, S. *B. Electrochim. Acta* **2014**, *116*, 118-128.
40. Mao, S.; Pu, H.; Chen, J. *RSC Adv.* **2012**, *2*, 2643-2662.
41. Wu, X.; Yang, D.; Wang, C.; Jiang, Y.; Wei, T.; Fan, Z. *Carbon* **2015**, *92*, 26-30.
42. Zhu, C.; Liu, T.; Qian, F.; Han, T. Y.-J.; Duoss, E. B.; Kuntz, J. D.; Spadaccini, C. M.; Worsley, M. A.; Li, Y. *Nano Lett.* **2016**, *16*, 3448-3456.
43. Gryglewicz, G.; Śliwak, A.; Béguin, F. *ChemSusChem* **2013**, *6*, 1516-1522.
44. Ruiz, V.; Blanco, C.; Santamaría, R.; Ramos-Fernández, J. M.; Martínez-Escandell, M.; Sepúlveda-Escribano, A.; Rodríguez-Reinoso, F. *Carbon* **2009**, *47*, 195-200.

Chapter 6

Carbon Coated Polyaniline and Polypyrrole Pseudo-capacitor Electrode with Excellent Stability

Abstract

Conducting polymers such as polyaniline and polypyrrole have been widely used as pseudo-capacitive electrode materials for supercapacitors. However, their structural instability resulting from repeated volumetric swelling and shrinking during charge/discharge process has been a major hurdle for their practical applications. This work demonstrates a simple and general strategy to substantially enhance the cycling stability of conductive polymer electrodes by deposition of a thin carbonaceous shell onto their surface. Significantly, carbonaceous shell coated polyaniline and polypyrrole electrodes achieved remarkable capacitance retentions of ~95% and ~85% after 10000 cycles. Electron microscopy studies revealed that the presence of ~5 nm thick carbonaceous shell can effectively prevent the structural breakdown of polymer electrodes during charge/discharge process. Importantly, the polymer electrodes with a ~5 nm thick carbonaceous shell exhibited comparable specific capacitance and pseudocapacitive behavior as the bare polymer electrodes. We anticipate that the same strategy can be applied for stabilizing other polymer electrode materials. The capability of fabricating stable polymer electrodes could open up new opportunities for pseudocapacitive devices.

6.1 Introduction

Conducting polymers, such as polyaniline (PANI) and polypyrrole (PPy), are promising pseudo-capacitive electrode materials for supercapacitors¹⁻⁶ due to their low cost,⁷ low environmental impact,⁸ high electrical conductivity in doped states ($\sim 100-10000 \text{ S m}^{-1}$),⁹⁻¹² and ease of fabrication for large-scale devices.¹³ Moreover, they exhibit excellent specific capacitance in the range typically between 500 to 3400 F g^{-1} depending on preparation conditions¹⁴, which is substantially larger than that of conventional carbon based electrodes ($\sim 100-200 \text{ F g}^{-1}$) and comparable to pseudo-capacitive metal oxides.^{8, 15} However, both PANI and PPy experience large volumetric swelling and shrinking during charge/discharge process as a result of ion doping and de-doping.^{16,17} This volumetric alternation often leads to structural breakdown, and thus, fast capacitance decay of conducting polymers.^{8, 18-20} Apparently, most PANI and PPy based electrode retain less than 50% of the initial capacitance after cycling for 1000 times. Therefore, cycling instability is a major obstacle for practical applications of conductive polymer electrodes.

A number of methods have been demonstrated to improve the cycling stability of polymer based pseudo-capacitor electrodes. For example, Wang *et al.* reported that PANI deposited on coral-like monolithic carbon can achieve high capacitance retention of 78.2% after 1000 cycles at a scan rate of 100 mV/s .²¹ Hai *et al.* demonstrated that carbon nanotube embedded PPy nanowires can retain 85%

of capacitance after testing for 1000 cycles at 1 A g^{-1} .²² Zhang *et al.* showed that PANI and PPy deposited on reduced graphene oxide substrate can achieve capacitance retention of ~82 and ~81% respectively, after 1000 cycles.²³ Encapsulating conducting polymer structures in titanium dioxide nanotubes²⁴ or Nafion coating²⁵ have been found to be alternative methods to enhance their cycling stability. However, the poor electrical conductivity of titanium dioxide ($10^{-7}\sim 10^{-4} \text{ S cm}^{-1}$) and Nafion ($10^{-7}\sim 10^{-2} \text{ S cm}^{-1}$) could increase the charge transfer resistance and negatively impact the capacitive performance of polymer electrodes. Moreover, conducting polymers doped with organic molecules such as para-toluenesulfonate (~96% capacitance retention after 500 cycles),²⁶ sulfanic acid azochromotrop (~92% capacitance retention after 1000 cycles)²⁷ and tiron (~93% capacitance retention after 1000 cycles)²⁸ have also shown enhanced cycling stability. Yet, the toxicity of these dopants could have an undesirable environmental impact. It is also noteworthy that, the cycling stability of polymer electrodes was tested for 1000 cycles only in most of the previous studies,²⁹⁻³⁵ while their cycling performance were improved. There is a lack of information about the electrode stability beyond 1000 cycles. To develop a facile, low-cost and environmentally friendly method that can improve the long-term cycling stability of pseudocapacitive polymer materials is essential for their practical applications. Here we demonstrate a facile strategy to improve the cycling stability of PANI and PPy nanowire (NW) pseudo-capacitor electrodes through deposition of a thin

carbonaceous shell onto the polymers. The carbonaceous shell maintains the structure of PANI and PPy during long-term cycling in 1 M H₂SO₄ electrolyte. The carbonaceous film coated PANI and PPy electrodes exhibit 95% and 85% capacitance retention after 10000 cycles. To our knowledge, these are the best capacitance retention values ever reported for PANI and PPy based pseudo-capacitor electrodes.

6.2 Experimental Section

Electrochemical synthesis of polyaniline (PANI) and polypyrrole (PPy)

nanowires (NWs): PANI NWs were deposited on carbon cloth (Fuel Cell Company, 45×45 yarns/inch) by electrochemical method reported elsewhere. Carbon cloth was cut into a rectangular piece (1.5cm×2cm), washed with ethanol and de-ionized water three times prior to deposition. Electrochemical deposition was carried out in a three electrode system, with the carbon cloth as working electrode, platinum as counter electrode and Ag/AgCl (in 1 M KCl) as reference electrode. PANI NWs were electrochemically deposited onto carbon cloth by cycling within the potential window between -0.2V and 0.8V vs. Ag/AgCl in aqueous electrolyte containing 0.1 M aniline and 1 M H₂SO₄ for 10 cycles. A uniform dark green film was obtained after electrochemical deposition. The mass loading of PANI NWs on carbon cloth is 3.8 mg cm⁻².

PPy NWs were deposited onto carbon cloth by using similar electrochemical method, in aqueous electrolyte containing 0.15 M pyrrole, 0.2 M Na₂HPO₄ and

0.002 M LiClO₄ by cycling within the potential window between -0.2V and 0.9V vs. Ag/AgCl for 10 cycles. A uniform black film was obtained after electrochemical deposition. The mass loading of the PPy NWs electrode is 0.9 mg cm⁻².

Deposition of carbonaceous shell onto PANI and PPy NWs: Uniform carbon shell was deposited onto the as-prepared conducting polymer NWs by a hydrothermal reaction using glucose as carbon precursor. Carbon cloth (1.5 cm×1.5 cm) coated with conducting polymer NWs and 25 mL 0.05 M glucose solution were transferred into a 30-mL Teflon lined stainless steel autoclave. The sealed autoclave was heated at 160 °C in an electric oven for 2 h and then allows it cool down at room temperature. The carbon cloth was then taken out, rinsed with DI water and blow dried with compressed air. The mass loadings of PANI@C-2h and PPy@C-2h on carbon cloth substrate were measured to be 4.2 mg cm⁻² and 1.2 mg cm⁻², respectively. Furthermore, carbonaceous shell coated PANI and PPy NWs with different carbonaceous shell thickness were synthesized by the same hydrothermal method for 1 h and 3 h. For comparison, polymer samples after hydrothermal treatment without carbonaceous shell (denoted as PANI-Hydrothermal and PPy-Hydrothermal) were synthesized under the same hydrothermal method except using de-ionized water as the solvent.

Material characterizations: Morphology of conducting polymer NWs was investigated by scanning electron microscope (SEM, FEI Quanta 3D FEG dual beam) and transmission electron microscope (TEM, FEI Tecnai G2 Spirit). Gold particles were deposited using a sputter (Technics Hummer VI) with a current of

15 mA for 2 min prior to TEM observation. The composition of as-prepared PANI and PPy NWs was confirmed by Raman spectroscopy (excitation wavelength: 532 nm, Advantage 532, DeltaNu Inc.). Cyclic voltammetry (CV) and chronopotentiometry (CP) were conducted in a standard electrolytic cell with a conventional three-electrode configuration using CHI 660D electrochemical workstation (CH Instruments Inc.) and 1 M H₂SO₄ aqueous solution as electrolyte. Conducting polymer NWs on carbon cloth with a geometric area of 0.8cm² (0.8cm×1.0cm) were used as working electrode. Graphite rod (~5mm diameter) and Ag/AgCl electrode (in 1 M KCl) were used as counter electrode and reference electrode, respectively. Electrochemical impedance spectroscopy (EIS) was conducted in 1 M H₂SO₄ in a range of 0.1 Hz to 1000 kHz at open circuit potential with a perturbation of 5 mV. ZsimpWin software was used to fit EIS data and obtain parameter of equivalent circuit elements. Cycling stability test was conducted in 1 M H₂SO₄ at a scan rate of 100 mV/s for 10000 cycles.

6.3 Results and Discussions

The cycling instability of pseudocapacitive polymer electrodes is believed to be due to the structural breakdown of polymer during repeated charging and discharging processes. The polymer volume increases when they are doped with ions in electrolyte (charging); and decreases when these ions diffuse back to electrolyte (discharging).⁸ However, most polymer electrodes cannot tolerate the mechanical stress created by the volume change, and thus, break into small pieces

during the cycling process. The structural pulverization leads to severe loss of active materials, resulting in degradation of capacitance. We hypothesize that cycling stability of PANI or PPy based pseudo-capacitor electrodes during cycling can be improved by deposition of a thin carbonaceous shell onto the polymers. There are two potential benefits of having a carbonaceous shell on polymer. First, the carbonaceous shell could serve as a physical buffering layer that helps to suppress the structural alternation of polymer electrodes during charge/discharge cycling. It has been reported that carbon coated metal oxide electrodes exhibit superior electrochemical stability in lithium ion batteries, in which the carbon coating can tolerate the volumetric alternation during Li^+ insertion/de-insertion, and thus, prevent the electrode pulverization.^{36,37} Second, even the carbonaceous shell is not able to prevent the structural pulverization of polymer electrodes, it could serve as a conductive network to hold the electrode fragments together and maintain their mechanical and electrochemical stability.

PANI and PPy NWs were electrochemically deposited onto carbon cloth substrate according to the previously reported methods (Experimental Section).^{38,39} Raman spectra of the polymer samples showed characteristic peaks of PANI and PPy (Figure 6.1). A layer of carbonaceous coating with controllable thickness was deposited onto these polymer NWs by a hydrothermal reaction using glucose as carbon precursor (Figure 6.2a).^{30, 40-42} The chemical composition of the carbonaceous shell is believed to be a mixture of carbon and other carbonaceous

products.⁴³ Transmission electron microscopy (TEM) studies were conducted to verify the core@shell structure of PANI@C and PPy@C. Since both the deposited carbonaceous shell and PANI or PPy NWs are amorphous in nature and have elements with similar molecular weight, it is challenging to observe the interface between carbonaceous shell and polymer core. Therefore, a thin layer of gold nanoparticles (average diameter of ~2 nm) was firstly sprayed on bare PANI and PPy NWs then followed by the hydrothermal reaction. As shown in Figure 1b-1d, the dark contrast regions are gold particles, which clearly present the boundary of polymer NW and carbonaceous shell. The TEM images also revealed that the variation of carbonaceous shell thickness as a function of hydrothermal reaction time between one and three hours. For one hour sample, the polymer NWs are only partially covered by a thin carbonaceous shell with a thickness less than 3 nm (Figure 6.2b). The carbonaceous shell thickness increases with the hydrothermal reaction time, and eventually the entire polymer surface were covered with carbonaceous shell. A uniform carbonaceous shell with a thickness of ~5 nm and ~9 nm were observed for two- and three-hour samples, respectively (Figure 6.2c and 6.2d). The carbonaceous shell coated PANI and PPy NW with different hydrothermal times are denoted as PANI@C-xh and PPy@C-xh, where x (=1, 2, 3) stands for reaction time in hour.

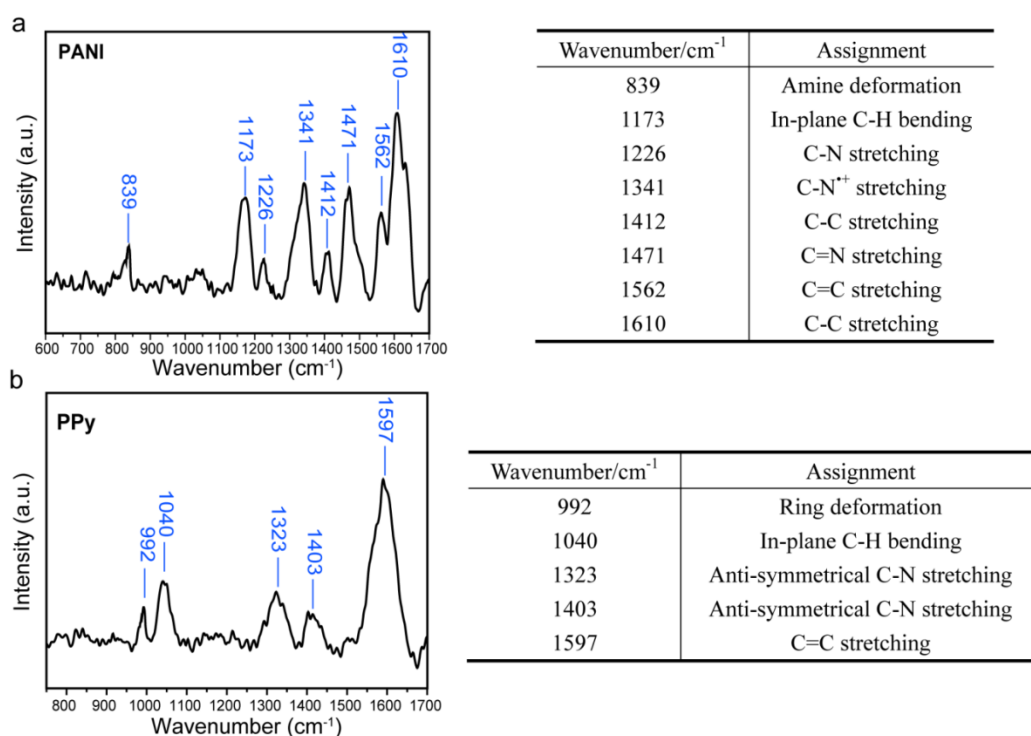


Figure 6.1 Raman spectra of (a) PANI NWs and (b) PPy NWs. The tables show the assignments for the major peaks in the spectra.

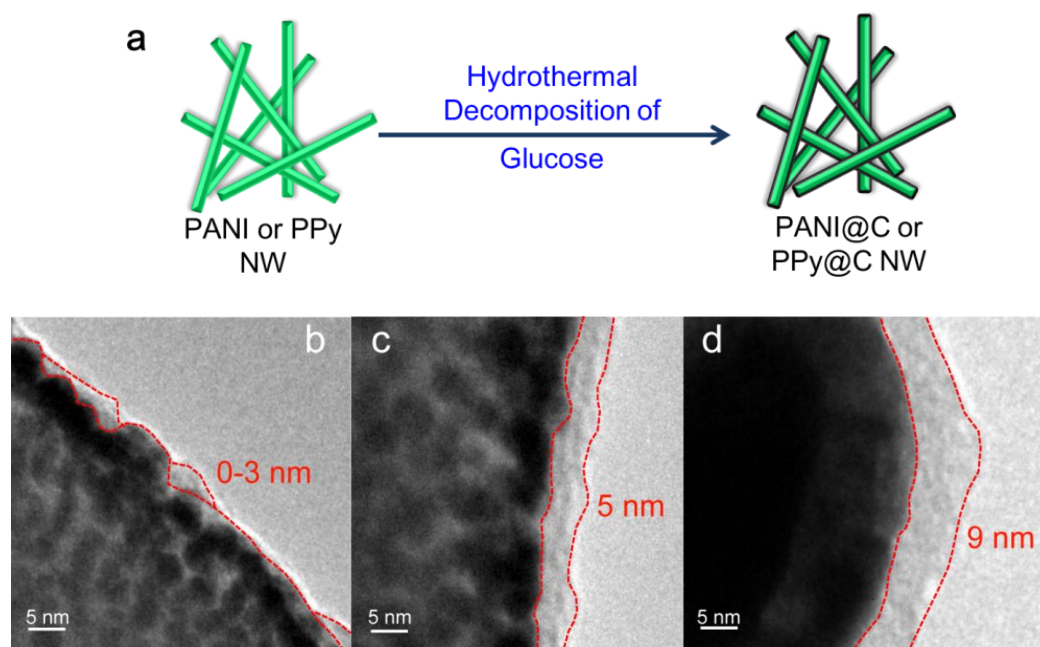


Figure 6.2 (a) Schematic illustration of the carbonaceous coating procedure using glucose as carbon precursor; (b-d) TEM images of PPy@C samples with different carbonaceous shell thicknesses, which was controlled through reaction time for

hydrothermal deposition of glucose: (b) 1 h, (c) 2 h and (d) 3 h.

The carbon cloth substrates grown with bare and carbonaceous shell coated polymer NWs were fabricated into working electrodes. These electrodes have a fixed geometric area of $\sim 0.8 \text{ cm}^2$ ($0.8 \text{ cm} \times 1.0 \text{ cm}$) were tested in a three-electrode electrochemical cell, with graphite rod ($\sim 5 \text{ mm}$ diameter) and Ag/AgCl electrode (in 1 M KCl) as counter electrode and reference electrode. The cycling stability test was carried out by cyclic voltammetry (CV) at a scan rate of 100 mV/s in 1 M H_2SO_4 electrolyte solution. As expected, bare PANI and PPy electrodes showed large capacitance drop after 10000 cycles, with less than 25% retention of their initial capacitance (Figure 6.3). Scanning electron microscopy (SEM) studies revealed that most of the PANI and PPy NWs disappeared after cycling for 10000 cycles (Figure 6.4). It suggests that the rapid decay of capacitance was mainly due to the loss of active capacitive materials.

Cycling stability test were performed for carbonaceous shell coated polymer electrodes under the the same conditions. Figure 6.5 shows that PANI@C-1h and PPy@C-1h retained 35% and 51% of its initial capacitance after 10000 cycles, respectively. These values are improved compared to that of bare polymer electrodes. And importantly, the SEM images collected from PANI@C-1h and PPy@C-1h following the cycling test indicated that the carbonaceous shell has positive effect on preserving the polymer materials. The loss of polymer materials during cycling is still considerably high, which could be attributed to the

incomplete carbonaceous shell coating.

Significantly, PANI@C-2h and PPy@C-2h electrodes exhibited exceptional capacitance retention of 95% and 85% after 10000 cycles compared with bare PANI and PPy electrodes (Figure 6.3). To our knowledge, these retention rates are the best values ever obtained for polymer based pseudocapacitive electrodes in aqueous electrolyte. SEM images also confirmed that PANI@C-2h and PPy@C-2h electrodes have no obvious structural change after tested for 10000 cycles (Figure 6.6). These results clearly showed that the carbonaceous shell was very effective in stabilizing the structure of PANI and PPy NW electrodes during charge/discharge cycling, resulting the excellent capacitance retention rates. It is also noteworthy that PANI@C-2h and PPy@C-2h electrodes have comparable pseudocapacitive behavior and specific capacitance compared to bare polymer samples (Figure 6.3 insets). It is crucial that the improved cycling stability is not at the expense of their electrochemical performance of polymer electrodes.

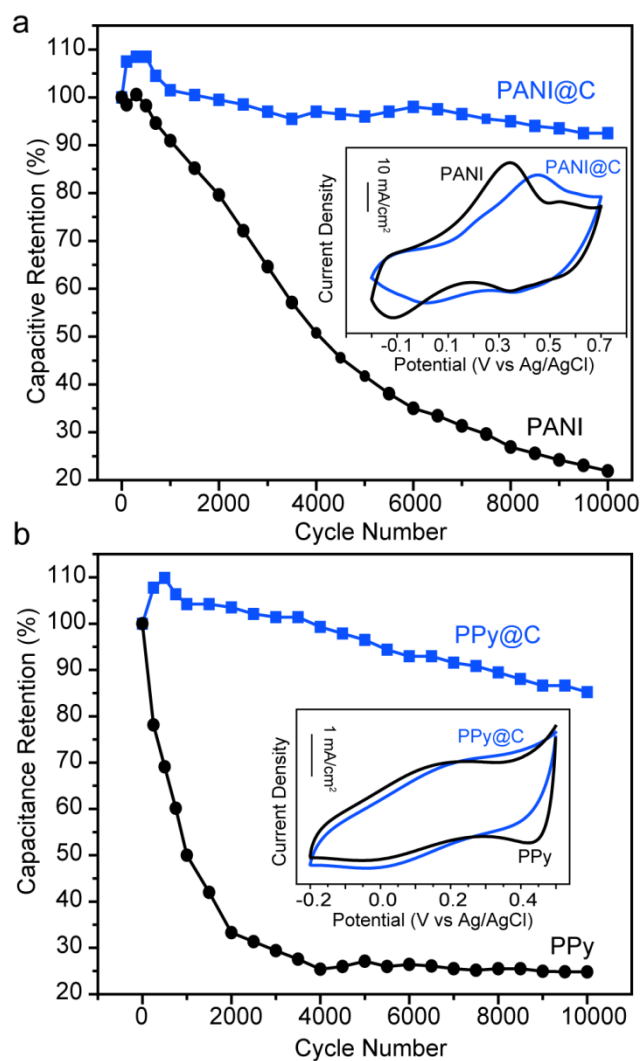


Figure 6.3 Cycling performance of (a) PANI and PANI@C electrodes; and (b) PPy and PPy@C electrodes, collected at a scan rate of 100 mV s^{-1} in $1 \text{ M H}_2\text{SO}_4$ electrolyte. Insets show CV curves collected for the bare polymer electrodes (black) and carbonaceous shell coated polymer electrodes (blue) at a scan rate of 20 mV s^{-1} in $1 \text{ M H}_2\text{SO}_4$.

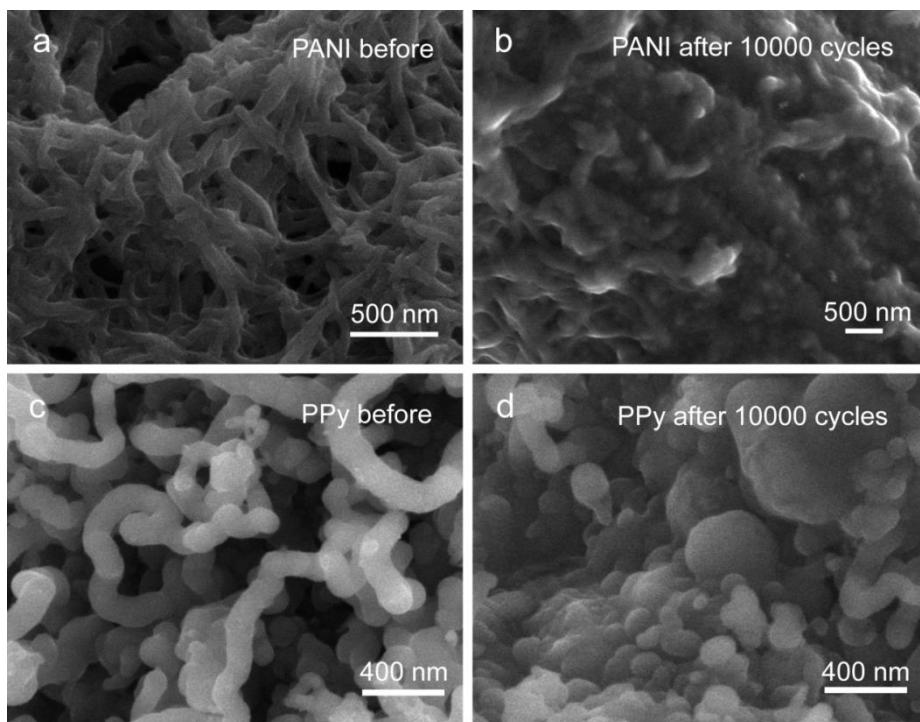


Figure 6.4 SEM images collected for (a, b) PANI and (c, d) PPy before and following the cycling stability test for 10000 cycles.

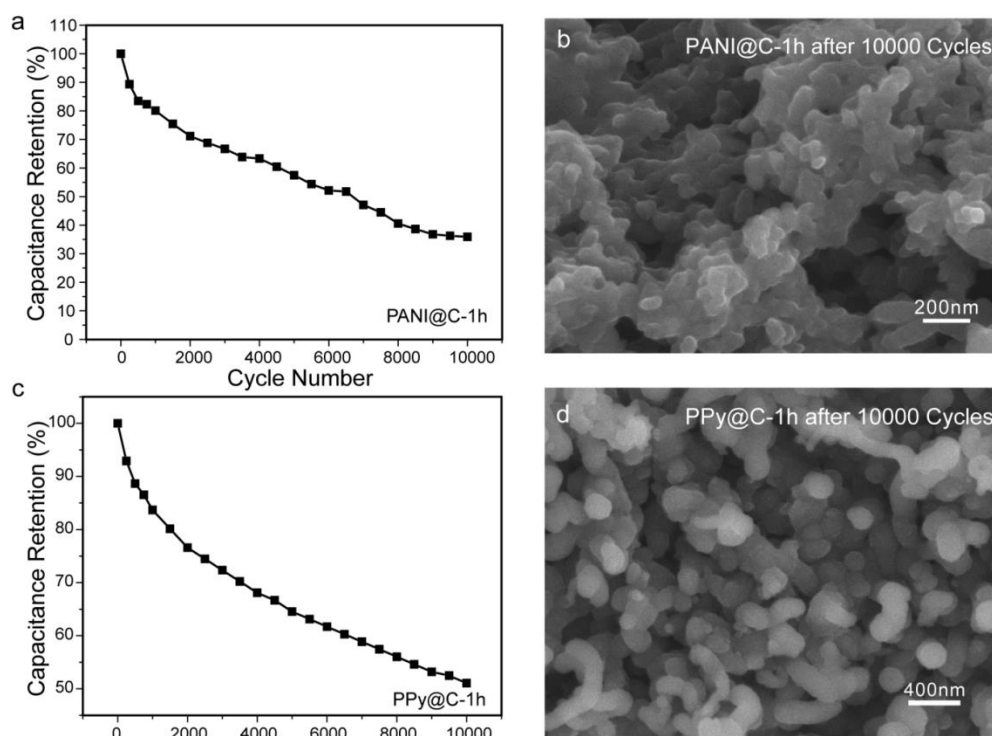


Figure 6.5 (a,c) Capacitance retention of (a) PANI@C-1h and (c) PPy@C-1h in 1 M H₂SO₄ as a function of charge/discharge cycles. (b,d) SEM images collected for

(b) PANI@C-1h and (d) PPy@C-1h following the cycling stability test for 10000 cycles.

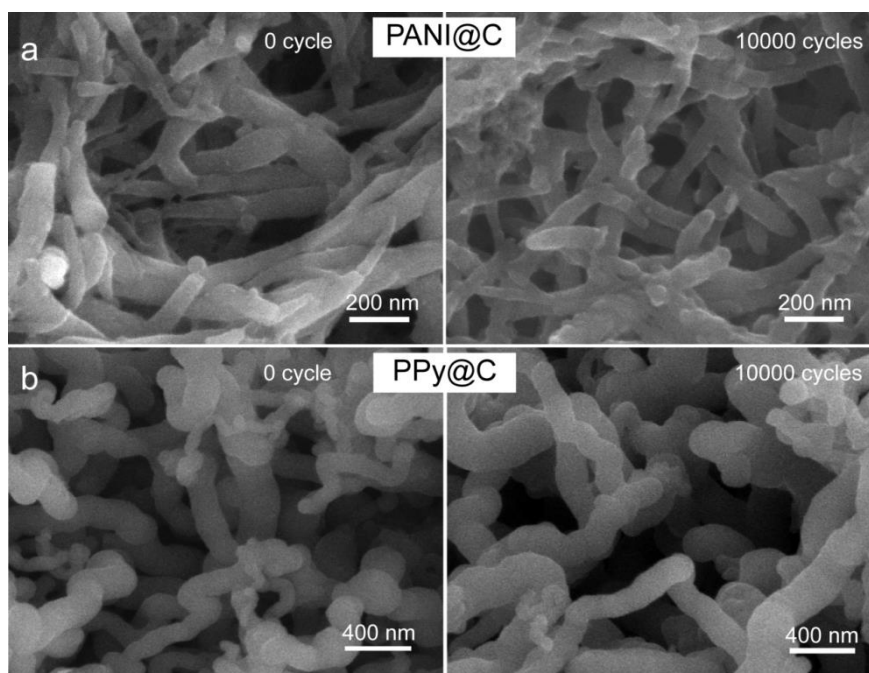


Figure 6.6 SEM images collected for (a) PANI@C-2h and (b) PPy@C-2h electrodes before and following the cycling test for 10000 cycles.

We also evaluate the performance of PANI@C-3h and PPy@C-3h electrodes.

Figure 6.7 compares the CV and capacitances of PANI@C-3h and PPy@C-3h with their two-hour samples. The results showed that the capacitances of PANI@C-3h and PPy@C-3h are substantially lower than that of the two-hour samples at all scan rates. This can be attributed to the increased thickness of carbonaceous shell, which makes it more difficult for ions in electrolyte to penetrate through the carbonaceous shell and react with the polymer, resulting in reduced pseudo-capacitance. Among the three carbonaceous shell-coated polymer electrodes, PANI@C-2h and PPy@C-2h samples have the best combination of cycling stability and pseudocapacitance. Therefore, the following studies will

focus on these samples only.

Since carbon is a conventional electrical double layer capacitive material, it is believed that the measured capacitances of PANI@C-2h and PPy@-2h have contribution from both carbonaceous shell and polymer NW core. We used Trasatti method to quantitatively differentiate the capacitance contribution from carbonaceous coating and polymer core.^{44, 45} The reciprocal of areal capacitance ($1/C$) for PANI@C-2h and PPy@C-2h NWs are plotted against the square root of scan rate ($v^{1/2}$) (Figure 6.8). The plots at slow scan rate region ($\leq 10 \text{ mV s}^{-1}$) were fitted with a straight line and extrapolating this line to the y-axis to obtain the y-intercept. The “total capacitance” of PANI@C-2h and PPy@C-2h equals to the reciprocal of the y-intercept. When the scan rate approaches to 0 mV s^{-1} , ions in electrolyte should have sufficient time to diffuse to the entire electrode surface for charge storage. In this case, the measured capacitance is not limited by the ion diffusion rate, and it should be the highest possible capacitance of the electrode. The “total capacitance” of PANI@C-2h and PPy@C-2h were calculated to be $787.40 \text{ mF cm}^{-2}$ (189.73 F g^{-1}) and $136.99 \text{ mF cm}^{-2}$ (114.08 F g^{-1}), respectively. These values are slightly higher than the calculated “total capacitances” of bare PANI NWs ($724.63 \text{ mF cm}^{-2}$ or 190.69 F g^{-1}) and PPy NWs (99.01 mF cm^{-2} or 110.01 F g^{-1}) using the same method (Figure 6.9). Therefore, the difference between these two “total capacitance” is the electric double layer capacitance contribution from the carbonaceous coating. Figure 6.8 insets summarize the

calculated capacitances based on Trasatti method. The carbonaceous shell contributes 62.77 mF cm^{-2} (156.93 F g^{-1}) to PANI@C electrode, and 37.98 mF cm^{-2} (126.6 F g^{-1}) to PPy@C electrode. The slight difference of capacitance contribution of carbonaceous shell could be attributed to the different surface area of PANI@C-2h and PPy@C-2h electrodes as they have different sizes.

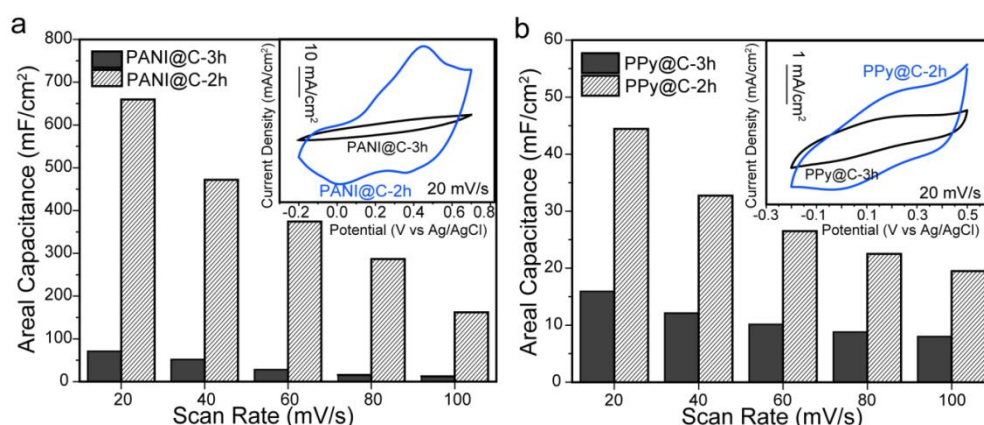


Figure 6.7 (a,b) Histograms compare the areal capacitance of (a) PANI@C-3h and PANI@C-2h and (b) PPy@C-3h and PPy@C-2h, at various scan rates. Insets show their CV curves collected in 1 M H₂SO₄ at a scan rate of 20 mV s^{-1} .

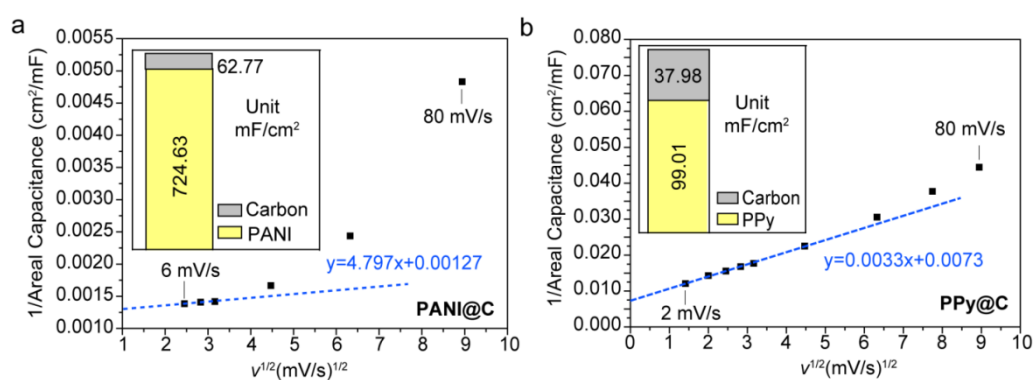


Figure 6.8 (a, b) The plots of reciprocal of areal capacitance ($1/C$) against square root of scan rate ($v^{1/2}$) for (a) PANI@C-2h and (b) PPy@C-2h. Dashed lines are the linear fitting curves for the data points in slow scan region. Insets: histogram illustration of capacitance contribution from polymer core and carbonaceous shell.

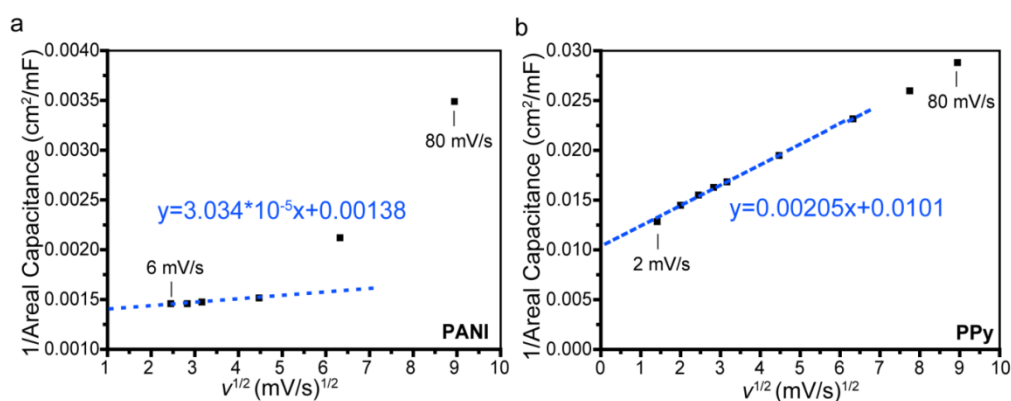


Figure 6.9 Plots of reciprocal of areal capacitance ($1/C$) against square root of scan rate ($v^{1/2}$) for (a) PANI and (b) PPy. Dashed lines are the linear fitting curves for the data points in slow scan region.

To further evaluate the influence of carbonaceous shell on pseudo-capacitive behavior of the PANI@C-2h and PPy@C-2h NWs, we performed a number of electrochemical measurements including CV, chronopotentiometry (CP) and electrochemical impedance spectroscopy (EIS). The CV curves collected at different scan rates exhibit obvious redox peaks, indicating the pseudo-capacitive behavior of polymer electrodes. The symmetric shape of CP curves suggested the polymer electrodes have excellent reversibility (Figure 6.10). Figure 6.11a and 6.11b shows the capacitance of PANI@C-2h and PPy@C-2h calculated based on CP results collected at different current densities. The initial capacitances of carbonaceous shell coated polymers are slightly higher than those of bare polymers, while their capacitances decrease relatively faster as the increase of current density. It is likely that the presence of carbonaceous shell affects ion diffusion to polymer core and therefore increase iR drop. We carried out EIS measurements to evaluate the effect of carbonaceous coating on the interfacial

charge transfer. Figure 6.12 shows equivalent electrical circuit model used for EIS data fitting. All the parameters of equivalent circuit elements are summarized in Table 6.1. As shown in Figure 6.11c and 6.11d, the combined series resistances (R_s) of PANI@C-2h and PPy@C-2h electrodes are slightly higher than the bare polymer electrodes (Figure 6.11c and 6.11d Insets), owing to the presence of additional contact resistance between carbonaceous shell and polymer core. Notably, the R_s of bare polymer without carbonaceous shell were not significantly changed after hydrothermal treatment (Figure 6.13). The increased R_s of carbonaceous coated polymer electrodes will increase the iR drop, and therefore lead to a slightly lower rate capability. These results proved that the addition of a thin carbonaceous shell (~5 nm) would not affect significantly the capacitive performance of polymer electrodes.

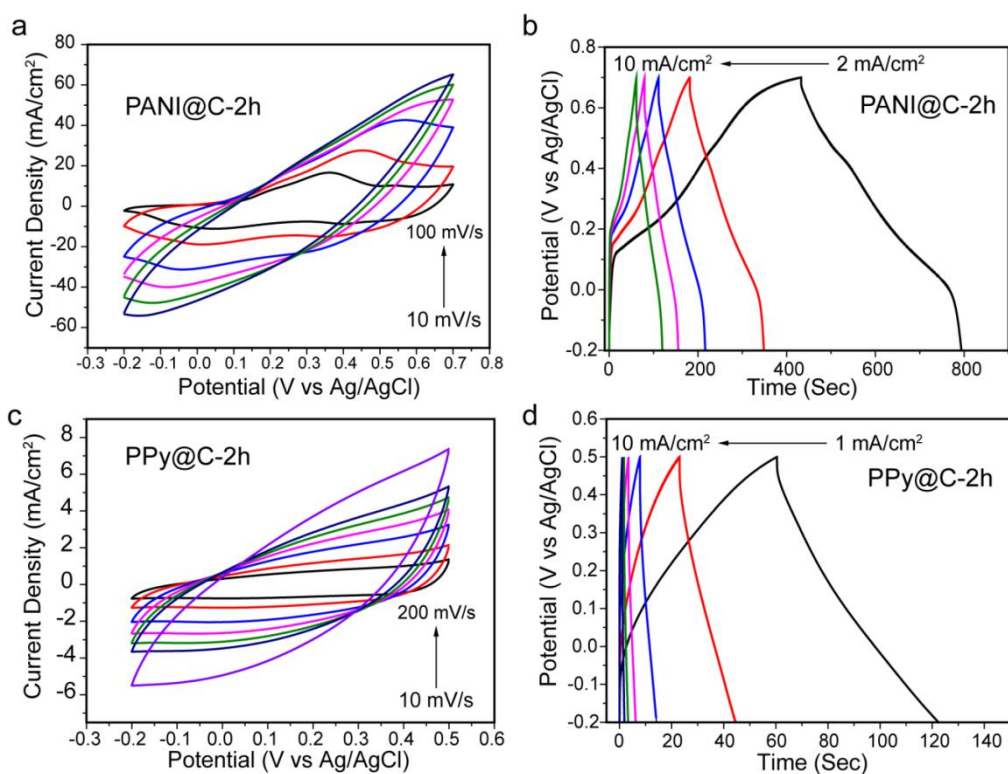


Figure 6.10 (a, b) CV curves collected at various scan rates for (a) PANI@C-2h and (b) PPy@C-2h. (c, d) CP curves collected at various current densities for (c) PANI@C-2h and (d) PPy@C-2h.

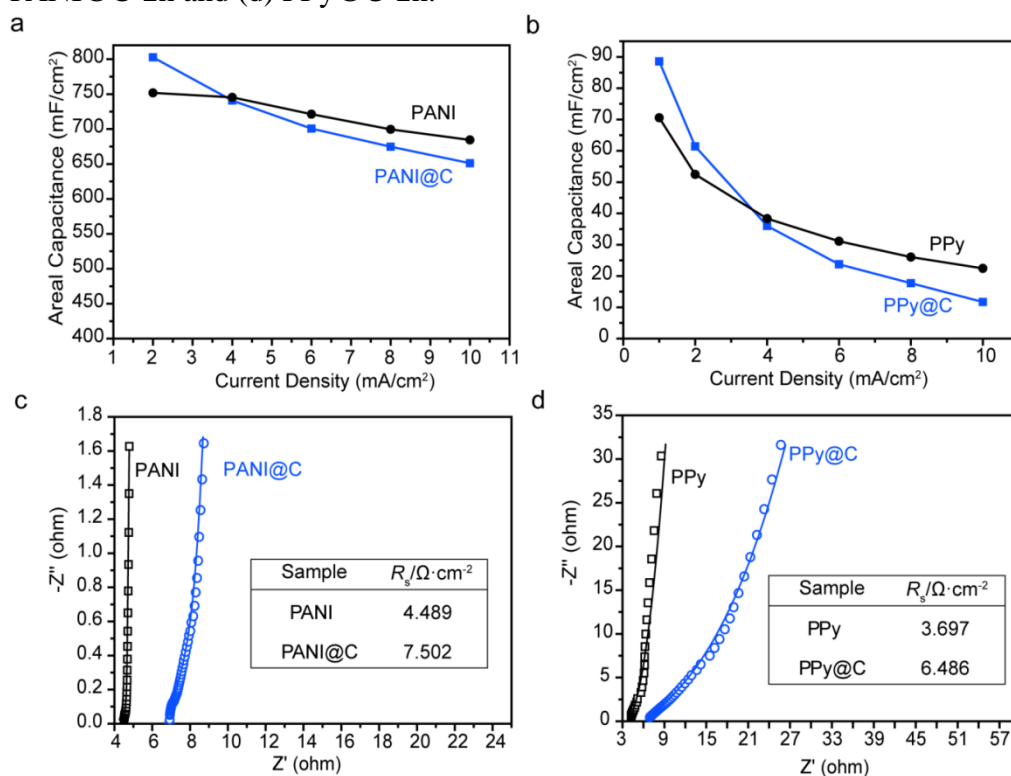


Figure 6.11 (a, b) Areal capacitance of bare polymer electrodes and carbonaceous

shell coated polymer electrodes collected at different current densities. (c, d) Nyquist plots of polymer electrodes and carbonaceous shell coated polymer electrodes measured in 1 M H₂SO₄ at open circuit potential with an amplification of 5 mV. Insets show the R_s values of the electrodes.

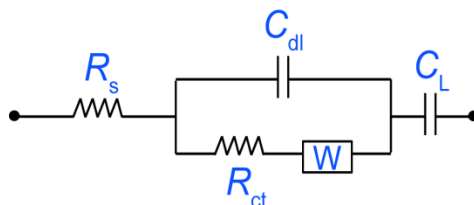


Figure 6.12 Equivalent circuit model used for EIS data fitting. (R_s : combined series resistance; R_{ct} : charge-transfer resistance; W : Warburg element; C_{dl} : electrical-double-layer capacitance; C_L : limit capacitance.)

Table 6.1 Parameters of equivalent circuit elements

Sample	$R_s/\Omega \cdot \text{cm}^{-2}$	$R_{ct}/\Omega \cdot \text{cm}^{-2}$	$W/\Omega \cdot \text{s}^{-0.5}$	$C_{dl}/\text{mF} \cdot \text{cm}^{-2}$	$C_L/\text{mF} \cdot \text{cm}^{-2}$
PANI	4.489	0.1001	0.2428	11.16	936.4
PANI@C	7.052	0.5057	2.418	13.262	957.6
PPy	3.697	0.09698	6.835	0.6879	50.35
PPy@C	6.486	0.4984	11.10	0.7765	83.72

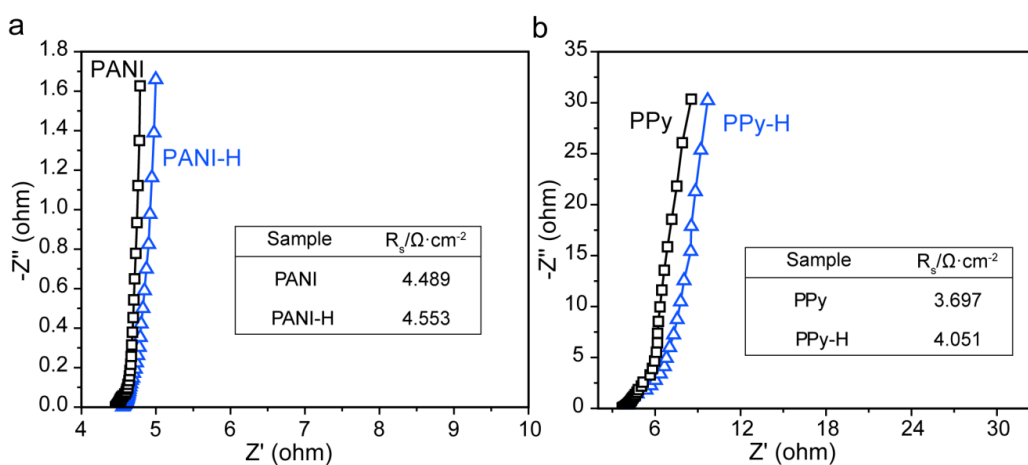


Figure 6.13 (a, b) Nyquist plots collected for polymer electrodes before and after hydrothermal treatment in the absence of glucose precursor, in 1 M H₂SO₄ at open

circuit potential with an amplification of 5 mV. Insets show the R_s values of the electrodes.

6.4 Conclusions

In summary, we have demonstrated, for the first time, the deposition of a thin carbonaceous shell (~5 nm) onto PANI and PPy can effectively improve their charge/discharge cycling stability. The carbonaceous shell coated PANI and PPy electrodes exhibited exceptionally high capacitance retentions of ~95% and ~85% after 10000 cycles, which are significantly improved compared to the retention rate of bare PANI (~20%) and PPy (~25%) obtained under the same conditions. Importantly, the carbonaceous shell coated polymer electrodes also exhibit comparable capacitance and rate capability as bare polymer electrodes, indicating the incorporation of a 5 nm thick carbonaceous shell have no obvious negative effect on their electrochemical performance. We believe this is a general strategy that can be further extended to other pseudocapacitive polymer electrodes. The successful stabilization of polymer electrodes could revolutionize the design, fabrication and applications of polymer based pseudo-capacitors.

References

1. Wang, G.; Lu, X.; Ling, Y.; Zhai, T.; Wang, H.; Tong, Y.; Li, Y. *ACS Nano* **2012**, *11*, 10296-10302.
2. Zheng, L.; Xu, Y.; Jin, D.; Xie, Y. *Chem.-Asian J.* **2011**, *6*, 1505-1514.
3. Xiao, X.; Ding, T.; Yuan, L.; Shen, Y.; Zhong, Q.; Zhang, X.; Cao, Y.; Hu, B.; Zhai, T.; Gong, L.; Chen, J.; Tong, Y.; Zhou, J.; Wang, Z. L. *Adv. Energy Mater.*

2012, 2, 1328-1332.

4. Pan, L.; Yu, G.; Zhai, D.; Lee, H. R.; Zhao, W.; Liu, N.; Wang, H.; Tee, B. C.-K.; Shi, Y.; Cui, Y.; Bao, Z. *PNAS* **2012**, 109, 9287-9292.

5. Yu, G.; Xie, X.; Pan, L.; Bao, Z.; Cui, Y. *Nano Energy* **2013**, 2, 213-234.

6. Wang, D.-W.; Li, F.; Zhao, J.; Ren, W.; Chen, Z.-G.; Tan, J.; Wu, Z.-S.; Gentle, I.; Lu, G. Q.; Cheng, H.-M. *ACS Nano* **2009**, 3, 1745-1752.

7. Peng, X.; Huo, K.; Fu, J.; Zhang, X.; Gao, B.; Chu, P. K. *Chem. Commun.* **2013**, 49, 10172.

8. Wang, G.; Zhang, L.; Zhang, J. *Chem. Soc. Rev.* **2012**, 41, 797-828.

9. Yu, G.; Hu, L.; Liu, N.; Wang, H.; Vosgueritchian, M.; Yang, Y.; Cui, Y.; Bao, Z. *Nano Lett.* **2011**, 11, 4438-4442.

10. Zhou, C.; Zhang, Y.; Li, Y.; Liu, J. *Nano Lett.* **2013**, 13, 2078-2085.

11. Snook, G. A.; Kao, P.; Best, A. S. *J. Power Sources* **2011**, 196, 1-12.

12. Hou, Y.; Cheng, Y.; Hobson, T.; Liu, J. *Nano Lett.* **2010**, 10, 2727-2733.

13. Chen, L.; Sun, L.-J.; Luan, F.; Liang, Y.; Li, Y.; Liu, X.-X. *J. Power Sources* **2010**, 195, 3742-3747.

14. Zhang, Q.; Uchaker, E.; Candelaria, S. L.; Cao, G. *Chem. Soc. Rev.* **2013**, 42, 3127-3171.

15. Lu, X.; Yu, M.; Zhai, T.; Wang, G.; Xie, S.; Liu, T.; Liang, C.; Tong, Y.; Li, Y. *Nano Lett.* **2013**, 13, 2628-2633.

16. Zhao, Y.; Liu, B.; Pan, L.; Yu, G. *Energy Environ. Sci.* **2013**, 6, 2856-2870.

17. Meng, C.; Liu, C.; Chen, L.; Hu, C.; Fan, S. *Nano Lett.* **2010**, *10*, 4025-4031.
18. Zhang, G.; Lou, X. W. D. *Adv. Mater.* **2013**, *25*, 976-979.
19. Cong, H.-P.; Ren, X.-C.; Wang, P.; Yu, S.-H. *Energy Environ. Sci.* **2013**, *6*, 1185-1191.
20. Liu, C.; Yu, Z.; Neff, D.; Zhamu, A.; Jang, B. Z. *Nano Lett.* **2010**, *10*, 4863-4868.
21. Wang, Y.; Tao, S.; An, Y.; Wu, S.; Meng, C. *J. Mater. Chem. A* **2013**, *1*, 8876-8887.
22. Fu, H.; Du, Z.-j.; Zou, W.; Lia, H.-q.; Zhang, C. *J. Mater. Chem. A* **2013**, *1*, 14943-14950.
23. Zhang, J.; Zhao, X. S. *J. Phys. Chem. C* **2012**, *116*, 5420-5426.
24. Xie, K.; Li, J.; Lai, Y.; Zhang, Z. a.; Liu, Y.; Zhang, G.; Huang, H. *Nanoscale* **2011**, *3*, 2202-2207.
25. Kim, B. C.; Kwon, J. S.; Ko, J. M.; Park, J. H.; Too, C. O.; Wallace, G. G. *Synthetic Met.* **2010**, *160*, 94-98.
26. Kumar, A.; Singh, R. K.; Singh, H. K.; Srivastava, P.; Singh, R. *J. Power Sources* **2014**, *246*, 800-807.
27. Chen, S.; Zhitomirsky, I. *J. Power Sources* **2013**, *243*, 865-871.
28. Shi, K.; Zhitomirsky, I. *J. Power Sources* **2013**, *240*, 42-49.
29. Fan, W.; Zhang, C.; Tjiu, W. W.; Pramoda, K. P.; He, C.; Liu, T. *ACS Appl. Mater. Inter.* **2013**, *5*, 3382-3391.

30. Cho, S.; Shin, K.-H.; Jang, J. *ACS Appl. Mater. Inter.* **2013**, *5*, 9186-9193.
31. Biswas, S.; Drzal, L. T. *Chem. Mater.* **2010**, *22*, 5667-5671.
32. Bian, L.-J.; Luan, F.; Liu, S.-S.; Liu, X.-X. *Electrochim. Acta* **2012**, *64*, 17-22.
33. Wang, Z.-L.; Guo, R.; Ding, L.-X.; Tong, Y.-X.; Li, G.-R. *Sci. Rep.* **2013**, *3*.
34. Fan, L.-Z.; Maier, J. *Electrochem. Commun.* **2006**, *8*, 937-940.
35. Weng, Y.-T.; Wu, N.-L. *Chem. Commun.* **2013**, *49*, 10784-10786.
36. Wang, W.; Li, P.; Fu, Y.; Ma, X. *J. Power Sources* **2013**, *238*, 464-468.
37. Koltypin, M.; Pol, V.; Gedanken, A.; Aurbach, D. *J. Electrochem. Soc.* **2007**, *154*, A605-A613.
38. Zou, B.-X.; Liang, Y.; Liu, X.-X.; Diamond, D.; Lau, K.-T. *J. Power Sources* **2011**, *196*, 4842-4848.
39. Al-Mashat, L.; Debiemme-Chouvy, C.; Borensztajn, S.; Wlodarski, W. *J. Phys. Chem. C* **2012**, *116*, 13388-13394.
40. Zhang, L.; Zhang, G.; Wu, H. B.; Yu, L.; Lou, X. W. D. *Adv. Mater.* **2013**, *25*, 2589-2593.
41. Zheng, H.; Zhai, T.; Yu, M.; Xie, S.; Liang, C.; Zhao, W.; Wang, S. C. I.; Zhang, Z.; Lu, X. *J. Mater. Chem. C* **2013**, *1*, 225-229.
42. Lu, X.; Liu, T.; Zhai, T.; Wang, G.; Yu, M.; Xie, S.; Ling, Y.; Liang, C.; Tong, Y.; Li, Y. *Adv. Energy Mater.* **2013**.
43. Patwardhan, P. R.; Satrio, J. A.; Brown, R. C.; Shanks, B. H. *J. Anal. Appl. Pyrolysis* **2009**, *86*, 323-330.

44. Ardizzone, S.; Fregonara, G.; Trasatti, S. *Electrochim. Acta* **1990**, *35*, 263-267.

45. Duay, J.; Sherrill, S. A.; Gui, Z.; Gillette, E.; Lee, S. B. *ACS Nano* **2013**, *7*, 1200-1214.

Chapter 7

Pushing the Cycling Stability Limit of Polypyrrole for Supercapacitors

Abstract

Polypyrrole (PPy) is a promising pseudocapacitive material for supercapacitor electrodes. However, its poor cycling stability is the major hurdle for its practical applications. Here we demonstrate a two-prong strategy to stabilize PPy film by growing it on a functionalized partial-exfoliated graphite (FEG) substrate and doping it with β -naphthalene sulfonate anions (NS^-). The PPy electrode achieved a remarkable capacitance retention rate of 97.5% after cycling between -0.8 and 0 V vs. SCE for 10000 cycles. Moreover, an asymmetric pseudo-capacitor using the stabilized PPy film as anode also retained 97% of capacitance after 10000 cycles, which is the best value reported for PPy based supercapacitors. The exceptional stability of PPy electrode can be attributed to two factors: 1) the flexible nature of FEG substrate accommodates large volumetric deformation and 2) the presence of immobile NS^- dopants suppress the counterion drain effect during charge-discharge cycling.

7.1 Introductions

Polypyrrole (PPy) is a promising pseudo-capacitor electrode material due to its low cost, low environmental toxicity, high electrical conductivity ($\sim 100 - 10000 \text{ S m}^{-1}$), wide potential window and ease of fabrication.¹⁻⁵ However, these advantages are offset by its very poor cycling stability (usually $< 50\%$ capacitance

retention after 1000 charge-discharge cycles in aqueous electrolytes).^{1,2,6,7} The charge/discharge cycling instability of PPy is mainly due to structural pulverization and counterion drain effect.^{1,2,6,8} Upon oxidation, positive charged nitrogen groups (polarons) are generated on PPy chains. To balance the charge, counterions in the electrolyte will diffuse into the backbone of PPy chains, causing PPy to swell. Upon reduction, polarons are neutralized by the injected electrons. Meanwhile, counterions diffuse back into electrolyte in order to maintain the neutrality of the PPy matrix, which subsequently causes PPy backbone to shrink.⁸⁻¹⁰ The repeated swelling and shrinking of PPy chains leads to structural pulverization, resulting the loss of active materials. Moreover, PPy also suffers from counterion drain effect, *i.e.*, less and less anions can dope into the PPy matrix after repeated charge and discharge cycling due to the irreversible insertion/extrusion of counterions.^{4,6,9-11} For instance, when anions diffuse back into electrolyte during reduction, some of the ion channels of PPy will collapse and form a compact structure. Re-oxidation of the PPy chains requires extra energy to re-open the compact structure,⁶ making anions more difficult to re-dope the PPy backbone. As a result, less polarons can be re-generated. Since the electrical conductivity of PPy is directly proportional to the number of polarons on the backbone of PPy chains,¹⁰ the counterion drain effect will slowly reduce the electrical conductivity of PPy, and hence, the capacitance.

Enormous efforts have been made to stabilize PPy-based materials for

pseudo-capacitors.^{1,3,4,12-17} One of the strategies is integrating PPy into flexible substrates/current collectors such as reduced graphene oxide^{13,14,18-20} and carbon nanotubes.²¹ Flexible substrates can accommodate large volumetric change of PPy during charge and discharge, and thus, effectively suppress structural pulverization of PPy. Our previous work showed that PPy anchored on partially exfoliated graphene substrate retains as high as 91% of its initial capacitance after 1000 cycles in 3 M KCl aqueous electrolyte.² Another strategy is to dope PPy with special anionic dopants. For example, PPy doped with Tiron¹⁵ and sulfanilic acid azochromotrop¹⁶ achieved excellent capacitance retention rate of 93.1% and 91.5% after 1000 charge-discharge cycles, respectively. It was believed that the hydroxyl groups in the dopants behave as chelating agents and form dative covalent bonds with the Ni current collector, thus improving adhesion of PPy film.^{15,16} However, the stability of these PPy electrodes is still far below the satisfactory level for commercial applications. And there is no report on how to simultaneously address the structural pulverization and counterion drain effect.

Here we demonstrate for the first time to improve the cycling stability of PPy by addressing both the structural pulverization and counterion drain effect. A functionalized partial-exfoliated graphite substrate (FEG) was synthesized by a two-step partial exfoliation method reported previously.²² We deposit PPy onto FEG substrate, and simultaneously dope the PPy film by β -naphthalene sulfonate anions (NS⁻) with high steric hindrance and low mobility²³ within the polymer

matrix to suppress counterion drain effect. The electrode exhibited excellent cycling stability with 97.5% of the capacitance can be retained after 10000 consecutive charge-discharge cycles in a negative potential window between 0 and -0.8 V vs. saturated calomel electrode (SCE). Moreover, an asymmetric pseudo-capacitor device composed of the stabilized PPy anode and FEG supported MnO₂ nanosheet (FEG/MnO₂) cathode showed remarkable cycling stability with only 3% capacitance loss after 10000 cycles. To our knowledge, this is the best capacitance retention rate ever achieved for PPy-based pseudo-capacitor devices.

7.2 Experimental Section

Materials: All the chemicals were purchased from Sinopharm Chemical Reagent Co., Ltd. (P. R. China) and used as received except pyrrole which was used after reduced pressure distillation (*ca.* 80 kPa, 110 °C, 40 min). Cellulose separators were purchased from Nippon Kodoshi Corporation (Japan) and used as received. Graphite foils are purchased from SGL group (Germany).

Preparation of functionalized partial-exfoliated graphite substrates (FEG) and FEG/MnO₂ electrode: FEG substrates were prepared by a two-step exfoliation method reported elsewhere.²² A piece of graphite foil was used as a working electrode in a three-electrode electrochemical cell with SCE reference electrode (0.2444 V vs. standard hydrogen electrode) and Pt plate as counter electrode. The graphite electrode was scanned between 0.5 V and 1.8 V vs. SCE at

20 mV s⁻¹ in 0.5 M K₂CO₃ aqueous solution (pH=11.8) for six cycles. The electrode was then further scanned for another ten cycles in a phosphate buffered saline containing 1 M KNO₃ (pH = 6.7) between -1.0 V and 1.9 V vs. SCE at 20 mV s⁻¹. In each cycle, the electrode was kept at 1.9 V vs. SCE for 5 s. Last, the electrode was washed with ethanol and deionized water to remove inorganic residuals on the surface. For preparing FEG supported MnO₂ electrode, MnO₂ nanosheets were deposited on the FEG substrate at a constant current density of 0.2 mA cm⁻² for 35 min at ambient conditions in an aqueous solution containing 0.01 M manganese acetate and 0.02 M ammonium acetate.

Electro-polymerization of pyrrole: PPy film doped with β -naphthalene sulfonic anions was electrochemically deposited on FEG substrate through electro-polymerization in a solution of 0.1 M pyrrole and 0.05 M β -naphthalene sulfonic acid at 2 mA cm⁻² for 6 min. The electrode is denoted as FEG/PPy-NS. For comparison, PPy films doped with sulfate ions, a smaller anion contains the same sulfonic acid group as NS⁻ (Figure 7.1), were prepared by electro-polymerization on FEG (denoted as FEG/PPy-S) and graphite foils (denoted as PPy-S) in a 0.1 M pyrrole and 0.05 M H₂SO₄ aqueous solution at 2 mA cm⁻² as control samples. After electro-deposition, the electrodes were washed with ethanol and deionized water. The mass loading was calculated based on the weight difference between the dried electrodes (vacuum dried at 60 °C for 24 h) before and after electro-deposition, using a Sartorius BT 25 S semi-microbalance

with a sensitivity of 0.01 mg. The mass loadings of PPy for the aforementioned three electrodes were adjusted to the same amount ($0.56 \pm 0.01 \text{ mg cm}^{-2}$) by controlling the time of electro-deposition. PPy-S electrodes with reduced mass loading of $0.12 \pm 0.01 \text{ mg cm}^{-2}$ were produced by the same condition as PPy-S except the electrodeposition time was reduced from 15 min to 2 min.

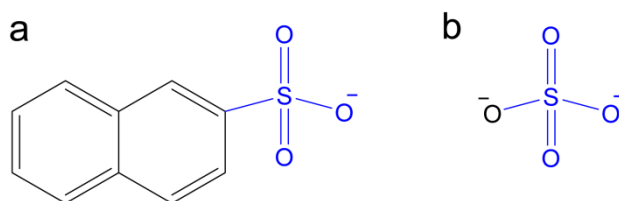


Figure 7.1 Molecular structure of (a) β -naphthalene sulfonate anion and (b) sulfate anion. The same sulfonic acid groups are in blue.

Assembly of FEG/PPy-NS//FEG/MnO₂ asymmetric pseudo-capacitor device:

The asymmetric pseudo-capacitor device was assembled using FEG/PPy-NS (working area $1 \times 1 \text{ cm}^2$) as anode and FEG/MnO₂ (working area $1 \times 1 \text{ cm}^2$) as cathode. The mass loading of anode ($0.56 \pm 0.01 \text{ mg cm}^{-2}$) and cathode ($0.23 \pm 0.01 \text{ mg cm}^{-2}$) were adjusted to balance the charge on both sides. A piece of cellulose paper was used to separate the two electrodes.

Characterizations: Morphologies of the electrodes were investigated by scanning electron microscopy (SEM, Ultra Plus, Carl Zeiss, Germany). Energy-dispersive spectroscopy (EDS, Ultra Plus, Carl Zeiss, Germany) measurements were performed to determine the elements of the synthesized electrodes. X-ray photoelectron spectroscopy (XPS) measurements were performed on a XPS spectrometer (ESCALAB 250Xi, Thermo Scientific Escalab, USA) with Al K_{α}

radiation ($\lambda=8.34 \text{ \AA}$) as the excitation source. The binding energies of peaks were calibrated using the C 1s photoelectron peak at 284.6 eV as reference. Electrochemical measurements were conducted in a three-electrode electrochemical reactor using a multichannel electrochemical analyzer (VMP3, Bio-Logic-Science Instruments, France). PPy-S, FEG/PPy-S and FEG/PPy-NS electrodes (working area: 1 cm^2) were used as working electrodes, with a Pt plate as the counter electrode and a SCE electrode as the reference electrode. Cyclic voltammetry (CV) and galvanostatic charge/discharge data were collected in 3 M KCl aqueous electrolyte. Electrochemical impedance spectroscopy (EIS) was performed at open-circuit potential from 20 kHz to 50 mHz with a perturbation of 10 mV in 3 M KCl aqueous electrolyte. Electrochemical cycling stability of the electrode and the device was tested by galvanostatic charge/discharge cycling measurements for 10000 cycles in 3 M KCl aqueous electrolyte.

7.3 Results and Discussions

Improvement of cycling stability of PPy film

The electrochemical performance of the three electrodes was tested in a three-electrode system. As shown in Figure 7.2a, all three electrodes exhibited a pair of broad redox peaks corresponding to pseudocapacitive reactions (insertion and extrusion of counterions).^{24,25} The FEG/PPy-NS and FEG/PPy-S electrodes have comparable pseudocapacitive behavior, rate capability (Figure 7.3) and specific capacitances (338 F g^{-1} and 326 F g^{-1} @ 50 mV s^{-1} , respectively). Their

specific capacitances are substantially higher than that of PPy-S (130 F g^{-1} @ 50 mV s^{-1}). The enhanced capacitance of FEG/PPy-S and FEG/PPy-NS can be ascribed to the increased surface area after electrochemical treatment²² (Figure 7.4). While the addition of NS⁻ doping has limited effect on the capacitance of PPy film, it significantly improve the cycling stability of PPy film. Figure 7.2b compares the electrochemical cycling stability of the three electrodes tested by galvanostatic charge/discharge cycling method for 10000 cycles. FEG/PPy-NS showed the best cycling stability with an excellent capacitance retention rate of 97.5% after 10000 cycles. The initial increase in capacitance is believed to be due to the electro-activation process. At the beginning, the electrolyte may not contact all the accessible surface of the electrode. During electro-activation process, the contact between electrode and electrolyte solution gradually improved and hence the capacitance was slightly increased. The similar observation has been reported by others.³ On the contrary, the FEG/PPy-S and PPy-S electrodes only retained 82.6% and 46.8% of their initial capacitances, respectively.

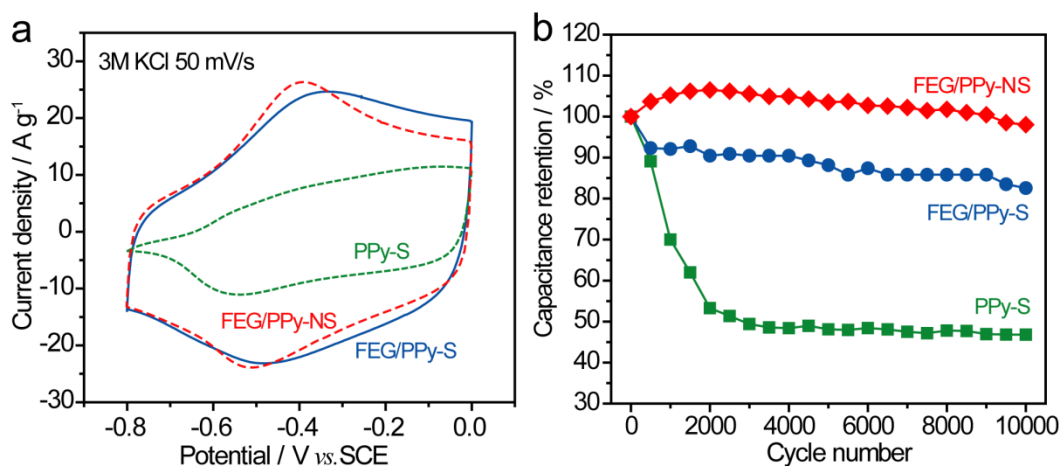


Figure 7.2 (a) Cyclic voltammograms of PPy-S, FEG/PPy-S and FEG/PPy-NS collected at a scan rate of 50 mV s⁻¹ in 3 M KCl electrolyte solution; (b) Electrochemical cycling stability of PPy-S, FEG/PPy-S and FEG/PPy-NS measured by galvanostatic charge/discharge cycling between -0.8 and 0 V vs. SCE at a current density of 4 mA cm⁻² in 3 M KCl electrolyte solution.

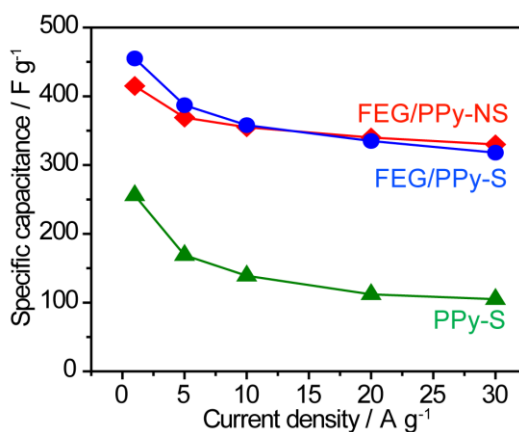


Figure 7.3 Rate capability curves collected for PPy-S, FEG/PPy-S and FEG/PPy-NS in 3 M KCl aqueous electrolyte.

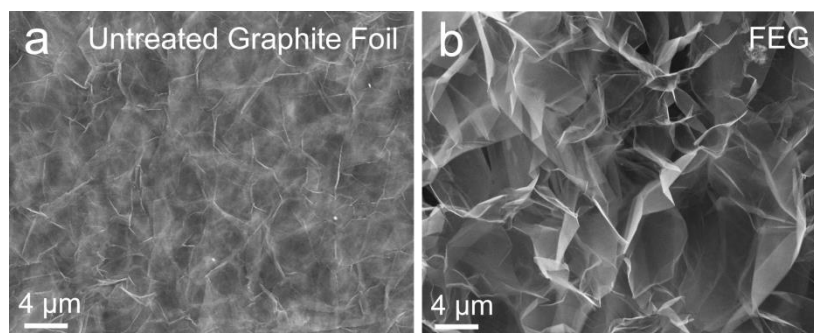


Figure 7.4 SEM image of (a) untreated graphite foil and (b) FEG.

Mechanism of stability enhancement

To understand the possible mechanisms leading to the exceptional stability of FEG/PPy-NS electrode, we performed the following experiments. First, SEM images were collected for the three electrodes before and after the cycling test. PPy-S film on graphite foil showed many cracks and started to peel off from the substrate after testing for 10000 cycles (Figure 7.5a). These cracks were formed as a result of structural pulverization due to the repeated volumetric swelling and shrinking. It correlates with the rapid capacitance degradation of PPy-S. In contrast, the morphology of FEG/PPy-S and FEG/PPy-NS electrodes remained unchanged after 10000 cycles (Figure 7.5c and 7.5d). The enhanced cycling stability can be ascribed to the mechanically flexible nature of the FEG substrate. It has been reported that flexible substrates can accommodate large volumetric expansion and so alleviate structural pulverization and improve the stability of PPy.^{1,21,25,26} Additionally, the reduced thickness of PPy film could also be responsible for the improved cycling stability since thin film is less bulky and the volumetric deformation is less drastic compared to thick film. To test this hypothesis, we have measured the cycling stability of PPy-S electrode with reduced film thickness (*ca.* 150-200 nm, comparable to the film thickness of FEG/PPy-S and FEG/PPy-NS), which was prepared in the same conditions as other PPy-S electrodes except the electrodeposition time is reduced from 15 min to 2 min. Figure 7.6 shows the cycling stability data of the thin PPy-S film. Indeed, the thin film electrode exhibits improved cycling stability compared to the

electrode with thick PPy-S film, with capacitance retention of 76.5% after 10000 cycles. While this value is still smaller than the retention rate of PPy-NS film (97.5%) or PPy-S film (82.6%) supported on FEG, the results suggest that reducing PPy film thickness is beneficial for achieving high cycling stability using flexible substrates. However, the improved stability of PPy-S electrode with reduced film thickness is at the cost of mass loading. In fact, the data again suggests that using FEG substrate with large surface area and flexibility is more favorable because it can improve the cycling stability of PPy film at high mass loading.

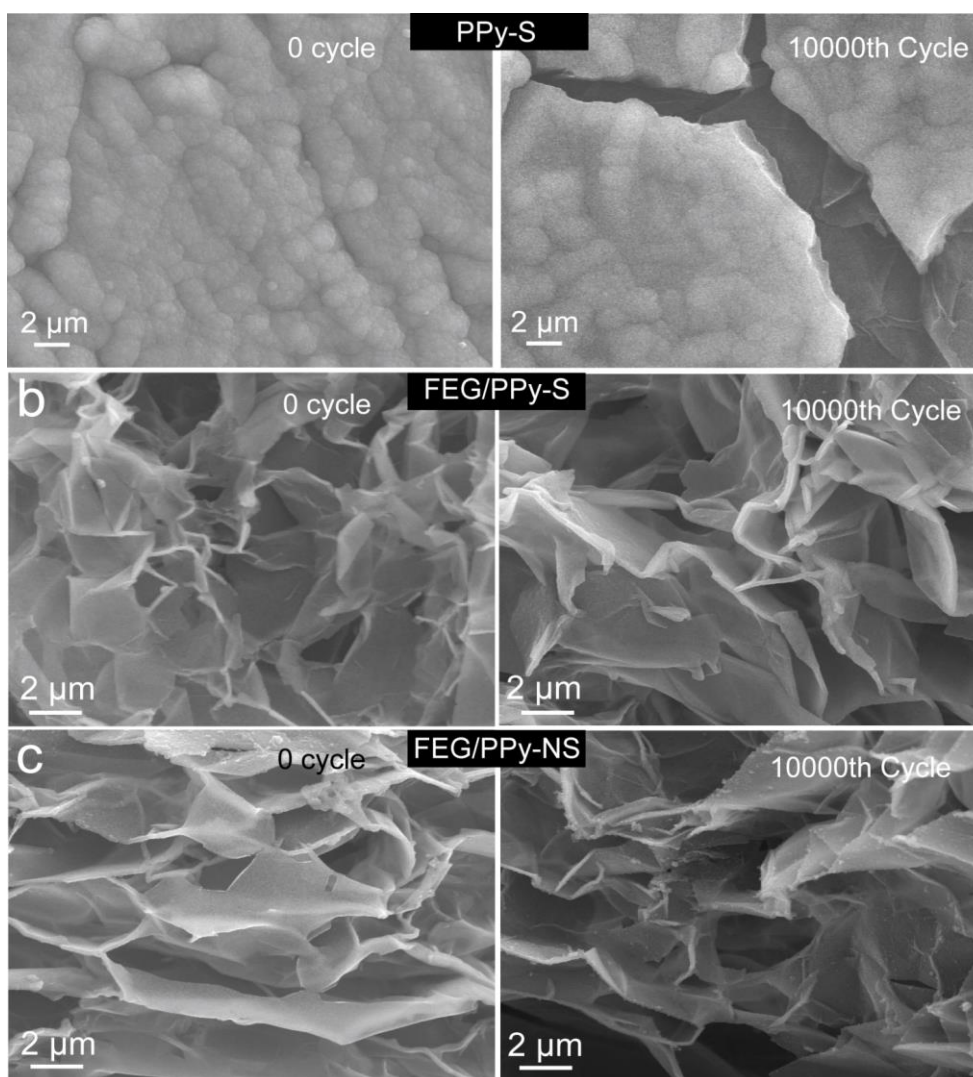


Figure 7.5 SEM images of (a) PPy-S, (b) FEG/PPy-S and (c) FEG/PPy-NS collected before and after testing 10000 cycles.

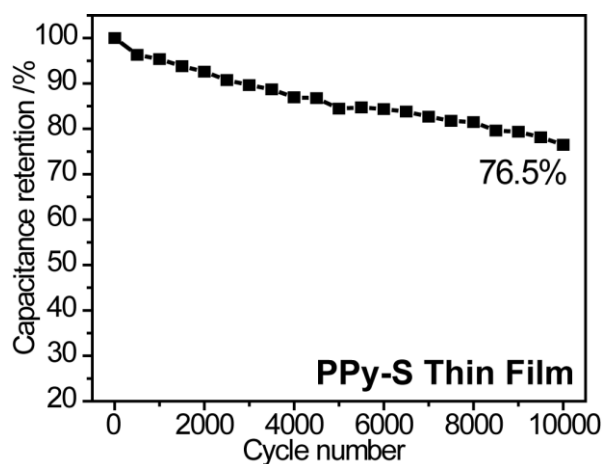


Figure 7.6 Cycling stability of PPy-S thin film electrode collected in 3 M KCl using galvanostatic charge/discharge.

To explain the difference of cycling stability between FEG/PPy-NS and FEG/PPy-S samples, we further collected EDS and XPS spectra for the two electrodes. Both EDS (Figure 7.7a) and XPS (Figure 7.8) data confirm the presence of S signal in both sample before cycling test, suggesting the successful doping of sulfate ions into the FEG/PPy-S electrode and NS⁻ into the FEG/PPy-NS electrode. Notably, the S signal of FEG/PPy-S almost disappeared after testing for 10000 cycles. This is believed to be due to the loss of sulfate ions caused by the counterion drain effect, which is consistent with the previous reports on PPy electrodes.^{6,8,24} On the contrary, there was no obvious decay of S signal in the FEG/PPy-NS sample after cycling stability test (Figure 7.7b). Apparently the introduction of NS⁻ doping can minimize the counterion drain effect, which has never been reported before. It is known that the mobility of anions in PPy structure is inversely proportional to their sizes.²⁴ In comparison to sulfate ions, we believe that NS⁻ anions are less likely to leave the backbone of PPy chain during redox processes due to its large molecular size and the strong π - π interactions between benzene rings of NS⁻ and pyrrole rings of PPy. As a result, the NS⁻ doped PPy suppresses counterion drain effect and retains excellent electrical conductivity during cycling test, and hence, the excellent capacitance retention rate.

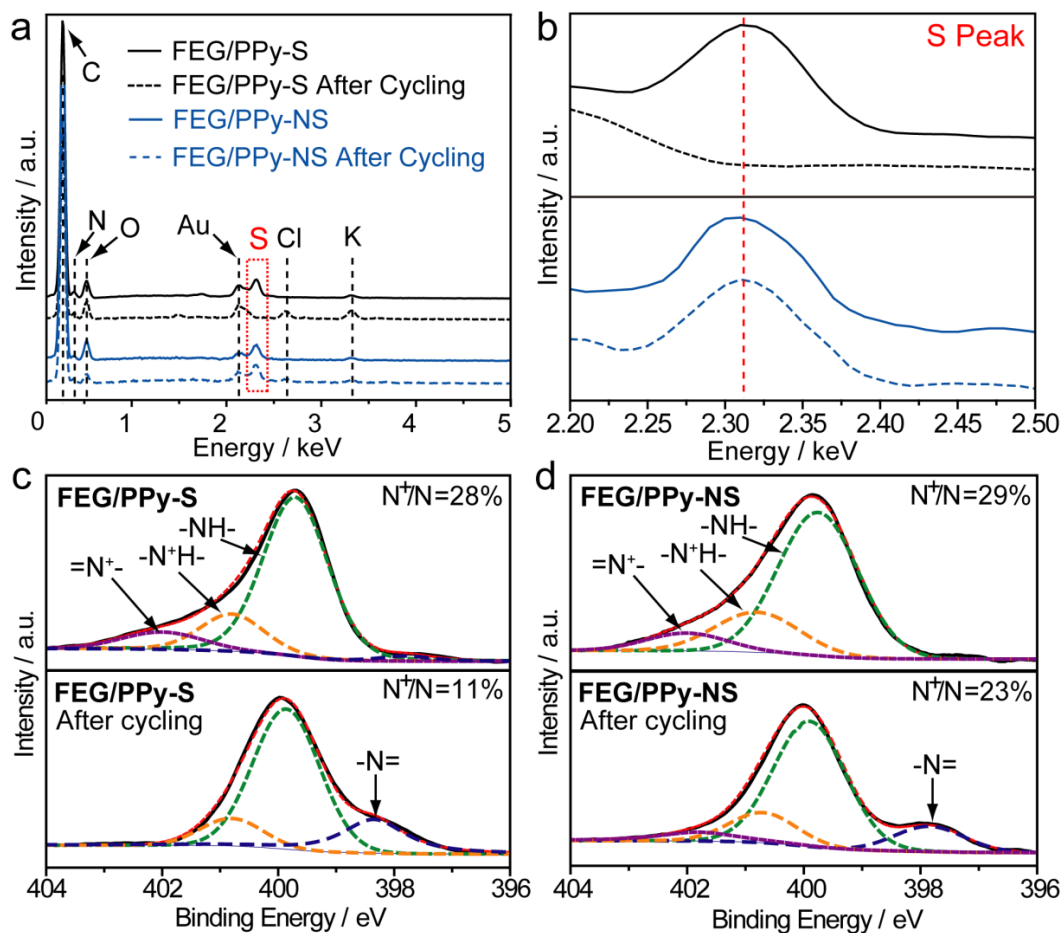


Figure 7.7 (a) EDS spectra and (b) S peak signal collected for FEG/PPy-S and FEG/PPy-NS before and after cycling test; N 1s spectra of (c) FEG/PPy-S and (d) FEG/PPy-NS before and after cycling test.

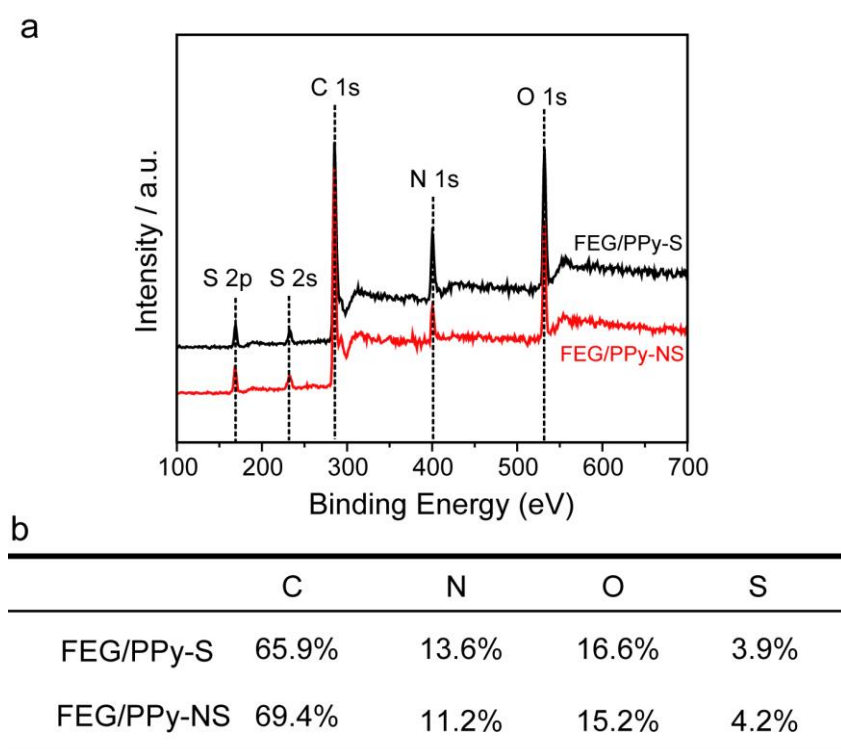


Figure 7.8 (a) XPS survey spectra of FEG/PPy-S and FEG/PPy-NS and (b) element concentrations (atomic percentage) in FEG/PPy-S and FEG/PPy-NS.

We carried out XPS experiments to test our hypothesis. Figure 7.7c and 7.7d show the N 1s core level spectra collected for FEG/PPy-S and FEG/PPy-NS samples before and after the cycling test. Before cycling, the N 1s core level spectra of both sample can be deconvoluted into two synthetic Gaussian peaks centered at 398.3 eV and 399.8 eV respectively, corresponding to -NH- and -N= nitrogen atoms in the backbone of PPy chain.² The high binding energy tail over 400 eV indicates the presence of polarons ($\text{-N}^+=$ and $\text{-N}^+\text{H-}$ cations).^{2,14,27} The synthetic peaks centered at 401.8 eV and 402.2 eV can be assigned to $\text{-N}^+\text{H-}$ cations and $\text{-N}^+=$ cations, respectively. After cycling, as shown in Figure 7.7c, the FEG/PPy-S electrode showed less pronounced high energy tail and much higher -N= signal. The increased amount of -N= is consistent with the previous report

that PPy polarons can be reduced to $-N=$ during reduction.²⁷ The polaron ratio, defined as the areal ratio between the polaron signals ($-N^{+}=$ and $-N^{+}H-$ peaks) and the total nitrogen signal ($-N^{+}=$, $-N^{+}H-$, $-NH-$ and $-N=$ peaks), decreased drastically from 28% to 11%. In contrast, the polaron ratio of FEG/PPy-NS only experienced a small decay from 29% to 23% as less of the $-N^{+}=$ cations were converted to $-N=$. Additionally, C 1s XPS spectra collected for FEG/PPy-S and FEG/PPy-NS before and after the cycling test are comparable (Figure 7.9), indicating the PPy carbon backbone was stable during cycling. XPS results clearly showed that the FEG/PPy-S suffers from the substantial loss of polarons during cycling, while PPy doped with NS^{-} can effectively minimize the counterion drain effect and retain the amount of polarons. It explains why FEG/PPy-NS has the best capacitance retention rate among the three electrodes.

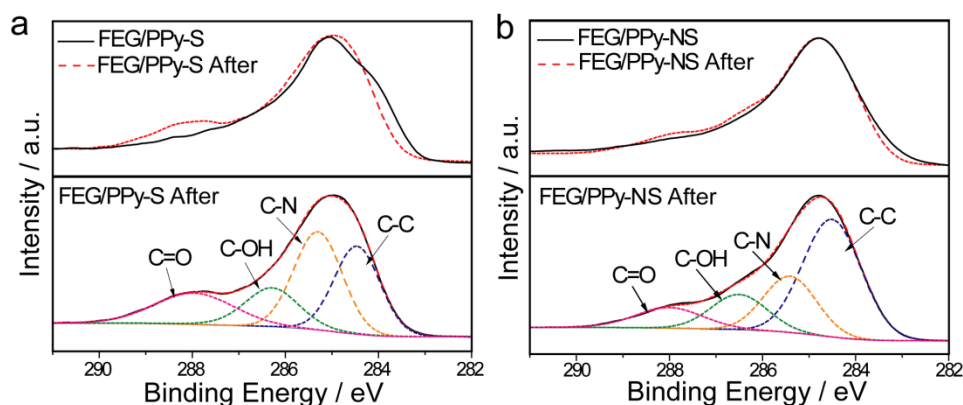


Figure 7.9 C 1s spectra of (a) FEG/PPy-S and (b) FEG/PPy-NS before and after cycling test for 10000 cycles.

Besides EDS and XPS, EIS data (Figure 7.10) exhibited that the charge transfer resistance of both PPy-S and FEG/PPy-S increased substantially after stability test. This is consistent with our hypothesis that the ion doping and

de-doping between electrolyte and electrode become more difficult as the electrical conductivity of electrode decays with the increasing cycle number due to the counter-ion drain effect. FEG/PPy-NS, on the contrary, showed similar EIS profile and charge transfer resistance before and after the cycling stability test. The results again prove that NS^- doping can minimize counterion drain effect of PPy electrode.

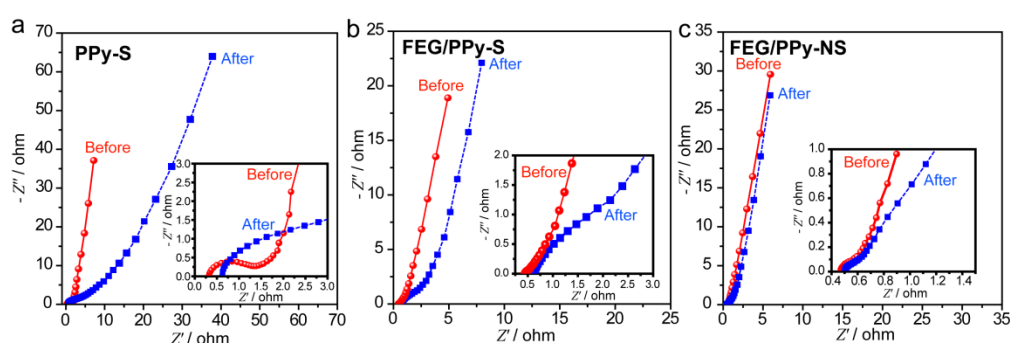


Figure 7.10 EIS spectra of (a) PPy-S, (b) FEG/PPy-S and (c) FEG/PPy-NS before and after cycling stability test in 3 M KCl. Insets show the enlarged middle- and high-frequency domains.

Stability of the asymmetric pseudo-capacitors based on FEG/PPy-NS as anode

The successful demonstration of stable PPy electrode can open up new opportunities for fabrication of pseudocapacitive devices. We assembled an asymmetric pseudo-capacitor device using FEG/PPy-NS as anode and MnO_2 nanostructures supported on FEG substrate (FEG/ MnO_2)²² as cathode (Figure 7.11). The device is denoted as FEG/PPy-NS//FEG- MnO_2 . FEG/ MnO_2 electrode shows excellent specific capacitance within a potential window of 0 ~ 1 V vs. SCE (Figure 7.12a). By coupling the FEG/ MnO_2 cathode and FEG/PPy-NS anode, the

asymmetric device exhibits a stable potential window up to 2 V (Figure 7.12).

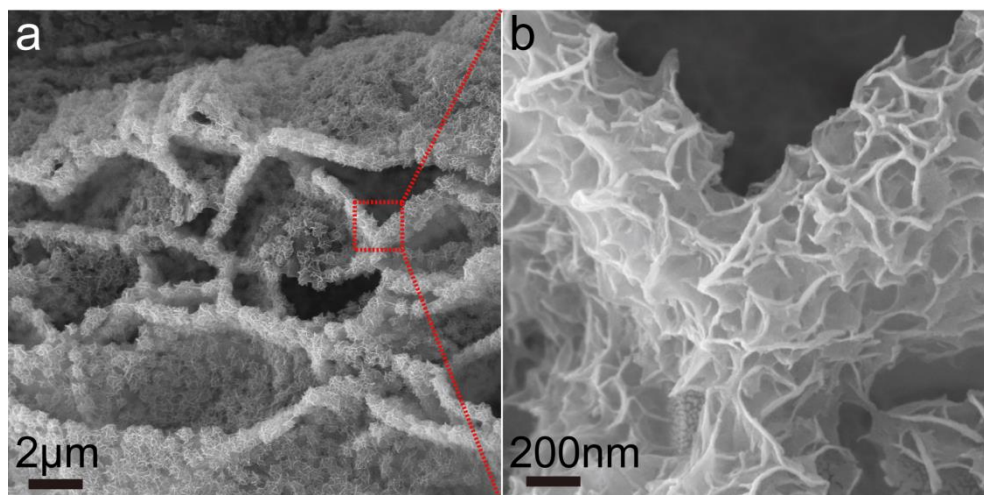


Figure 7.11 (a) SEM image of FEG/MnO₂ and (b) Magnified image of FEG/MnO₂ highlighted in the dashed box in (a).

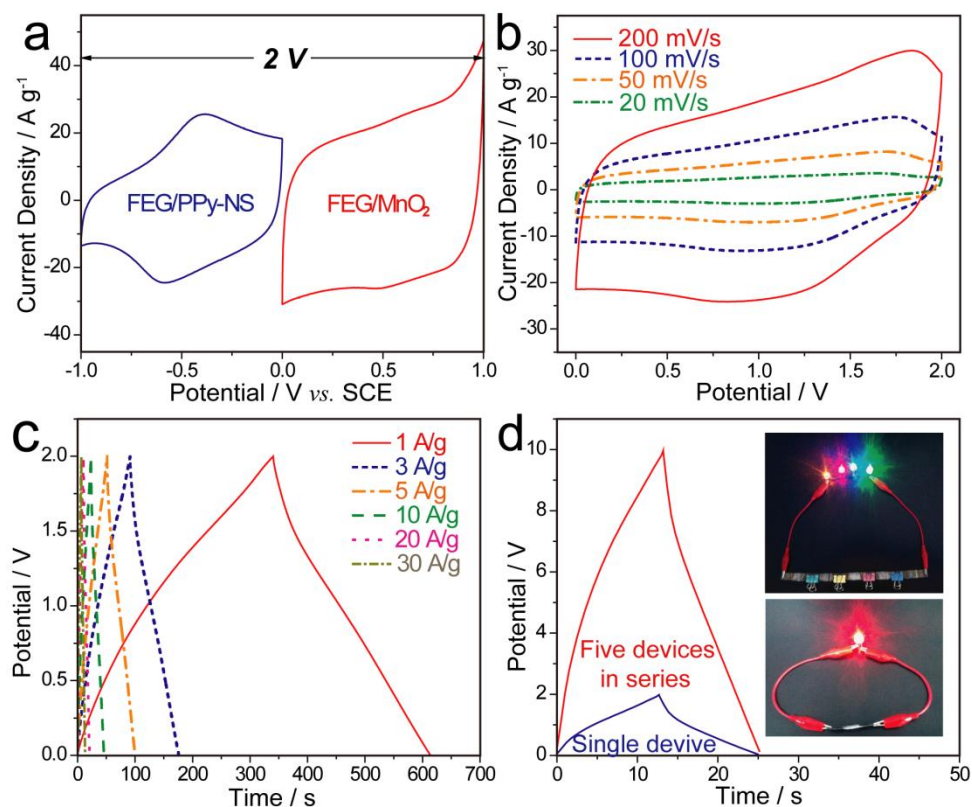


Figure 7.12 (a) CV curves of FEG/PPy-NS and FEG/MnO₂ electrodes collected at 50 mV s⁻¹ in a three-electrode cell; (b) CV curves of the FEG/PPy-NS//FEG/MnO₂ pseudo-capacitor measured at different scan rates; (c) Galvanostatic charge/discharge profiles of the FEG/PPy-NS//FEG/MnO₂

pseudo-capacitor at different current densities; (d) Galvanostatic charge/discharge profiles of a single pseudo-capacitor and five pseudo-capacitors in series collected at a current density of 10 mA cm^{-2} . Insets are digital pictures showing light emitting diodes powered by these pseudo-capacitors.

Significantly, the asymmetric pseudo-capacitor showed an exceptional electrochemical cycling stability with capacitive retention rate of 97% after testing for 10000 galvanostatic charge/discharge cycles at the current density of 6 A g^{-1} . Coulombic efficiency remains almost 100% at all cycles (Figure 7.13a). The initially increased capacitance can be ascribed to the electro-activation process, which has been commonly observed for metal oxide based devices.^{3,28-32} For comparison, the capacitance retention rate of FEG/PPy-S//FEG/MnO₂ and PPy-S//FEG/MnO₂ under the same test conditions were only 78% and 46% respectively (Figure 7.14). It clearly shows that the stable PPy electrode is the key for achieving the outstanding device cycling stability. To our knowledge, the capacitance retention rate obtained from FEG/PPy-NS//FEG/MnO₂ device is the best value reported for PPy-based electrochemical capacitors (Table 7.1). Furthermore, the improved cycling stability is not at the price of electrochemical performance. As shown in Figure 7.13b, FEG/PPy-NS//FEG/MnO₂ device is able to deliver a maximum energy density of 75 Wh kg^{-1} at power density of 1 kW kg^{-1} or 48 Wh kg^{-1} at an ultra-high power density of 50 kW kg^{-1} . These values are among the best values reported for pseudo-capacitor devices using PPy-based anode, such as V₂O₅-PPy//V₂O₅-PPy (53.5 Wh kg^{-1} at 1.2 kW kg^{-1}),³³ GF/CNT/PPy//GF/CNT/MnO₂ (22.2 Wh kg^{-1} at 3.2 kW kg^{-1}),³⁴

$\text{V}_2\text{O}_5\text{-PPy-rGO//V}_2\text{O}_5\text{-PPy-rGO}$ (60.3 Wh kg^{-1} at 0.5 kW kg^{-1}),³⁵ and PPy//3D

MnO_2 (27.2 Wh kg^{-1} at 0.85 kW kg^{-1}).³⁶

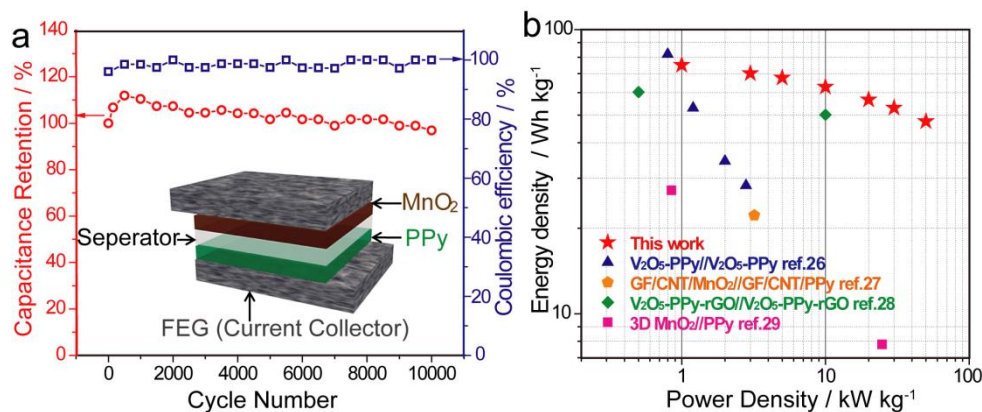


Figure 7.13 (a) Cycling stability and coulombic efficiency of $\text{FEG/PPy-NS//FEG/MnO}_2$ pseudo-capacitor measured by galvanostatic charge/discharge at a current density of 6 A g^{-1} in 3 M KCl aqueous electrolyte. Inset shows the schematic illustration of the $\text{FEG/PPy-NS//FEG/MnO}_2$ asymmetric pseudo-capacitor; (b) Ragone plot of $\text{FEG/PPy-NS//FEG/MnO}_2$ pseudo-capacitor with other reported values for comparison.

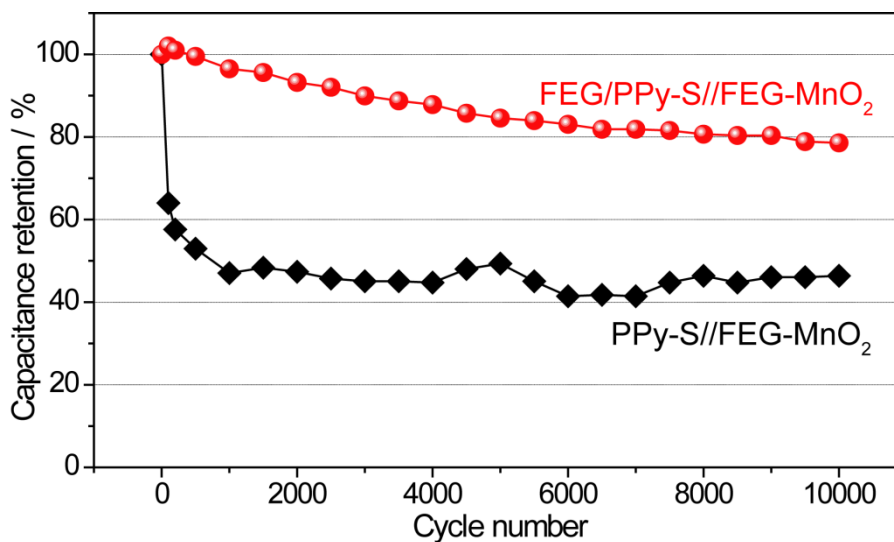


Figure 7.14 Stability performance of PPy-S//FEG/MnO_2 and $\text{FEG/PPy-S//FEG/MnO}_2$ pseudo-capacitors. Test condition: galvanostatic charge-discharge with a current density of 6 A g^{-1} for 10000 cycles.

Table 7.1 Cycling stability of PPy-based pseudo-capacitor devices

Device^{a)}	Electrolyte^{b)}	Current density / Scan rate	Capacitance retention
V ₂ O ₅ -PPy/RGO symmetric ³⁵	PVA/H ₂ SO ₄	10 [A g ⁻¹]	88.1% (5000 cycles)
V ₂ O ₅ -PPy symmetric ³³	PVA/LiCl	9 [mA cm ⁻²]	80% (5000 cycles)
GF/CNTs/PPy//GF/ CNTs/MnO ₂ ³⁴	0.5 M Na ₂ SO ₄	1.5 [mA cm ⁻²]	83.5% (10000 cycles)
PPy@MoO ₃ //AC ³⁷	0.5 M K ₂ SO ₄	0.5 [A g ⁻¹]	83% (600 cycles)
PPy-NPG//MnO ₂ -NP G ³⁸	1 M LiClO ₄	100 [mV s ⁻¹]	85% (2000 cycles)
PPy@cellulose symmetric ²⁵	2 M NaCl	30 [mA cm ⁻²]	84% (8500 cycles)
PPy hydrogel symmetric ³⁹	PVA/H ₂ SO ₄	----- ^{c)}	90% (3000 cycles)
PPy-MWCNT symmetric ⁴⁰	0.5 M Na ₂ SO ₄	20 [mA cm ⁻²]	94.2% (5000 cycles)
BC/PPy/MWCNTs symmetric ⁴¹	2 M LiCl	10 [mA cm ⁻²]	94.5% (5000 cycles)
PPy//MnO ₂ ³⁶	1 M Na ₂ SO ₄	-----	80% (2000 cycles)
WO ₃ @PPy//CF-Co(OH) ₂ ⁴²	3 M NaOH	100 [mV s ⁻¹]	85% (5000 cycles)
FEG/PPy-NS//FEG/ MnO₂ (This work)	3 M KCl	6 [A g⁻¹] (ca. 5 mA cm⁻²)	97% (10000 cycles)

- a) All asymmetric devices are denoted as “anode//cathode”.
- b) PVA: polyvinyl alcohol gel electrolyte
- c) Not reported

7.4 Conclusions

We have demonstrated that the cycling stability of PPy thin film can be greatly improved by preparing PPy film on a functionalized partial-exfoliated graphite substrate and dope the film with β -naphthalene sulfonate anions. The flexible nature of FEG substrate accommodates large volumetric deformation of PPy during repeated charge and discharge processes. β -naphthalene sulfonate anion doping compared to the conventional SO_4^{2-} doping can better minimize the counterion drain effect and retains good electrical conductivity of PPy film. These two factors substantially enhance the cycling stability of PPy. The FEG/PPy-NS electrode exhibited outstanding capacitance retention of 97.5% after 10000 cycles in 3 M KCl aqueous electrolyte, whereas the PPy-S and FEG/PPy-S retain only 46.8% and 82.6% of the capacitance under the same test conditions. Moreover, an asymmetric pseudo-capacitor based on the stabilized FEG/PPy-NS anode showed a remarkable capacitive retention of 97% in aqueous electrolyte, which is the best value achieved for PPy-based electrochemical capacitor device.

References

1. Liu, T.; Finn, L.; Yu, M.; Wang, H.; Zhai, T.; Lu, X.; Tong, Y.; Li, Y. *Nano Lett.* **2014**, *14*, 2522-2527.

2. Song, Y.; Xu, J.; Liu, X. *J. Power Sources* **2014**, *249*, 48-58.
3. Bai, M.; Liu, T.; Luan, F.; Li, Y.; Liu, X. *J. Mater. Chem. A* **2014**, *2*, 10882-10888.
4. Zhao, Y.; Liu, B.; Pan, L.; Yu, G. *Energy Environ. Sci.* **2013**, *6*, 2856-2870.
5. Zhang, W.; Wen, X.; Yang, S. *Langmuir* **2003**, *19*, 4420-4426.
6. Heinze, J.; Frontana-Uribe, B. A.; Ludwigs, S. *Chem. Rev.* **2010**, *110*, 4724-4771.
7. Yu, G.; Xie, X.; Pan, L.; Bao, Z.; Cui, Y. *Nano Energy* **2013**, *2*, 213-234.
8. Otero, T. F.; Martinez, J. G. *Adv. Funct. Mater.* **2013**, *23*, 404-416.
9. Otero, T. F.; Alfaro, M.; Martinez, V.; Perez, M. A.; Martinez, J. G. *Adv. Funct. Mater.* **2013**, *23*, 3929-3940.
10. Otero, T. F.; Martinez, J. G. *Adv. Funct. Mater.* **2014**, *24*, 1259-1264.
11. Meng, C.; Liu, C.; Chen, L.; Hu, C.; Fan, S. *Nano Lett.* **2010**, *10*, 4025-4031.
12. Fan, L.-Z.; Maier, J. *Electrochem. Commun.* **2006**, *8*, 937-940.
13. Biswas, S.; Drzal, L. T. *Chem. Mater.* **2010**, *22*, 5667-5671.
14. Zhang, J.; Zhao, X. S. *J. Phys. Chem. C* **2012**, *116*, 5420-5426.
15. Shi, K.; Zhitomirsky, I. *J. Power Sources* **2013**, *240*, 42-49.
16. Chen, S.; Zhitomirsky, I. *J. Power Sources* **2013**, *243*, 865-871.
17. Wu, Q.; Xu, Y.; Yao, Z.; Liu, A.; Shi, G. *ACS Nano* **2010**, *4*, 1963-1970.
18. Liu, Y.; Wang, H.; Zhou, J.; Bian, L.; Zhu, E.; Hai, J.; Tang, J.; Tang, W. *Electrochim. Acta* **2013**, *112*, 44-52.

19. Weiss, N. O.; Zhou, H.; Liao, L.; Liu, Y.; Jiang, S.; Huang, Y.; Duan, X. *Adv. Mater.* **2012**, *24*, 5782-5825.
20. Bonaccorso, F.; Colombo, L.; Yu, G.; Stoller, M.; Tozzini, V.; Ferrari, A. C.; Ruoff, R. S.; Pellegrini, V. *Science* **2015**, *347*, 1246501-1246501.
21. Fu, H.; Du, Z.; Zou, W.; Li, H.; Zhang, C. *J. Mater. Chem. A* **2013**, *1*, 14943-14950.
22. Song, Y.; Feng, D.; Liu, T.; Li, Y.; Liu, X. *Nanoscale* **2015**, *7*, 3581-3587.
23. Ingram, M. D.; Staesche, H.; Ryder, K. S. *J. Power Sources* **2004**, *129*, 107-112.
24. Weidlich, C.; Mangold, K. M.; Jüttner, K. *Electrochim. Acta* **2005**, *50*, 1547-1552.
25. Wang, Z.; Tammela, P.; Zhang, P.; Strømme, M.; Nyholm, L. *J. Mater. Chem. A* **2014**, *2*, 16761-16769.
26. Zhang, J.; Chen, P.; Oh, B. H. L.; Chan-Park, M. B. *Nanoscale* **2013**, *5*, 9860-9866.
27. Ge, H.; Qi, G.; Kang, E.-T.; Neoh, K. G. *Polymer* **1994**, *35*, 504-508.
28. Lu, X.; Yu, M.; Zhai, T.; Wang, G.; Xie, S.; Liu, T.; Liang, C.; Tong, Y.; Li, Y. *Nano Lett.* **2013**, *13*, 2628-2633.
29. Beidaghi, M.; Wang, C. *Adv. Funct. Mater.* **2012**, *22*, 4501-4510.
30. Jiang, W.; Yu, D.; Zhang, Q.; Goh, K.; Wei, L.; Yong, Y.; Jiang, R.; Wei, J.; Chen, Y. *Adv. Funct. Mater.* **2015**, *25*, 1063-1073.

31. Huang, M.; Zhang, Y.; Li, F.; Zhang, L.; Ruoff, R. S.; Wen, Z.; Liu, Q. *Sci. Rep.* **2014**, *4*.
32. Augustyn, V.; Simon, P.; Dunn, B. *Energy Environ. Sci.* **2014**, *7*, 1597-1614.
33. Bai, M.; Bian, L.; Song, Y.; Liu, X. *ACS Appl. Mater. Inter.* **2014**, *7*, 12656-12664.
34. Liu, J.; Zhang, L.; Wu, H. B.; Lin, J.; Shen, Z.; Lou, X. W. *Energy Environ. Sci.* **2014**, *7*, 3709-3719.
35. Yu, C.; Ma, P.; Zhou, X.; Wang, A.; Qian, T.; Wu, S.; Chen, Q. *ACS Appl. Mater. Inter.* **2014**, *6*, 17937-17943.
36. Grote, F.; Lei, Y. *Nano Energy* **2014**, *10*, 63-70.
37. Liu, Y.; Zhang, B.; Yang, Y.; Chang, Z.; Wen, Z.; Wu, Y. *J. Mater. Chem. A* **2013**, *1*, 13582-13587.
38. Hou, Y.; Chen, L.; Liu, P.; Kang, J.; Fujita, T.; Chen, M. *J. Mater. Chem. A* **2014**, *2*, 10910-10916.
39. Shi, Y.; Pan, L.; Liu, B.; Wang, Y.; Cui, Y.; Bao, Z.; Yu, G. *J. Mater. Chem. A* **2014**, *2*, 6086-6091.
40. Zhu, Y.; Shi, K.; Zhitomirsky, I. *J. Mater. Chem. A* **2014**, *2*, 14666-14673.
41. Li, S.; Huang, D.; Yang, J.; Zhang, B.; Zhang, X.; Yang, G.; Wang, M.; Shen, Y. *Nano Energy* **2014**, *9*, 309-317.
42. Wang, F.; Zhan, X.; Cheng, Z.; Wang, Z.; Wang, Q.; Xu, K.; Safdar, M.; He, J. *Small* **2015**, *11*, 749-755.

Chapter 8

Outlook

As discussed in the previous chapters of this dissertation, carbon and carbonaceous materials are widely applied in electrochemical energy storage, as i) protective coatings for stabilizing materials with inherent instability; ii) electrically conductive substrates for loading other relatively insulating pseudo-capacitive materials and iii) active materials themselves. The challenge for purpose i) is to develop methodologies that are capable of depositing carbon thin films with controllable thickness and uniformity. Understanding on how ions interact with the underneath electrode materials via the coated carbon shell is currently lacking, and requires further investigations. Application ii) needs carbon structures with large ion-accessible surface and excellent electrical conductivity. The following parts elaborate on challenges and opportunities associated with application iii), and specifically related to a promising active carbonaceous materials, the hierarchical porous carbons.

With their unique connectivity of various scales of pores, hierarchical porous carbons have already displayed superior performance over traditional carbon materials. They are receiving increasing attention as promising carbon materials directly used for charge storage. A number of hierarchical carbon-based materials have achieved outstanding gravimetric capacitance beyond 300 F g^{-1} . Yet, an undeniable fact is that most hierarchical porous carbons fail to retain their

outstanding capacitance at rapid charge and discharge rates, *i.e.*, they exhibit poor rate capability performance as illustrated in Figure 8.1. This is particularly unfavorable for supercapacitors, a charge storage device expected to have large power density.^{1,2} Overcoming this bottleneck requires long-term joint efforts from both theoretical and experimental studies.

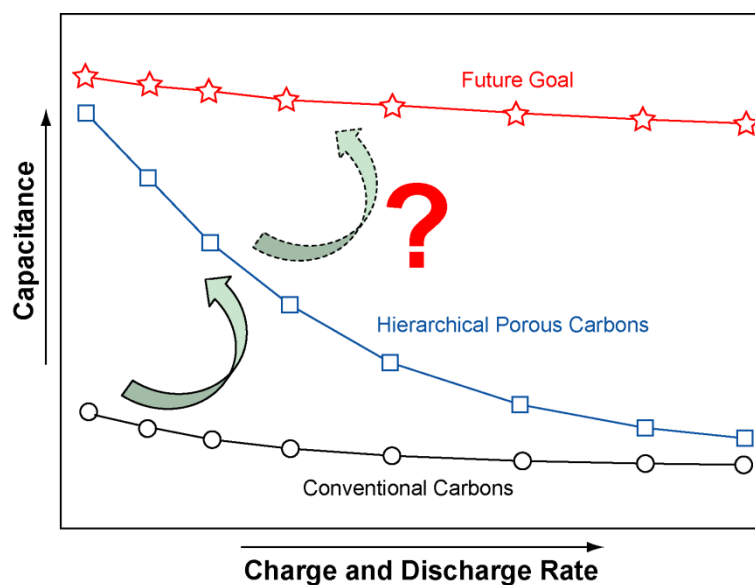


Figure 8.1 Comparison of capacitance among conventional carbons, hierarchical porous carbons and the future goal.

Molecular simulation is a powerful tool for investigating ion behaviors in complex electrochemical systems and expected to provide experimentalists the important insights on how to design and construct the “silver bullet”. Previous studies have been primarily focused on modelling ion diffusion within ultra-small pores,³⁻⁵ while revealing the collaborative roles of hierarchical pores is equally important but rarely studied. For example, the roles of mesopores and macropores in facilitating ion diffusion deserve further investigation, possibly including the

influences from hetero-atoms. Also, the correlation between total pore/micro-pore volumes and capacitances seems rather ambiguous. Simulations on hierarchical porous systems that take different pore sizes, structures and distributions into consideration could possibly solve the puzzle. Another direction that needs to be explored is simulating ion behaviors in aqueous electrolytes. To date, most theoretical studies choose ionic liquids as electrolyte mainly because ions in ionic liquids have comparable size as pore widths;^{4,6-9} however, aqueous electrolytes are more popular in supercapacitor community owing to safety consideration, ease of fabrication and fast ion diffusion rate. Changing ionic liquids to aqueous electrolytes will bring significant changes in simulations: presence of solvation shell, different ion size and diffusion coefficients, and possible pseudo-capacitive contributions from doped heteroatoms, *etc.* The new results might alter our current understandings on ion-pore interactions and possibly induce unprecedented discoveries that inspire experimentalists to design novel structures to further push the performance of supercapacitors.

Once optimal structures are obtained by simulation, the next big challenge is to explore synthetic strategies that can achieve the proposed electrode architecture and experimentally confirm the simulation prediction. At this stage, most high-performance carbons are derived from direct pyrolysis of bio-masses due to the hierarchical porosity and rich amount of heteroatoms, indicating bio-mass derived carbons are promising carbon precursor candidates. However,

template-free methods have limitations in tuning the pore structures. On the other hand, both hard and soft template methods are able to change pore structures simply by tailoring the shape and number of templates and how they are incorporated in host materials. Therefore, a promising synthetic strategy to achieve the optimal structures is to combine these methods. For example, if the ion-desolvation theory holds true for aqueous electrolytes, electrodes with comparable pore size to ultra-small de-solvated ions (*e.g.*, H⁺, Li⁺, Na⁺) will perhaps achieve much higher capacitance than the state-of-the-art level. It is because ions in aqueous electrolytes are generally much smaller than ions in ionic liquids, resulting in more compact ion-packing. However, how to acquire these ultra-fine pores remains challenging and deserves extensive efforts in material synthesis.

Finally, it is extremely critical to develop a set of fair and consistent metrics for evaluating performance of porous carbon materials. First, gravimetric capacitance, areal capacitance and volumetric capacitance are three equally important performance metrics. In terms of portability and assuming the volume of electrodes or devices is not a concern, gravimetric capacitance is the most meaningful among the three. Whilst for applications with limited space for installing energy storage devices, areal capacitance and volumetric capacitance are more significant than gravimetric capacitance. Given that most hierarchical porous carbons are ultralight (low mass density), they are promising electrodes for

light-weight charge storage devices but are disadvantageous in areal and volumetric capacitance. Therefore, it is unreasonable to judge their performance by merely taking their areal or volumetric capacitance into consideration.

Second, it should be noted that high gravimetric/areal/volumetric capacitance will become less meaningful if the corresponding active mass loading/working area/total volume is ignored. Taking gravimetric capacitance as an example, the gross capacitance, or total capacitance (C_T), is evaluated by multiplying gravimetric capacitance (C_S) by active material mass loading (m):

$$C_T = C_S \times m$$

C_T will be ultra-small if the mass loading is tiny. It infers that a supercapacitor with limited amount of active material, though might exhibit outstandingly high gravimetric capacitance, will still be impractical as it can only store a small amount of charges. Similar arguments can be made for areal capacitance and volumetric capacitance. Moreover, because capacitance is a function of not only scan rate or current density, but also mass loading, arbitrarily comparing capacitance without considering mass loading is unfair for high active mass loaded electrodes. It is therefore critical for researchers to be aware of this issue, and present mass loading, area or volumetric capacitance for evaluation and comparison. It is more meaningful to push performance at high mass loadings rather than to pursue large numbers with ultra-small amount of active materials.

References

1. Lu, X.; Yu, M.; Wang, G.; Tong, Y.; Li, Y. *Energy Environ. Sci.* **2014**, *7*, 2160-2181.
2. Salunkhe, R. R.; Lee, Y.-H.; Chang, K.-H.; Li, J.-M.; Simon, P.; Tang, J.; Torad, N. L.; Hu, C.-C.; Yamauchi, Y. *Chem.-Eur. J.* **2014**, *20*, 13838-13852.
3. Urita, K.; Ide, N.; Isobe, K.; Furukawa, H.; Moriguchi, I. *ACS Nano* **2014**, *8*, 3614-3619.
4. Prehal, C.; Weingarh, D.; Perre, E.; Lechner, R. T.; Amenitsch, H.; Paris, O.; Presserbd, V. *Energy Environ. Sci.* **2015**, *8*, 1725-1735.
5. Galhena, D. T. L.; Bayer, B. C.; Hofmann, S.; Amaratunga, G. A. J. *ACS Nano* **2016**, *10*, 747-754.
6. Jiang, D.-e.; Jin, Z.; Wu, J. *Nano Lett.* **2011**, *11*, 5373-5377.
7. Pean, C.; Merlet, C.; Rotenberg, B.; Madden, P. A.; Taberna, P.-L.; Daffos, B.; Salanne, M.; Simon, P. *ACS Nano* **2014**, *8*, 1576-1583.
8. He, Y.; Huang, J.; Sumpter, B. G.; Kornyshev, A. A.; Qiao, R. *J. Phys. Chem. Lett.* **2015**, *6*, 22-30.
9. Zhan, C.; Lian, C.; Zhang, Y.; Thompson, M. W.; Xie, Y.; Wu, J.; Kent, P. R. C.; Cummings, P. T.; Jiang, D.; Wesolowski, D. J. *Adv. Sci.* **2017**, 1700059.